Drag Reduction of Bluff Bodies by Passive Control of Boundary Layer Transition & Separation

Ben Lewis Clapperton Surfleet

Department of Aeronautics

Imperial College London

Submitted in partial fulfilment of the requirements for the degree of

Doctor of Philosophy of Imperial College London

and the Diploma of Imperial College London

Submitted 21st November 2016

Revised 21st April 2017

Statement of Originality

I do hereby declare that this thesis, and the research upon which it is written, is entirely my own work apart from that which is clearly indicated to be otherwise, but where I have used the work of others I have acknowledged and referenced it appropriately.

Ben L. Clapperton Surfleet

21 November 2016

Copyright Declaration

The copyright of this thesis rests with the author and is made available under a Creative Commons Attribution Non-Commercial No Derivatives licence. Researchers are free to copy, distribute or transmit the thesis on the condition that they attribute it, that they do not use it for commercial purposes and that they do not alter, transform or build upon it. For any reuse or redistribution, researchers must make clear to others the licence terms of this work.

Abstract

In many sporting activities the athletes and their associated equipment often operate in a range of Reynolds number, Re, that is close to the critical regime where the boundary layer flow undergoes transition from a laminar to a turbulent state. It is well known from numerous studies on circular cylinder and sphere flows that boundary layer transition can be forced to occur at lower Re, and hence drag reduced by delaying flow separation, through the application of, for example, roughness to the surface. This thesis is aimed at increasing understanding of how passive flow control methods might be employed to influence boundary layer flow in order to reduce the drag of bluff bodies.

A wind tunnel based research programme was undertaken to study these aspects, including a review of a selection of commonly studied boundary layer tripping methods. The main body of the thesis is devoted to the investigation of two novel passive flow control concepts, developed for this research, which were found to significantly reduce the drag coefficient in the sub-critical Re flow regime of a plain cylinder.

Of these two concepts, the main research focus was on identifying the drag reducing mechanisms of a system of passive, continuously blowing jets. It was found that the interaction of the jets and cross-flow induced a very high frequency instability which leads to the downstream formation of tornado-like vortices which are shed into, and identified in the near-wake. It is postulated that the introduction of stream-wise vorticity into the separating shear layer develops favourable drag reducing mechanisms. Discrete cylindrical surface protrusions were additionally found to develop similar effects on flow topology and drag reduction, and were more effective than the passive jets at low Reynolds numbers.

Acknowledgements

First and foremost I would like to thank my supervisor, Professor Peter Bearman, and co-supervisor, Professor Jonathan Morrison, for giving me the opportunity to work on this research. I am particularly grateful for the guidance and assistance provided by Professor Bearman, who deserves great credit not only for his unceasing enthusiasm for my research, but also for his kind patience, counsel and commitment to getting me through my PhD.

I would like to thank Professor Spencer Sherwin for his generous and willing help in reviewing my work and progress at various stages of my research, and for his assistance in securing additional funding in the latter stages of my PhD. Thanks are also due to Dr Andy Peace of Aircraft Research Association and Professor Sherwin for their supervision of my MSc project which helped propel me into doctoral research.

I must thank UK Sport and the English Institute of Sport (EIS) for funding this research in collaboration with the Engineering and Physical Sciences Research Council (EPSRC) through a Co-operative Awards in Science and Engineering (CASE) collaboration with Imperial College of Science, Technology and Medicine. I am also very grateful for the financial assistance from the Royal Aeronautical Society (RAeS) who provided me with additional funding in the latter stages of my PhD.

This body of research would not have been possible without the great skill and knowledgeable assistance of the Aeronautics Workshop staff who have help me in countless ways throughout my research. I'm especially grateful for the support over the years from Ian James, Roland Hutchins, Alan Smith, Mark Grant and Ian Pardew.

For help with numerous equipment and apparatus issues, in addition to ever-fair adjudication of negotiations for wind tunnel bookings, I would like to thank Dr Nigel MacCarthy.

The work and assistance from those who deal with the management and administration of the Department for Aeronautics is perhaps less acknowledged than it should be and so I would also like to give thanks in particular to Molly Ip and Lisa Kelly for the innumerable times they have helped and guided me throughout my time at Imperial College.

For all of the enlightening company, conversations, inspiration and support over the years in the Aero department I would like to thank Salvatore Maraniello, David Hankin, Duncan McNae, Kevin Gouder, Georgios Rigas, Jean-Eloi Lombard, Marcos Garcia de la Cruz Lopez, and Rowan Brackston.

I am immensely grateful for the kind and unfailing support from my family to get me to the point of submitting this thesis. In particular, for all of their help during my write-up period, I would like to thank my mother, Helen, and mother-in-law, Joyce, for their weekly childcare and financial support. My father, Bruce, and father-in-law, Roddy, have helped out at times too.

Finally, my deepest and most sincere gratitude is reserved for my wife, Gill, for her love, patience and resilience over the years and, more recently, for my special little boy, Roddy, who has shown me that there are more difficult and complicated things to manage than a PhD. I love you both.

Note about presentation of figures:

All plots generated by the author for this thesis have been produced using a colour-blind safe, print-friendly colour scheme as devised by Tol (2012). For further information, the reader is directed to his notes at https://personal.sron.nl/~pault/

Contents

Abstract **5**

Acknowledgements **7**

List of Figures **19**

Nomenclature **29**

1 Introduction **35**

1.1 Definition of research problem 35

1.2 Background & motivation 35

1.2.1 Typical Reynolds numbers for professional cycling 37

1.3 Aims & objectives of research 39

2 Literature review **41**

2.1 Overview of smooth cylinder flow regimes in Re range of interest . . . 42

2.1.1 Transition in Shear Layers (TrSL) 43

2.1.2 Transition in Boundary Layers (TrBL) 44

2.1.3 Reynolds number range of interest 44

2.2 Sub-critical state of flow, or Transition in Shear Layers (TrSL) 45

2.3 Critical state of flow, or Transition in Boundary Layers (TrBL) 46
2.3.1 Pre-critical regime 46
2.3.2 Single-bubble regime 47
2.3.3 Two-bubble regime 49
2.3.4 Super-critial regime 50
2.3.5 Post-critical regime 51
2.4 Passive methods for altering the C_D characteristics of bluff bodies . . 53
2.4.1 Surface roughness 53
2.4.1.1 Flow specific positioning of surface roughness 61
2.4.1.2 Summary of conclusions: Surface roughness 62
2.4.2 Surface roughness texture 63
2.4.2.1 Consistent classification of relative roughness 63
2.4.2.2 Representation of relative roughness parameter . . . 64
2.4.2.3 Roughness Reynolds number 64
2.4.2.4 Summary of conclusions: Surface roughness texture . 65
2.4.3 Tripping the flow 66
2.4.3.1 Tripping wires 66
2.4.3.2 Effect of tripping wire location 67
2.4.3.3 Fluid mechanics of the tripping wire 69
2.4.3.4 Summary of conclusions: Tripping wires 70
2.4.4 Vortex generators 71
2.4.4.1 Summary of conclusions: Vortex generators 74
2.4.5 Grooves 75
2.4.5.1 Circumferential grooves 75
2.4.5.2 Partially grooved surface 78

2.4.5.3 Spanwise grooves 78
2.4.5.4 Summary of conclusions: Grooves 80
2.4.6 Dimples 80
2.4.6.1 Comments on dimples v. sand-roughness 84
2.4.6.2 Summary of conclusions: Dimples 84
2.5 Final notes on passive drag reduction 86
2.5.1 General passive flow control methodology 87
2.5.2 Optimal placement of passive flow control devices 87
2.5.3 Note on separation bubble 88

3 Experimental setup **89**

3.1 Wind tunnel 89
3.2 Cylinder setup 91
3.2.1 Coordinate system 91
3.3 Force measurements 92
3.4 Passive jet simulation 95
3.5 Jet flow-rate measurements 97
3.6 Flow visualisation 98
3.7 Constant temperature anemometry 100
3.7.1 Wake traversing 100
3.7.2 Jet shear layer instability 101
3.8 Particle image velocimetry 104
3.8.1 Single camera, (x, y) plane 104
3.8.2 Stereo configuration, (y, z) plane 106

4 Review of dimples and tripping wires **109**

4.1 Experimental arrangement 110

4.2 Results 111

4.3 Discussion 114

4.4 Conclusions 117

5 Transverse jets: Primary investigations **119**

5.1 Conception 119

5.2 Feasibility study 121

5.3 Passive control of transverse jets 130

5.3.1 Effect of jet velocity on C_D reduction 136

5.4 Directional sensitivity 138

5.5 Disruption of von Kármán vortex shedding 142

6 Transverse jets: Investigation of flow mechanisms **147**

6.1 Overview of jets in cross-flow 147

6.2 Estimation of cross-flow velocity 150

6.3 Transverse jet velocity 154

6.4 Low velocity-ratio jets in cross-flow 160

6.5 Spectral analysis of jet instability 162

6.5.1 The shear layer instability 162

6.5.2 Formation of hairpin vortices 167

6.5.3 Parameters which affect formation and structure 169

6.5.4 Outline of experimental approach 175

6.5.5 Results and discussion 177

7 Transverse jets: Flow topology **193**

7.1 Introduction . . . 193

7.2 Passive jets, $z_J = 20mm$ . . . 197

7.2.1 SOFV results . . . 197

7.2.2 Interpretation of flow visualisation . . . 200

7.2.3 Similar flow topology in the literature . . . 208

7.2.4 Imposing three-dimensional flow topology . . . 212

7.3 Passive jets, $z_J = 10mm$ . . . 216

7.4 Development of skin friction lines with Re_D . . . 224

7.4.1 $0.94 \times 10^5 \leqslant Re_D \leqslant 1.13 \times 10^5$ . . . 228

7.4.2 $1.38 \times 10^5 \leqslant Re_D \leqslant 1.70 \times 10^5$ . . . 234

7.4.3 $Re_D = 2.74 \times 10^5$ . . . 235

8 Transverse jets: Shear layer development and wake dynamics **237**

8.1 Flow separation . . . 238

8.2 Shear layer development/mixing . . . 245

8.3 Mean-flow correlation with jet spacing . . . 249

8.4 Correlation with skin friction line patterns and flow topology . . . 252

8.5 Development of vorticity with Reynolds number . . . 255

8.6 Shear layer span-wise waviness and correlation with wake vorticity . . . 261

9 Discrete boundary layer protrusions – "Pins" **269**

9.1 C_D v. Re_D characteristics . . . 273

9.1.1 Variation of pin spacing . . . 275

9.2 Skin friction line patterns and flow topology . . . 277

9.2.1 Comparison of $z_P = 10mm$ & $z_P = 20mm$ . . . 281

9.2.2 Schematic interpretation of skin friction patterns 284
9.3 Shear layer development & wake dynamics 293
9.3.1 Comparison with passive jets at high Reynolds numbers . . . 293
9.3.2 Correlation of skin friction line patterns with near-wake structure 296
9.3.3 Comparisons of near-wake characteristics of pins and passive jets in the low – mid Re_D range 298

10 Summary of conclusions **307**
10.1 General approach to passive drag reduction of bluff-bodies 307
10.2 Transverse jets: Primary investigations 308
10.3 Transverse jets: Flow mechanisms 310
10.4 Transverse jets: Flow topology 311
10.5 Transverse jets: Shear layer and wake dynamics 313
10.6 Discrete boundary layer protrusions – "Pins" 314
10.7 Final comments 317

11 Suggestions for further work **319**

References **323**

Appendix A Feasibility study: Calculations for passive jet flow **343**
A.1 Method: Part 1 344
A.1.1 Pipe-flow ancillary losses 347
A.1.1.1 Bends and junctions 347
A.1.1.2 Entry and exit losses 348
A.2 Method: Part 2 349

A.3 Example calculation: jet velocity prediction 351
A.4 Laminar flow velocity profile 353
A.5 Note on the calculation methodology 354

Appendix B Feasibility study: Supplementary test results 357

Appendix C Mass flux coefficient, C_J, of passive jets system 361

Appendix D von Kármán vortex shedding: Supplementary periodogram covering full Re_D test range 363

Appendix E Jet instability: Supplementary periodograms 365

Appendix F Flow topology: Supplementary results & graphics 369

F.1 Variation in skin friction line patterns with Re_D, $z_J = 10mm$ passive jets 370
F.2 Proof of attachment node, $z_J = 20mm$ 372
F.3 Alternative flow topology, owl type-2 skin friction pattern 373

Appendix G Shear layer development & wake dynamics: Supplementary results 375

G.1 (x, y) plane 376
G.1.1 Cross-flow velocity, u/U_∞ 376
G.1.2 Plots of u_x/U_∞ with full velocity scale 378
G.2 (y, z) plane 381
G.2.1 Plain cylinder reference data: Vorticity, Ω 381
G.2.2 Plain cylinder reference data: Free-stream velocity component, u_x/U_∞ 384

G.3 Near-wake u_x/U_∞ in (y, z) plane for cylinder with $z_P = 20mm$ pins . 387

Appendix H Wind tunnel blockage corrections **393**

H.1 Free stream velocity , U_∞ 395

H.2 Drag coefficient, C_D 396

H.3 Lift coefficient , C_L 396

H.4 Pressure coefficient, C_p 397

List of Figures

1.1 Range of *Re* experienced in professional cycling 37

2.1 Characteristic Drag Coefficient Curve of a Plain Cylinder, Achenbach (1971) 42

2.2 Skin friction and local pressure distribution for a smooth cylinder (sub-critical regime), Achenbach (1968) 45

2.3 Skin friction and local pressure distribution for a smooth cylinder (pre-critical regime), Achenbach (1968) 47

2.4 Variation of base pressure coefficient with Reynolds number for a plain cylinder, Bearman (1969) 48

2.5 Skin friction and local pressure distribution for a smooth cylinder (critical regime), Achenbach (1968) 49

2.6 Flow regimes for a plain circular cylinder, Zdravkovich (1990) 51

2.7 Skin friction and local pressure distribution for a smooth cylinder (post-critical regime), Achenbach (1968) 52

2.8 Drag coefficient curves for a cylinder with varying grades of surface roughness, Fage and Warsap (1930) 55

2.9 Boundaries between flow regimes for varying grades of surface roughness, Buresti (1981) . . . 58
2.10 Percentage of friction forces with respect to total drag for a circular cylinder, Achenbach (1971) . . . 60
2.11 Effect on C_D of limited surface roughness on a circular cylinder, Fage and Warsap (1930) . . . 61
2.12 Critical and trans-critical drag v. surface roughness for a circular cylinder, Niemann and Holscher (1990) . . . 65
2.13 Effect on C_D of tripping wires at $\phi_w = \pm 65^\circ$ on a circular cylinder, Fage and Warsap (1930) . . . 67
2.14 Plot of C_D v. Re for various tripping wire locations on a sphere, Son et al. (2011) . . . 68
2.15 2D flow schematics for cylinders with span-wise tripping wires at various angular positions, Igarashi (1986) . . . 70
2.16 Schematics of vortex generators, Johnson and Joubert (1969) . . . 72
2.17 C_D v. Re curves for a circular cylinder fitted with vortex generators at varying angles, Johnson and Joubert (1969) . . . 74
2.18 Schematic of a grooved cylinder, Ko et al. (1987) . . . 76
2.19 Comparison of C_D of V-groove and rough cylinders, Ko et al. (1987) . . . 77
2.20 Proposed cavity flow mechanism of a spanwise groove, Kimura and Tsutahara (1991) . . . 79
2.21 Variation of C_D with Reynolds number for smooth, sand-roughened and dimpled circular cylinders, Bearman and Harvey (1993). . . . 82
2.22 Variation of C_D with Reynolds number for two orientations of dimple surfaced circular cylinders, Bearman and Harvey (1993). . . . 83

2.23 Variation of C_D with Reynolds number for smooth, surface roughened and dimpled spheres, Bearman and Harvey (1976). 85
2.24 Variation of C_D with Reynolds number for smooth, surface roughened, dimpled and tripping wire affixed spheres, Son et al. (2011). 86

3.1 Cylinder mounted in wind tunnel 90
3.2 Coordinate system schematic 92
3.3 Wind tunnel setup for force balance measurements 93
3.4 Cylinder Schematic for Compressed Air Supply 96
3.5 Photograph of wake traversing hot-wire probe in position 101
3.6 Hot wire acquisition position for measuring jet instability 102
3.7 Wind tunnel setup for jet instability hot-wire experiments 103
3.8 Photograph and schematic of (x, y) plane PIV setup 105
3.9 Stereo PIV Wind Tunnel Setup 2 106
3.10 Stereo PIV Wind Tunnel Setup 107

4.1 Schematic of dimpled cylinder arrangement, from Bearman and Harvey (1993) 110
4.2 Drag Coefficient of Various Cylinder Arrangements 112
4.3 Drag coefficient and Strouhal number for plain and tripping wire cylinders 113

5.1 Theoretical ΔC_p available for passive jet concept 120
5.2 Schematic of cylinder with passive jet concept 121
5.3 Exploded assembly schematic; passive jets feasibility study setup . . . 124
5.4 C_D v. Re curves for passive jets feasibility study 126
5.5 C_L v. Re curves for passive jets cylinder with no air supply 128

5.6 Model design schematic; cylinder with passive jets 130
5.7 C_D v. Re for passive jets 131
5.8 $C_{p(int)}$ v. Re and C_L v. Re for passive jets 134
5.9 Comparison of internal cylinder pressures with C_D 137
5.10 Directional sensitivity study for passive jets, C_D 139
5.11 Directional sensitivity study for passive jets, C_L 140
5.12 Directional sensitivity study for passive jets, C_p 141
5.13 Power spectral density of cylinder wake with passive jets 143

6.1 Schematic of a jet in cross-flow, from Ilak et al. (2012) 149
6.2 Estimated variation of $C_{p,\phi=\pm65^\circ}$ with Re_D 151
6.3 Linear trend of Re_{cf} with Re_D 153
6.4 Variation of jet Reynolds number, Re_J, with cylinder Reynolds number, Re_D, for passive jets 155
6.5 Variation of $C_{p,(int)}$ with Re_D for passive jet flow-rate tests 156
6.6 Variation of jet to cross-flow velocity ratio, R, with Re_D 158
6.7 Trajectory of 'CRVP' for jets in cross-flow with varying R, from Cambonie et al. (2013) 161
6.8 Summary of jet in cross-flow phenomena, from Kelso et al. (1996) . . 165
6.9 Hairpin vortex shedding $R = 1$, from Sau and Mahesh (2008) 166
6.10 Vorticity contours of a jet in cross-flow, $R = 1$, from Sau and Mahesh (2008) 168
6.11 Variation in St_{d_J} and St_{δ_θ} with R, from Megerian et al. (2007) 171
6.12 Trajectory for jets in cross-flow with $R = 0.5$, from Peterson and Plesniak (2004) 172

6.13 Hot-wire position for shear layer instability detection 176

6.14 Periodogram of lowest Re_D detections of jet shear layer instability . . 178

6.15 Periodogram of hot-wire signal between holes 180

6.16 PSD of jet instability, $1.28 \times 10^5 \leqslant Re_D \leqslant 2.36 \times 10^5$ 182

6.17 Variation of jet instability frequency with Re_D 184

6.18 Jet instability $St_{U_{cf}}$ v. Re_{cf} 185

6.19 Jet instability $St_{U_{v_J}}$ v. Re_J 187

6.20 Jet instability $St_{U_{cf}}$ v. R 189

6.21 Variation of cylinder C_D and jet St_{U_∞} with Re_D 191

7.1 Classification of critical points 195

7.2 SOFV photograph, passive jets, $z_J = 20mm$ 198

7.3 SOFV photograph: passive jets, $z_J = 20mm$, reverse flow region . . . 199

7.4 Skin friction line schematic (a), 20mm spaced jets 202

7.5 Skin friction line schematic (b), 20mm spaced jets 203

7.6 Flow topology schematics of 'owl type-2' separation pattern in 3D, from Perry and Chong (1986) 210

7.7 Comparison of separation lines for tripping wires and passive jets, $Re \approx 2.8 \times 10^5$ 213

7.8 Video still of a SOFV test showing wavy separation line at $Re = 2.80 \times 10^5$ 214

7.9 Schematic of surface pattern for a cylinder with discrete protuberances, from Mizuno (1970) 215

7.10 SOFV photograph, passive jets, $z_J = 10mm$ 217

7.11 SOFV photographic comparison of $z_J = 10mm$ and $z_J = 20mm$ passive jets . . . 218

7.12 Skin friction line schematic (a), 10mm spaced jets . . . 220

7.13 SOFV instantaneous video still, passive jets, $z_J = 10mm$ . . . 221

7.14 Skin friction line schematic (b), 10mm spaced jets . . . 223

7.15 SOFV acquisition Re_D for $z_J = 10mm$ jets SOFV analysis . . . 225

7.16 Schematic of wall shear stress and critical points for a jet in cross-flow at $R = 0.3$, from Foss (1980) . . . 227

7.17 SOFV Jets, $z_J = 10mm$: $0.94 \times 10^5 \leqslant Re_D \leqslant 2.74 \times 10^5$ . . . 230

7.18 Comparison of C_D and angles of separation with Re_D for passive jets, $z_J = 10mm$ . . . 233

8.1 Flow separation angle for plain cylinder at $Re_D = 1.5 \times 10^5$ . . . 240

8.2 Flow separation angles for cylinder with $z_J = 20mm$ passive jets . . . 243

8.3 Time-mean length of recirculation region at $Re_D = 1.5 \times 10^5$; plain cylinder . . . 246

8.4 Time-mean length of recirculation region at $Re_D = 1.5 \times 10^5$; cylinder with passive jets . . . 248

8.5 Vorticity in (y, z) plane, $z_J = 20mm$, $Re_D = 2.5 \times 10^5$ . . . 250

8.6 Vorticity in (y, z) plane, plain cylinder, $Re_D = 2.5 \times 10^5$ . . . 251

8.7 Composite graphic of skin-friction pattern schematic with time-mean wake vorticity, $z_J = 20mm$, $Re_D = 2.7 \times 10^5$ . . . 254

8.8 C_D profile for $z_J = 20mm$ passive jets overlaid with SPIV acquisition Re_D . . . 256

8.9 Development of near-wake vorticity in (y, z) plane with Re_D, $z_J = 20mm$ passive jets 258

8.10 Comparison of near-wake vorticity, Ω, and stream-wise velocity, u_x/U_∞, in (y, z) plane with Re_D, $z_J = 20mm$ passive jets 262

9.1 Photograph of cylinder with "pin" protrusions test model 271

9.2 C_D v. Re_D for cylinder with "pins", $10mm \leqslant z_J \leqslant 20mm$ 273

9.3 C_D v. Re_D for cylinder with "pins", $10mm \leqslant z_J \leqslant 40mm$ 275

9.4 Schematic of hairpin vortex formation around cylindrical protrusion, from Doligalski et al. (1994) 277

9.5 Flow around a surface mounted cylindrical protrusion (Delery, 2001, 2011) 279

9.6 Near wall and boundary layer flow around a cylindrical protrusion and transverse jet, from Fric and Roshko (1994) 280

9.7 SOFV photographs for cylinder with pins, $z_P = 10mm$ & $z_P = 10mm$, $Re_D = 2.7 \times 10^5$ 282

9.8 Topology of the surface skin friction line pattern of the flow around a cylindrical protrusion, from Delery (2001) 284

9.9 Skin friction line schematic for cylinder with pins, $z_P = 10mm$ 286

9.10 U-shaped separation bubble schematic, from Perry and Chong (1986) 287

9.11 SOFV photographic comparison of $z_P = 10mm$ pins and $z_J = 10mm$ passive jets 288

9.12 Skin friction line schematic for cylinder with pins, $z_P = 20mm$ 290

9.13 SOFV photographic comparison of $z_P = 20mm$ pins and $z_J = 20mm$ passive jets 292

9.14 Comparison of near-wake vorticity and stream-wise velocity component in (y, z) plane, between $z_P = 20mm$ pins and $z_J = 20mm$ passive jets, $Re_D = 2.5 \times 10^5$ 294

9.15 Composite graphic of surface skin friction pattern with wake vorticity for cylinder with $z_P = 20mm$ pins 297

9.16 C_D profile for $z_P = 20mm$ pins and $z_J = 20mm$ jets, overlaid with SPIV acquisition Re_D 298

9.17 Comparison of near-wake vorticity, Ω, in (y, z) plane, for cylinders with $z_P = 20mm$ pins and $z_J = 20mm$ passive jets, at various Re_D . . 300

A.1 Moody chart, by Beck and Collins (2008) 346

B.1 C_D v. Re curves for various cylinder pressures 359

B.2 Passive jets C_D v. Re prediction from feasibility study 360

C.1 Variation of mass flux coefficient, C_J, with cylinder Reynolds number, Re_D for cylinder with passive jets 362

D.1 PSD of cylinder wake with passive jets over full Re test range 364

E.1 Periodogram of jet instability, $2.03 \times 10^5 \leqslant Re_D \leqslant 2.15 \times 10^5$ 366

E.2 Periodogram of jet instability, $2.46 \times 10^5 \leqslant Re_D \leqslant 2.56 \times 10^5$ 367

F.1 Photographic comparison of SOFV results for passive jets, $z_J = 10mm$, at various Re_D 370

F.2 Experimental proof of (re)attachment node 372

F.3 Skin friction lines and topology schematics of an ‘owl type-2’ separation bubble, from Fairlie (1980) 373

G.1 Local cross-flow velocity (u/U_∞) in the vicinity of $\phi = 65°$, from (x, y) plane PIV data, $Re_{D,\infty} = 1.5 \times 10^5$ 376
G.2 Mean u_x/U_∞ at full velocity scale for Plain, Jet and Pin cylinder arrangements 378
G.3 Full velocity scale ($\bar{u}_x/U_\infty$) plots of shear layer and wake at $Re = 1.5 \times 10^5$ 379
G.4 Near-wake vorticity in (y, z) plane, of a plain cylinder at various Re_D 381
G.5 Mean u_x/U_∞ plotted in (y, z) plane of the near wake of a plain cylinder at various Re_D 384
G.6 Mean u_x/U_∞ in (y, z) plane of the near wake of cylinder; comparison of pins and passive jets flow control at various Re_D 387

Nomenclature

Acronyms

CA Compressed Air

CCD Charge Coupled Device (camera image sensor)

CRVP Counter Rotating Vortex Pair

CRVQ Counter Rotating Vortex Quartet

DNS Direct Numerical Simulation

FFT Fast Fourier Transform

FOV Field Of View

HWA Hot Wire Anemometry

JICF Jets In Cross Flow

PID Proportional Integral Derivative (controller)

PIV Particle Image Velocimetry

PSD Power Spectral Density

SOFV Surface Oil Flow Visualisation

SPIV Stereo Particle Image Velocimetry

TrBL Transition in Boundary Layers (flow regime)

TrSL Transition in (free) Shear Layers (flow regime)

Greek letters

Δ	Difference of, or change in variable	–
δ	Boundary layer thickness; distance, normal to the wall, to $u_\delta = 0.99U_\infty$	m
$\delta_$	Small difference or change in a variable or parameter	–
δ_*	Boundary layer displacement thickness	m
δ_θ	Boundary layer momentum thickness	m
μ	Dynamic viscosity	$kg/(s.m)$
ν	Kinematic viscosity	m^2/s
Ω	Vorticity (time-mean)	s^{-1}
ϕ	Angle, relative to frontal stagnation point ($\phi = 0°$), on cylinder surface	$^\circ$
ϕ_s	Angle of separation on cylinder surface	$^\circ$
ρ	Density	kg/m^3

Roman letters

A_J	Area of jet exit hole	m^2
C_D	Drag coefficient	-
C_f	Skin friction coefficient	-
C_J	Jet mass flux coefficient	-
C_L	Lift coefficient	-
C_p	Pressure coefficient	-
$C_{p(int)}$	Internal cylinder pressure coefficient	-
D	Cylinder diameter	m
d_J	Jet diameter	m
d_P	Pin diameter	m
F	Focus (critical point)	-
f	Instability frequency	Hz
f	Pipe friction factor	-
g	Gravitational constant	ms^{-2}
h_f	Pipe head loss to friction	m
h_l	Pipe ancillary head loss	m
J	Jet to cross-flow momentum flux ratio	-

K	Mean excrescence height, relative to body surface	m
k	Pipe loss coefficient	-
K_s	Sand-roughness-equivalent mean excrescence height	m
L	Cylinder span	m
l_J	Jet supply 'pipe' or 'stroke' length	m
l_P	Pin length (protruding length, normal to wall)	m
M	Jet to cross-flow blowing ratio	-
N	Node (critical point)	-
n_J	Total number of jet exit holes	-
p	Pressure	Pa
$p_{(add)}$	Added cylinder pressure from compressed air supply	Pa
$p_{(int)}$	Internal cylinder pressure	Pa
R	Jet to cross-flow velocity ratio	-
r	Pipe radius	m
Re	Reynolds number	-
Re_{crit}	Critical Reynolds number	-
Re_D	Cylinder Reynolds number, based on cylinder diameter, D	-
Re_J	Jet Reynolds number, based on jet exit hole diameter, d_J	-

Re_K	Roughness Reynolds number, based on mean excrescence height, K	-
Re_P	Pin Reynolds number, based on pin diameter, d_P	-
S	Saddle point (critical point)	-
St	Strouhal number	-
T_e	Surface texture	-
T_i	Turbulence intensity	%
T_s	Turbulence scale	%
u	Local velocity	m/s
U_∞	Free stream velocity	m/s
u_x	Local velocity, x-direction component	m/s
V_J	Jet velocity	m/s
x	Horizontal coordinate, free stream direction; left→right	m
y	Vertical coordinate; down→up	m
z	Horizontal coordinate, span-wise direction; near→far	m
z_J	Jet spacing	m
z_P	Pin spacing	m

Other subscripts, superscripts etc.

The following notation is given where X is a generic variable or parameter to be replaced as required:

$\overline{X}$	Mean value of X
X'	Fluctuating component of X
X_∞	Free stream value of X
X_{cf}	Cross-flow value of X
X_g	Groove value of X
X_{int}	Internal cylinder volume value of X
X_J	Jet value of X
X_{max}	Maximum value of X
X_{min}	Minimum value of X
X_{vg}	Vortex generator value of X
X_w	Tripping wire value of X

Chapter 1

Introduction

1.1 Definition of research problem

This research study is aimed at increasing understanding of how passive flow control methods might be employed to influence boundary layer flow in order to reduce the drag of bluff bodies. A wind tunnel based research programme has been undertaken to study these aspects. The bluff body shape analysed is a circular cylinder and, unless otherwise stated, the characteristic length used to calculate Reynolds number is the cylinder diameter. While the research is fundamental in nature it has wide ranging application including the possibility of improving sporting performance.

1.2 Background & motivation

In many sporting activities the athletes and their associated equipment often operate in a range of Reynolds number (Re, Equation 1.1) that is close to the critical regime where the boundary layer flow undergoes transition from a laminar to a turbulent

state (see section 2.1). In a gradually increasing pressure gradient, the enhanced momentum of a turbulent boundary layer can delay flow separation. It is well known from numerous studies on circular cylinder and sphere flows that boundary layer transition can be forced to occur at a lower Re, and hence drag reduced by delaying flow separation, through the application of roughness to the surface. Indentations such as dimples produce a similar effect, as is well known from studies of the golf ball. The research for this thesis was carried out in collaboration with UK Sport, and latterly the English Institute of Sport (EIS), with the aim of improving understanding of bluff body drag reduction methods with potential application to professional cycle racing, among other sports. In the case of professional cycle racing, the flow over the arms and legs of the rider and the helmet approach the critical regime – see Figure 1.1. Technologies now exist to enable the incorporation of various surface textures and porosities into fabrics and materials that might be used for sports' clothing and equipment, offering the potential to reduce aerodynamic drag. The way surface textures and other passive flow control methods affect the flow around bluff bodies will be studied in this research.

$$Re = \frac{\rho U D}{\mu} \tag{1.1}$$

... where ρ, U and μ are the flow density, velocity and dynamic viscosity, respectively; and D is the characteristic length.

1.2.1 Typical Reynolds numbers for professional cycling

It is worth noting that, for a professional cyclist, up to – and perhaps in excess of – 90% of the total resistance the athlete must overcome is aerodynamic drag (see Defraeye et al., 2014; Zdravkovich et al., 1996). By far the largest contributor to this aerodynamic drag is that of the rider and thus there are significant gains to be made by concentrating research and development in this area as opposed to the

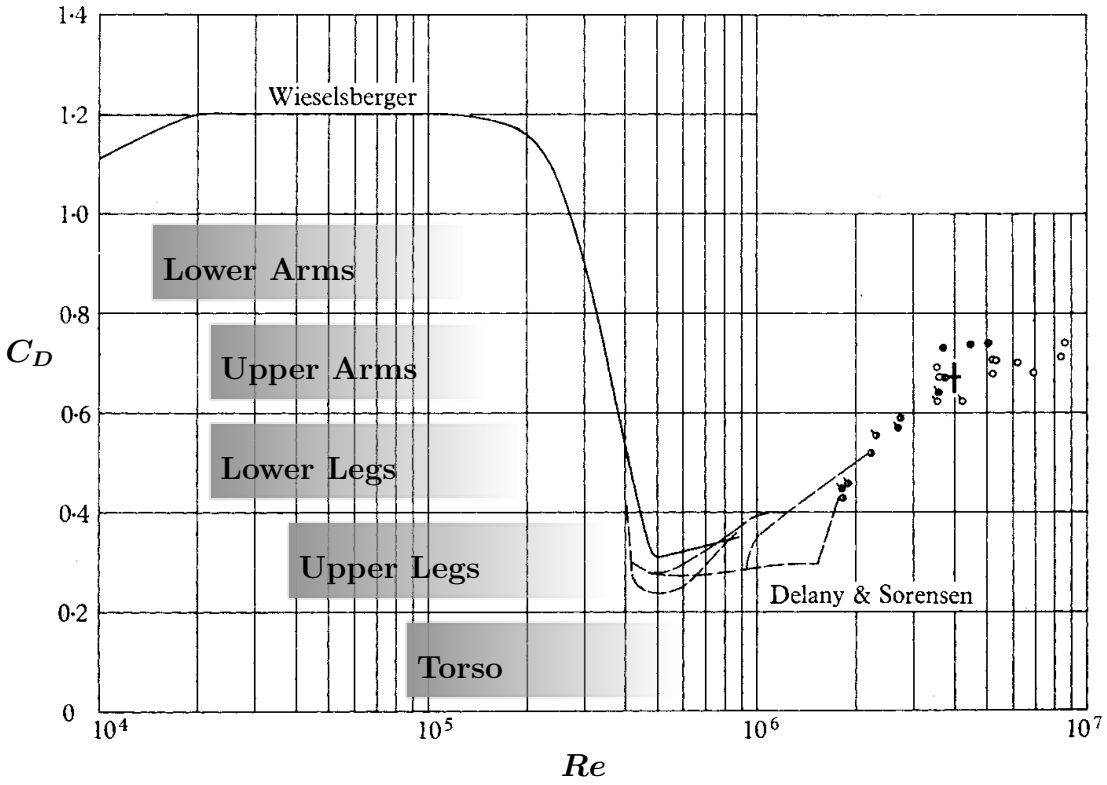

Figure 1.1 – Estimated ranges of Re for rider anatomy in professional cycling (shaded horizontal bars cover calculated Re range), for typical flow speeds experienced in both track and road disciplines of $5m/s \leqslant \bar{U}_\infty \leqslant 20m/s$ $(18 - 72km/h)$, overlaid on a C_D v. Re curve for a circular cylinder (from Roshko, 1961)), where C_D is the drag coefficient associated with the cylinder diameter (Equation 1.2). For the majority of flow speeds experienced in professional cycling, the rider will remain in the high drag, pre-critical regime.

limited benefits that can be had by improving the aerodynamics of the bicycle.

The average speed of the winner of le Tour de France in 2015 was 40km/h (Amaury Sport Organisation, 2015) and at this speed – from Figure 1.1 – all but back length (distance from shoulders to base of spine) and torso anatomy remain in the sub critical, high drag flow regime. The Reynolds number and drag of a rider varies considerably with their size and shape; for example, it is considered by Zdravkovich et al. (1996) that the height-to-waist width ratio strongly influences drag coefficient, so clearly the speeds at which the critical regime is reached varies considerably even amongst professional cyclists. The plot shown in Figure 1.1 accounts for a wide variety of anatomical sizes, yet no part of even the largest riders travelling at 40km/h will reach the Re range of the minimum C_D (see Equation 1.2) shown here. Based on the numbers generated here, an average sized cyclist would have to be travelling at 225km/h for anatomy such as the arms to approach a near critical drag coefficient at $Re = 4 \times 10^5$, or $100km/h$ to achieve similar conditions for the helmet. There are, therefore, significant opportunities for drag reduction of the cyclist where a large number of areas remain within the sub critical regime. Thus, the motivation for this research is to develop novel ways of inducing the critical regime to occur at lower Reynolds numbers with application in sporting activities, such as cycling.

$$C_D = \frac{F_D}{\frac{1}{2}\rho {U_\infty}^2 LD} \tag{1.2}$$

... where F_D is the drag force and LD represents the cross-sectional area in the plane normal to the flow direction (for cylinder flow this corresponds to the length of the span, L, multiplied by the diameter, D.)

1.3 Aims & objectives of research

The primary aim of this research study is to develop and investigate the fundamental mechanics of novel flow-control methods which reduce the drag of bluff-bodies operating in the sub-critical Re range, such as those which may be applied in sporting activities. The research was not dictated primarily by a specific field application, however the methods investigated were to be passively operational such that they could be legally operated in a professional sporting capacity. On the classification of flow control methods, Gad-el Hak (2000) states that a passive device requires no auxiliary power and no control loop, whereas active flow control requires both energy expenditure and a control loop. The fundamental approach, through which this passive drag reduction may be achieved, was by manipulation of boundary layer transition and separation to achieve favourable flow characteristics – in both the boundary layer and wake – throughout the Re range of interest for this research.

A fundamental understanding of the flow mechanisms created by these passive flow control methods, and the influence they have on the flow characteristics and development, was to be sought and harnessed such that proper application and optimisation of the flow control may be achieved for a variety of bluff-body setups. The arrangement and positioning of a flow control device is central to its ability to impart a beneficial effect on the flow characteristics and therefore requires significant investigation in tandem with the method. Drag reduction flow control methods can be unidirectional or omnidirectional; that is, they can be designed to operate effectively in one (known) flow direction, or in many or all flow directions, respectively. This research is concerned with applications which generally have a known mean flow direction (e.g. cycling), but beyond the simple case of two-dimensional straight-line

transition or separation, real-world flows are not often ideally incident to the body or optimally aligned with the flow control device. As such, directional sensitivity and deviation from the optimal design conditions will also be investigated.

A thorough analysis and explanation of the flow control methods of this research will be presented primarily by means of experimental investigation.

To summarise, the intended outcomes of this thesis were to:

- Develop effective passive drag-reducing flow control methods which operate in the range $3{\times}10^4 \leqslant Re_D \leqslant 3{\times}10^5$;
- Understand, describe and provide evidence of the fundamental flow mechanisms of the flow control methods developed, relating these to the drag characteristics;
- Broaden insight on the methods of delaying flow separation and inducing strongly three-dimensional wake dynamics along with their corresponding effect on cylinder drag;
- Further knowledge of low jet to cross-flow velocity ratio transverse jets, particularly when applied in an array to curved surfaces with pressure gradients;
- Hypothesise optimum flow control strategies based on the research, relating to desired boundary layer and wake characteristics which provide the best drag reduction over the Re_D range of interest.

Chapter 2

Literature review

Bluff bodies, by definition, are not streamlined in shape and therefore produce substantial areas of flow separation which generate large losses through an asymmetrical mean pressure distribution between the front and back of the body. There has long been a desire to understand and beneficially influence fluid flows around bluff bodies for a multitude of applications. The circular cylinder, in particular, has historically received much attention from researchers studying bluff-body flows. As the test model of this research, the circular cylinder and its flow regimes – along with the passive methods devised to reduce its aerodynamic drag – are the primary focus of this literature review.

2.1 Overview of smooth cylinder flow regimes in *Re* range of interest

Historically, researchers of circular cylinder flow have used numerous and subtly different terms to describe the various flow states encountered. With the proliferation of conflicting terminology, confusion has arisen out of a need for a definite nomenclature. Wieselsberger (1921) refers to flow regimes above and below the 'critical Reynolds number' or 'critical point' at which a sudden and large fall in C_D occurs and continues to decrease with increasing Reynolds number – the 'drag

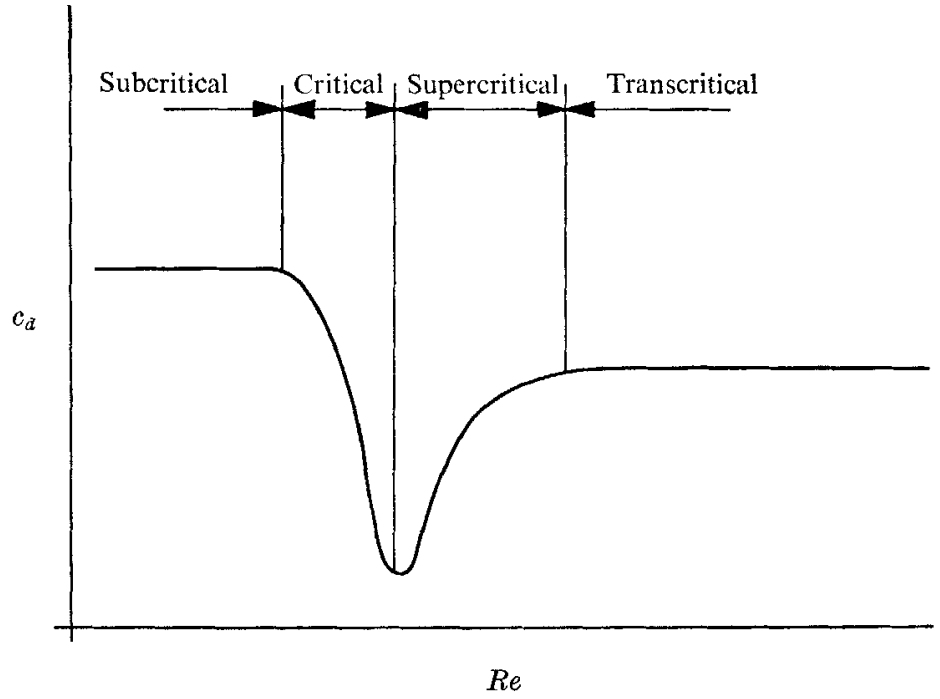

Figure 2.1 – Plot outlining the main flow states, with respect to the variation in C_D with Reynolds number, for a Plain Cylinder. From Achenbach (1971), where 'transcritical' is equivalent to post-critical. This research is focused on manipulating the C_D within the sub-critical regime.

crisis'. With increasing research in the area, several other flow regimes have been discovered around and within these 'sub-critical' and 'critical' phases. Once the fall in C_D ceases, a new state of flow is established – the 'super-critical' regime – marked by an increase in C_D Figure 2.1.

With increasing Re another distinct change in the trend of C_D marks an additional flow state. The plateau in C_D at high Re is now commonly referred to as the 'post-critical' regime. There has been much debate among researchers about the naming of this final flow state and here, in Figure 2.1, Achenbach (1971) uses the term 'transcritical'.

Zdravkovich (1997) proposes a more detailed breakdown of the flow states discovered fore and aft of the Wieselsberger (1921) critical point, based on the location in the flow where transition from a laminar to turbulent flow occurs. Of interest in this project are the flow states described by Zdravkovich (1997) as 'Transition in Shear Layers' (TrSL) and 'Transition in Boundary Layers' (TrBL).

2.1.1 Transition in Shear Layers (TrSL)

This term is used to describe a flow which transitions along the free shear layers while maintaining a laminar boundary layer. The term 'subcritical' was used by Wieselsberger (1921) to describe a state of flow with fully laminar boundary layers. The following Re ranges are for a plain, smooth circular cylinder:

- TrSL1: Development of transition waves; $(350 - -400) < Re < (1k - -2k)$
- TrSL2: Formation of transition vortices; $(1k - -2k) < Re < (20k - -40k)$
- TrSL3: Burst to turbulence; $(20k - -40k) < Re < (100k - -200k)$

2.1.2 Transition in Boundary Layers (TrBL)

The terms 'subcritical' and 'supercritical' are used to describe the flow states below and above the 'crisis' in drag force. There are, however, distinct flow regimes preceding the minimum drag coefficient and beyond it which have subsequently been discovered. The following names are suggested by Zdravkovich (1997):

- TrBL0: Pre-critical regime; $(100k - -200k) < Re < (300k - -340k)$
- TrBL1: One-bubble regime; $(300k - -340k) < Re < (380k - -400k)$
- TrBL2: Two-bubble regime; $(380k - -400k) < Re < (0.5M - -1M)$
- TrBL3: Super-critical regime; $(0.5M - -1M) < Re < (3.4M - -6M)$
- TrBL4: Post-critical regime; $(3.5M - -6M) < Re < (unknown)$

2.1.3 Reynolds number range of interest

This research is concerned with a Reynolds number range from around $Re = 40k$, which falls in the TrSL3 (burst to turbulence) regime for a smooth cylinder, up to around $Re = 300k$ which spans the extent of the TrBL0 (pre-critical regime) and nudges the start of the TrBL1 (one-bubble regime) for a smooth cylinder.

2.2 Sub-critical state of flow, or Transition in Shear Layers (TrSL)

Zdravkovich (1997) describes the TrSL3 regime by stating that as Re increases from the TrSL2 regime – where discrete vortices are formed in the free shear layers (Kelvin Helmholtz vortices) before becoming turbulent and subsequently rolling up into alternating vortices (von Kármán vortex street) – the free shear layers suddenly transition from a laminar to turbulent state (burst to turbulence) close to the separation point and the formation of alternating vortices takes place closer to the rear

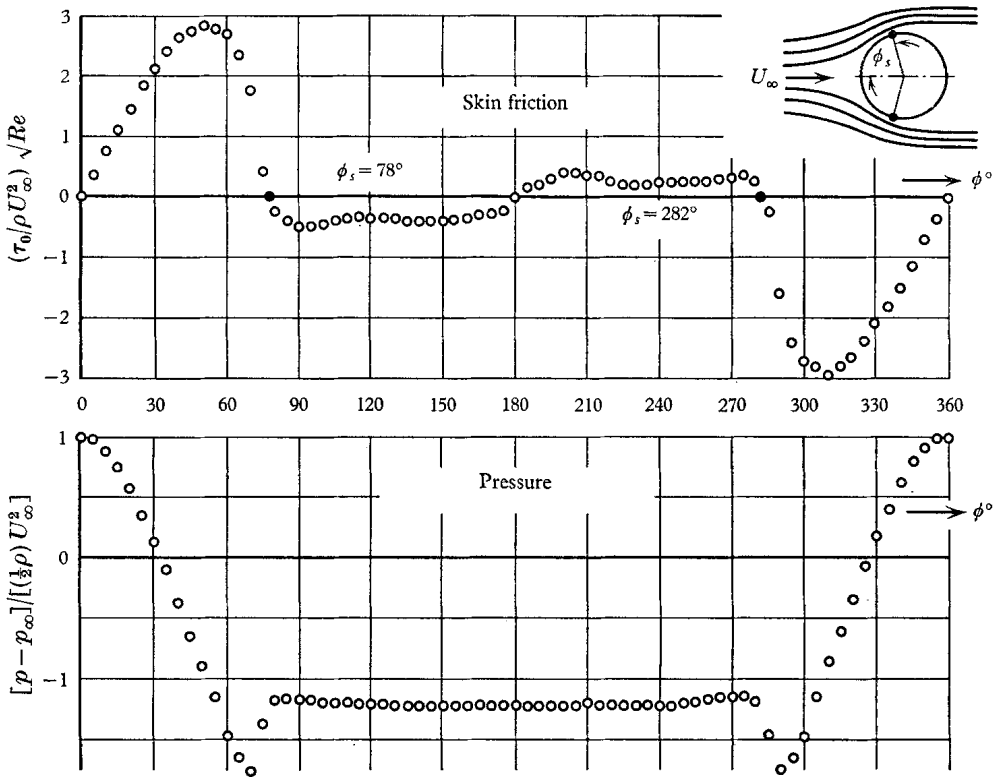

Figure 2.2 – Skin friction and local pressure distribution for a smooth cylinder in the sub-critical regime, from Achenbach (1968), where $Re = 1 \times 10^5$ and separation angle, $\phi_s = \pm 78°$ from the frontal stagnation point.

of the cylinder.

Figure 2.2 indicates that laminar separation occurs around $\phi_s = \pm 78^\circ$ as skin friction goes to zero. The plot of local pressure distribution shows that there is a large pressure deficit occurring between front ($C_p = 1$) and rear of the cylinder where, between the separation points, $C_p \approx -1.2$.

2.3 Critical state of flow, or Transition in Boundary Layers (TrBL)

2.3.1 Pre-critical regime

The pre-critical regime is characterised by the first onset of transition in the free shear layers along the lines of separation.

- The inherent three-dimensional nature of the onset of transition disturbs the near-wake, delaying eddy formation;

- This results in an initial fall in the drag coefficient while the eddy shedding remains prominent.

In the pre-critical regime, separation occurs further downstream than in the sub-critical flow state, as shown in Figure 2.3 with a laminar separation point of $\phi_s = \pm 94^\circ$. Consequently there is an increased recovery of pressure at the rear of the cylinder, $C_p \approx -0.9$, though a large pressure deficit front-to-rear clearly remains.

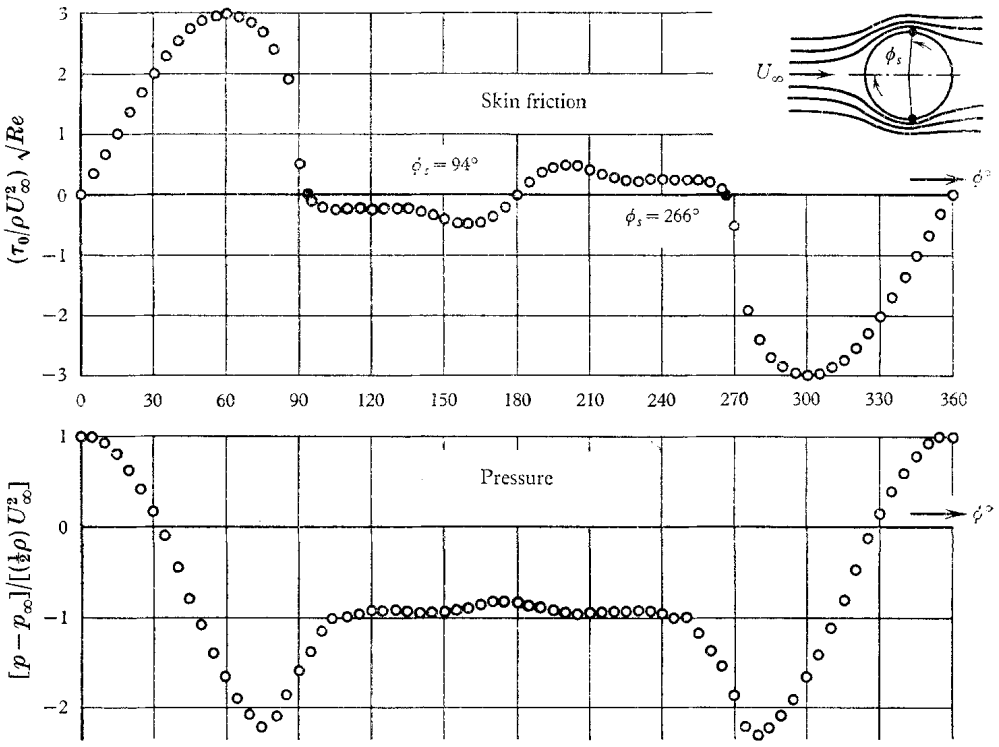

Figure 2.3 – Skin friction and local pressure distribution for a smooth cylinder in the pre-critical regime, from Achenbach (1968), where $Re = 2.6 \times 10^5$ and separation angle, $\phi_s = \pm 94°$ from the frontal stagnation point.

2.3.2 Single-bubble regime

The pre-critical regime terminates abruptly at a certain Re with a discontinuous fall in the drag coefficient, a jump in the frequency of eddy shedding, and the appearance of a mean lift force.

- Bearman (1969) found that on one side of the cylinder the free shear layers underwent sufficient transition to be able to reattach onto the cylinder surface;
- The closed thin separated region was termed a separation bubble;
- The subsequent turbulent separation was considerably delayed in TrBL1.

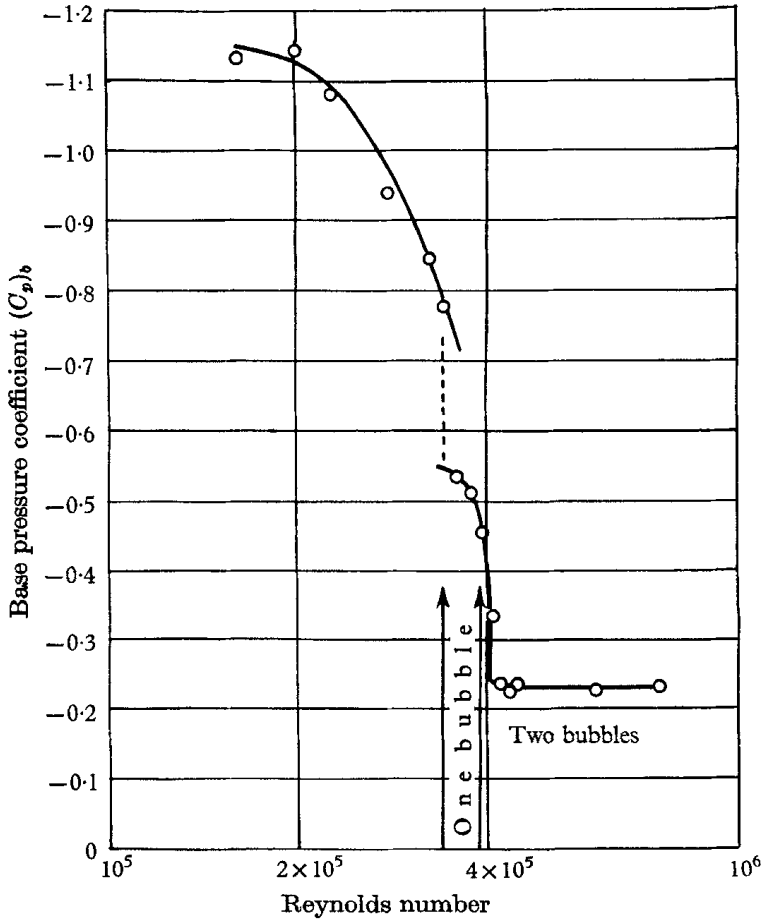

Figure 2.4 – Variation of base pressure coefficient with Reynolds number for a plain cylinder throughout the critical regime. From Bearman (1969).

The formation of a single separation bubble on one side of the cylinder generates an asymmetrical pressure distribution top to bottom in addition to the wake induced pressure imbalance front and rear. The production of a separation bubble reduces the static pressure acting on that side of the cylinder – by enabling the flow to remain attached for a further distance around the cylinder – thus generating a net force acting towards this side, produced by the mean pressure difference between the two sides (where the static pressure remains higher on the side without the bubble). The base pressure recovery is again increased with an increase in separation angle

on the side with the separation bubble, as shown in Figure 2.4.

2.3.3 Two-bubble regime

The asymmetric single-bubble regime terminates at higher Re with yet another discontinuous fall in the drag and lift, and a jump in the shedding frequency when a second bubble is formed on the other side of the cylinder. The symmetric two-bubble regime is a complex and delicate combination of laminar separation, transition, reattachment and turbulent separation of the boundary layers on both sides of the cylinder.

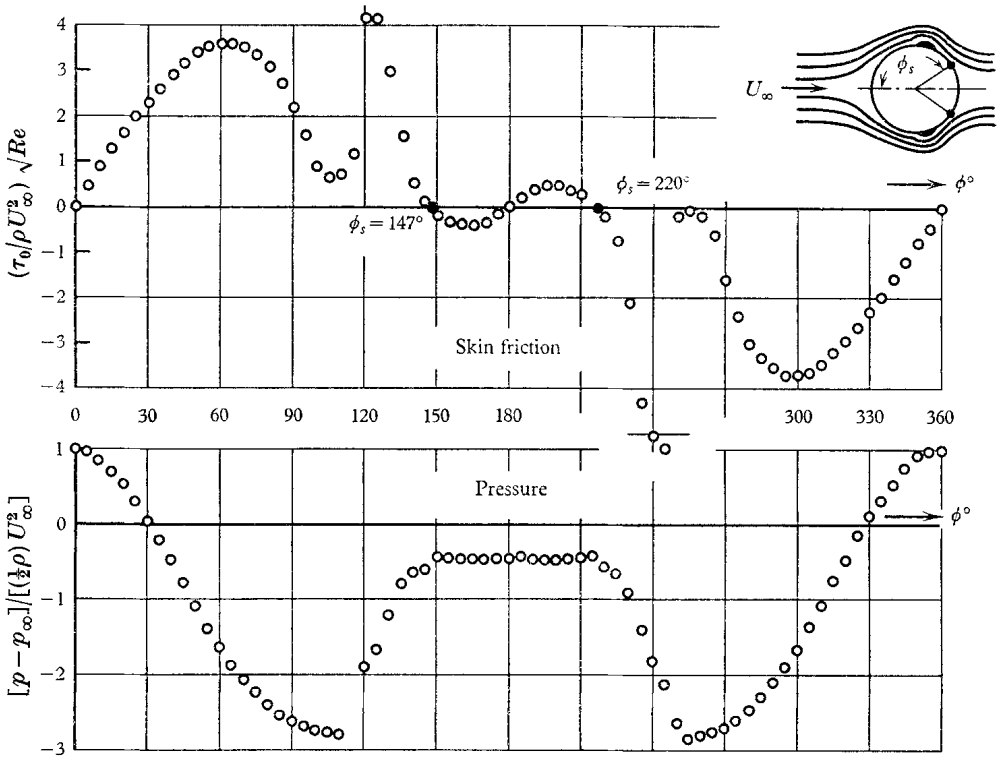

Figure 2.5 – Skin friction and local pressure distribution for a smooth cylinder in the critical regime, from Achenbach (1968), where $Re = 8.5 \times 10^5$ and separation angle, $\phi_s = \pm 147°$ from the frontal stagnation point.

- The single and two-bubble regimes are very sensitive to disturbances and can be eliminated by a sufficiently rough surface or turbulent free stream;

- The formation of separation bubbles causes a considerable narrowing of the near-wake by a delayed turbulent separation.

Figure 2.5 shows that laminar separation occurs around $\phi_s = \pm 115°$, marked by the disappearance of skin friction (data resolution may be the reason laminar skin friction disappearance is only clearly indicated on one side). Transition occurs and the almost immediate and rapid rise in skin friction is indicative of the turbulent reattachment of the flow, before separating again at around $\phi_s = \pm 147°$. Base pressure recovery is greater in this regime than in any other flow state.

2.3.4 Super-critial regime

Further increases in Re brings transition to the primary laminar separation line in an irregular manner and a rise in drag. This leads to the disruption and fragmentation of separation bubbles along the cylinder span and with it a wide variation of local C_D along the span (see TrBL3, Figure 2.6).

The lower range of C_D in the supercritical regime corresponds to the part of the span where the bubbles are sustained, whereas the upper range of C_D in this regime is related to a maximum break-up of bubble formations. This range of C_D may differ by as much as 50% along the span.

- The irregularly fragmented separation lines prevent periodic eddy shedding – the absence of which is an indicative feature of the supercritical regime.

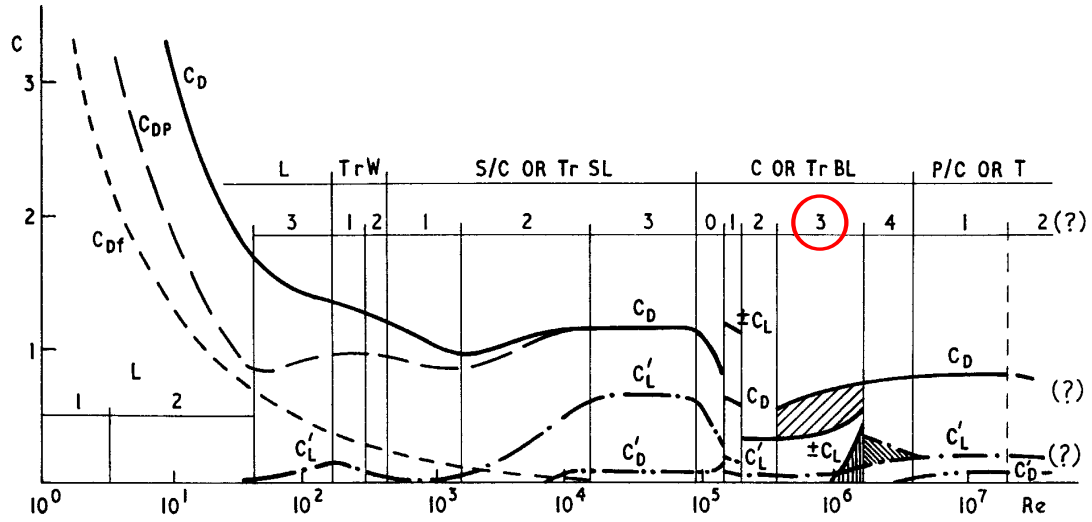

Figure 2.6 – Discretisation of flow regimes for a plain circular cylinder, from Zdravkovich (1990), showing how the total, pressure and skin-friction drag coefficients vary with Reynolds number. The TrBL3, i.e. super-critical regime, is circled.

2.3.5 Post-critical regime

Roshko (1961) discovered that regular eddy shedding reappears at higher Re when the boundary layers are turbulent before separation all along the span.

- The post-critical regime is characterised by the transition in boundary layers being somewhere between the stagnation and separation lines;
- As Re increases, the transition region advances towards the stagnation point asymptotically;
- The reappearance of eddy shedding in the post-critical regime coincides with the obliteration of the irregularly fragmented separation bubbles of the super-critical regime.

Transition in the post-critical regime occurs in the boundary layer at a point upstream of separation and in the example shown in Figure 2.7, transition occurs

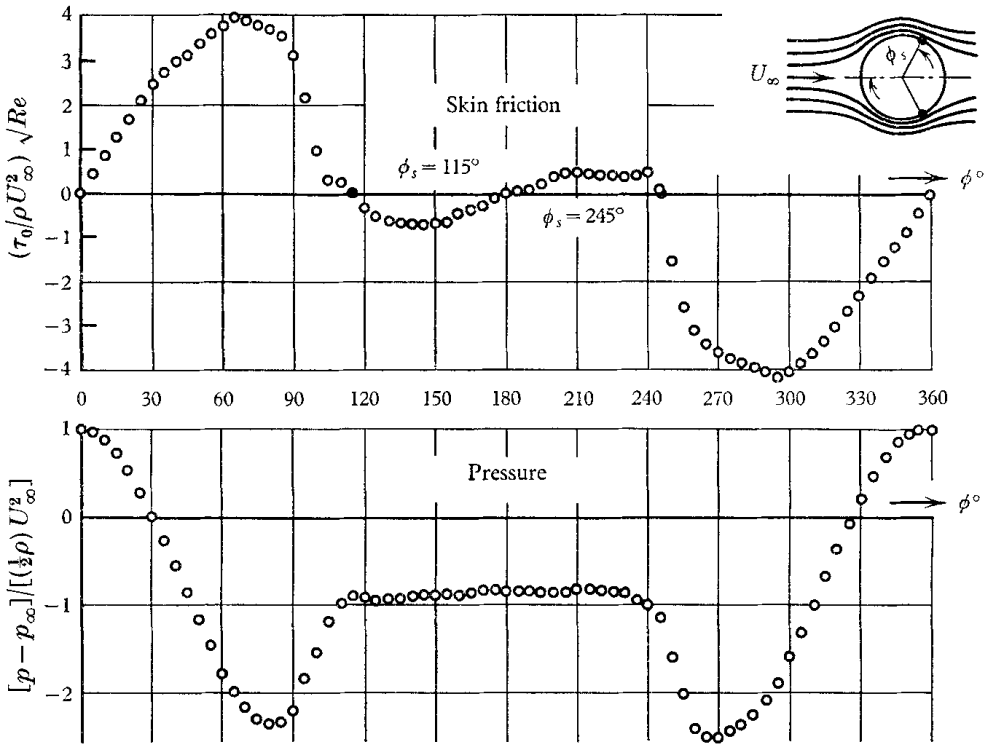

Figure 2.7 – Skin friction and local pressure distribution for a smooth cylinder in the post-critical regime, from Achenbach (1968), where $Re = 3.6 \times 10^6$ and separation angle, $\phi_s = \pm 115°$ from the frontal stagnation point.

around $\phi_t = \pm 65°$ when there is a short rise in skin friction prior to the drop as the now turbulent flow runs against an adverse pressure gradient. The increased energy of the turbulent boundary layer allows the flow to remain attached further downstream than the sub and pre-critical flow states, to about $\phi_s = \pm 115°$. The delayed separation brings with it an increase in the base pressure recovery over sub and pre-critical flow, with $C_p \approx -0.8$.

2.4 Passive methods for altering the C_D characteristics of bluff bodies

2.4.1 Surface roughness

Bearman and Harvey (1993) draw attention to the fact that there is a broad Reynolds number range spanning the transition between the sub-critical and post-critical regimes and stretching far above it – where the flow around a circular cylinder can be influenced significantly by increasing the roughness of its surface. The flow regime of interest for this project is dominated by the transition between the sub-critical and post-critical regimes, also known as the transition in boundary layers (TrBL) regime. Zdravkovich (1997) comments that the flow around a cylinder in the TrBL state of flow is strongly influenced by a very low intensity of turbulence and thus, analogously, the TrBL state of flow should also be sensitive to roughness created turbulence.

Fage and Warsap (1930) carried out numerous experiments measuring the drag of cylinders wrapped in various grades of glass paper and proposed that turbulence created by surface roughness is analogous to that created by free-stream turbulence; the stated difference being that the boundary layer is disturbed by the free-stream turbulence from the 'outside' while surface roughness acts to generate turbulence from the 'inside'.

Furthermore, they propose that the surface roughness generated turbulence intensity, T_i, and scale, T_s, should be related to the:

- Relative roughness, defined by the ratio K/D, where K is the average height

of the excrescence and D is the characteristic length (e.g. diameter for a cylinder);

- Shape of excrescences;
- Distribution of excrescences.

Zdravkovich (2003) proposed that surface roughness can be characterised both by:

- The relative size of roughness, K/D, and;
- Its texture, T_e, comprising the shape and distribution of excrescences.

Prandtl (1961) related the influence of surface roughness on a fluid flow with the thickness of the boundary layer by stating that slightly rough surfaces may be regarded as effectively smooth when excrescences are completely embedded in the laminar boundary layer, whereas at a high Reynolds number – when the boundary layer becomes thinner – such roughness may then become effective (in disturbing the boundary layer and thus influencing the flow behaviour).

Zdravkovich (2003) also explains that the effect of roughness created turbulence strongly depends on the thickness, δ, and state (laminar or turbulent) of the boundary layer.

- If $K < \delta$ in a sub-critical Reynolds number flow, for example, surface roughness has little effect on a stable, laminar boundary layer in triggering transition;
- The same K/D, however, can become highly effective at promoting transition in the Reynolds number range of the TrBL regime.

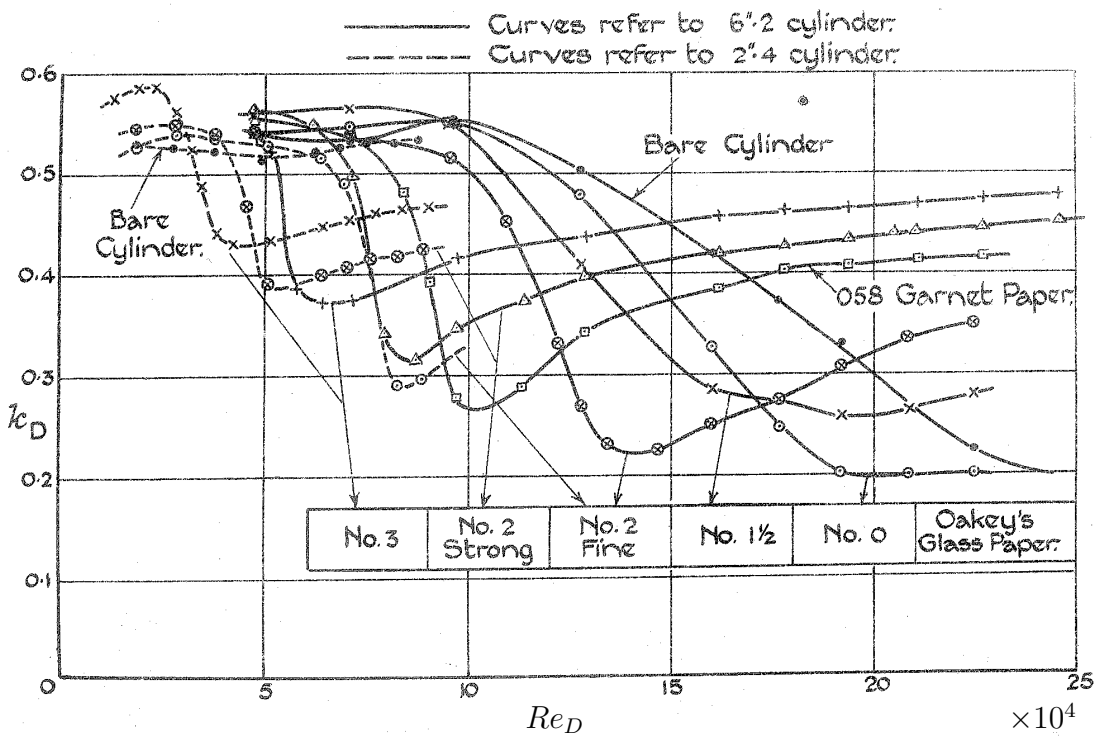

Figure 2.8 – Drag coefficient curves for a cylinder with varying grades of surface roughness, from Fage and Warsap (1930), where the drag coefficient is given as $k_D = C_D/2$. The surface roughness parameter, K/D, is unknown for the stated glass paper grades (e.g. No. 3, No. 2 Strong etc.).

The work done by Fage and Warsap (1930) provided a clear correlation between the drag of a circular cylinder and its surface roughness throughout the Reynolds number range Figure 2.8. As the surface roughness parameter, K/D, is increased, the Reynolds number at which the drag 'crisis' occurs decreases; the surface roughness promoting transition at lower flow speeds. The ultimate reduction in drag is, however, lessened as the surface roughness is increased; a rough cylinder will produce an earlier drop in the drag coefficient, but the minimum drag coefficient achieved will be higher than that of a smooth cylinder.

Fage and Warsap (1930) remarked of their research that if roughening is continued, eventually the fall in drag would disappear. Commenting further on the

mechanisms at work, they proposed that a roughened surface effectively impedes the boundary layer such that separation moves upstream and as a consequence the drag of the cylinder increases. A clearer explanation may be stated in terms of the boundary layer thickness: a rough surface thickens a turbulent boundary layer and thick boundary layers are less able to resist separation in an adverse pressure gradient. Achenbach (1971) therefore found from his own experiments that the post-critical drag coefficient increases with rising roughness parameter.

From the plot of Figure 2.8, it is clear that with rising K/D the slope of the C_D v. Re_D curve – during the drag crisis – becomes steeper, indicating that the roughness generated turbulence becomes increasingly effective in promoting transition in the boundary layer.

Linking the plot of Fage and Warsap (1930) with the flow regimes described previously for smooth cylinders:

- The single-bubble, two-bubble and super-critical regimes found for smooth cylinders are redistributed to lower Reynolds numbers by the increasing level of surface roughness for small K/D values;
- For higher K/D, all three of these flow regimes are obliterated, and the pre-critical regime is immediately followed by the post-critical regime;
    - The fact that eddy shedding does not cease is indicative of the obliteration of the super-critical regime.

Buresti (1981) also carried out tests with various emery cloths and cylinder sizes to achieve varying levels of K/D. Evaluating the drag coefficient from the measured pressure distribution at the mid-span, his data showed a progressive displacement

of C_D vs Re curves towards lower Re – matched by the displacement in the jump in Strouhal number (St) – with increasing roughness. The jump in St is indicative of a drop in drag coefficient, with these parameters generally providing almost a mirror image of each other when plotted against Re. Increasing K/D promotes the 'drag crisis' though the minimum value of drag achieved is not as low as that of a smooth cylinder. For cylinders with increasing K/D, the gradual rise in drag profiles above the minimum C_D of a smooth cylinder, and the decrease in Strouhal number, reflect the widening of the near wake (as the separation point moves further upstream).

The data of Buresti (1981) also shows that for K/D of 0.5% and 0.7%, there is a disappearance of the peak in frequency spectra between the low Re, low St regime and the jump to high St after a relatively small rise in Re. This is typical of the super-critical regime, where vortex shedding ceases before returning again in the post-critical regime. As discussed for the results of Fage and Warsap (1930), for an increased roughness, $K/D = 1.2\%$, the jump from low to high Strouhal number is not separated by the cessation of eddy shedding. This shows that the regimes associated with smooth cylinders cannot simply be transposed to lower Reynolds numbers without considering the level of roughness; roughness can be used to simulate higher Re flows on smooth cylinders at lower Re, but the regime transition – namely the inclusion of the super-critical regime – is not consistent and disappears beyond a certain level of roughness.

Buresti (1981) commented that transition to super-critical conditions seems to be a function both of the degree and of the type of surface roughness. Evaluating the results of four different grades of emery cloth, Buresti (1981) noticed that the behaviour of one cloth differed from the other three. Investigating further, the cloth in question was produced by a different manufacturer and seemed to be made of

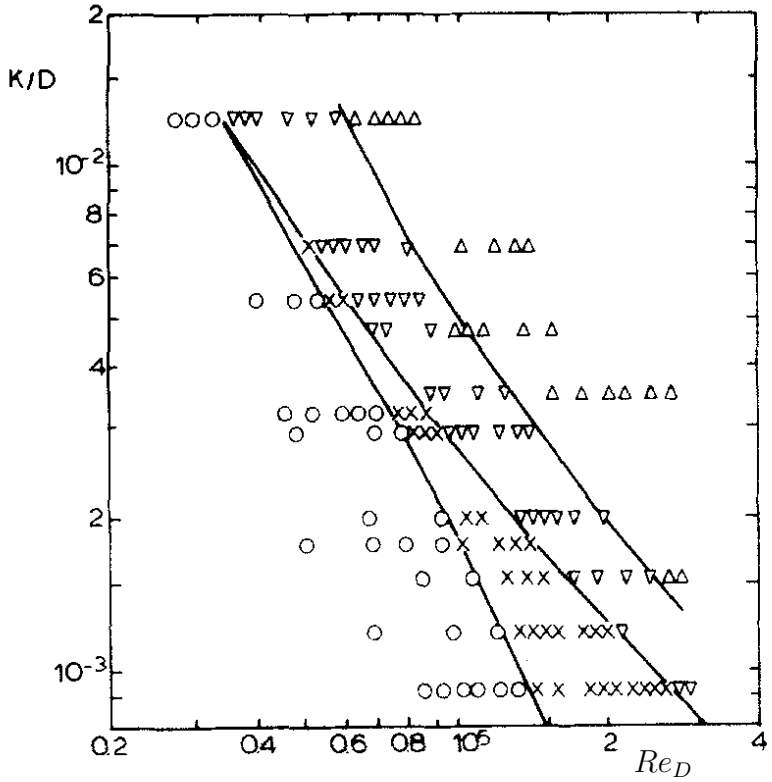

Figure 2.9 – Boundaries between flow regimes for a cylinder with varying grades of surface roughness, from Buresti (1981), where ◯ = sub-critical, × = critical, ▽ = super-critical and △ = post-critical.

particles of a different material and with a different distribution. He therefore noted from these results that the type of surface roughness can have a significant influence on the transitions between the various flow regimes and that it is not possible, in general, to define absolutely the degree of roughness by means of a single parameter (the K/D relative roughness parameter). Thus, while post-critical Strouhal number is a function of the relative degree of roughness, the influence on turbulence generating mechanisms of a particular type of roughness differs with additional parameters – which may be collected into the general term 'roughness texture', T_e, as proposed by Zdravkovich (2003). This term may take into account the shape and

arrangement of surface excrescences which describe a particular surface roughness, independently of the relative roughness height, K/D. A simple example might be to consider the comparative effectiveness of regularly spaced hemispheres and, say, randomly spaced and oriented wedge-shaped roughness elements of equal height and average packing density.

By analysing the changes in flow regime produced by the emery cloths of similar behaviour (of the same type of roughness by the same manufacturer), Buresti (1981) marked out the relationship of K/D with the position of the flow regime boundaries with respect to Re Figure 2.9. The area to the left of the first line is the sub-critical regime; the area enclosed within the converging first and second lines represents the critical regime; the area to the right of this, between the second and third lines is the super-critical regime; and beyond the third and final marked line is the post-critical regime.

The limits of K/D for which separation bubbles are able to form are shown by the boundaries containing the appearance of the critical regime. The two converging curves designate the appearance and fragmentation of separation bubbles respectively, with the Re range of the critical regime diminishing and eventually disappearing with increasing K/D.

The beginning of the post-critical regime is represented by the third line which produces a plateau in the drag and Strouhal number. The constant values of C_D and St in the fully turbulent regime indicate that separation has reached an extreme upstream position. All three C_D, St and separation angle, ϕ_s, values are constant in the post-critical regime, but these sets of values vary with K/D.

Achenbach (1971) comments on the contribution of skin friction (wall shear) forces to the total drag and shows that, in the Re range investigated, friction forces

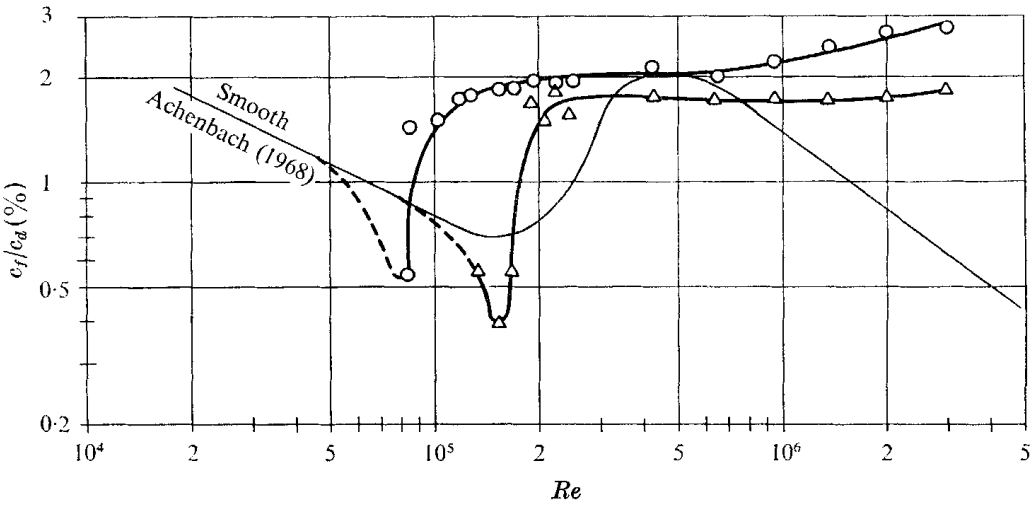

Figure 2.10 – Percentage of friction forces with respect to the total drag for a circular cylinder, from Achenbach (1971), where ◯ is $K_s/D = 450 \times 10^{-5}$ and △ is $K_s/D = 110 \times 10^{-5}$.

contribute only marginally to the flow resistance ($0.4\% < C_f/C_D < 3\%$). Thus, more than 97% of the total drag of a circular cylinder – in free-stream flow of the Re range of interest – is attributed to losses associated with an asymmetrical fore-aft pressure distribution; influencing pressure drag is key to altering the C_D of a circular cylinder.

As shown in Figure 2.10, the highest skin friction percentage occurs when the boundary layer is turbulent at higher Re. However, it is interesting to note that at this point in the post-critical regime, skin friction for the smooth cylinder begins to decrease with increasing Re whereas with the rough cylinder it remains almost constant. Achenbach (1971) commented further that this result is in good agreement with the suggestion that, in the post-critical flow regime, the magnitude of wall shear stress is independent of Re, and a function only of K_s/D.

2.4.1.1 Flow specific positioning of surface roughness

Fage and Warsap (1930) carried out experiments with the angular positioning of roughness around the circumference of a plain cylinder and found that placement of the roughness in the stagnation and base regions, $|\phi| \leqslant 37.5°$ and $100° \leqslant \phi \leqslant 260°$ respectively, had little effect on the flow compared with the plain cylinder Figure 2.11:

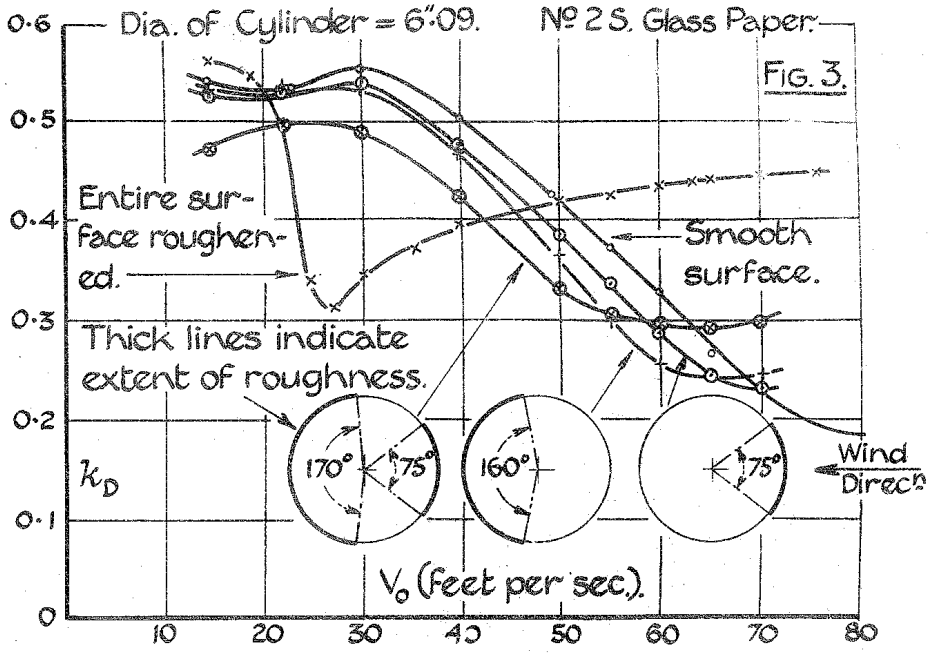

Figure 2.11 – Effect on C_D of a limited covering of surface roughness on a circular cylinder, from Fage and Warsap (1930), where $k_D = C_D/2$.

They concluded, therefore, that the region $\phi = \pm(37.5° \rightarrow 100°)$ is most particularly sensitive to surface roughness, which is to be expected given this region includes the parts where flow transitions and separates. They found however, that it was not possible to obtain direct measurement of the effect of roughness in this region because, despite all care to prevent it, the front edge of the glass-paper greatly influenced the flow, thus masking the behaviour of the roughness.

2.4.1.2 Summary of conclusions: Surface roughness

Increasing K/D promotes boundary layer transition for sub-critical Reynolds numbers and consequently the sudden fall in drag, but, by increasing K/D sufficiently, the sensitive separation bubbles – associated with the single, two bubble and supercritical regimes – are unable to form, thus preventing the same drastic drop in drag attainable in the critical regime by a smooth cylinder. This prohibits the accurate transposition up and down the Reynolds number range of regime characteristics for varying surface roughness.

The minimum C_D is marked by the peak in Strouhal number which is linked to the size of the near wake. A decrease in peak Strouhal number – arising from an increase in K/D – reflects a widening of the near wake and hence an increase in drag resulting from the separation point moving upstream.

The influence of surface roughness on flow properties cannot solely be characterised by the relative roughness parameter, K/D, and must include texture, T_e, as an additional factor.

A plateau in drag, Strouhal number and separation angle at high Reynolds numbers indicates the independence of wall shear stress from Reynolds number with K/D the only determining factor.

The operational region for surface roughness on a circular cylinder positioned with the stagnation point at $\phi = 0^\circ$ is $\phi = \pm(37.5^\circ \rightarrow 100^\circ)$, however the transition between the smooth and roughened surface causes an additional disturbance more akin to tripping the flow. Hence, the usefulness of specifically positioning roughness is difficult to determine.

2.4.2 Surface roughness texture

2.4.2.1 Consistent classification of relative roughness

Nikuradse's (1933) diagram of the pressure loss of the flow through rough circular pipes was used by Achenbach (1971) to classify the roughness of the emery papers he used into a system of the equivalent sand-grain roughness, K_s/D. Nikuradse sifted and precisely measured sand grains before adhering them to the insides of pipes in a very lengthy and laborious process, to produce a known uniform roughness parameter to provide similitude in his various experiments.

In the review by Zdravkovich (2003) of pyramid-shaped, brick wall and wire gauze roughness, it would appear, from the investigations of these aforementioned regular (uniform) roughness textures – carried out respectively by Achenbach (1977), Ackeret (1936), Farell and Fedeniuk (1988) and Farell and Arroyave (1990) – that all exhibit similar behaviour, and can thus be matched, to an equivalent sand roughness, K_s/D.

From an analysis of the sand-paper tests of Fage and Warsap (1930) with the subsequent addition of surface conditions for said tests by Schlichting (1964), Achenbach (1971) concluded that for the case of circular cylinders with spherical roughness, "the equivalent sand-grain roughness is not 1d (where d is the grain diameter) but only 0.55d". This leads on from previous work by Schlichting (1936) from which he found that for closely packed spheres on the inner surface of a square duct, the equivalent sand-grain roughness had a value of $K_s = 0.627d$.

2.4.2.2 Representation of relative roughness parameter

Achenbach (1971) commented that the roughness parameter K_s/D is of less physical meaning than of practical profit: "From the physical point of view the boundary layer thickness must be introduced as the reference length, so the roughness parameter might have the form K_s/δ. However, the boundary layer of the cylinder in cross-flow varies with angular position and Re. Therefore one prefers to introduce the diameter D as an auxiliary characteristic length."

2.4.2.3 Roughness Reynolds number

Szechenyi (1975) proposed that for sufficiently large K/D and high Re (where C_D is found to plateau as a function only of K/D) the mean C_D should be independent of D and depend on K instead. As such, Re based on D should be replaced with Re_K based on K and termed 'roughness Reynolds number'. Zdravkovich (2003) points out that it might also be expected that the new similarity number should also lead to a single value of Re_K for minimum C_D. Zdravkovich (2003) has shown the replacement of D by K does not produce a new similarity variable, with values of Re_K for minimum C_D changing widely even for the same set of data.

Niemann and Holscher (1990) compiled the available data for C_D minimum and C_D ultimate (occurring at the start of the fully turbulent regime) over a wide range of relative roughness: $0.001\% < K/D < 1.2\%$, with the results plotted here in Figure 2.12.

Figure 2.12 shows that neither C_D minimum nor C_D ultimate reach final values, however C_D minimum and C_D ultimate are drawn towards each other with increasingly large K/D (though it is doubtful that they will meet, as proposed by Fage and

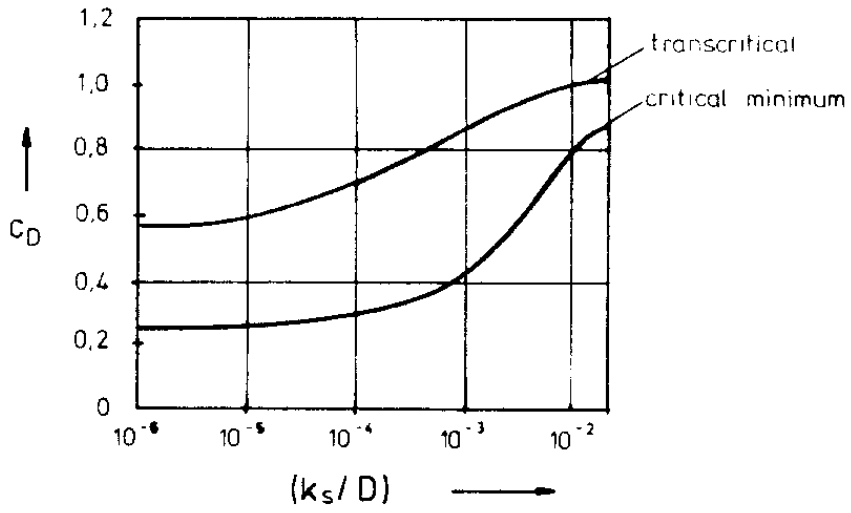

Figure 2.12 – Effect of surface roughness on minimum and ultimate C_D of a circular cylinder, from Niemann and Holscher (1990).

Warsap (1930), as it would appear that the relations are asymptotic towards final values which will maintain a gap with continually increasing K/D);

- This indicates that a drop in C_D with increasing Re will occur regardless of the level of surface roughness;
- The relationships between C_D minimum and K/D, and C_D ultimate and K/D, are non-linear.

2.4.2.4 Summary of conclusions: Surface roughness texture

The roughness Reynolds number, Re_K, when applied to cylinder surface roughness, is not a reliable similarity parameter since a consistent correlation between C_D and Re_K does not exist.

It would appear that roughness elements which are arranged in a closely packed, uniform and regular manner can be considered to impart a similar influence on flow

behaviour. For roughness textures produced in this way, an equivalent 'sand-grain' relative roughness, K_s/D, may typically be equated to textures of this type.

In order to quantify and correlate the influence of a texture on the flow, reference should be made to the boundary layer thickness at the position of the texture element, however, this may add significantly to the complexity of analysis and can be considered extraneous with uniform roughness.

2.4.3 Tripping the flow

2.4.3.1 Tripping wires

Tripping wires are generally characterised by the physical sizing ratio, d/D, where d is the trip-wire diameter and D is the cylinder diameter. Depending on this ratio and the flow characteristics, the tripping wires may be fully submerged in or protruding from the boundary layer.

- This may trigger transition or separation (or separation and transition), respectively;
- The optimal location of the wire, ϕ_w, depends on d/D and Re.

Fage and Warsap (1930) conducted investigations into the effects of straight trip-wires, in the range $d/D = 0.33\% - -0.02\%$, attached at $\phi_w = \pm 65^\circ$ to a plain cylinder. For the plot shown in Figure 2.13, the size of the tripping wires, d, were less than the local thickness of the cylinder boundary layer, i.e. $d/\delta < 1$, where $D = 6.09$" as indicated.

Fage and Warsap (1930) also tested wires of a diameter larger than the thickness of the boundary layer, concluding that wires of $d \geqslant \delta$, when placed at $\phi_w = \pm 65^\circ$,

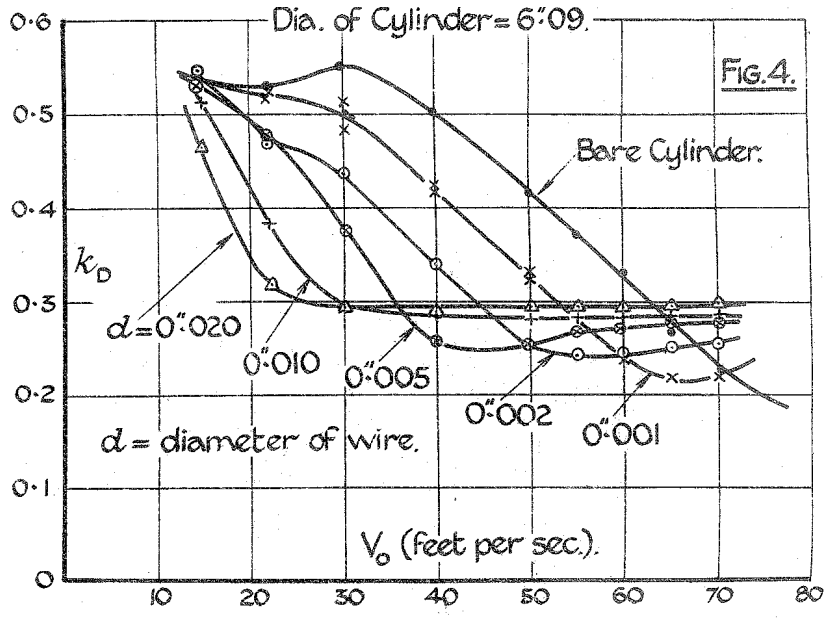

Figure 2.13 – Effect on C_D of tripping wires at $\phi_w = \pm 65^\circ$ on a circular cylinder, from Fage and Warsap (1930).

cause the boundary layer to separate at the same angle independently of Re. This was found from measurements of the cylinder with a $d/\delta = 1.61$ trip wire over the range $9 \times 10^4 \leqslant Re \leqslant 26.2 \times 10^4$; all points collapsed to the same pressure distribution line.

2.4.3.2 Effect of tripping wire location

James and Truong (1972) highlighted, for small d/D, that the optimal trip-wire placement is at $\phi_w = \pm 65^\circ$. A large d/D has quite a different effect, with $\phi_w = \pm 45^\circ$ being most suitable, while placing the large wire at $\pm 65^\circ$ generates high C_D values (same as $\phi_w = \pm 90^\circ$).

Fujita et al. (1985) found that for high values of $\phi_w = (60^\circ - -90^\circ)$, the tripping wire location coincided with the separation point, $\phi_w = \phi_s$; as such, these "tripping wires" become "separation wires". They also showed that up to $\phi_w = 30^\circ - -40^\circ$,

the tripping wire has no effect, with ϕ_s remaining unchanged.

Igarashi (1986) showed that, in the range $3 \times 10^4 \leqslant Re \leqslant 6.5 \times 10^4$, small values of d/D provide a significant reduction in drag, whereas larger values ($d > \delta$) increased drag over that of a plain cylinder (positioning the wire at 60° from the stagnation point).

- These larger values of d/D produce separation with no reattachment, and hence increased wake size, reduced Strouhal number and an increase in pressure drag;

- However, using similarly large values of d/D but moving the trip wire to an angle closer to the stagnation point produces flow regimes which do reattach (turbulent reattachment), hence the importance of trip wire angular location.

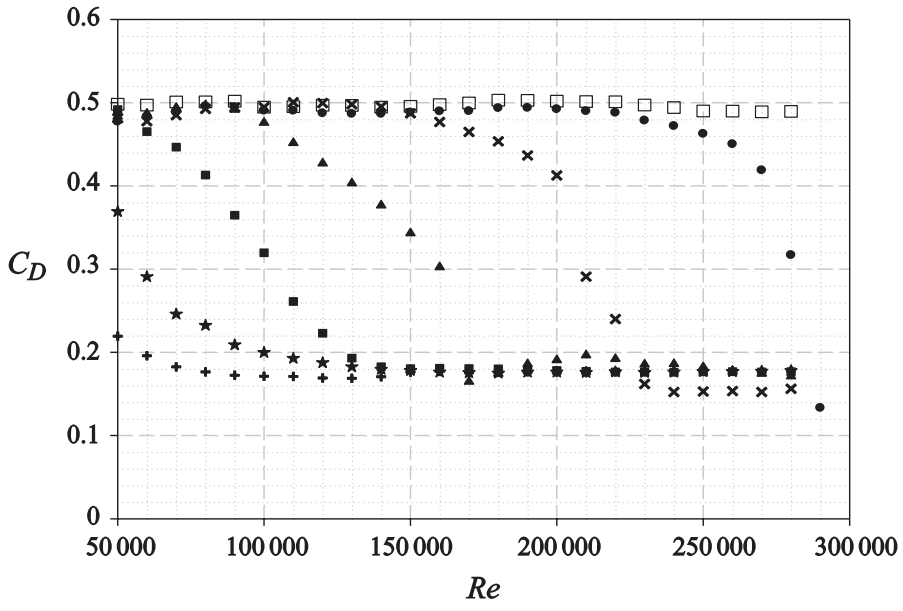

Figure 2.14 – Plot of C_D v. Re for various tripping wire locations on a sphere, from Son et al. (2011), where ▫, smooth sphere; all tripping wires are $K/D = 0.67 \times 10^{-2}$, located $\phi_w = 20°$, ●; 30°, ✖; 40°, ▲; 50°, ■; 60°, ★; 70°, ✚.

As Reynolds number increases the boundary layer becomes thinner and as a consequence a trip wire fully submerged at low Re begins to protrude from the boundary layer at higher Re. Thus, trip wire d/D and ϕ_w need to be selected collectively for the Reynolds number operating range, and if this range varies significantly then the trip-wire will influence the flow in differing ways, becoming less efficient at reducing drag depending on the initial setup.

Son et al. (2011) carried out extensive analysis of tripping wires on spheres. They found that the position of the tripping wire affected only the critical Reynolds number, Re_{crit}, and all angular positions led to the same minimum C_D (Figure 2.14).

2.4.3.3 Fluid mechanics of the tripping wire

Igarashi (1986) found that the flow around a circular cylinder fitted with tripping wires strongly depends on Re, d/D and the angular position of the trip wire, ϕ_w, with respect to the stagnation point. Regarding the mechanisms of the flow around tripping wires, Igarashi (1986) used flow visualisations during his experiments to produce the schematics shown in Figure 2.15.

- The boundary layer upstream of the trip wire first decelerates, then separates, forming a separated region upstream of the wire;
- Another separation takes place from the tripping wire itself;
- Depending on Re, d/D and ϕ_w, the flow either encloses another recirculating separated region as the flow reattaches to the cylinder (pattern A and C) or separates from the tripping wire without subsequent reattachment to the cylinder surface (pattern D).

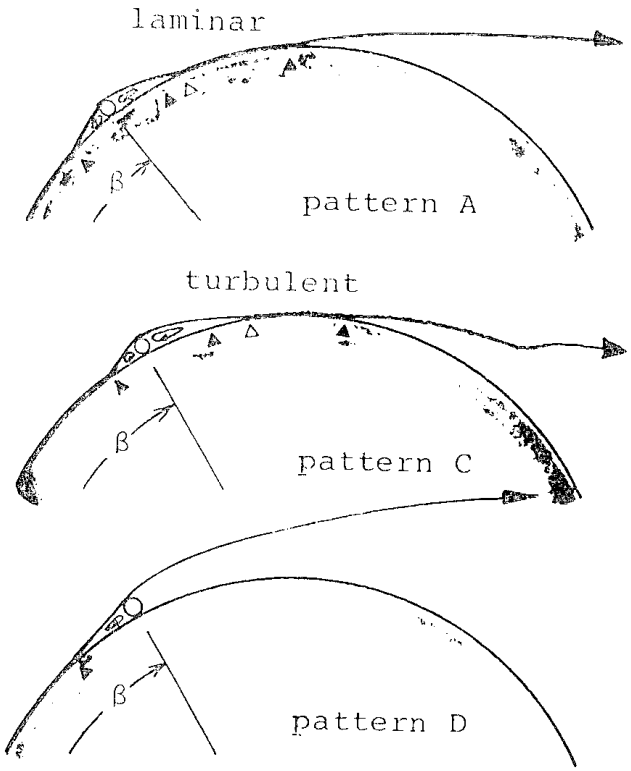

Figure 2.15 – 2D flow schematics for cylinders with span-wise tripping wires at various angular positions, from Igarashi (1986), where pattern A: $\phi_w = 50°$, $d/D = 1.5\%$, $U = 10m/s$; pattern C: $\phi_w = 50°$, $d/D = 2.5\%$, $U = 20m/s$; pattern D: $\phi_w = 60°$, $d/D = 2.5\%$, $U = 20m/s$.

2.4.3.4 Summary of conclusions: Tripping wires

An optimal tripping wire depends on its location, ϕ_w, relative size d/D and Reynolds number. For wires $d < \delta$, the optimal position found by many researchers was discovered to be $\phi_w = \pm 65°$. This position allows the boundary layer to become energised without immediately separating and provides optimal timing to promote transition from a laminar to turbulent boundary layer; this energised state enables the boundary layer to remain attached for longer against an adverse pressure gradient and thus separates with a narrower near wake, consequently reducing drag.

Wires of a diameter greater than the boundary layer thickness, δ, cause the flow to separate, however, if they are placed at an angular position sufficiently far upstream the flow may reattach, and in its energised state remain attached for longer, hence reducing drag.

Trip wires appear to be an efficient way of inducing the critical regime to a lower Reynolds number than that of a smooth cylinder, while maintaining some advantages over surface roughness; the boundary layer can remain attached for longer – because of the reduced disruption after transition – and hence achieve a more substantial minimum C_D which is additionally maintained for a larger range of Reynolds number. Following transition, the growth of the turbulent boundary layer thickness increases with the level of surface roughness and hence a smooth surface is desirable to minimise this and prolong attachment of the flow to the body.

The behaviour of tripping wires, based on the data from Son et al. (2011), would appear to have a more beneficial influence on drag reduction for spheres than on cylinders. This may be due to three-dimensional effects compared to the nominally two-dimensional trip wire applied to a cylinder.

2.4.4 Vortex generators

In Zdravkovich's (2003) review of stream-wise eddy generators, he comments that surface roughness generates turbulence in the form of small eddies of random orientation, hence the effect of energising the boundary layer with the application of roughness compared to a smooth surface.

- Spanwise tripping wires, with their essentially two-dimensional geometry, generate vorticity mostly parallel to the cylinder axis;

- The flow in the vicinity of separation is sensitive to streamwise vorticity and the related transfer of momentum to the boundary layer.

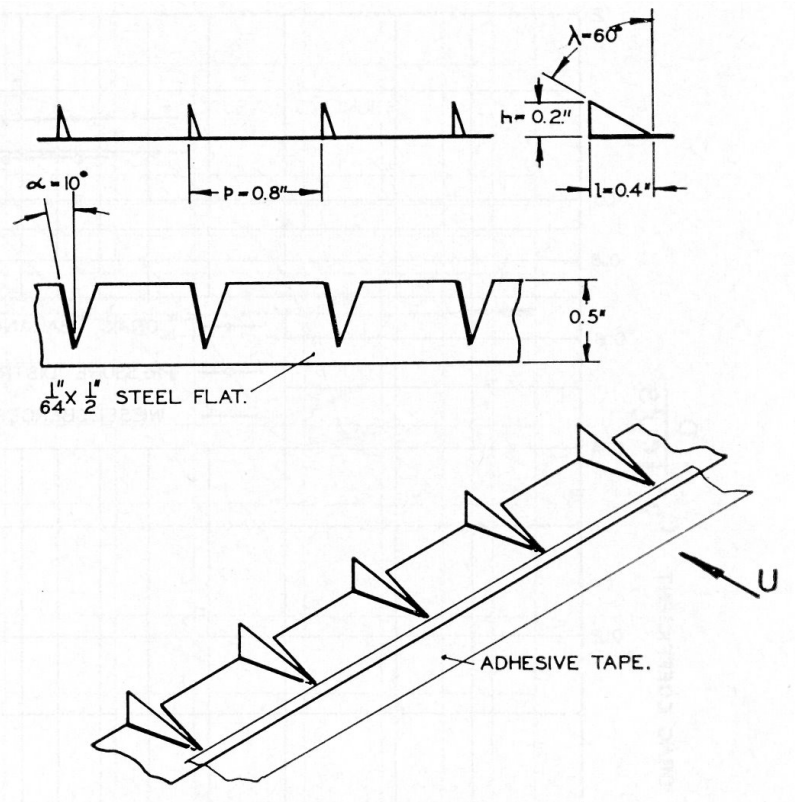

Figure 2.16 – Schematics of vortex generators used to control flow over a circular cylinder, from Johnson and Joubert (1969).

Joubert and Hoffman (1962) experimented with streamwise vortex generators on a circular cylinder. They explain their motivation for pursuing this research thus:

- In an adverse pressure gradient, such as exists on regions of a circular cylinder, a boundary layer will lose its momentum and will eventually separate, producing high form drag.

    - One possible method of delaying this separation and so producing a lower drag, is to use vortex generators whose trailing vortices introduce

high momentum fluid particles from outside the boundary layer into the slower moving region near the wall, which region is then swept away from the surface thus re-energising the boundary layer;

- A reduction in the overall drag for the cylinder will occur if the reduction in pressure drag, due to the delayed separation, is greater than the sum of form, induced and interference drags of the vortex generators.

Johnson and Joubert (1969) also investigated streamwise vortex generators, of the type shown in Figure 2.16, which were positioned symmetrically either side of the cylinder $\pm\phi_{vg}$ from the stagnation point. Zdravkovich (2003) comments that the shape and orderly displacement of the C_D curves produced are similar to those obtained with tripping wires (Figure 2.17), and that for $\phi_{vg} > 40°$ the minimum C_D plateaus, which reflects an independence of Re. This is similar to that achieved with dimples; a review of which follows.

In surface shear flow visualisations by Johnson and Joubert (1969) it can clearly be seen that the vortex generators have a marked influence on the flow:

- The wavelength of the separation line coincides with the pitch of the triangles;
- Distinct lines of high shear stress can be seen trailing from each blade, indicating the transfer of high-momentum fluid into the boundary layer under the action of the trailing vortices;
- The separation line becomes wavy with a period equal to the spacing of the streamwise vortices, resulting in a periodic spanwise variation in the momentum of the boundary layer;

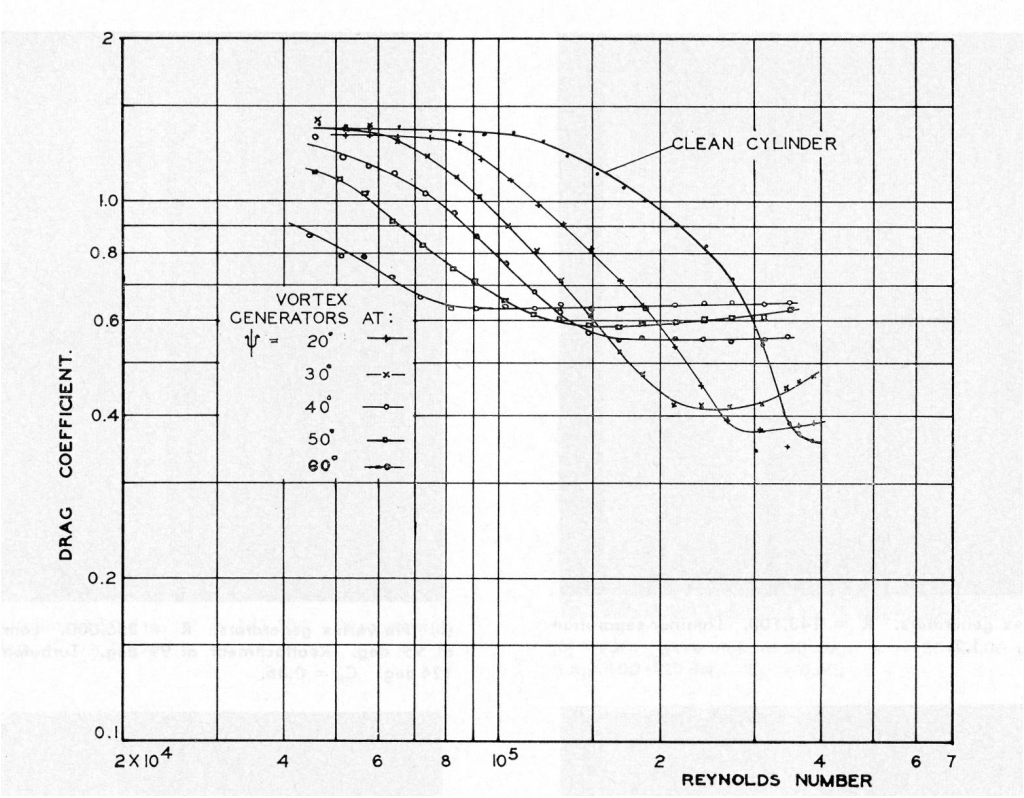

Figure 2.17 – C_D v. Re curves for a circular cylinder fitted with vortex generators at varying angles, from Johnson and Joubert (1969), where the vortex generator angle is designated here by $\Psi(= \phi_{vg})$.

- The separation is delayed considerably; the higher momentum regions being able to sustain a greater adverse pressure recovery before finally separating;
- Maximum ϕ_s along the span coincides with the position of the streamwise eddies.

2.4.4.1 Summary of conclusions: Vortex generators

Vortex generators appear to have some similar influences on the flow as tripping wires and dimples; they are able to energise the flow at a specific point by imparting vorticity, and hence momentum, into the boundary layer and having done so the

turbulent boundary layer is able remain attached further downstream. From the data of Johnson and Joubert (1969), vortex generators also have the desirable quality of maintaining the drop to minimum C_D over a larger Reynolds number range, though this drop is not as significant as that of a smooth cylinder.

2.4.5 Grooves

2.4.5.1 Circumferential grooves

Ko et al. (1987) experimented with both smooth and circumferentially grooved cylinders (see Figure 2.18). From the data collected, they found that flow past a circumferentially grooved cylinder surface appeared analogous to a roughened cylinder surface, as shown in Figure 2.19 by the comparison with data from Achenbach (1971). The groove depth seems to have an equivalent effect to relative roughness, K/D; increasing groove depth provides an orderly displacement of minimum C_D towards low Re.

Leung and Ko (1991) examined the effect of grooves on boundary layer development, compared to that of a smooth cylinder.

- For smooth cylinders, δ/D decreases with a rise in Re, and increases beyond separation, but all δ/D curves for the grooved cylinders are well above the curves for smooth cylinders, and agree with δ/D for rough cylinders;

- The three-fold increase in δ/D for grooved cylinders in comparison with smooth cylinders corresponds to a similar increase in surface area by grooves and related skin friction;

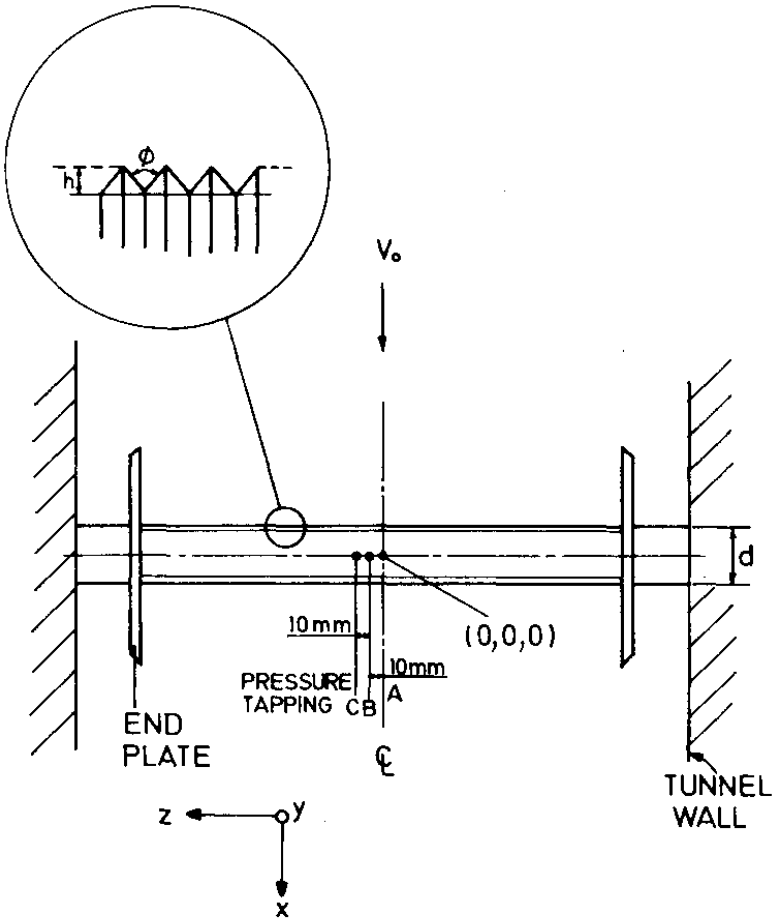

Figure 2.18 – Schematic of a circumferentially grooved cylinder, from Ko et al. (1987).

- Zdravkovich (2003) points out that the analogy between grooved and rough cylinder surfaces seems to stem from a similar increase in skin friction;

Measuring the boundary layer thickness from the bottom of the grooves, Leung and Ko (1991) found that up to a circumferential angle $\approx 60°$ from the stagnation point, much of the boundary layer was submerged in the groove (entirely submerged up to $\approx 30°$ in the sub-critical regime, $\approx 45°$ in the critical regime and $\approx 60°$ in

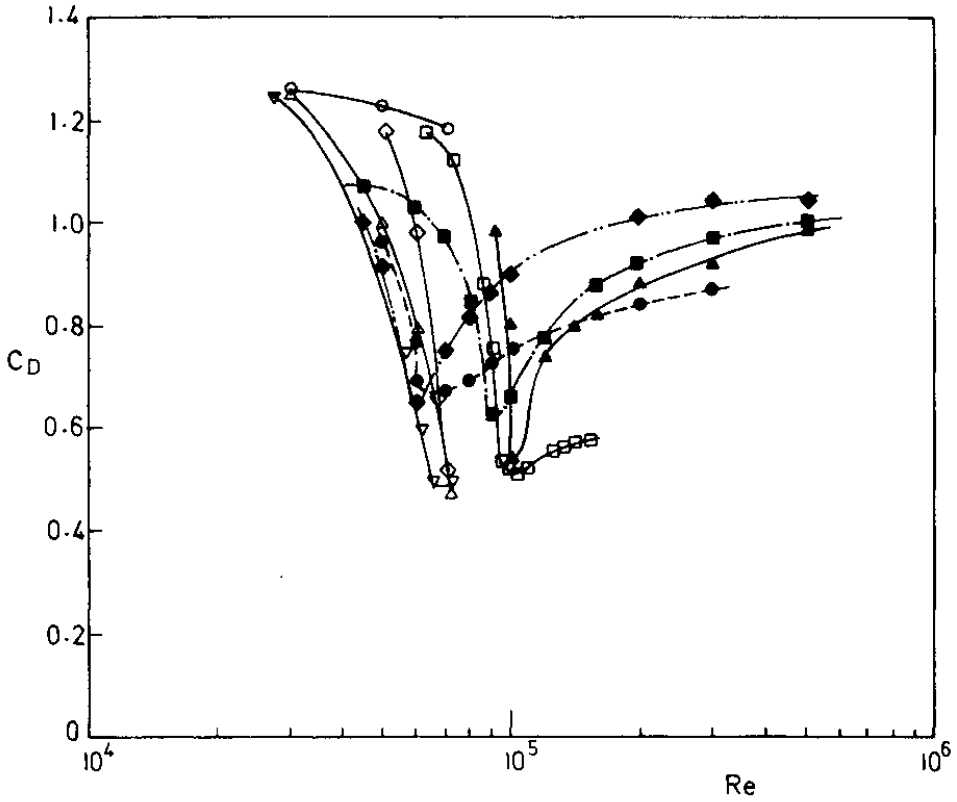

Figure 2.19 – Comparison of C_D of circumferentially V-grooved and rough cylinders, from Ko et al. (1987), where grooved surfaces are represented by □ $K/d = 4.2\times10^{-3}$, ○ $K/d = 6.2 \times 10^{-3}$, ◇ $K/d = 8.2 \times 10^{-3}$, △ $K/d = 9 \times 10^{-3}$, ▽ $K/d = 9.6 \times 10^{-3}$; rough surfaces are taken from: Achenbach (1971) ■ $K_s/d = 4.5 \times 10^{-3}$, ◆ $K_s/d = 9 \times 10^{-3}$; Güven et al. (1980) ▲ $K_s/d = 3.1 \times 10^{-3}$; and Fage and Warsap (1930) ● $K_s/d = 7 \times 10^{-3}$.

the super-critical flow regime). They noted that the characteristic increase in the boundary layer thickness with an increase in circumferential angle and decrease in Re is observed with grooved cylinders as it is for smooth cylinders, and that in the sub-critical regime the boundary layer thickness for the grooved cylinders increased from that of the smooth cylinder by an amount approximately equal to the height of the groove.

- As such, they commented that flow within the grooves is retarded and displaces

the boundary layer outward, resulting in the observed increase in boundary layer thickness;

- Zdravkovich (2003) commented on this finding that the gradual retardation of flow inside the grooves with increasing ϕ may lead to flow overspill at the tips of the grooves and, as such, there might be some analogy between the action of the groove tips and streamwise eddy generators.

2.4.5.2 Partially grooved surface

Leung et al. (1992) attempted to examine which segment of the grooved circumference had a dominant effect on C_D reduction, however it was found that the ends of the grooving has a greater effect on the flow than the grooves themselves.

- The measured pressure distribution showed that the end of grooving caused a pressure recovery due to a sudden increase in the local flow area;
- The most effective grooves are up to $\phi_g = \pm 75^\circ$, with a further increase in the grooved surface up to $\phi_g = 90^\circ$ increasing in the minimum drag coefficient.

2.4.5.3 Spanwise grooves

Kimura and Tsutahara (1991) investigated the effect of a single circular-arced groove, of three different depths, at various angular positions on a cylinder. Their tests showed that a spanwise groove can delay laminar separation in the sub-critical regime.

As depicted in Figure 2.20, the laminar boundary layer separates from the leading edge of the groove, and reattaches at the trailing edge and consequently the shear stress is reduced in the separated region above the groove.

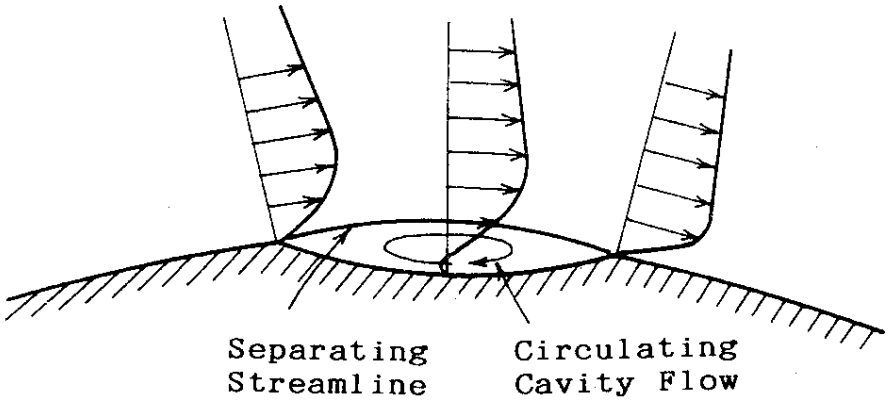

Figure 2.20 – Proposed cavity flow mechanism of a spanwise groove, from Kimura and Tsutahara (1991).

- The optimum placement of the groove was found to be $\phi_g = 80°$ from the stagnation point for the sub-critical flow state;
- Kimura and Tsutahara (1991) argue that the boundary layer is energised just downstream of a groove or shallow cavity, allowing the boundary layer to remain attached further downstream before separating;
    - They also found that the groove could promote separation rather than delay it, depending on its circumferential positioning. At a critical position, the flow fails to reattach after separating from the front edge of the groove.

If the spanwise grooves were to be regularly distributed around the circumference of the cylinder, say for a non-specific flow direction, it is unlikely that this arrangement would have any benefit over surface roughening of a cylinder. Furthermore, it is likely that separation would be fixed by the tip of one of the grooves which would restrict the minimum C_D achievable. The author, however, is unaware of any research to date which provides data to assert this notion.

2.4.5.4 Summary of conclusions: Grooves

Circumferential grooves, with their regular, uniform arrangement, appear to have an influence on flow analogous to surface roughness by similarly producing a substantial C_D rise in the post-critical regime. The increasing depth of the groove increases the surface area of the cylinder and this, combined with the choking effect of the groove channels and subsequent overspill, retards the flow and energises the boundary layer in the area of the groove tips which seem to act as a kind of vortex generator.

As with surface roughness, it is difficult to quantify the effects of specific groove positioning due to the effect of the boundary between smooth and grooved surfaces, which act as a kind of tripping device.

Spanwise grooves appear to be more difficult than circumferential grooves to achieve a desirable flow influence due to their transverse positioning to the flow. Kimura and Tsutahara (1991) found that there was only a small change in angular position of the groove required to turn a drag reduction into a drag increase, and that a single groove has no effect at $\phi_g < 70°$. This implies that this method would be successful only with applications of a very specific, known flow direction.

2.4.6 Dimples

Bearman and Harvey (1976) conducted experiments to clarify the influence dimples have on allowing a golf ball to travel further than a smooth sphere, given the same initial conditions. They equated the K/D ratio of surface roughness with the ratio of dimple depth to cylinder diameter, where K similarly represents dimple depth or roughness element height. In doing so they pointed out that for the same value of K/D dimples are more effective than surface roughness at reducing the critical

Reynolds number and maintaining a low drag coefficient with increasing Reynolds number. Zdravkovich (2003) commented that this much reduced rate of increase in drag with Reynolds number – after the critical value – suggests that the dimples are effective in tripping the boundary layers without causing the same level of thickening associated with positive roughness.

Comparing data from dimpled spheres in Bearman and Harvey (1976) with Achenbach's (1974*a*) sand-roughened sphere experiments (Figure 2.23), it is clear that increasing K/D on sand roughened spheres reduces the Re critical value but, after the minimum C_D value is reached, C_D increases rapidly again with increasing Re.

- The increased drag arising from the roughened surfaces at higher post-critical Re is thought to be due mainly to the effect of roughness on the development of the turbulent boundary layer growing on the sphere;

- The increased roughness leads to a thickening of the boundary layer and consequently earlier separation of the flow.

At sub-critical Re, the drag of smooth and dimpled cylinders are similar, however, the critical flow regime occurs at a much lower Reynolds number for the dimpled cylinder. As shown in Figure 2.21, for a sand-roughened cylinder with similar K/D the fall in drag is induced at lower Re still, but the dimples generate a lower minimum drag coefficient.

In the sub-critical regime for the two configurations of dimpled cylinders tested by Bearman and Harvey (1993), there is a marked difference in drag coefficient (Figure 2.22). In this Re range, the arrangement with the dimples on the flow axis had a lower C_D than the setup with the dimples arranged symmetrically either side

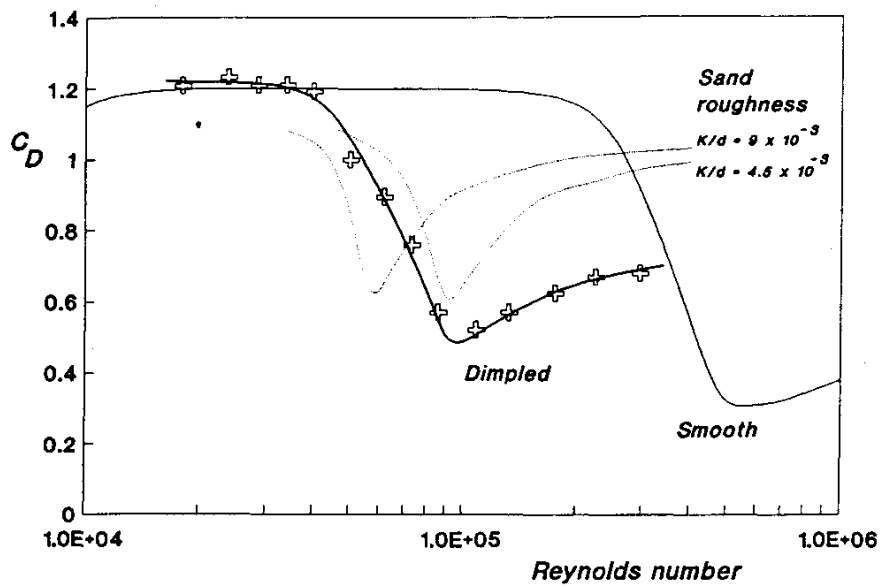

Figure 2.21 – Variation of C_D with Reynolds number for smooth, sand-roughened and dimpled circular cylinders, from Bearman and Harvey (1993).

of the flow axis. The super-critical and post-critical C_D values are, however, in close agreement. For the dimple on flow axis configuration, a plateau is observed in the drag coefficient in the critical regime Figure 2.22, believed to be caused, as similarly observed by Kimura and Tsutahara (1991), by a separation occurring at the front of a dimple or a little way after it.

Bearman and Harvey (1993) commented on their experiments that the small scale of the flow features being studied made it very difficult to draw many definite conclusions of the flow physics from their analysis by oil flow and hot-wire just downstream of a dimple. They proposed, however, that:

- A pair of vortices trail back from each dimple and that these vortices may help to energize the cylinder's boundary layer;
- The disturbance introduced by a dimple promotes transition, and it is likely that at a particular Re, transition, and similarly separation, occurs at a fixed

angular position across the span of the cylinder.

Bearman and Harvey (1993) further noted that the weak and irregular shedding characteristic of the super-critical flow regime for a smooth cylinder was not found for the dimpled cylinder and that vortex shedding remained strong and regular throughout the Re range examined.

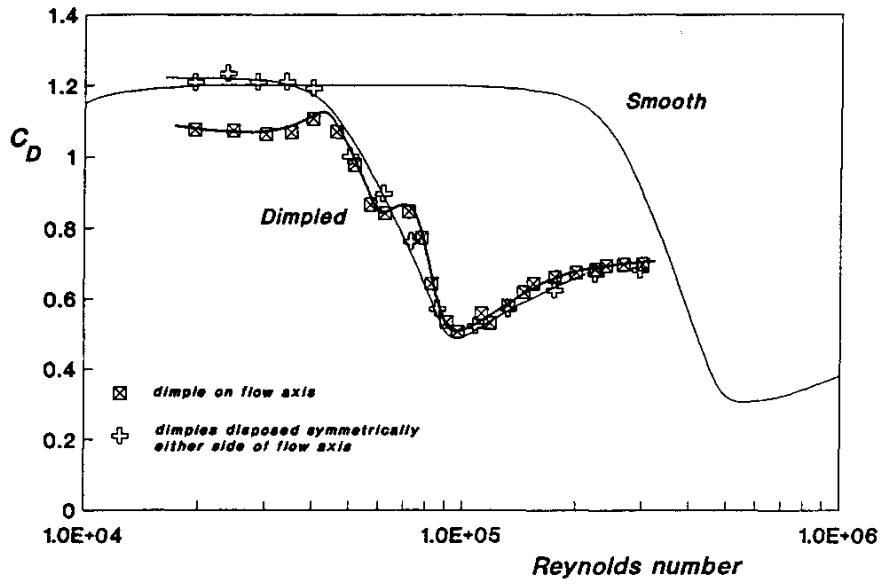

Figure 2.22 – Variation of C_D with Reynolds number for two orientations of dimple surfaced circular cylinders, from Bearman and Harvey (1993).

Choi et al. (2006) report that dimples cause a local flow separation, triggering shear layer instability along the separating shear layer, resulting in the generation of large turbulence intensity. This in turn imparts energy back into the boundary layer in a method analogous to vortex generators, narrowing the near wake to reduce pressure drag by extending the separation point upstream.

2.4.6.1 Comments on dimples v. sand-roughness

In a comparison of dimple application to spheres Bearman and Harvey (1976) and cylinders, Bearman and Harvey (1993) pointed out that for similar values of K/D, dimples cause C_D to fall at lower Re than sand-roughened spheres but for cylinders the opposite is the case.

- After the C_D fall, drag remains almost constant for a dimpled sphere with increasing Re, whereas for sand-roughened spheres C_D rises sharply after the minimum then asymptotes in post-critical region with increasing Re;
    - The post-critical drag is shown to have a more pronounced increase for dimpled cylinders than the plateau generated by similarly dimpled spheres Figure 2.23;
- It is clear, however, from both sphere and cylinder experiments that a dimpled surface has a much more beneficial effect on flow development than sand roughness in the post-critical regime.

2.4.6.2 Summary of conclusions: Dimples

Experiments on dimpled spheres and cylinders have shown that a dimple appears to be a very efficient means of promoting the critical Reynolds number while maintaining the low CD over a large Reynolds number range. They seem to have the quality of being able to simultaneously trip the flow and entrain vortices into the boundary layer to energise it, while preventing a thickening of the boundary layer to allow the flow to remain attached much further downstream – and throughout a wider range of Reynolds number – than most other surface textures or roughness.

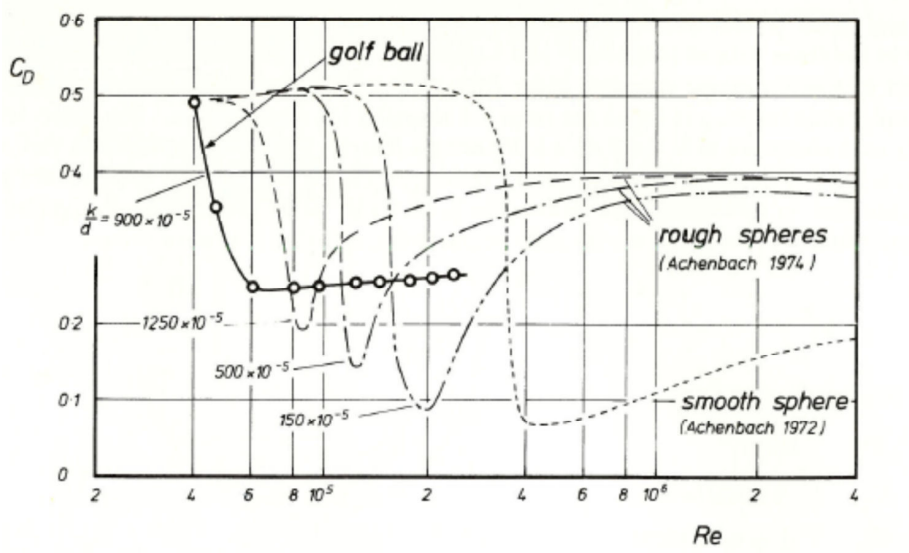

Figure 2.23 – Variation of C_D with Reynolds number for smooth, surface roughened and dimpled spheres, from Bearman and Harvey (1976).

Again, as with tripping wires, it is interesting to note that the effectiveness of dimples appears to be greater on spheres than on cylinders. A regularly arranged dimple pattern is useful for variable flow incidence, however there is also a drawback in that the separation line may be fixed to the front of a spanwise set of dimples. The ultimate reduction in drag will likely not be able get close to that of a smooth cylinder due to the perceived inability of such a textured surface to allow separation bubbles to form.

2.5 Final notes on passive drag reduction

The plot shown in Figure 2.24 by Son et al. (2011) provides a comparable indication of the characteristic effectiveness of a number of the above discussed passive drag reduction measures applied to spheres. The point to note here is not the comparative minimum C_D values but the characteristic C_D v. Re curve associated with each method of boundary layer control.

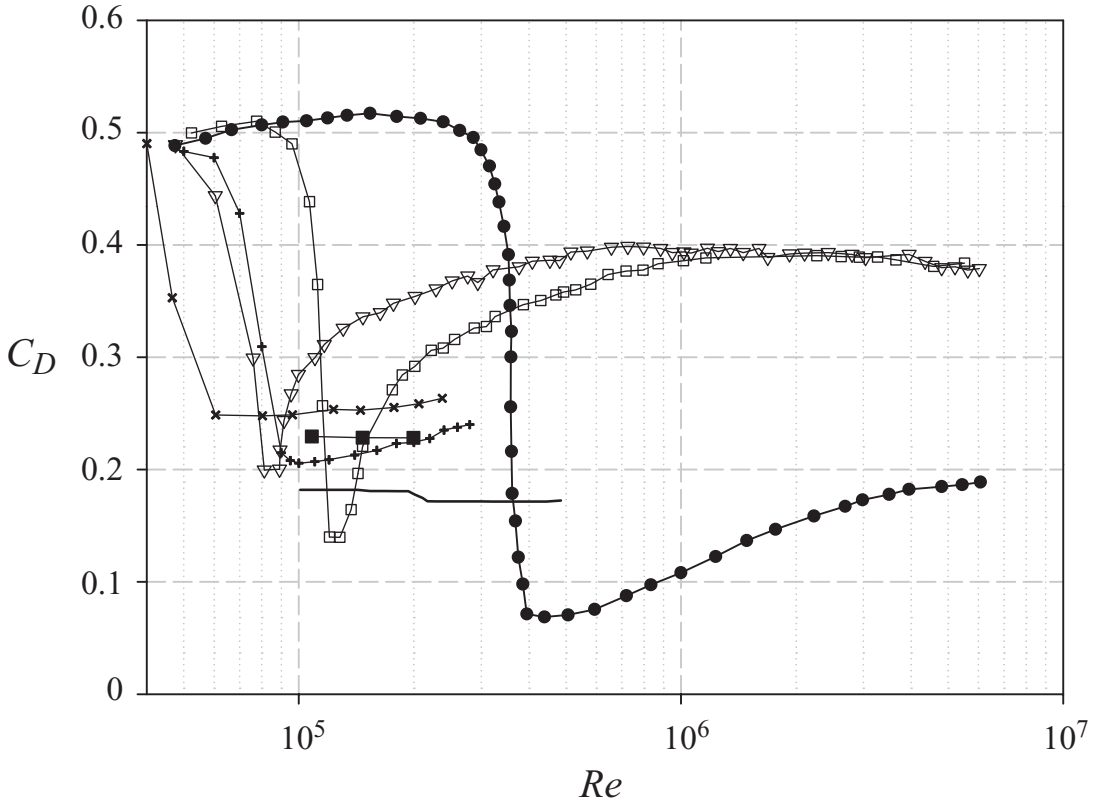

Figure 2.24 – Variation of C_D with Reynolds number for smooth, surface roughened, dimpled and tripping wire affixed spheres, from Son et al. (2011), where ● smooth Achenbach (1972); ✖ dimpled $[k/d = 0.9 \times 10^{-2}]$ Bearman and Harvey (1976); ✚ dimpled $[k/d = 0.4 \times 10^{-2}]$ Choi et al. (2006); ▽ roughened $[k/d = 1.25 \times 10^{-2}]$ Achenbach (1974*a*); □ roughened $[k/d = 0.5 \times 10^{-2}]$ Achenbach (1974*a*); ■ tripped $[k/d = 0.33 \times 10^{-2}]$ Maxworthy (1969); —— tripped [k/d not available] Wieselsberger (1914).

2.5.1 General passive flow control methodology

As is shown by a considerable body of literature on the subject – a fraction of which is reviewed here – the essential methodology of surface mounted passive flow control devices is as follows:

- Induce transition from a laminar to a turbulent boundary layer;
- The increased energy of a turbulent boundary layer allows flow to remain attached further downstream against an adverse pressure gradient;
- Delaying flow separation reduces wake width, hence increasing base pressure and lowering pressure drag.

2.5.2 Optimal placement of passive flow control devices

It is pertinent to make the point that, throughout the literature on circular cylinders, the optimum placement of discrete passive flow control devices submerged within the cross-flow boundary layer seems to converge on or around $\pm 65^{\circ}$ (see, for example, Fage, 1929; Fujita et al., 1985; Heine et al., 2010; Igarashi, 1986; Mizuno, 1970). This circumferential position is located just a few degrees upstream of the mean point of minimum static pressure, $C_{p(min)}$, in the pre-critical regime (Figure 2.2 and Figure 2.3). One can logically reason from this that it is more effective to disturb the boundary layer prior to the onset of an adverse pressure gradient, after which the flow has already begun to lose momentum.

2.5.3 Note on separation bubble

As explained in section 2.3.3, the occurrence of the separation bubble regimes, and in particular the two-bubble regime, maximise the delay in flow separation from a circular cylinder. The consequent narrowing of the near wake generates a recovery of base pressure which is unsurpassed in any other flow regime; this leads, ultimately, to a drop to $C_{D(min)}$ unmatched by any passive flow control method which promotes the critical regime. Naturally, this $C_{D(min)}$ is the target for drag reduction in the sub-critical flow regime, and observing the fluid mechanics of the separation bubble regime it is desirable to somehow recreate them in the sub-critical regime. However, due to the lack of an ability to finely control – passively – the stability and thickness of the cylinder boundary layer (naturally in constant oscillation over the cylinder surface), it is generally thought not to be possible to replicate the separation bubble regime of a plain cylinder throughout the pre-critical Reynolds number range.

Chapter 3

Experimental setup

3.1 Wind tunnel

All experimental investigations were conducted in the low-speed, closed return, Donald Campbell wind tunnel laboratory in the Department for Aeronautics at Imperial College London. The working section measures 1.37m wide (z) $\times$ 1.22m high (y) $\times$ 2.98m long (x) and delivers a maximum sustainable speed of $\approx 44m/s$. The contraction ratio is $4.92:1$ and the flow within the working section is of good quality; as described in Bearman et al. (1976), at the mid-point of the working section at $30.5m/s$, the flow of 93% of the cross-sectional area maintains centreline speed to within $\pm 0.375\%$ and the maximum turbulence intensity is 0.15%. The laboratory is equipped with a force balance measuring lift and drag, and a 3-axis traverse gear for accurate positioning of measurement apparatus, such as hot-wires, within the working section.

The wind speed was measured via a Pitot-static tube placed upstream of the model in the working section of the tunnel, and flow temperature was measured

using a thermocouple probe inserted into the working section, downstream of the model. An atmospheric pressure probe in the tunnel control room, along with both the Pitot-static tubing and thermocouple cable, were all connected to a Furness FCO510 Micromanometer which in turn was connected to a PC to digitally record the flow variables in the wind tunnel. The potentiometer of the wind tunnel motor inverter was connected via a National Instruments NI-DAQ unit to the PC which enabled the use of a proportional-integral-derivative (PID) controller to be used to set and maintain the tunnel flow speed or Reynolds number to within 0.5% of the parameter set-point during testing.



Figure 3.1 – Photograph of typical cylinder arrangement mounted in the working section – looking downstream from the settling chamber of the Donald Campbell wind tunnel, Department for Aeronautics, Imperial College London.

3.2 Cylinder setup

All cylinder models measured $99.5mm$ in diameter, D, and were mounted with end plates to reduce end-effects – in particular the influence on base pressure, as shown by Stansby (1974) – to provide an active length, $L = 1,220mm$ (aspect ratio, $L/D = 12.26$). Depending on the experiment, and hence mounting used, the blockage was in the range $8.16\% - -9.30\%$ and corrections were made throughout for flow velocity, U_∞ – and hence Reynolds number, Re_D, drag coefficient, C_D, and lift coefficient, C_L, using the method of Allen and Vincenti (1944). The end plates were steel and measured $500mm(x) \times 300mm(y) \times 1.7mm(z)$ for all experiments, apart from the PIV tests in the (x, y) plane (see section 3.8.1 for more details) for which one end plate was made of transparent perspex and had an increased thickness of $6mm(z)$. The final section of this end plate tapered to approximately $1mm(z)$ at its trailing edge and the perimeter edges exposed to the oncoming flow (front, top and bottom) were rounded off on all end plates – with particular attention paid to the thicker perspex plate.

3.2.1 Coordinate system

The spatial references made throughout this body of research refer to the axes system as shown in Figure 3.2. The system follows a right-handed coordinate system with the free stream flow direction assigned to the x-direction (positive downstream), the vertical component is the y-axis (positive upwards) and the cylinder span-wise component is the z-axis (positive to the left when looking from upstream). The angle about the z-axis of the cylinder, ϕ, is given as shown where $\phi = 0^\circ$ is taken to be the foremost upstream point of the cylinder circumference (the mean position of the

frontal stagnation point of the cylinder). ϕ is given as positive in an anti-clockwise direction when viewing in the (x, y)-plane with flow from left to right.

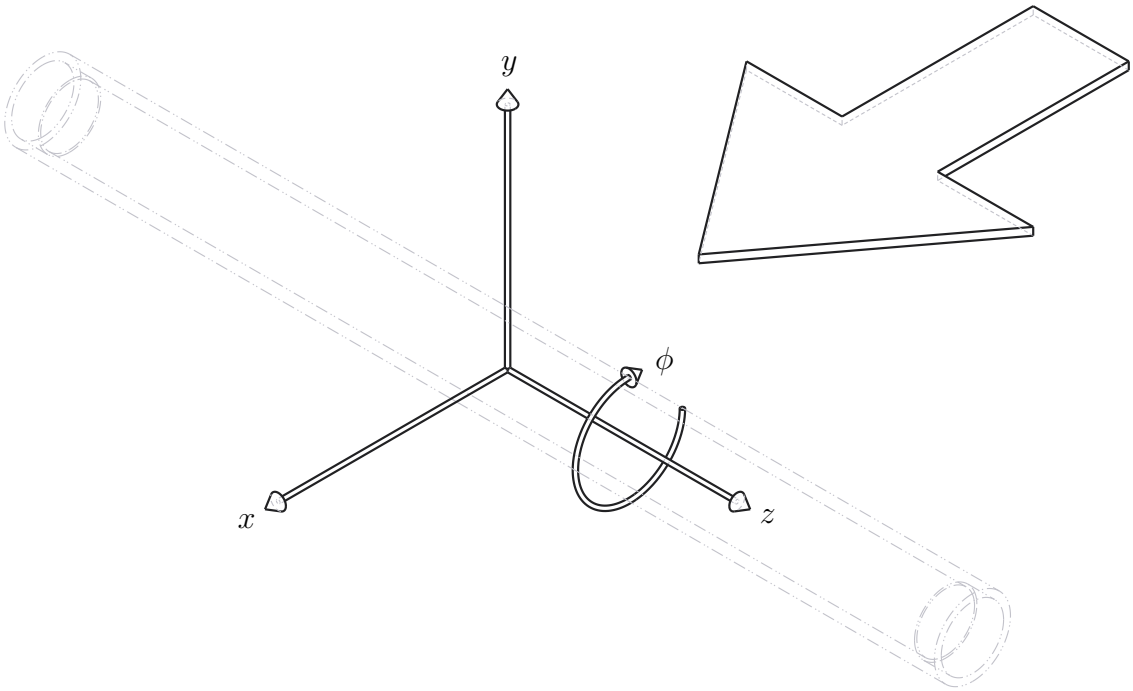

Figure 3.2 – Schematic definition of axes coordinate system.

The origin of the axes system is located where the central axis and centre-span of the cylinder coincide.

3.3 Force measurements

During experiments which included lift and drag force measurements, the model was mounted via the force balance through the walls of the tunnel. Dummy cylinder sections were used as fairings to cover the cylinder mountings within the tunnel and thus isolate them from the loads generated on the model. The dummy-ends were $100mm$ diameter, providing a total blockage ratio of 8.16%. This setup provided

force measurements of the cylinder and end-plates only, with the forces on the end-plates considered negligible.

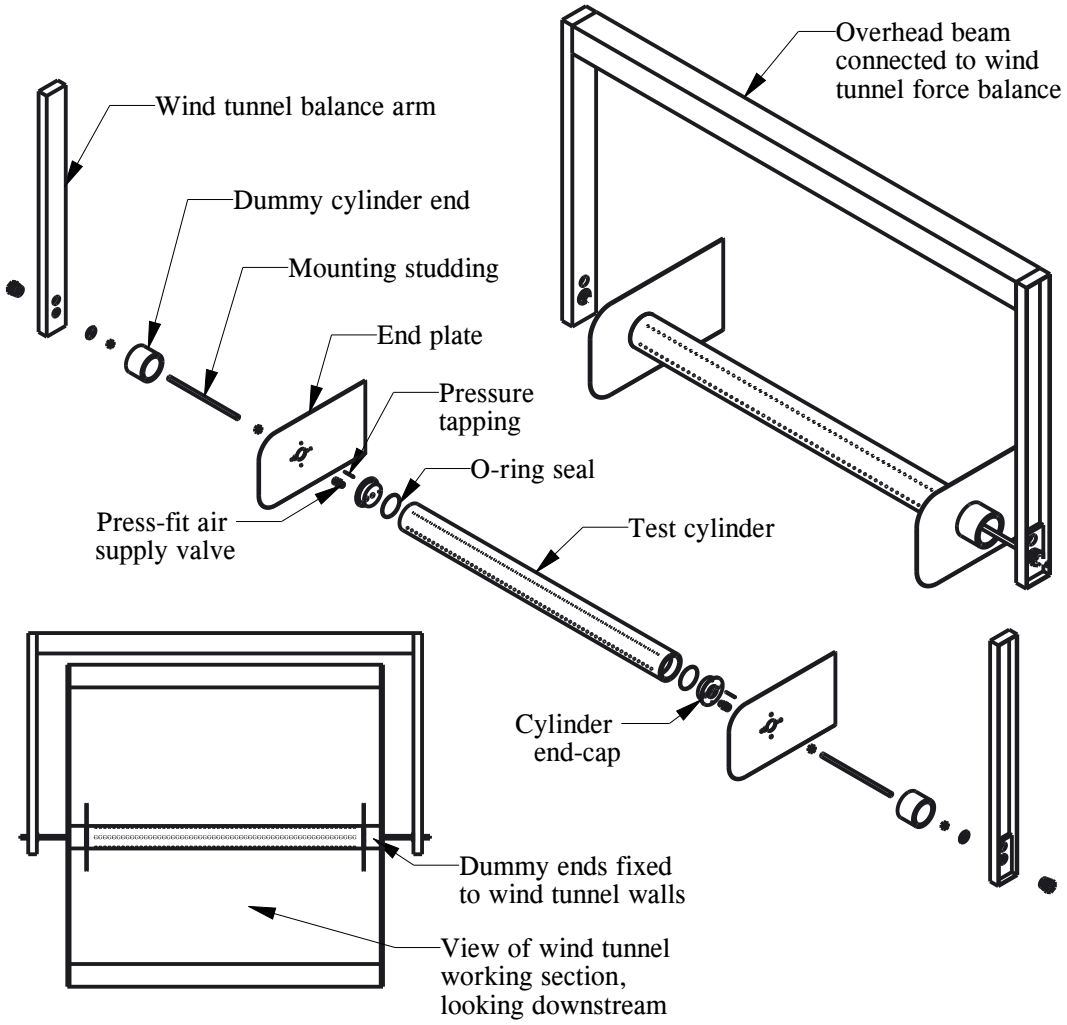

Figure 3.3 – Exprimental setup of wind tunnel for force balance measurement tests.

It should be noted that the nature of the operation of the force balance used, rather than the accuracy of the balance itself, leads to an inevitable reading uncertainty. Measurements were taken by manually balancing the weigh-beams and readings were written by hand once a satisfactory judgement of the mean position

of the electronic display gauge was found; unsteady forcing on the model required the operator to make a judgement as to the average balance point while the gauge fluctuates – often in an unpredictable and irregular manner. Though readings were noted to a resolution of $0.05N$, the uncertainty in these measurements varied with the nature of the forcing experienced by the cylinder at the time of measurement, and thus cannot be noted simply as a scale reading uncertainty. At high Reynolds numbers the magnitude of the force fluctuations could be high, making the determination of a mean balance point difficult and thus the absolute uncertainty was high, but as a proportion of the total force measured, the relative uncertainty was low. In contrast, at low Re_D, the mean balance points were more easily estimated due to a smoother and more predictable oscillation in the forces transmitted through the balance, resulting in a lower absolute uncertainty but higher relative uncertainty. As shown throughout the following sections in the main body of the thesis, a good correlation is found when comparing the results acquired for this body of research with relevant data in peer-reviewed literature, however, an estimation of the relative uncertainties in drag force, F_D, measurements of a typical set of readings for this research are given here as a reference:

- For the lowest Re_D measurements, the approximate reading error was $\pm 0.05N$, equating to a relative error of $F_D \pm 12.0\%$;
- For the highest Re_D measurements, the approximate reading error was $\pm 0.45N$ equating to a relative error of $F_D \pm 0.7\%$.

As mentioned in section 3.1, the wind tunnel flow speed was maintained to within $U \pm 0.5\%$. The maximum and minimum uncertainties in the calculation of drag coefficient, C_D (see Equation 1.2 in section 1.2.1), can therefore be calculated

as follows, where the uncertainties in the acquired values of temperature and atmospheric pressure are considered negligible in their impact on the relative uncertainty of air density, ρ:

The relative uncertainty of C_D at the lowest Re_D measurements is:

$$12.0\% + (2 \times 0.5\%) = C_D \pm 13.0\% \tag{3.1}$$

... and the relative uncertainty of C_D at the highest Re_D measurements is:

$$0.7\% + (2 \times 0.5\%) = C_D \pm 1.7\% \tag{3.2}$$

The high relative uncertainty at the lowest Re_D force measurements rapidly diminishes with a small increase in Re_D; for example, by the time the Reynolds number is increased to $Re_D = 4 \times 10^4$ (still within the sub-critical Re_D range for most of the cylinder drag reduction methods covered in this thesis), the relative uncertainty in F_D measurements drops to around $\pm 1\%$.

3.4 Passive jet simulation

Part of this body of research involved a feasibility study of a passive flow control method by simulating its action – in the first place – by actively controlling it. The concept was to supply air jets – positioned at the cylinder surface – through passive ventilation of the cylinder volume. The passive supply was simulated by pressurising the cylinder with an external compressed air supply, manually controlled with gate valves, with the pressure of the internal cylinder volume monitored via pressure tappings in the cylinder end-caps.

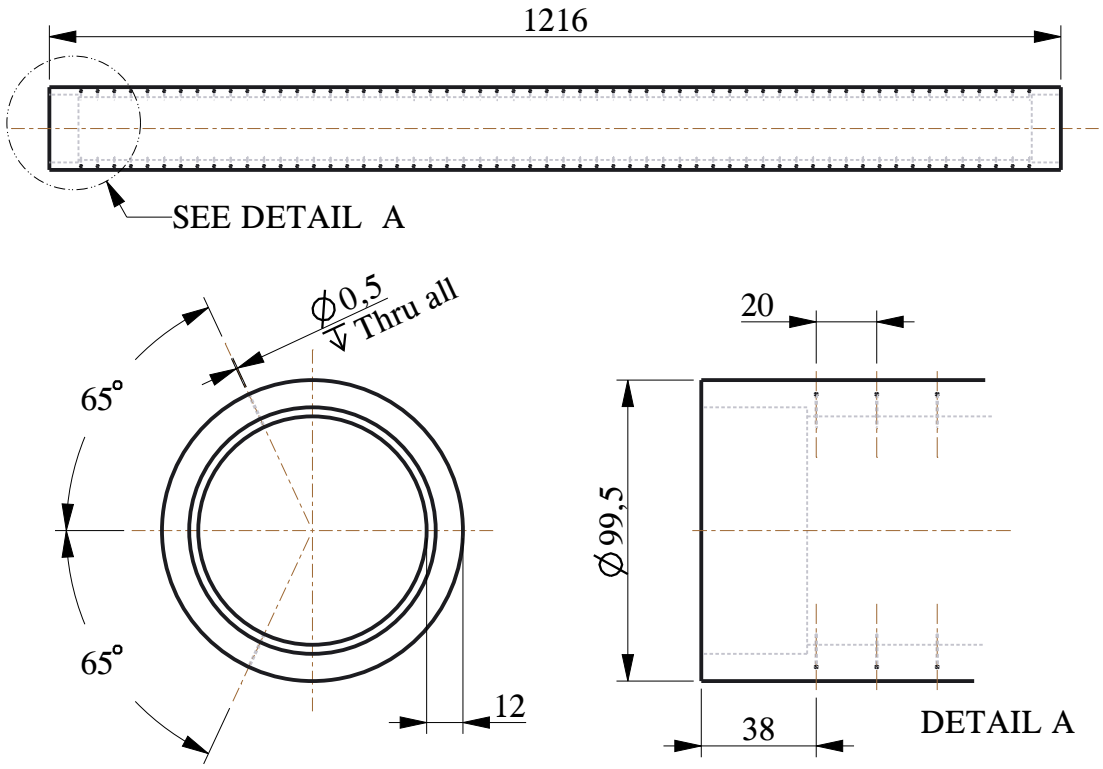

Figure 3.4 – Cylinder schematic showing the arrangement of jet exit holes for the passive jets feasibility study. All dimensions in mm.

The additional cylinder pressures predicted to be available by passive means were applied continuously to the cylinder volume while drag measurements were taken to record the simulated impact of the jets on C_D as compared to a plain cylinder. The cylinder was mounted as detailed in section 3.3, which also details the assembly of the cylinder setup. Prior to testing, the jet holes were sealed over and the cylinder was pressure tested to check for air leaks.

Two span-wise rows of 58 holes ($0.5mm$ diameter, $20mm$ spacing) were drilled through the cylinder wall, of thickness $12mm$ (thus providing a stroke length, l_J, of $l_J = 12mm$), such that they were interconnected by the internal cylinder volume. As shown, these jet exit holes were positioned $\pm 65^\circ$ from the frontal stagnation point.

Due to fixing restrictions at the cylinder ends, there was a larger gap between the final jet exit hole and end of the cylinder.

3.5 Jet flow-rate measurements

Using ball-float flow meters, the total volume flow-rate of the air out of the cylinder via the jet exit holes was measured by simulating the experimental conditions of the passive jet setup. With the passive air supply holes sealed off, the flow-rate through the jet exit holes was controlled by valves on a compressed air supply circuit into the cylinder. The pressure within the cylinder was maintained to the levels measured during the passive flow control setup, such that the time-averaged pressure differential between the internal cylinder volume and static pressure at the jet exit holes (and hence jet flow-rate) was consistent between the two setups.

The internal cylinder volume was supplied with air from each end, protected from the wind tunnel flow by the dummy cylinder ends discussed in section 3.3. Balancing valves allowed an equal supply of air to both ends of the cylinder and it was assumed that the internal volume of the cylinder – acting as a plenum chamber – had a broadly uniform pressure throughout the volume. As per previous setup iterations, and consistent with the measurements taken during the passive jets setup, the cylinder pressure was measured via pressure tappings within the end caps of the cylinder and connected to a Chell pressure transducer with a high frequency response.

Other than the inclusion of the flow meters and accompanying piping and valve connections, the wind tunnel and experimental setup was identical to that shown in Figure 3.3 and used in experiments to measure drag and lift forces, and internal

cylinder pressure. Care was taken to ensure that the arrangement of the additional pipework and valves did not impede or alter the measurements taken by the force balance, with test measurements taken to ensure consistency and corroboration with previous measurements.

3.6 Flow visualisation

For the flow visualisation tests, the wind tunnel setup and cylinder configuration were as detailed in section 3.1 – 3.3.

The method employed was the surface oil flow visualisation (SOFV) method; a volatile mixture of oils and tracer particles applied to an observation surface on the test model and as the flow interacts with the body the oil evaporates to leave a trail of particles in the pattern of the time-averaged skin friction streak lines.

This method is particularly useful for acquiring time-averaged surface flow topology where the flow remains attached, and can provide means of identifying critical points and hence the points of flow separation from a surface. It is not ideally suited to all flow conditions and geometrical setups, but the mixture can be adjusted to an extent to allow for varying flow conditions and hence desired evaporation rates; there is inevitably a conflict with gravity on less than flat surfaces so this has to be taken into consideration when designing the experiment – and analysing the results.

The process of obtaining surface oil flow visualisation images was as follows:

The basis of the oil mixture used in these experiments consisted of the following, with the mixture continuously adjusted according to the testing conditions and results obtained:

- Talcum powder (tracer particles) [1 part];

- Paraffin (kerosene, low viscosity, volatile) [5 parts];
- Tonna 68 Oil (Heavy, high viscosity) [1 part];

The solution was mixed to a thin consistency and applied with a fine-haired paint brush to provide a smooth, even coating on the observation surface. Once applied, the test section was quickly cleared and sealed before running the wind tunnel at the desired testing conditions. A proportional-integral-derivative (PID) controller was used to ensure that the testing conditions were maintained throughout in order to provide consistent results for comparison with other data. Specifically, in these tests, the Reynolds number, Re_D, of the flow was maintained automatically via the controller to mitigate the effects of the change in flow temperature and hence density over longer runs.

Depending on the observation being made, images were captured in two different ways; either by still photographs within the wind tunnel – after the run was complete – or video recordings made during the test run to observe and capture dynamic properties of the surface flow. The video recordings were useful to provide evidence of, for example, the direction of rotation of vortical structures close to the surface and the development of the skin friction lines as the flow speed varies. To obtain the still photographic recordings, flow conditions in the wind tunnel are maintained until the skin friction streak lines are suitably visible on the observation surface and the oil solution has set sufficiently to maintain its shape. The wind tunnel flow is switched off and allowed to settle before entering the working section to set up the camera equipment and take the stills.

It was also possible during these tests, for example, to measure the points of flow separation relative to the stagnation point of the cylinder and hence determine

these points in terms of circumferential angle, ϕ.

3.7 Constant temperature anemometry

Two different constant temperature anemometry (CTA) experiment configurations were used: one to measure the wake vortex shedding frequency; and the other to measure the instability emanating from the interaction of the passive jets with the cylinder cross-flow.

3.7.1 Wake traversing

For the cylinder vortex shedding measurements, a Dantec Dynamics 55P16 (single-sensor, miniature, straight) hot-wire probe was placed in the bottom shear layer of the near wake (as shown in Figure 3.5) – ensuring that the probe holder and traverse system were not buffeted by the cylinder wake during acquisition.

The hot-wire voltage signals were acquired using a Dantec Dynamics 54T42 MiniCTA system, which was connected through a National Instruments NI-DAQ unit to a PC which managed the data acquisition. The sampling frequency was $2kHz$ and $N = 2^{15}$ samples were taken for each acquisition location.

Relative to the cylinder axis centreline, the hot-wire probe was positioned $x/D = 1.5$, $y/D = -0.5$ and traversed over 16 acquisition locations of the central span in the z-axis. Selecting the two jet holes either side of the centre-span ($z = 0$) of the $z_J = 20mm$ cylinder, the hot-wire traversed a $z = 30mm$ distance, beginning $5mm$ to the left of one jet hole ($z = -15mm$) and finishing $5mm$ to the right of the adjacent jet hole ($z = 15mm$).

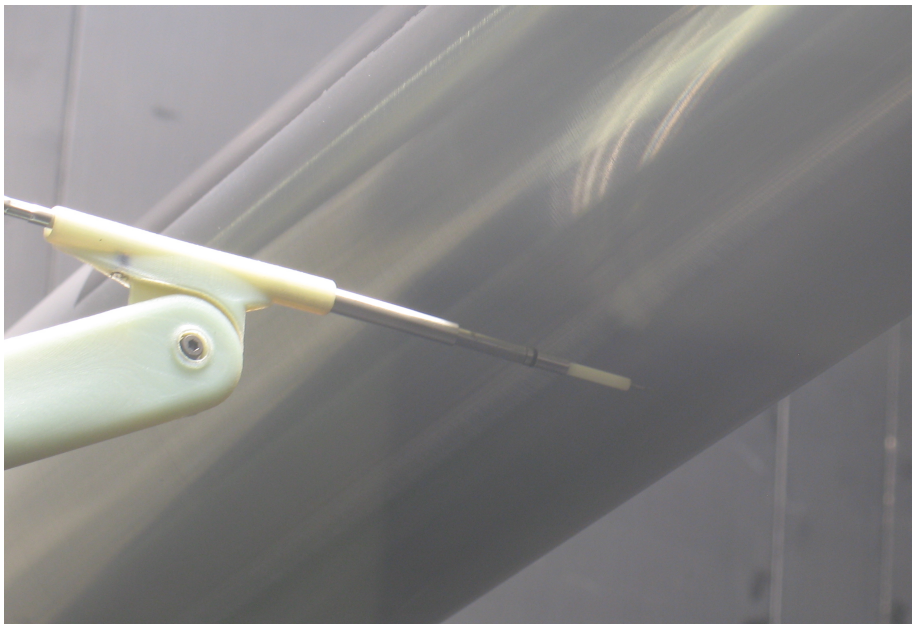

Figure 3.5 – Photograph of the wake traversing hot-wire probe, where the shedding frequency of the bottom shear layer was acquired.

3.7.2 Jet shear layer instability

The shear layer instabilities were acquired using a boundary layer probe placed as shown in Figure 3.6. Figure 3.7 shows an experimental design schematic of the setup in the wind tunnel working section.

For the high-frequency jet instability, a Dantec Dynamics 55P15 (single-sensor, miniature, boundary layer) probe was positioned very close to a jet exit hole in the middle of the cylinder span using a custom made probe holder which affixed to the wind tunnel traverse system. The hot-wire voltage signals were acquired with a Dantec Dynamics StreamLine Pro Anemometer system.

To mitigate aliasing, low and high-pass filters were set on the Dantec Dynamics Streamline hardware via the Dantec Dynamics Streamware software. The filters were set on the original input signal to remove energy from the higher and lower

frequencies, respectively, which are found beyond the desired measurement range.

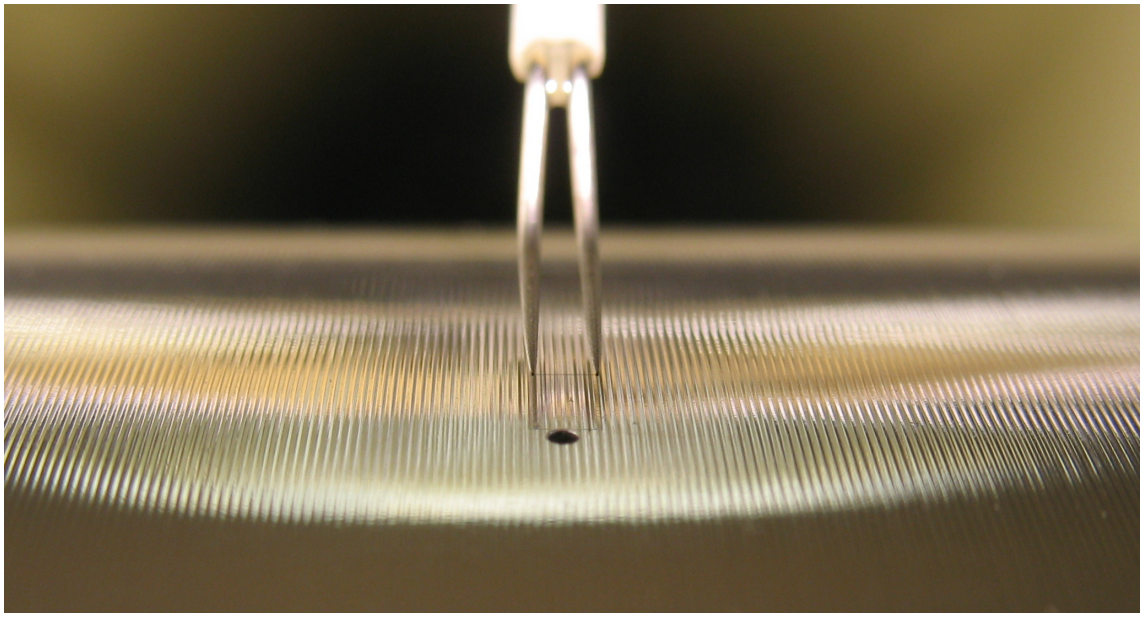

Figure 3.6 – Hot wire acquisition position for measuring jet instability.

The sample rates were set to $f_s = 60kHz$ for the low Re_D range of tests, where $N = 2^{24}$ samples were taken for each run, and $f_s = 120kHz$ for tests in the mid to high Re_D range, where $N = 2^{25}$ samples were taken for each run. The sensitive nature of the experiment and extremely close proximity of the delicate hot-wire sensor to the cylinder surface meant that a new cylinder mount support was designed to minimise any movement or vibration of the cylinder up to the highest test Reynolds numbers. The new supports were bolted though the floor of the working section and into the wind tunnel frame, as shown in Figure 3.7. This, however, meant there was an increase in the wind tunnel blockage to 9.30%.

Generally, with increasing tunnel flow speed the movement of the hot-wire probe and/or cylinder model also increased, leading to higher risk of hot-wire sensor breakage due to contact between the cylinder surface and the wire. This meant that as flow speed was increasing the hot-wire was necessarily positioned at an increasing

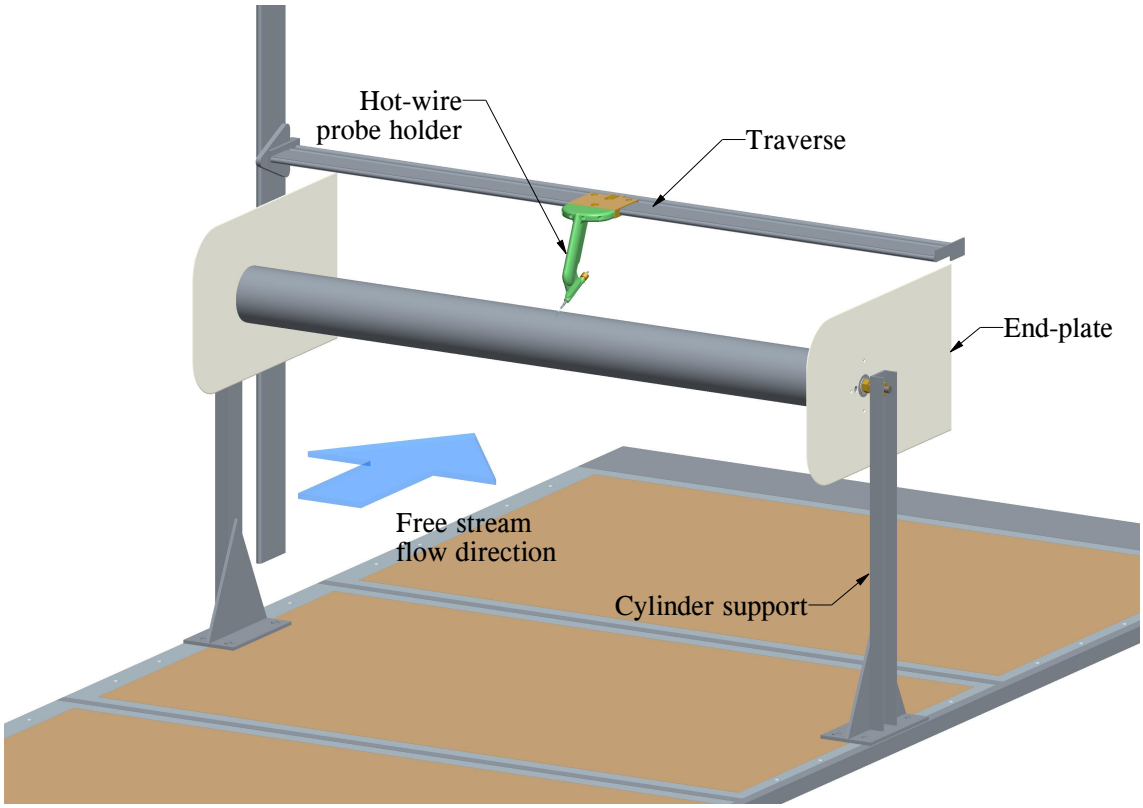

Figure 3.7 – Experimental setup of wind tunnel for hot-wire measurement of jet instability.

distance from the cylinder surface to prevent contact. This created a problem in picking up the desired instability because as the flow speed increased the boundary layer was also becoming thinner.

For cross-flow instability measurements, the hot-wire was aligned by eye directly behind a centrally located jet exit hole and as close as possible to the cylinder surface – allowing for probe deflection during tunnel running. From this position low speed measurements were taken, but as the flow speed increased and the movement of the probe in relation to the cylinder surface became greater – such that the probe was in danger of grounding on the cylinder – the probe was traversed vertically away, in very small increments, via the tunnel traverse system.

3.8 Particle image velocimetry

Investigations were made with two different particle image velocimetry (PIV) experimental setups in order to analyse aspects of the cylinder wake and boundary layer separation in two different coordinate planes. For both experimental arrangements, the flow was seeded with a 1:4 solution of polyethelene glycol (PEG) and water fed through a TSI 9307-6 atomiser, which produces a mist of particles with a mean diameter of $1\mu m$ (Oxlade, 2013).

3.8.1 Single camera, (x, y) plane

A single camera, two-dimensional (2D), two-component (2C) PIV experimental arrangement was used to capture the separating cylinder shear layer and wake in the (x, y) plane at four progressive stream-wise (x-coordinate) locations for two span-wise (z-coordinate) locations based on the array-spacing of flow control elements.

The setup comprised a single Dantec Dynamics HiSense 4MC camera (4MP resolution, maximum double-frame trigger frequency of $5.6Hz$) and Litron Nano L 200-15 laser (Nd:YAG laser medium) which were both mounted to a common traverse system to allow synchronised relocation of the camera field of view (FOV) and light-sheet position. The images were recorded using Dantec Dynamic Studio software before post-processing with LaVision DaVis software.

The standard deviation of fit parameter for the target calibration, for the plain cylinder and cylinder with passive jets, was $0.796pixels$ and $0.777pixels$, respectively.

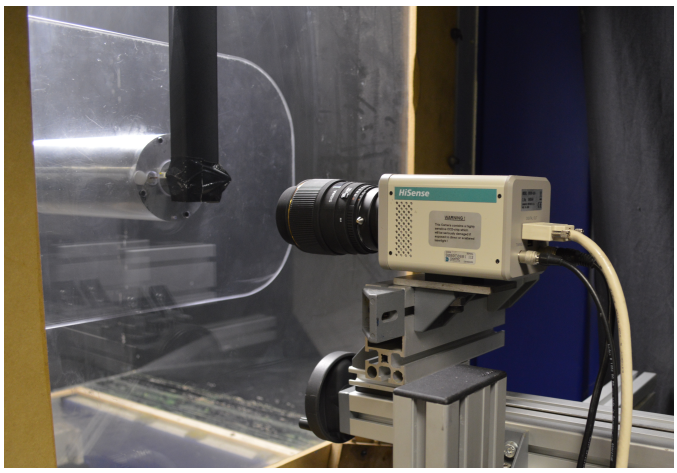

(a)

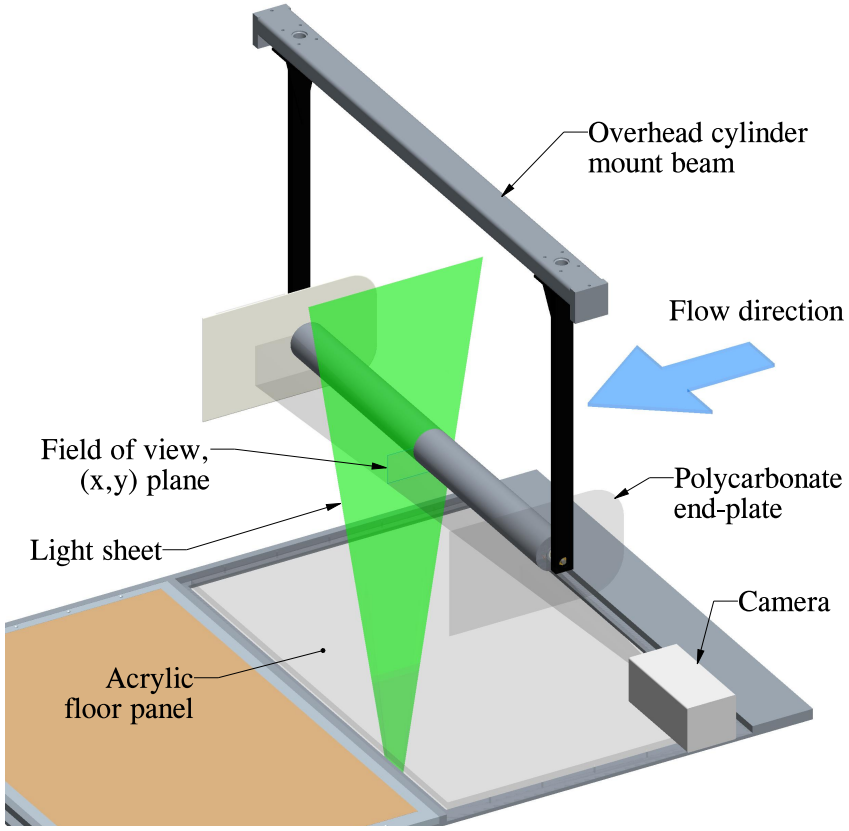

(b)

Figure 3.8 – (x, y) plane PIV setup: (a) photograph of camera mounted on the traverse system – positioned to capture PIV data of the bottom shear layer of the circular cylinder – mounted, as shown, in the wind tunnel working section; and, (b) schematic showing one of the light-sheet and FOV positions.

3.8.2 Stereo configuration, (y, z) plane

The stereo particle image velocimetry (SPIV) experiments involved a more complex arrangement of two symmetrically opposed high-speed 4MP cameras with an overlapping field of view (FOV), as shown in Figure 3.10. This setup provided a single plane, stereo image with all three vector components (u_x, u_y, u_z) resolved. For the high-speed stereo setup, a Nd:YLF Litron LDY300-PIV laser was used to generate a light-sheet in the (y,z) plane, immediately downstream of the cylinder, to observe spanwise wake dynamics as shown in Figure 3.9. Vision Research Phantom V641 cameras with a double frame rate of $725Hz$ were used with Nikon Nikkor 300mm $f^{\#}4$ telephoto lenses to create a small but high resolution field of view (FOV) in the centre-span of the bottom shear layer. The FOV was located $7mm$ downstream of

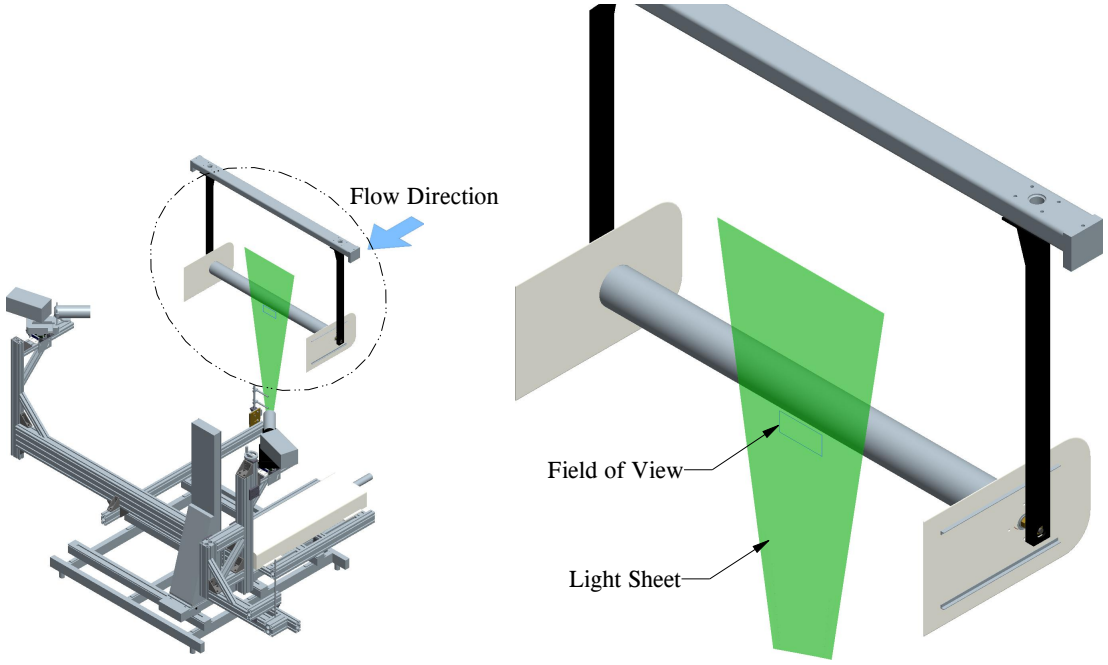

Figure 3.9 – Exprimental setup of wind tunnel for stereo PIV tests, showing light-sheet and FOV position in the (y, z) plane. The traverse system provides synchronous movement of the cameras and laser light-sheet.

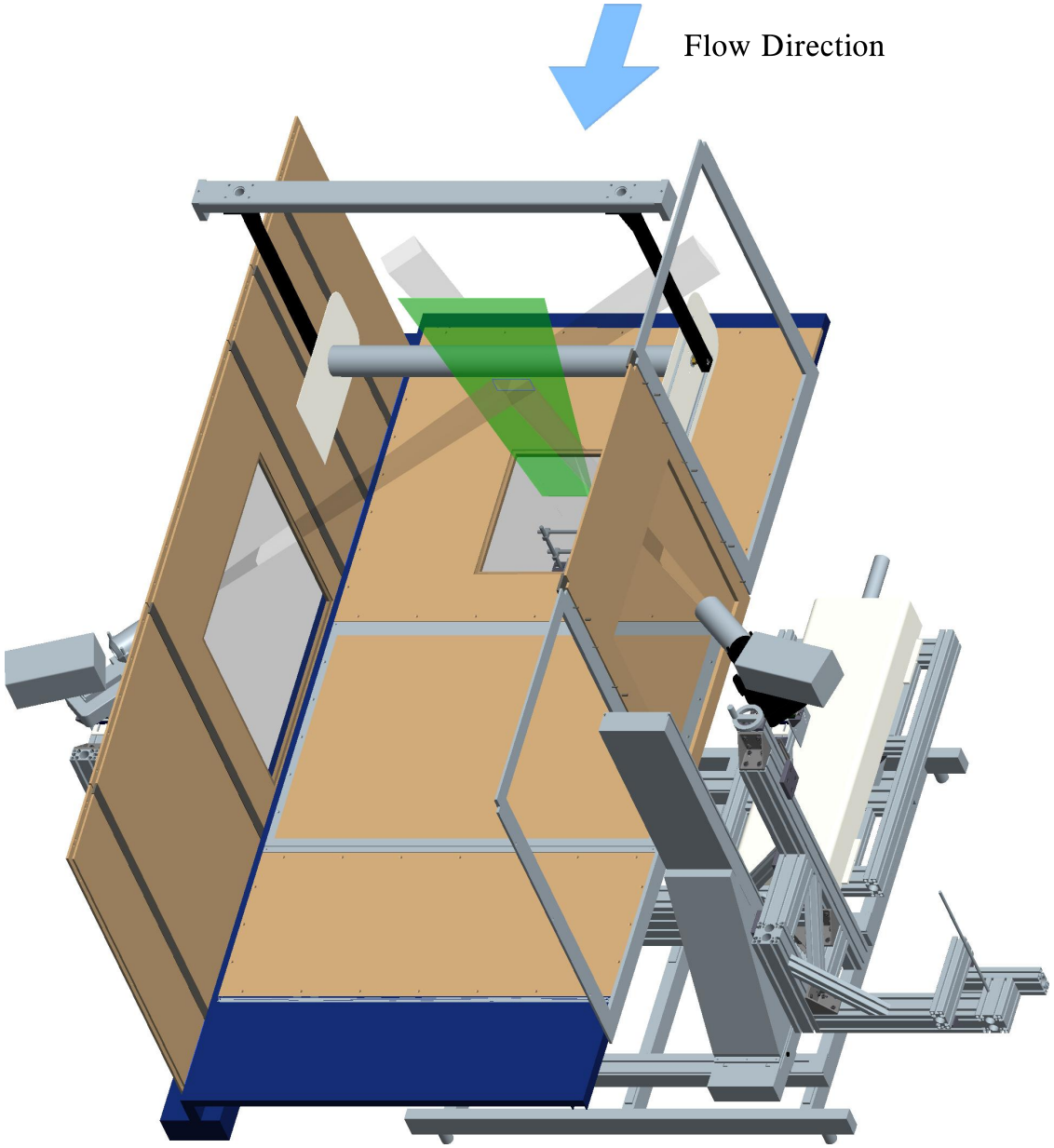

Figure 3.10 – Exprimental setup of wind tunnel working section for stereo PIV tests in the (y, z) plane.

the $\phi = 180^{\circ}$ point of the cylinder, with the FOV centre located approximately at the point where the centre-span and bottom $\phi = 90^{\circ}$ point on the cylinder coincide.

The standard deviation of fit parameters for the target calibration (where $x = 1mm$ between target planes of the three-dimensional target planes) were as follows: for the plain cylinder, camera 1 was 0.12 *pixels* and 0.09 *pixels* for planes 1 and 2, respectively; camera 2 was 0.11 *pixels* and 0.10 *pixels* for planes 1 and 2, respectively; for the cylinders with passive jets and pins, camera 1 was 0.11 *pixels* and 0.09 *pixels* for planes 1 and 2, respectively; camera 2 was 0.11 *pixels* and 0.10 *pixels* for planes 1 and 2, respectively.

Chapter 4

Review of dimples and tripping wires

The objective of this review was to obtain characteristic data for the flow behaviour of a smooth-surfaced cylinder in addition to that of two cylinders modified in different ways to passively induce the critical flow regime to a lower Reynolds number, using the testing environment to be used throughout this body of research. Drag measurements were taken for three cylinder arrangements and data was also captured from the wake of two of the cylinder configurations.

The three cylinder configurations were:

1. A 'Plain' cylinder (smooth surface, unadorned);
2. A Plain cylinder with tripping wires, and;
3. A Dimpled cylinder.

4.1 Experimental arrangement

For full details of the experimental setup and procedure, see section 3.1 – 3.3.

For the cylinder with tripping wires, the tripping wires were fixed to the plain cylinder surface ±65° from the frontal stagnation point of the cylinder, an angle chosen on the basis of findings by Fage and Warsap (1930) and James and Truong (1972) for the optimal placement of a small trip-wire. The trip wire had a diameter of 0.47mm, and was fixed to the cylinder with tape of 0.02mm thickness. This gave a trip wire to cylinder ratio d/D = 0.49%. The dimpled cylinder was the same model as tested by Bearman and Harvey (1993), with dimples machined into the cylinder surface in the arrangement shown in Figure 4.1.

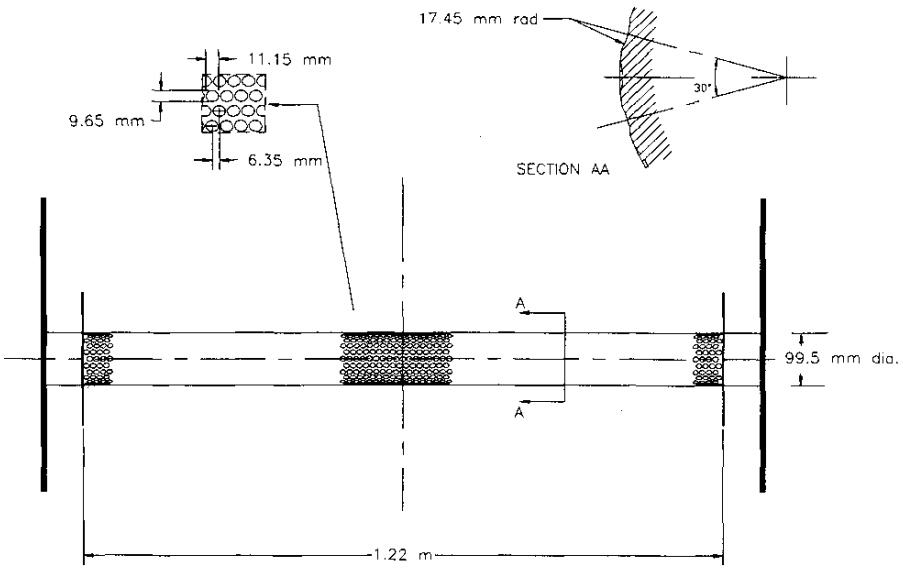

Figure 4.1 – Schematic of dimpled cylinder arrangement, from Bearman and Harvey (1993).

Twelve equally spaced dimples were machined around the cylinder circumference, to a depth of 0.91mm, and this set of dimples was repeated along the span at 6.35mm

intervals with every other set rotated by half a dimple spacing to provide a staggered arrangement. The cylinder was mounted in the wind tunnel such that a row of dimples was placed normal to the flow, i.e. at 0° where this represents the mean frontal stagnation point of a cylinder. If the depth of the dimple is taken as the roughness height, the relative roughness K/D = 0.91%.

4.2 Results

The plot shown in Figure 4.2 displays the drag coefficient measurements made for the three cylinder arrangements. The results for the plain cylinder are consistent with those found throughout literature on this subject, with a relatively steady C_D value of around 1.22 demonstrating a sub-critical flow regime up to $Re = 2.2{\times}10^5$. Beyond this point the drag loading limit of the wind tunnel force balance was reached, preventing measurements of the critical flow state for this arrangement.

The drag coefficient data obtained for the dimpled cylinder matches closely with the that of the 'dimple on the flow axis' results (see Figure 2.22) from the original data obtained for this cylinder arrangement by Bearman and Harvey (1993). In the sub-critical region the drag coefficient is slightly lower than that of the plain cylinder before reaching the critical regime at around $Re = 4.4 \times 10^4$. The drag coefficient plateaus shortly afterwards for a small band of Re before dropping again to its minimum of $C_{D(min)} = 0.53$ at $Re = 9.4 \times 10^4$. The drag coefficient begins to rise from $C_{D(min)}$ with increasing Re and looks to flatten, finally, from approximately $Re = 1.8 \times 10^5$ with a drag coefficient of $C_D = 0.7$.

The sub-critical C_D for the cylinder with tripping wires shows an irregular trend before reaching a critical Reynolds number beyond $Re = 4.8 \times 10^4$. The C_D drop

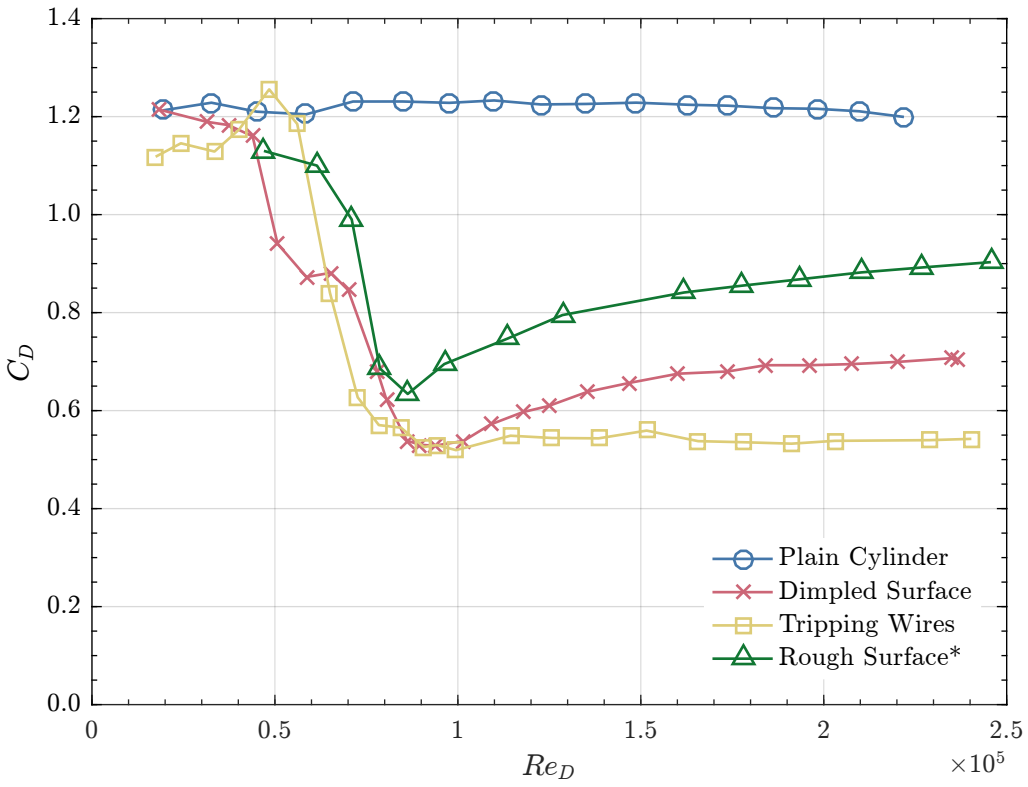

Figure 4.2 – Variation of drag coefficient with Reynolds number for: Plain cylinder; Cylinder with dimpled surface, K/D = 0.91%; Cylinder with tripping wires positioned ±65° from frontal stagnation point, d/D = 0.05%; and, Cylinder with rough surface (*Fage and Warsap, 1930, no end plates or blockage correction) – formed by wrapping cylinder in John Oakey's glass paper (grade 2, Strong) – K/D unknown.

through the critical regime is continuous until $C_{D(min)} = 0.52$ is reached at $Re = 9.9 \times 10^4$. Beyond this point the drag coefficient briefly rises slightly but stays relatively constant around $C_D = 0.54$ for the remainder of the Re range tested.

For both the dimpled cylinder and cylinder with tripping wires setups, there is a somewhat anomalous initial increase in C_D with Re_D for the first two data points. This can be attributed to the uncertainty of the measurements associated with the drag coefficient calculation found at low Re_D, as discussed in section 3.3, where the relative uncertainty of the first data point is calculated to be of the order of

$C_D \pm 13\%$. With an increase in the drag force magnitude with increasing Re_D, the relative uncertainty of the drag coefficient at $Re_D = 4\times10^4$ reduces to approximately $C_D = \pm 2\%$.

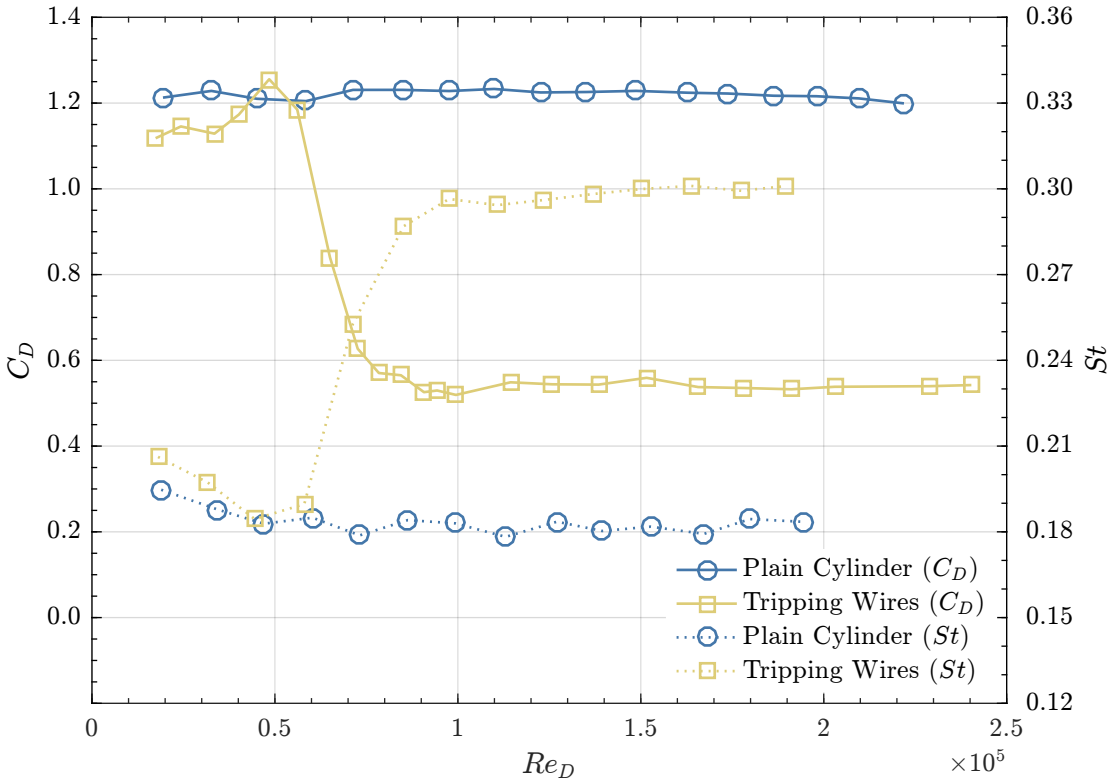

Figure 4.3 – Variation of drag coefficient and Strouhal number with Reynolds number for: Plain cylinder; and, Cylinder with tripping wires positioned ±65° from frontal stagnation point, d/D = 0.05%.

Vortex shedding measurements were taken for two of the cylinder arrangements (plain and with tripping wires) by placing a hot-wire probe in the wake and filtering the data using a Fourier transform. Figure 4.3 displays a plot of C_D overlaid with the corresponding variation of Strouhal number, St, with Re for the plain and tripped cylinders. Vortex shedding remains approximately constant at $St = 0.18$ for the plain cylinder whereas the tripped cylinder rises from this value in the sub-

critical regime to $St = 0.3$ beyond the critical Reynolds number. The plot clearly demonstrates the reflection of vortex shedding frequency from a bluff body on its aerodynamic drag; a reduction in C_D is accompanied with an increase in St. Though Figure 4.3 presents what looks like a direct correlation of C_D and St with increasing Re, Lock (1925) has shown that the calculation of drag directly from a correlation with vortex shedding does not prove to be accurate; though they are clearly closely linked, bluff body drag is not entirely dependent on the rate of vortex shedding and vice versa.

4.3 Discussion

It is difficult and still quite subjective to make a direct comparison of the efficiency of geometrical modifications to induce a critical flow regime over a bluff body, for example by equating the modification to an equivalent relative roughness, K/D, due to the different mechanisms each introduces to the flow. Between the tripping wire and the dimpled surface there are fundamental differences in the operation and effectiveness of each, however in this case the chosen geometrical parameters and arrangements both produce almost the same minimum C_D at similar Reynolds numbers, enabling a convenient comparison of the characteristics of each.

The most obvious and clear difference is that once the C_D minimum is achieved the drag measurements diverge with increasing Reynolds number. For the dimpled cylinder, the drag coefficient begins to rise whereas the plain cylinder with the tripping wires remains fairly constant. This is as a result of the difference in surface texture, specifically in the region of the cylinder over which the air flows once the boundary layer has undergone transition and before it separates. Because the

majority of the dimpled cylinder's surface is textured, the flow encounters continual disturbances as it remains attached to the cylinder. This increasingly impedes the boundary layer at the cylinder surface and culminates in an increased rate of boundary layer thickening as the pressure continues to rise beyond the point of minimum pressure; despite the increased momentum of a turbulent boundary layer the increased boundary layer growth promotes separation. This contrasts to the characteristic of the tripping wire on a smooth cylinder, were the flow encounters minimal additional disturbance once the wire has transitioned the boundary layer. The smooth surface which follows the wire allows the newly energised boundary layer to remain attached for longer by minimising the growth of the boundary layer thickness.

To explain with confidence the results of the sub-critical flow for each drag reduction device tested is more difficult. For the dimpled cylinder the drag coefficient at $Re = 1.8 \times 10^4$ is the same as for the plain cylinder but with increasing Re it descends gradually before reaching the critical value of $Re = 4.4 \times 10^4$. Bearman and Harvey (1993) noted this reduction of C_D in the sub-critical region, where flow is expected to be laminar, and it is proposed here that perhaps the uneven surface may sufficiently inhibit straight line separation so as to slightly reduce the strength of the vortex shedding associated with a smooth cylinder. The cylinder with tripping wires is more unusual in this region and it is interesting to note that, for these measurements, the Strouhal number still mirrors the general trend of rising C_D prior to the sudden fall within the critical Re region. The inequality of the sub-critical drag coefficient for the plain cylinder and cylinder with tripping wires is unexpected because the flow is laminar in the sub-critical regime and hence the drag force is expected to scale with ${U_\infty}^2$. There is no apparent reason that the drag

coefficient should be lower than that of a plain cylinder prior to the critical regime being induced, and since C_D for the cylinder with tripping wires does rise to the same value as the plain cylinder before reaching the critical regime, it is thought that experimental uncertainty is the reason for the irregular trend. The nature of the operation of the force balance used, rather than the accuracy of the balance itself, leads to an inevitable reading error; measurements are taken by manually balancing an electronic gauge and readings are written by hand once a satisfactory balance is assumed. Unsteady forcing on the model requires the operator to make a judgement as to the average balance point while the gauge fluctuates over a wide range. Though readings were noted to a resolution of $0.05N$, the uncertainty in the reading can be much larger and depends upon the nature of the forcing experienced at the time of measurement. However, this error is only significant towards higher Reynolds numbers – when large force fluctuations occur – and is not seen as a factor for sub-critical Re. Of greater significance in the low Re range is the uncertainty in the manometer reading for the tunnel flow speed; Strouhal number and drag coefficient are factors of U_∞ and ${U_\infty}^2$ respectively and hence flow speed reading errors are magnified – through the calculation of St and particularly C_D – at low flow velocities due to their percentage contribution. For example, adjusting a flow speed reading from 3.6 m/s to 3.4 m/s can change the calculation of drag coefficient from $C_D = 1.13$ to $C_D = 1.26$, with the latter being the expected value but the former becoming the registered value by virtue of a reading error. Despite re-zeroing the manometer immediately prior to a test run, with the tunnel switched off and flow stationary, the manometer would continue to read a pressure difference between the total and static ports of the Pitot-static tube amounting to a flow speed of up to 0.7 m/s. These low flow speed reading errors therefore appear to give rise

to uncertain trends up to $Re \approx 5 \times 10^4$ but become decreasingly significant with increasing flow speed.

The plateau of $C_D \approx 0.87$, found over a small band of Re midway in the critical region of the dimpled cylinder results, is thought to be as a result of the separation point being fixed along the front edge of a row of dimples (Bearman and Harvey, 1993), before increasing Re provides the boundary layer with sufficient momentum to push the separation point beyond it. Although the fall in C_D is precipitated more quickly with the dimples than the tripping wire, the dimpled cylinder's plateau in C_D allows the tripping wire to gain an advantage in the race to minimum C_D. It is also interesting to note that the gradient of the fall in C_D with Re in the critical range for both cylinder arrangements is very similar, especially for the initial drop in C_D for the dimpled cylinder before the plateau, indicating that the point of separation is progressing rearwards with increasing Re at the same rate.

4.4 Conclusions

It is clear from this basic set of experiments that both the optimum arrangement for the promotion of the critical regime and maintaining the minimum C_D over a bluff-body is to have a smooth surface with the boundary layer tripped at a single location (with reference to a 2D slice of the (x, y) plane). This means that the laminar boundary layer is perturbed significantly only once – to promote transition – and the smooth surface thereafter mitigates thickening of the turbulent boundary layer to allow the flow to remain attached for as long as possible. This, however, is an optimisation for unidirectional flow applications and so does not preclude the use of surface treatments which cover an entire body because of their suitability for

omnidirectional flow applications. The scope for improvements in passive flow control concepts suitable for omnidirectional flow applications is limited because of the restriction imposed by continuous perturbation of the boundary layer post transition or, alternatively, the requirement to self-align with a varying flow direction. The focus of this research, as stated in section 1.3, is for applications which generally have a known mean flow direction, e.g. sports such as cycling, and hence the direction of investigation was for optimisation of unidirectional flow control concepts.

Chapter 5

Transverse jets: Primary investigations

5.1 Conception

Following the conclusions and hypothesis formed from a review of the literature and initial tests of passive flow control methods (chapter 4), the concept of using passive, transverse air jets was devised to discretely induce transition of the boundary layer such that a drag reduction would be achieved throughout the Re_D range which would normally constitute a sub-critical flow regime. The idea was that the pressure difference, which naturally forms around the circular cylinder in the pre-critical regime, could be exploited to provide passively supplied, open-loop flow control for manipulation of boundary layer transition and separation.

As noted in the literature study (section 2.5), the optimum location on the cylinder surface for introducing perturbations to the flow was found to be $\phi = \pm 65^{\circ}$, just upstream of the point of $C_{p(min)}$. Observing the mean pressure distribution

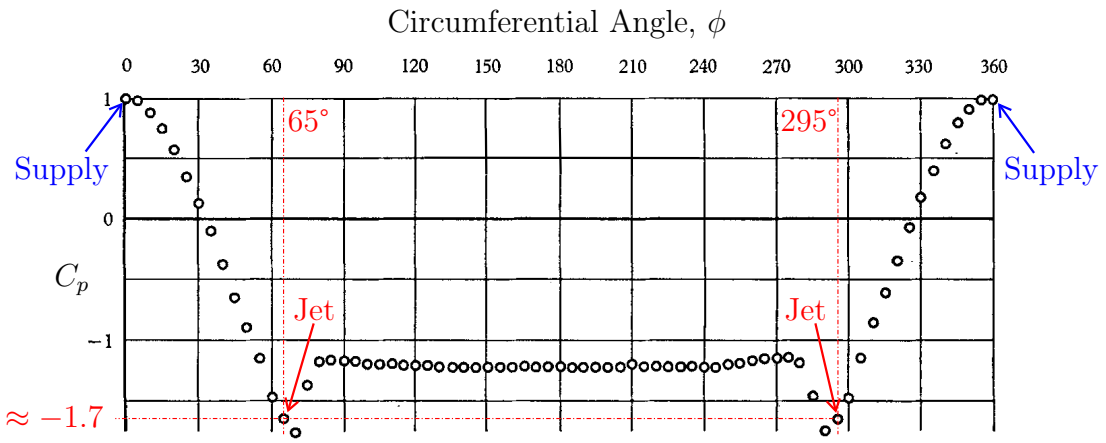

Figure 5.1 – Plain cylinder; mean pressure coefficient, C_p, plotted with respect to the circumferential angle on the cylinder surface for $Re = 1 \times 10^5$ from Achenbach (1968). The plot is overlaid with markers indicating theoretical $\Delta C_p \approx 2.7$ available for exploitation with passive jets concept.

around a cylinder in the sub-critical regime (Figure 5.1), there is a considerable pressure head of $\Delta C_p \approx 2.7$ available between the frontal stagnation point, where $C_p = 1$ – hereafter also referred to as $\phi = 0°$ – and $\phi = \pm 65°$ where $C_p \approx -1.7$ at $Re = 1 \times 10^5$. For a plain cylinder, this pressure difference continues to increase with Reynolds number to $\Delta C_p \approx 3.3$ at $Re = 2.6 \times 10^5$ (Figure 2.3). Using this pressure difference, airflow was to be channelled from $\phi = 0°$ to $\phi = \pm 65°$ through the internal cylinder volume by drilling holes at these points, normal to cylinder surface, as shown in Figure 5.2. This arrangement would provide a continuous flow of jet fluid as opposed to a mass-less synthetic jet which is common in research literature for active flow control applications (see, for example, Amitay et al., 1997; Crook and Wood, 2001; Glezer and Amitay, 2002; Leschziner and Lardeau, 2011).

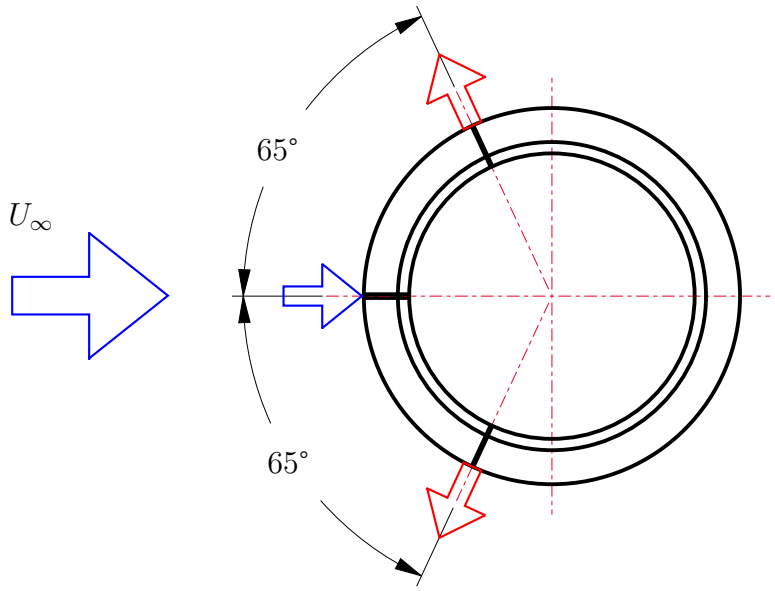

Figure 5.2 – Schematic of cylinder illustrating passive jet concept. Air is tapped-off from the free stream at the frontal stagnation point, where $C_p = 1$, and enters the hollow cylinder volume. The low static pressure at the points $\phi = \pm 65^\circ$ on the cylinder surface serves to draw the air from the cylinder volume directly into the boundary layer in a continuous cycle.

5.2 Feasibility study

A set of experiments was devised to investigate the potential effectiveness of the passive jets concept in transitioning the boundary layer flow. The passive air supply was simulated using a manually controlled compressed air supply to regulate the jet flow rate and analyse the pressure requirements for drag reduction in order to determine the feasibility of the passive supply option. Estimates of the potential passive jet flow rates, and hence estimates of internal cylinder pressures, throughout the testing Re_D range were made in order to find a suitable range of control pressures for the feasibility study. The details of these calculations can be found in Appendix A, along with a short discussion of some of the difficulties in making this

type of estimation – in particular the fact that despite operating within the laminar Reynolds number range for pipe flows (Figure A.1), flow within both the supply and jet exit 'pipes' only occasionally becomes fully developed within the stroke length ($l_J = 12mm$, Figure 3.4) of these pipes throughout the Re_D test range. Thus, the friction factor varies over the pipe length and where the flow is not fully developed the pressure loss is increased – see Appendix A.5 for more details. In the passive jet arrangement studied here, from the simplified analysis of the pressure losses covered in Appendix A, the overall contribution to pressure loss from the stroke length can be considered important; from Equation A.23, it is shown that the pressure losses attributable to friction, h_f, through the supply and jet exit pipes varies linearly with stroke length, l_J, and these provide a more significant contribution to the total pressure loss through the test Re_D range compared to that attributable to the sudden contraction and expansion losses on entry and exit to each 'pipe', though they are comparable at the maximum Re_J. Equation A.23 also shows that the friction loss is four times greater for the jet exit pipes than for the supply pipes, confirming that the jet flow rate is limited chiefly by the jet exit holes.

Following on from the initial review experiments of smooth, dimpled surface and tripping wire affixed cylinders, the mounting assembly and wind tunnel setup was maintained for the feasibility study of the passive jets. The smooth, plain aluminium circular cylinder of the review experiments was modified by drilling two rows of $0.5mm$ diameter holes (58 each row, 116 in total) at an angular position $\pm 65^\circ$ from the foremost stagnation point as shown in Figure 3.4. The jet exit holes were spaced at $20mm$ intervals across the span ($z_J = 20mm$) to provide a ratio of jet spacing to cylinder diameter of $\frac{z_J}{D} = 0.2$. This ratio was thought to be a reasonable starting point for the research but was not based on any previous or specific findings.

Due to a restriction imposed by the test cylinder mounting, the outermost holes had a $38mm$ gap to the end of the cylinder – once the end-caps and plates were fixed to the cylinder, the gap between the first hole at each end and the end-plates was $40mm$.

From the estimation of passive jet velocity throughout the Re_D testing range (Appendix A), the jet to free-stream mass flux coefficient, C_J, for this jet arrangement was calculated as shown in Equation 5.1.

$$C_J = \frac{A_J n_J V_J}{LDU_\infty} \tag{5.1}$$

... where A_J, n_J and V_J are the area of a single jet hole, the total number of jet exit holes and mean jet velocity, respectively. L and D are the span length and diameter of the cylinder, respectively, and U_∞ is the free stream velocity.

Based on the predicted passive jet flow rates for the $z_J = 20mm$ cylinder arrangement, the mass flux coefficient was calculated to be of the order $\mathcal{O}10^3$ lower than that found in typical base bleed applications for drag reduction of bluff bodies, (see, for example, Bearman, 1967; Tanner, 1975; Wood, 1964), which would classify the primary effect of the passive jets as a perturbation of the boundary layer – as opposed to significantly redistribute mass flux or momentum as in the case of base bleed applications. Verification of this premise, by plotting the range of C_J found subsequently from direct measurement of jet flow rates (see section 6.3), is presented in Appendix C.

In order to pressurise the cylinder internal volume, the cylinder was assembled with an air-supply fitting ($12mm$ tubing connection) screwed into each end-cap. Pressure tappings (to fit $1.6mm$ diameter tubing) were also installed in each end-

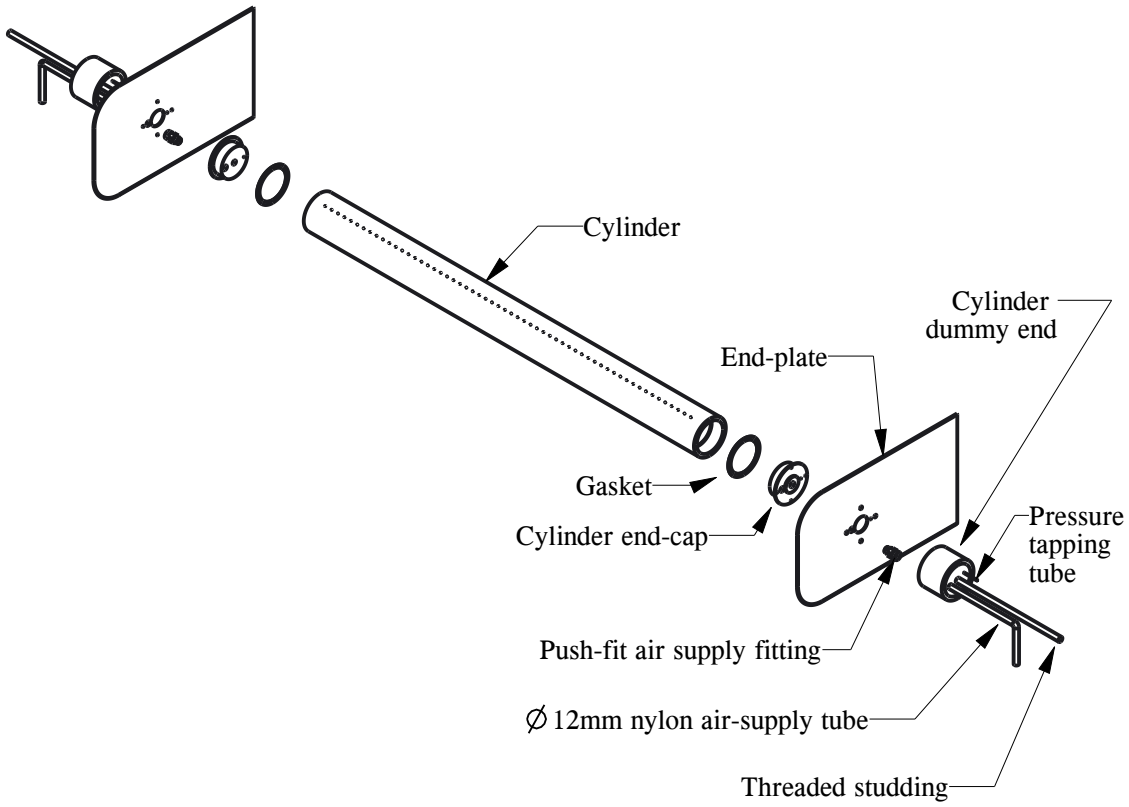

Figure 5.3 – Exploded assembly schematic; passive jets feasibility study setup.

cap in order to measure the pressure of the internal cylinder volume. In addition to the studding used to mount the cylinder, the air-supply and pressure tapping fittings and tubing were fed through the dummy cylinder ends and fixed to the force balance arms such that they were shielded from the free stream and prevented from influencing the force measurements – see exploded assembly schematic in Figure 5.3. Mechanical gate valves were used to control the air-supply to each end.

A multi-channel pressure scanner was used to record the cylinder pressure, p_{cyl}, from tappings in the end-caps at either end of the cylinder. The reference pressure for the cylinder pressure measurements was the static pressure of wind tunnel flow, tapped off from the Pitot-static tube (used to record tunnel flow speed) positioned

in the working section, upstream of the model. For more detailed information on the setup, see section 3.4.

Selected drag measurements from the passive jets feasibility tests are shown in Figure 5.4 along with the plain cylinder reference. The cylinder was first tested with the air supply closed in order to obtain a reference for how the jet exit holes drilled into the cylinder surface at $\phi = \pm 65^\circ$ would affect the C_D v. Re curve without air blowing through them. It was soon found that the results of this test were somewhat flawed, however, because of the flow dynamics induced by the design of the cylinder in this arrangement. With a common plenum chamber (i.e. the hollow cylinder volume) from which air is supplied to both rows of jet exit holes, and the rest of the cylinder sealed – it was found that an unavoidable pressure asymmetry would form to generate suction in one row of holes and blowing out of the other.

As shown in Figure 5.4, the C_D curve for the cylinder with the air supply closed deviates from that of the plain cylinder at $Re = 1.4 \times 10^5$. A gradually steepening drop in C_D is seen until the curve plateaus briefly at $Re = 2.3 \times 10^5$ and continues to fall on a flattening gradient up to the limit of Re tested. This trend can be followed in the plot of lift coefficient, C_L, shown in Figure 5.5 for the "No jet supply ($\delta\phi = 0^\circ$)" line, where a slight lift force is detected above $Re = 1.5 \times 10^5$ before a sudden large increase in C_L followed by a flattening decline in C_L with increasing Re. That the jump in C_L is so sudden and large indicates a drastic change and difference in the boundary layer development top to bottom, hence the asymmetry in the pressure distribution around the cylinder. Further testing revealed that small angular changes – as little as $\delta\phi = \pm 0.5^\circ$ – could "flip" the direction of lift force from positive to negative, as shown in Figure 5.5. As a result of these tests, it was concluded that the sudden and drastic pressure asymmetry must be

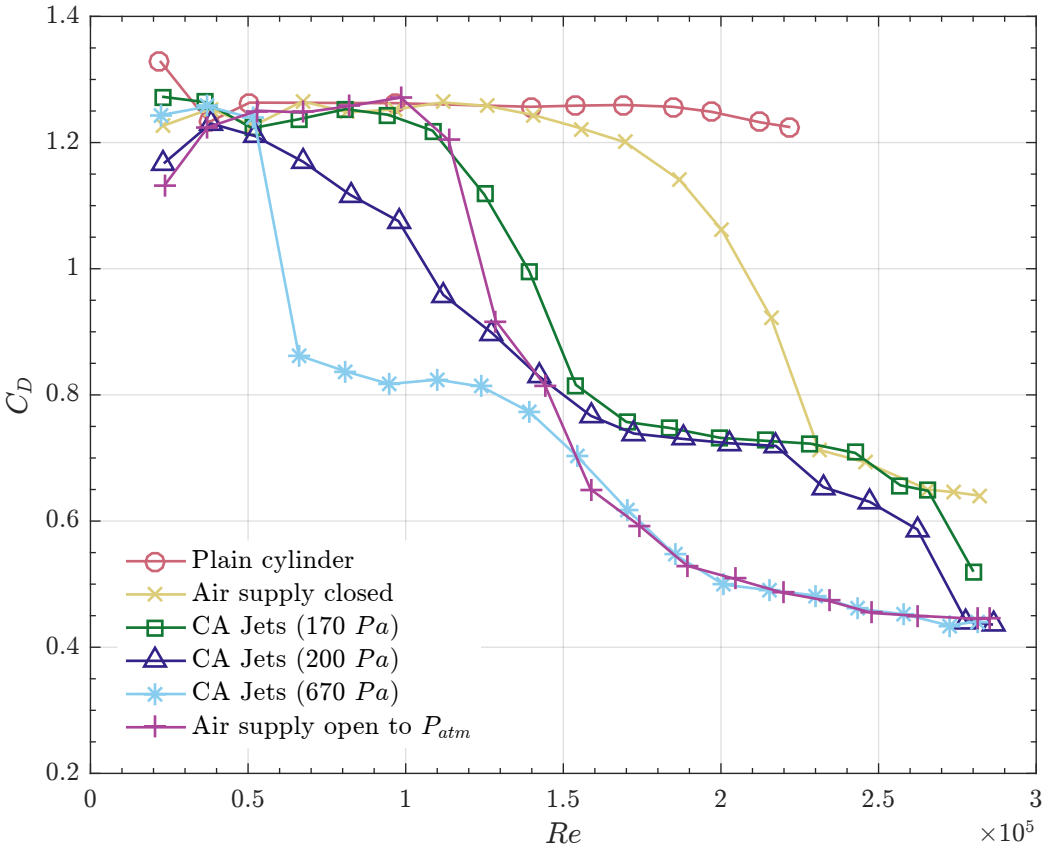

Figure 5.4 – C_D v. Re curves for a selection of feasibility study tests; a compressed air (CA) supply was used to maintain a variety of fixed pressures – noted in brackets – within the cylinder to assess the feasibility of a passive supply. The cylinder was also tested with the air supply closed and open to atmosphere.

accompanied by a pressure difference between the two rows of jet exit holes and that this could thus stimulate a continuous flow through the cylinder – from one row of jet exit holes to the other – producing significantly different boundary layer separation characteristics on either side. This appears to occur suddenly around $2.1 \times 10^5 \leqslant Re \leqslant 2.3 \times 10^5$ and at a particular instant within this Re range it is thought that a pressure difference between the two rows of holes is generated either by: transition occurring on one side slightly quicker than the other – as a result of

the boundary layer disturbance generated by the holes on the surface; or, an oscillation of surface pressure distribution – typically associated with the Kármán vortex shedding cycle of cylinder flow. This pressure difference draws air from one side of the cylinder surface to the other – suction through one row of holes, blowing through the other. On the side of the cylinder with the blowing holes the boundary layer is thought to remain attached further downstream than on the side with the suction holes – which are likely to draw momentum from the boundary layer. Consequently, as pressure increases on the suction side and decreases further on the blowing side, the pressure difference between the two rows of holes increases again to compound the effect. With increasing free stream velocity this system of through-cylinder flow is effectively locked in; flow from one side of the cylinder to the other will continue in the same direction and the asymmetric boundary layer development, and hence lift force, will thus be maintained into the upper test range of Re.

That the boundary layer flow was drastically different on either side of the cylinder clearly affected the drag generated beyond simply the surface disturbance of the holes. A solution to this issue would have been to internally block the jet holes but owing to the limited access to the cylinder's interior, and a reluctance to seal the $0.5mm$ diameter jet exit holes by externally inserting a blockage, a suitable fix was not found and unfortunately a reference for the effect the holes themselves have on the boundary layer flow and drag characteristics was not obtained.

The uncertainty associated with the alignment of the cylinder was $phi = \pm 0.5^{\circ}$ and given that the measurements for internal cylinder pressure and drag coefficient were very similar for cylinder alignments $\phi = \pm 2.5^{\circ}$ from $\phi = 0^{\circ}$ (where $\phi = 0^{\circ}$ represents the cylinder aligned symmetrically about the horizontal plane) a consistent method – outlined in section 3.2 – was performed for cylinder alignment in all

experiments.

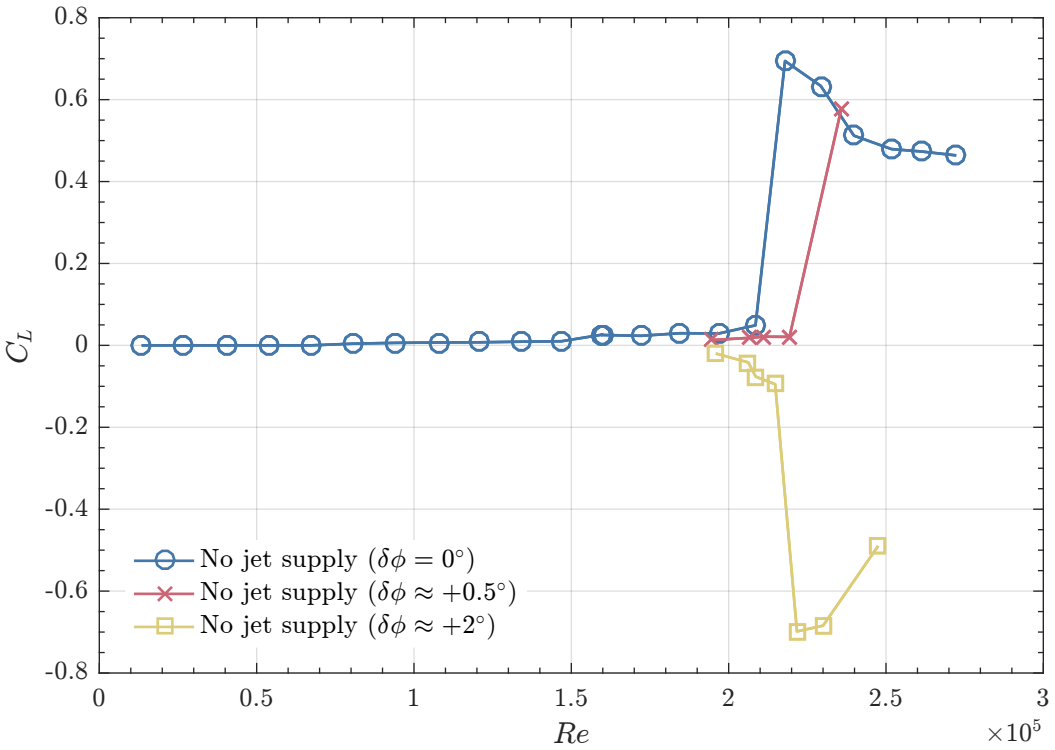

Figure 5.5 – C_L v. Re curves for a selection of angular sensitivity tests; the air supply was closed off and the cylinder tested with the two rows of jet "exit" holes left open. At sufficiently high Re one row of jets holes generates suction and the other blowing to produce an asymmetric pressure distribution and hence lift force.

The trend of the C_D v. Re curve for the closed air supply is similarly repeated when air is supplied to the cylinder – up to a constant additional pressure of $p_{add} = 170Pa$ – as detailed in sub-figure Figure B.1(a) in Appendix B. The critical regime is promoted to progressively lower Re – with the drop in C_D occurring at an ever steeper gradient – with increasing added pressure supply. For this range of pressure application, all of the C_D curves appear to asymptote towards a drag coefficient of $C_D \approx 0.7$ before continuing to drop again to a value which decreases with increasing pressure application at $Re \approx 2.6 \times 10^5$.

Increasing the pressure of the air supplied internally to the cylinder by only $30Pa$, from $p_{add} = 170Pa$ to $p_{add} = 200Pa$ (Figure 5.4), produces a C_D curve which departs significantly from the initial trends developed by lower pressures up to this point. The gradual promotion of the critical flow state to lower Re ends abruptly as the initial fall in C_D jumps from $Re = 1.1 \times 10^5$ to $Re \approx 5 \times 10^4$ – the number at which, for this experiment, the initial fall in C_D commences for all cylinder air-supply pressure of $p_{add} \geqslant 200Pa$ – again, see Appendix B for a more detailed breakdown of the test results for the feasibility study. The C_D curve of $p_{add} = 200Pa$ re-joins that of the lower pressure tests as it similarly asymptotes to $C_D \approx 0.7$, however in this case it peels off from this plateau at a lower Re to drop again in two steps to the minimum drag coefficient ($C_D = 0.44$) achieved in any of the tests during this experiment at $Re = 2.8 \times 10^5$.

Subsequently, the C_D curves obtained for all cylinder air-supply pressures $p_{add} \geqslant 270Pa$ all overlay each other for the initiation of the critical regime at approximately $Re = 5 \times 10^4$. With increasing air-supply pressure the final two-step drop to minimum C_D is promoted to lower Re up to an air-supply pressure of $p_{add} = 400Pa$ (see Figure B.1(c) in Appendix B) which, as with all added cylinder pressures above this value, almost identically follows the trend obtained for the maximum p_{add} tested of $670Pa$ (see Figure 5.4). For $470 \leqslant p_{add} \leqslant 670$, the drag coefficient plateaus initially around $C_D = 0.83$ between $Re = 6.6 \times 10^4$ and $Re = 1.2 \times 10^5$ before sweeping down in a gradually flattening curve to the minimum C_D.

5.3 Passive control of transverse jets

Once it was established that the passive jets arrangement was a feasible design for a drag reduction flow control method, the test model was modified by drilling a row of jet supply holes at the design location of the frontal stagnation point, $\phi = 0°$, as shown in Figure 5.6. The supply holes were vertically aligned with the jet exit holes and measured $1mm$ in diameter, thus providing four times the cross-sectional area of a single jet exit hole, or twice the total area for each pair of aligned exit holes, to provide a plentiful air supply when pipe-flow losses were taken into account (see Equation A.23).

A second cylinder with 10mm spaced passive jets ($z_J = 10mm$) was additionally

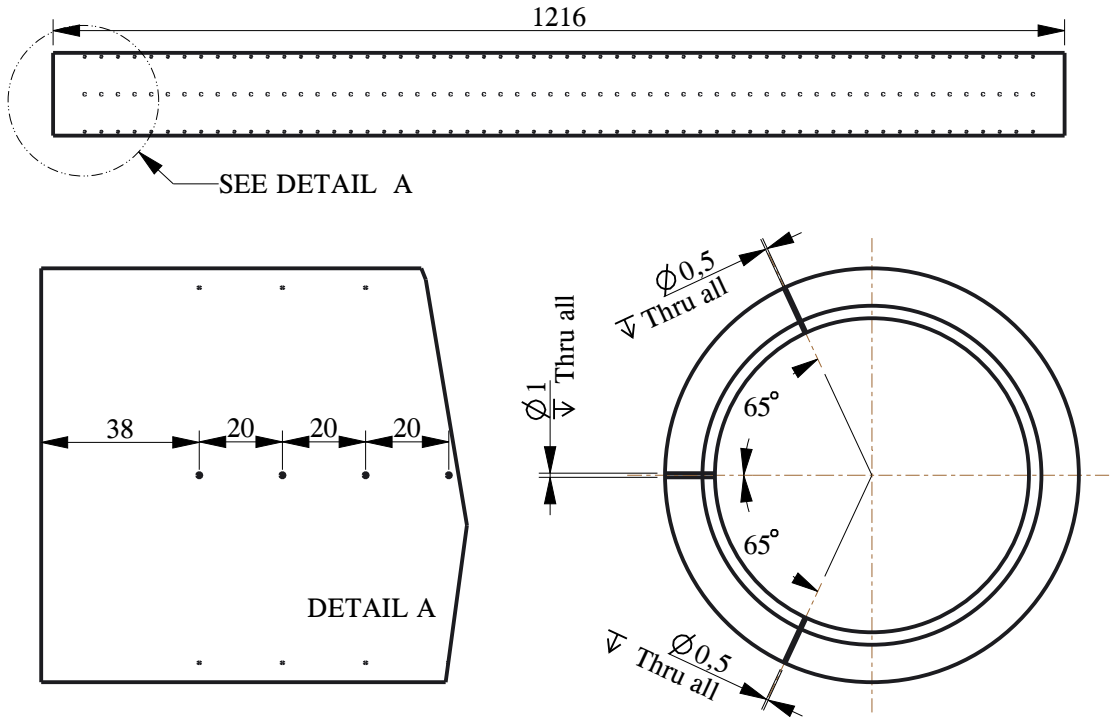

Figure 5.6 – Model design schematic; cylinder with 20mm spaced passive jets.

manufactured to provide comparison with the original $z_J = 20mm$ arrangement. Apart from the reduced jet spacing – and hence increase in number of holes per row from 58 to 115, all other specifications were identical. Figure 5.7 shows the relationship between drag coefficient, C_D and Reynolds number, Re, for both configurations along with a plain cylinder reference.

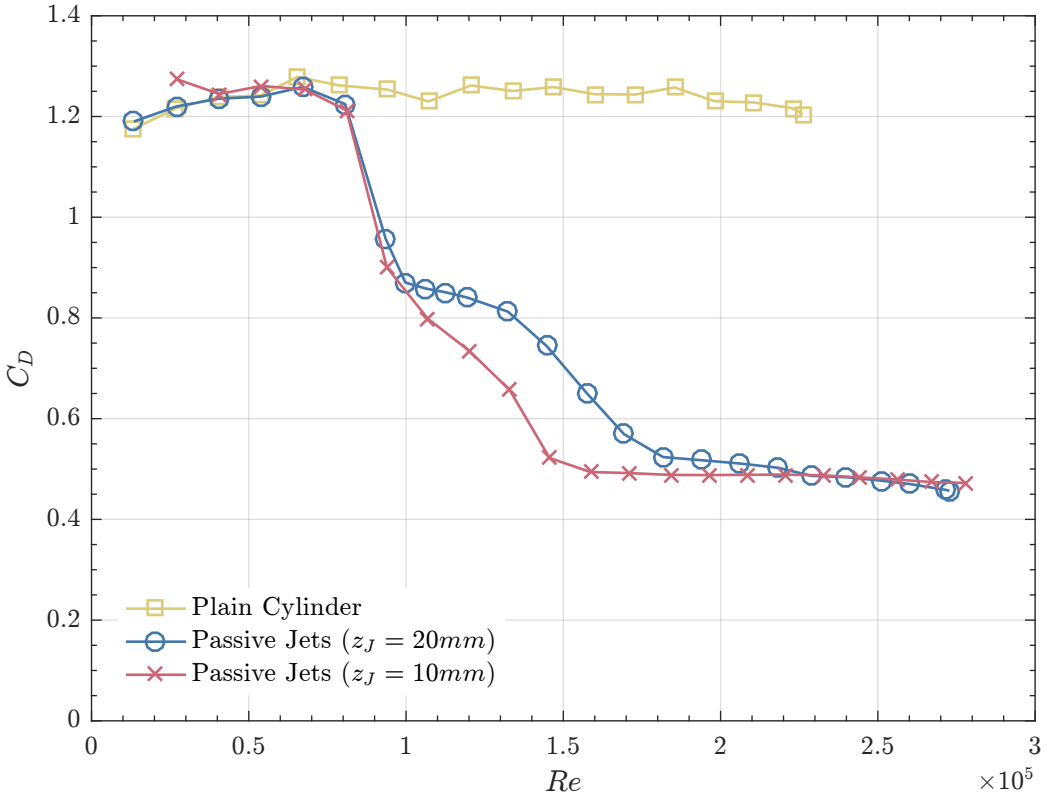

Figure 5.7 – Variation of drag coefficient, C_D, with Re for cylinders with passive jets located $\phi_j = \pm 65°$ from the frontal stagnation point (designated $\phi_0 = 0°$), spaced at intervals $z_J = 10mm$ and $z_J = 20mm$.

The critical regime is initiated at the same Re for both $z_J = 10mm$ and $z_J = 20mm$ cylinders at about $Re = 8 \times 10^4$. Both jet arrangements yield a similar gradient of slope for the initial C_D drop – 10mm spacing is marginally better – but the main deviation comes at around $Re = 1.1 \times 10^5$ when C_D for the $z_J = 10mm$

arrangement continues to drop steeply with increasing Re while $z_J = 20mm$ briefly plateaus around $C_D = 0.84$ before beginning to drop again at $Re = 1.3 \times 10^5$. The C_D curves for both jet spacing arrangements drop steeply with similar gradients from $C_D \approx 0.8$, but at different Reynolds numbers; this phase occurring at lower Re for the closer, $z_J = 10mm$, spacing. The drop in C_D then flattens significantly from $C_D = 0.54$ – occurring again at the same C_D for both $z_J = 10mm$ and $z_J = 20mm$ cylinders but at a lower Re for $z_J = 10mm$. This might indicate that similar flow regimes develop with increasing Reynolds number for both jet spacing arrangements, but that they are promoted to lower Re with smaller z_J. There is a slight difference worth noting in the C_D trend with increasing Re – once C_D flattens out – between $z_J = 10mm$ and $z_J = 20mm$. After reaching $C_D = 0.49$ at $Re = 1.59 \times 10^5$, C_D remains constant with Re for $z_J = 10mm$ up to $Re = 2.33 \times 10^5$ before starting to drop again very gradually with increasing Re down to $C_D = 0.47$ at $Re = 2.78 \times 10^5$. The drag coefficient for the $z_J = 20mm$ cylinder, however, continues to drop unceasingly with increasing Re from $C_D = 0.52$ at $Re = 1.82 \times 10^5$, down to $C_D = 0.46$ at $Re = 2.73 \times 10^5$. While C_D does not increase with Re, the $z_J = 10mm$ cylinder seems to be limited in generating another drop in C_L with increasing Re. The $z_J = 20mm$ cylinder on the other hand – though the differences are marginal up to the limit of the Reynolds number range tested – appears more likely to produce a further drop in C_D with increasing Re. This type of relationship is observed with other passive flow control devices where an increase in the intensity of the perturbation to the boundary layer – such as by increased K/D surface roughness or larger diameter tripping wires – leads to improved drag performance at low Re but a higher $C_{D(min)}$. It cannot be said for certain, however, that this is the case with the passive jets since data at higher Reynolds numbers does not presently exist.

It is possible, for example, that the two curves asymptote to a common $C_{D(min)}$ with an increase in Re.

The internal cylinder pressure coefficient, $C_{p(int)}$, follows the same trend for both $z_J = 10mm$ and $z_J = 20mm$ cylinders (Figure 5.8(a)), however, $C_{p(int)}$ is higher for 20mm spaced jets with is a near-constant gap of $\Delta C_{p(int)} \approx 0.06$. The reduced $C_{p(int)}$ of $z_J = 10mm$ indicates that either the air flow from supply to exit suffers from greater losses than $z_J = 20mm$, or the pressure at exit for $z_J = 10mm$ was consistently lower than that of $z_J = 20mm$ throughout the Re test range. Given that the ratio of supply-to-jet hole cross sectional area was the same between the two cylinder arrangements, and the drag coefficient only varies between the two configurations in the middle of the Re range while maintaining a constant $\Delta C_{p(int)}$ throughout, it was unclear why this was the case. Since the cylinder surface pressure at supply and jet exit can be largely assumed to be the same for both cylinders, the losses must occur between supply and exit so the discrepancy may be as a result of the increased throughput of air relative to the internal cylinder volume or perhaps slight manufacturing differences such as a slightly increased wall thickness of the $z_J = 10mm$ which would add a proportionally constant extra loss through the system compared to $z_J = 20mm$.

Both passive jet configurations record a spike in lift force of just over $C_L = 0.25$ in the range $0.9 \times 10^5 < Re < 1.0 \times 10^5$, as shown in Figure 5.8(b). These spikes coincides with bumps in the $C_{p(int)}$ trend with similar pressure differences recorded between the internal cylinder volume and static pressure at jet exit on the cylinder surface. In both cases, the lift force first occurs with a pressure difference of $\Delta p_{(int-\phi_J)} \approx 180Pa$ before peaking in the range $240Pa \leqslant \Delta p_{(int-\phi_J)} \leqslant 280Pa$ and subsequently rebalancing when $330Pa \leqslant \Delta p_{(int-\phi_J)} \leqslant 350Pa$.

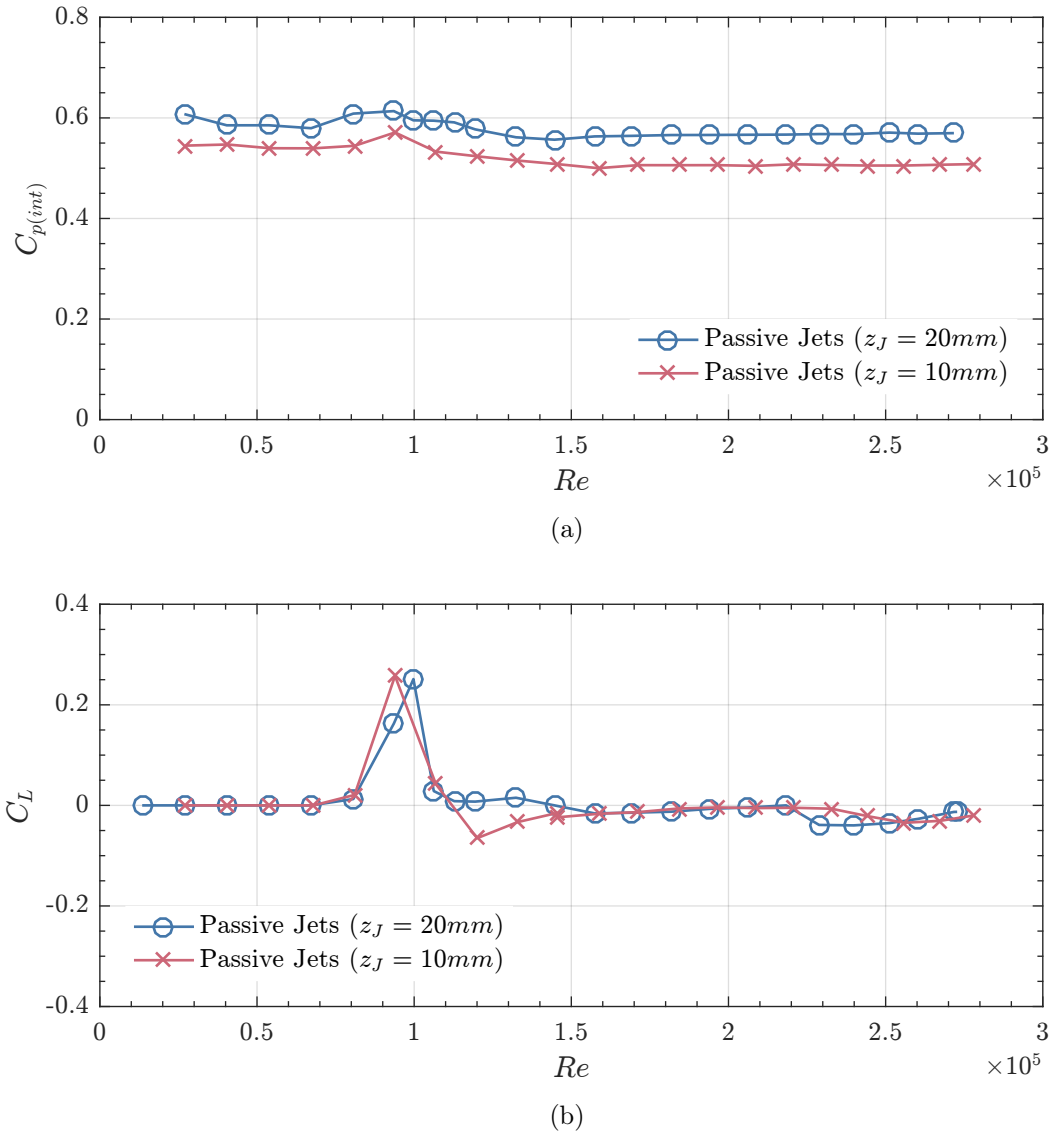

Figure 5.8 – Cylinders with passive jets located $\phi_j = \pm 65^\circ$ from the frontal stagnation point (designated $\phi_0 = 0^\circ$), spaced at intervals $z_J = 10mm$ and $z_J = 20mm$, where: (a) variation of cylinder internal pressure coefficient, $C_{p(int)}$, with Re and; (b) variation of lift coefficient, C_L, with Re.

The appearance of the lift force coincides with the initiation of the critical regime for both jet arrangements which suggests that the onset of drag reduction comes about initially due to the flow transitioning on one side of the cylinder before the

other. Similarly, as with the cylinder setup with no air supply where lift force was generated by an asymmetric pressure distribution occurring at a particular Re, the jet flow in the passive supply setup is likely to be biased to the side of the cylinder which transitions first and hence generates a lower surface pressure. Unlike the "no jet supply" setup, however, both rows of jet exit holes continue to blow due to the pressure difference between the cylinder volume and static pressure on the cylinder surface at the position of the jet exit holes, $\phi_J = \pm 65°$.

As the cylinder pressure increases with Re, so too will the flow rate and velocity of the jets, inducing a critical flow regime on both sides of the cylinder and thus re-balancing the time-mean pressure distribution around the cylinder. For the $z_J = 20mm$ cylinder, this seems to coincide with a plateau in C_D at about $Re = 1.1 \times 10^5$, whereas for the $z_J = 10mm$ cylinder C_D continues to fall steeply with Re from the same point. C_L for $z_J = 20mm$ re-balances to $C_L \approx 0$ at this point, whereas the lift coefficient for $z_J = 10mm$ swings straight to a negative value of $C_L = -0.065$ before re-balancing to $C_L \approx 0$ around $Re = 1.6 \times 10^5$. This re-balancing of the time-mean pressure distribution also coincides with a plateau in C_D for the remainder of the Re range tested for $z_J = 10mm$.

Both passive jet arrangements are fairly lift-neutral for $Re > 1.5 \times 10^5$ but for some small asymmetries occurring: around $Re = 2.3 \times 10^5$ for $z_J = 20mm$ where a small drop in C_D is recorded and C_L creeps back to zero with increasing Re; and, around $Re = 2.5 \times 10^5$ for $z_J = 10mm$ which does not seem to significantly influence C_D.

It is not surprising that a spike in C_L should coincide so regularly with a distinct change in C_D since the development of the flow phenomena around a circular cylinder is very unstable and sensitive to small changes in the boundary layer. Slight

fluctuations in the introduction of jet fluid into the boundary layer on either side could lead to the development of a new flow regime on one side prior to the other and hence pressure asymmetries will occur while the imbalance in flow development exists. This is similarly the case if the introduction of jet fluid on one side of the cylinder is slightly offset relative to the other such that a favourable flow regime will be consistently promoted on one side of the cylinder prior to the other.

5.3.1 Effect of jet velocity on C_D reduction

The plot in Figure 5.9 provides an interesting insight into the effect of the continuous transverse jets emitting into the boundary layer on the development of the flow regime it creates to reduce drag. The feasibility study test conducted for the cylinder with an added pressure of $p_{(add)} = 470Pa$ was the lowest added pressure for which the C_D v. Re curve closely followed the optimum C_D v. Re curve obtained for all tests with the $z_J = 20mm$ passive jets cylinder. When tested in the passive supply setup, the internal cylinder pressure reached higher levels than in all other tests with the $z_J = 20mm$ passive jets cylinder. Yet, from $Re = 1 \times 10^5$ both of these test essentially produce the same C_D v. Re curve.

That the internal cylinder pressure is intrinsically linked to the jet flow rate, and hence velocity, suggests a few interesting points:

There appears to be a significant range of jet flow rates which can be introduced at high Reynolds numbers without detriment to the effect on drag reduction. As shown in Figure 5.9, as little added pressure as $470Pa$ to the internal cylinder volume (i.e. a $470Pa$ pressure difference between the cylinder volume and the static pressure at $\phi = \pm 65°$) to generate jet flow into the boundary layer is enough to maximise the C_D reduction benefits of this method. When the cylinder is operating in passive

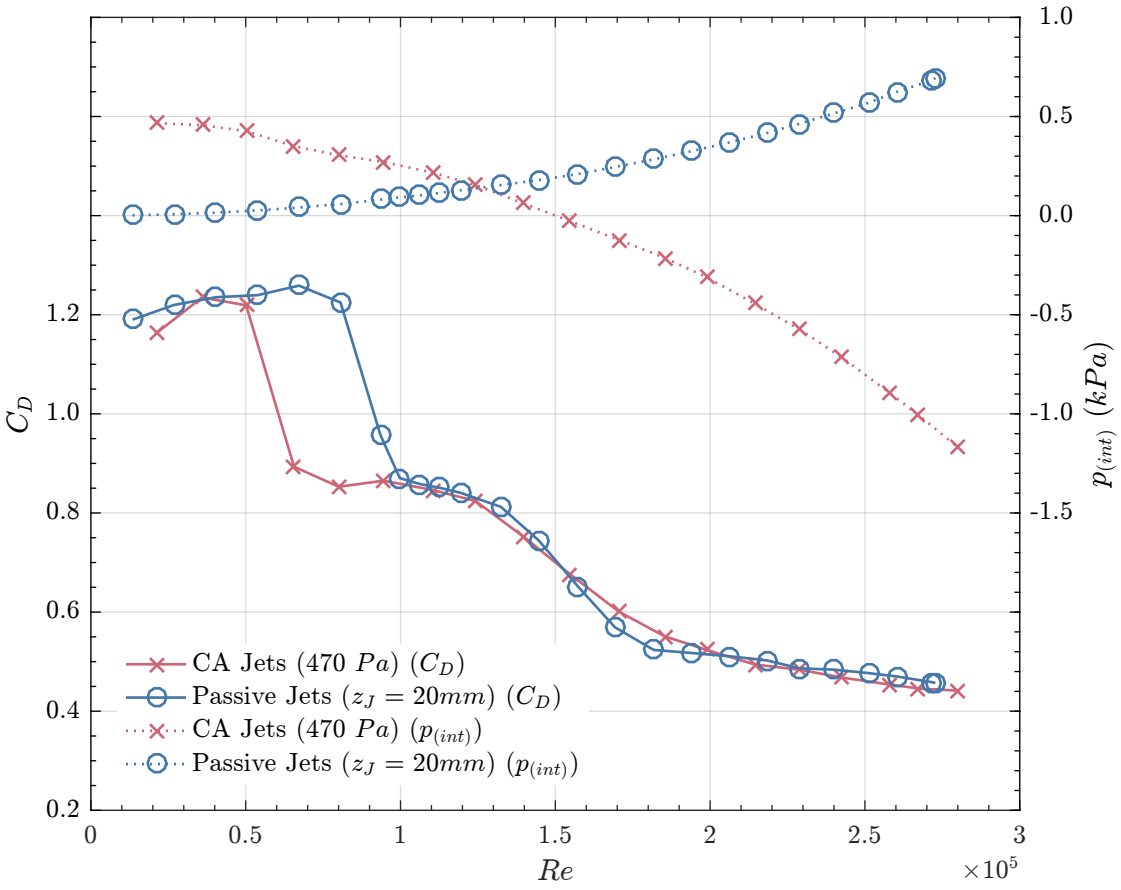

Figure 5.9 – Comparison of internal cylinder pressures with C_D; despite a large differences in cylinder pressure, $p_{(int)}$, the relationship of C_D with Re is unchanged from $Re = 1 \times 10^5$.

mode, the difference in pressure between the internal cylinder volume, $p_{(int)}$, and the static pressure $p_{\phi=\pm 65^\circ}$ can be as high as $\Delta p = 2,655Pa$ and yet the same value of C_D is obtained.

The levels of $p_{(int)}$ converge about $Re = 1.3 \times 10^5$ and from here up to the maximum Re tested the divergence of $p_{(int)}$ consequently leads to an increase in the disparity between the jet velocities introduced by each setup into the boundary layer. This indicates a generous degree of flexibility in the application of continuous

transverse jets in this way since there is little drawback to over-supplying the jets – at least in the ranges tested. It also suggests that for a particular arrangement of jets, e.g. $z_J = 20mm$, the maximum C_D reduction will be obtained so long as the minimum jet velocity (i.e. internal cylinder pressure) is generated; values significantly higher than this will produce the same effect without penalty.

That this is in contrast to, for example, surface roughness or tripping wires where an increased level of disturbance of the boundary layer (i.e. by increased k/D surface roughness or larger diameter tripping wires) is detrimental to C_D reduction, indicates that the drag reducing flow regimes created by the continuous transverse jets do not depend wholly on jet velocity or flow rate, but by mechanisms which are triggered as a result of its presence – once sufficiently established – in the boundary layer flow. That is to say that it is a different type of interaction with the boundary layer than surface roughness or other kinds of solid protrusions from the cylinder surface.

5.4 Directional sensitivity

To test the flexibility of this novel flow control method, a directional sensitivity investigation was conducted by varying the circumferential angle, ϕ, of the cylinder model with respect to the free stream direction.

Though the passive jets concept was designed on the basis of a unidirectional flow application, as shown in Figure 5.10 the $z_J = 20mm$ arrangement offset by $\Delta\phi = \pm 10^\circ$ develops only a small drop in C_D reduction performance throughout the Re_D testing range and delivers the same value of C_D as the optimally aligned case for $Re_D \geqslant 2.0 \times 10^5$ – despite an asymmetric pressure distribution forming

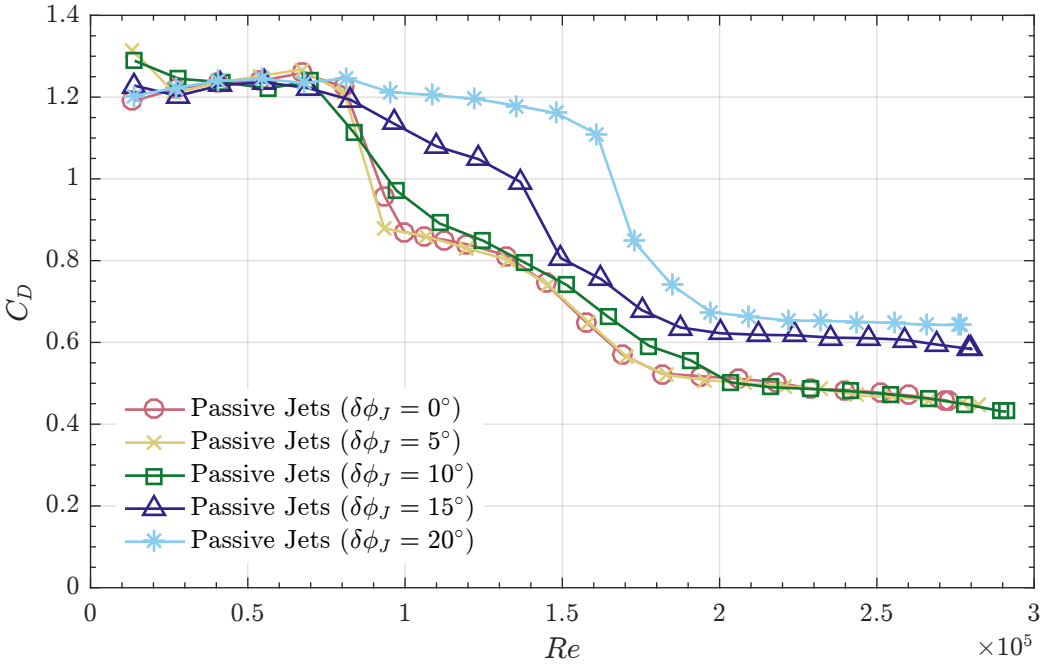

Figure 5.10 – Directional sensitivity study for passive jets; variation of drag coefficient, C_D, with Re for the cylinder with passive jets rotated about its circumferential axis by the angle $\delta\phi$ with respect to the free stream, where $\delta\phi = 0°$ represents the design orientation with the cylinder rotated such that the supply holes are located at the mean frontal stagnation point.

and deviating from the baseline ($\delta\phi_J = 0°$) measurement for $Re_D > 1 \times 10^5$, as shown by the plot of lift coefficient in Figure 5.11. However, as Re_D increases from $Re_D \approx 1.85 \times 10^5$ the time-mean pressure distribution (and hence lift force) of the $\delta\phi = \pm 10°$ setup begins to return towards the baseline measurement; as that happens, C_D begins to converge with that of the optimised arrangement – despite the disparity of the $\phi_{J(row1)} = +55°$ and $\phi_{J(row2)} = -75°$ arrangement of passive jet arrays.

The internal cylinder pressure, $C_{p(int)}$, was recorded throughout the directional sensitivity study and Figure 5.12 indicates that at low Re – up to approximately $Re = 1.5 \times 10^5$ – there is a clear correlation between the cylinder alignment offset

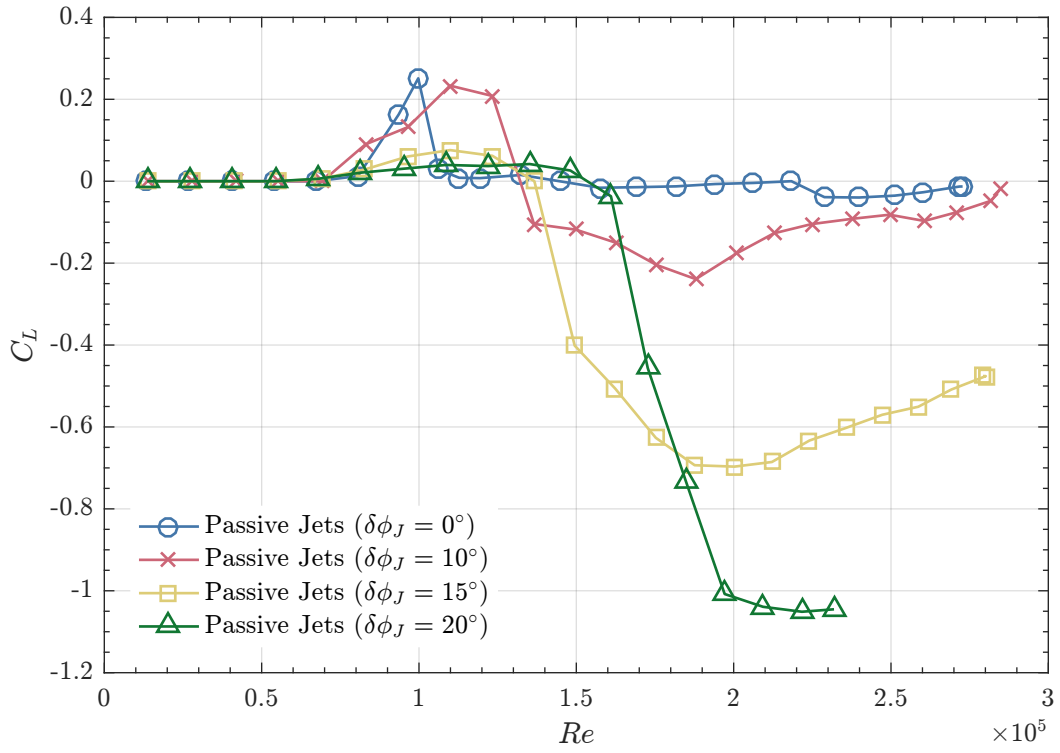

Figure 5.11 – Directional sensitivity study for passive jets; variation of lift coefficient, C_L, with Re for the cylinder with passive jets rotated about its circumferential axis by the angle $\delta\phi$ with respect to the free stream, where $\delta\phi = 0°$ represents the design orientation with the cylinder rotated such that the supply holes are located at the mean frontal stagnation point.

angle, $\delta\phi_J$, and the pressure head generated inside the cylinder to supply the jets; the greater the offset angle the lower the jet pressure available. At around $Re = 1.5 \times 10^5$ the spread of $\Delta C_{p(int)}$ between the different setup angles is quite small for $0° \leqslant \delta\phi_J \leqslant 15°$ and the $C_{p(int)}$ values remain fairly constant throughout the rest of the Re test range for $\delta\phi_J \leqslant 5°$ and $\delta\phi_J = 20°$ but decrease gradually with Re for $10 \leqslant \delta\phi_J \leqslant 15°$.

While the internal cylinder pressure coefficient for $0° \leqslant \delta\phi_J \leqslant 10°$ remains fairly constant throughout the Re test range, there is a clear deviation from this trend for $\delta\phi_J \geqslant 15°$. Both $\delta\phi_J = 15°$ and $\delta\phi_J = 20°$ maintain a significantly lower, yet

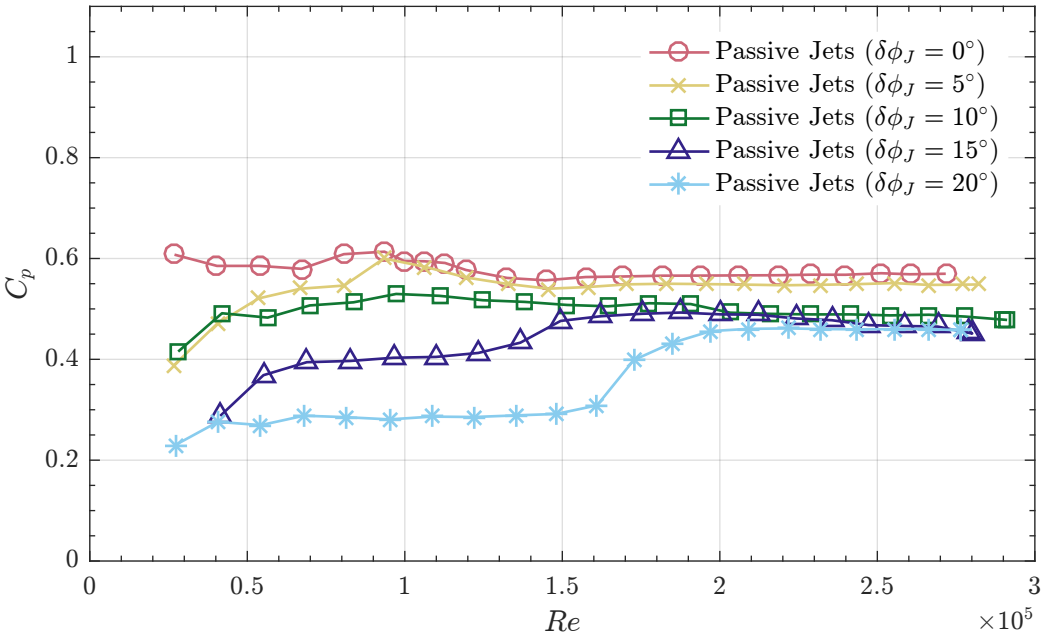

Figure 5.12 – Directional sensitivity study for passive jets; variation of cylinder internal pressure coefficient, $C_{p(int)}$, with Re for the cylinder with passive jets rotated about its circumferential axis by the angle $\delta\phi$ with respect to the free stream, where $\delta\phi = 0°$ represents the design orientation with the cylinder rotated such that the supply holes are located at the mean frontal stagnation point.

still largely constant, value of $C_{p(int)}$ at low Re before rising in a smooth step to a higher plateau of $C_{p(int)}$ midway through the range of Reynolds number tested. For $\delta\phi_J = 20°$ up to $Re = 1.6 \times 10^5$, $\overline{C}_{p(int)} = 0.28$ which is half of what is available with the optimally aligned $\delta\phi_J = 0$. At $Re = 1.6 \times 10^5$, the internal cylinder pressure coefficient begins rising up in a smooth arc to plateau at $\overline{C}_{p(int)} = 0.46$ (compared to $\overline{C}_{p(int)} = 0.57$ for $\delta\phi_J = 0°$) just beyond $Re = 1.9 \times 10^5$ where it remains up to the highest Re tested.

It is particularly evident for $\delta\phi_J = 20°$ that concurrently with this change in $C_{p(int)}$, both C_D (Figure 5.10) and C_L (Figure 5.11) also rapidly change. It can be assumed that the large drop in C_D accompanied by a drastic spike in transverse

force is as a result of the jets "working" (i.e. reducing drag) on the underside of the cylinder – where they are located $\phi_J = +85°$ – and the jets on the top side, located $\phi_J = -45°$, are having a very limited effect, thus creating a particularly asymmetric pressure distribution.

5.5 Disruption of von Kármán vortex shedding

It has long been known that disrupting straight-line separation from bluff bodies reduces the strength of vortex shedding into the wake and hence pressure drag on the body (see, for example, Naumann and Quadflieg, 1968; Tanner, 1972). In order to determine the effect of the passive jets on von Kármán type vortex shedding into the wake, a hot-wire probe was traversed in the near-wake of the cylinder and data acquired at regular intervals throughout the Re_D range of interest. The power spectral density (PSD) was computed by ensemble averaging of the Fast Fourier Transform (FFT) of the fluctuating component of the hot-wire signal by the method of Welch (1967). The hot-wire probe was traversed in the z-axis over a section of the central span while maintaining its position in the x-axis, $1.5D$ downstream of the cylinder centreline, and y-axis, $0.5D$ from the wake centreline. Hot-wire data was acquired in $2mm$ intervals over a $30mm$ section of the span in order to overlap two adjacent $20mm$ jet spacings and cover any possible span-wise variance with z_J. It was found, however, that no coherent span-wise variance existed in relation to the jet spacing or acquisition position. If a PSD peak was generated at a particular flow speed, a peak with the same frequency, f, would be found at all span-wise positions – with the variance in power between acquisition points bearing no correlation with the position on the cylinder span directly upstream; if no PSD peak was to be found

at one particular acquisition point for a set flow speed, then no peaks would be found at any other span-wise location for that flow speed. As such, to improve the clarity of the PSD extracted from the data, the PSD was averaged over the 30mm span of acquisition points for each tested flow speed. The plot in Figure 5.13 therefore displays the *mean* power spectral density for a selection of tests at the specified Reynolds numbers. The data shown in Figure 5.13 is not corrected for blockage. For more details on the setup and procedure of this set of experiments, see section 3.7.1.

While traversing the hot-wire probe in the near-wake of the cylinder with passive jets, it was found that von Kármán vortex shedding into the wake is no longer discernible from $Re = 9.8 \times 10^4$, as shown in the plot of mean power spectral density

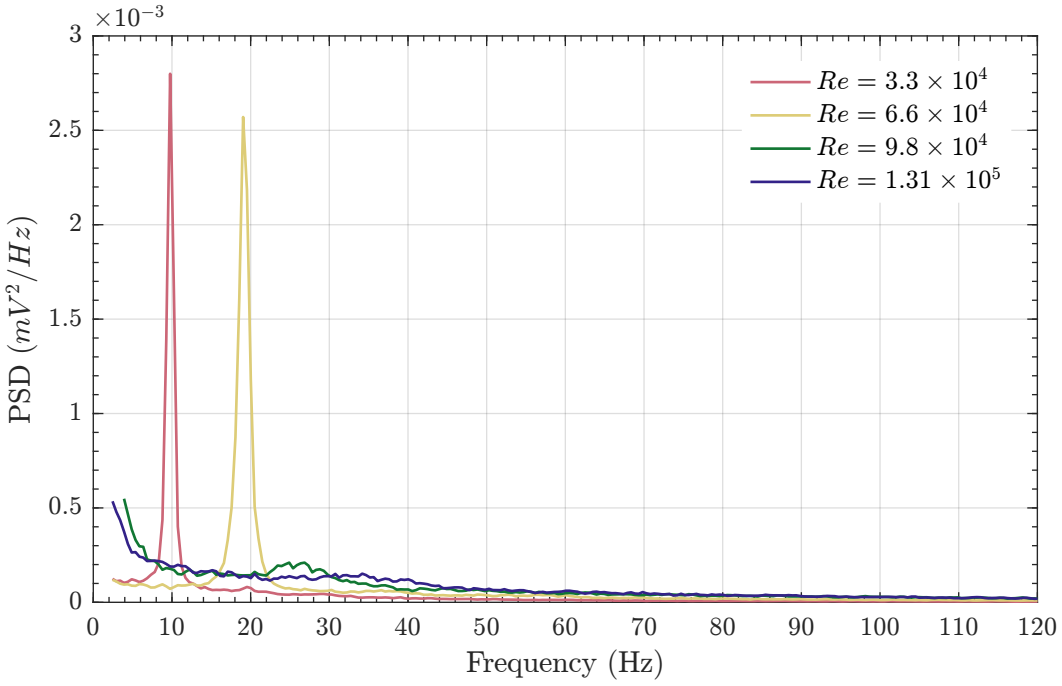

Figure 5.13 – Plot of power spectral density (PSD) of cylinder wake with passive jets showing an absence of any signal peak to indicate von Kármán vortex shedding above $Re = 6.6 \times 10^4$.

(PSD) in Figure 5.13. The mean PSD trace for $Re = 3.3 \times 10^4$ and $Re = 6.6 \times 10^4$ show distinct peaks at $9.8Hz$ and $19Hz$ respectively – corresponding to very similar Strouhal numbers of $St = 0.194$ and $St = 0.190$ – to indicate that von Kármán vortex shedding is present. These values of Strouhal number are typical of those found for a plain cylinder in the critical regime – see Figure 4.3 in chapter 4. All regular vortex shedding ceases at $Re = 9.8 \times 10^4$, and as Reynolds number increases there is no return of regular shedding of the von Kármán type vortices into the wake throughout the Re range tested. There are some small rises over the PSD power base-level along with some barely perceptible bumps – not peaks – in the PSD power at low frequencies up to $\approx 44Hz$ throughout the Reynolds number range $Re = 9.8 \times 10^4 \leqslant Re \leqslant Re = 1.63 \times 10^5$. There is insufficient data to rule out the possibility that some sporadic shedding or wake instability exists in this Re range, but given – as previously mentioned – that for a sub-critical regime one would expect a Strouhal number of $St \approx 0.2$, or up to $St \approx 0.45$ in the critical regime (Bearman, 1969), the rises or broadband 'bumps' in PSD power would occur at higher frequencies (e.g. $30 \leqslant f \leqslant 68$ for $Re = 9.8 \times 10^4$ and $50 \leqslant f \leqslant 113$ for $Re = 1.63 \times 10^5$). At $Re \geqslant 1.94 \times 10^5$ these low frequency broadband 'bumps' no longer occur in the PSD trace (see Figure D.1 in Appendix D for a PSD plot covering the full range of Re tested) which may indicate a completed breakdown of any regular fluctuation in the vertical (y) coordinate of the free shear layers at high Re.

Comparing the PSD data in Figure 5.13 with the equivalent C_D v. Re curve (Figure 5.7) for the cylinder with $z_J = 20mm$ passive jets, it is clear that the elimination of regular vortex shedding coincides with the initial drop in C_D over that of a plain cylinder; von Kármán vortex shedding only exists on the cylinder

with passive jets where the C_D v. Re curve matches that of the plain cylinder. This suggests that once the jet flow rate into the boundary layer is sufficient to destabilise straight-line separation from the cylinder surface, the resulting breakdown of von Kármán type vortex shedding into the wake serves to immediately increase the base pressure and reduce the drag. The aforementioned elimination of low frequency broadband 'bumps' from $Re \geqslant 1.94 \times 10^5$ coincides with the C_D v. Re curve reaching the final 'phase' in the rate of change of dC_D/dRe where the drop in C_D slows – perhaps, it is proposed, because a limit has been reached in the number of regular vortex shedding modes (in the vertical (x, y) plane) that can be broken down by this passive jet arrangement.

Chapter 6

Transverse jets: Investigation of flow mechanisms

Here marks the beginning of the documentation of a more in-depth investigation into the fundamental fluid mechanics which underpin the drag reduction generated by the passive jets flow control method. The following sections present the results of experiments which were designed to provide deeper insights into these drag reducing mechanisms with the aim of furthering understanding which might enhance the design and application of these methods to bluff bodies more generally.

6.1 Overview of jets in cross-flow

The fluid mechanics and flow structure of jets in cross-flow have been keenly studied by many researchers and for a wide variety of applications (see, for example, Andreopoulos and Rodi, 1984; Camussi et al., 2002; Cortelezzi and Karagozian, 2001; Fearn and Weston, 1974; Foss, 1980; Fric and Roshko, 1994; Gopalan et al., 2004;

Kelso and Smits, 1995; Mahesh, 2013; McMahon et al., 1971; Schlatter et al., 2011). Most of the available literature on these studies have concentrated on the problem of a transverse jet emitted into low Re cross-flow over a flat plate, often with zero pressure gradient and most commonly with a velocity ratio parameter greater than one. Depending on the specific arrangement of the transverse jet studied, various velocity ratios are employed as characteristic parameters; either the momentum flux ratio, J, blowing ratio, M, or jet-to-crossflow velocity ratio, R, is generally used. The definition of these parameters varies somewhat among authors, however they are typically defined in the following way:

Momentum flux ratio:

$$J = \frac{\rho_J \overline{V}_J{}^2}{\rho_\infty U_\infty{}^2} \tag{6.1}$$

Blowing ratio:

$$M = \sqrt{\frac{\rho_J \overline{V}_J{}^2}{\rho_\infty U_\infty{}^2}} \tag{6.2}$$

and when the density of the jet and cross-flow are equal, the blowing ratio simplifies to the more commonly termed jet-to-cross-flow velocity ratio:

$$R = \frac{\overline{V}_J}{U_\infty} \tag{6.3}$$

where $\overline{V}_J{}^2$ is usually calculated as the time averaged jet volume flow rate divided by the area of the jet exit hole.

The studies of jets in cross-flow reveal a very complex, three dimensional flow topology comprising several distinct vortical structures, Figure 6.1. Some of the main flow features identified and studied are:

(a) the distinctive counter rotating vortex pair (CRVP), characteristic of the jet

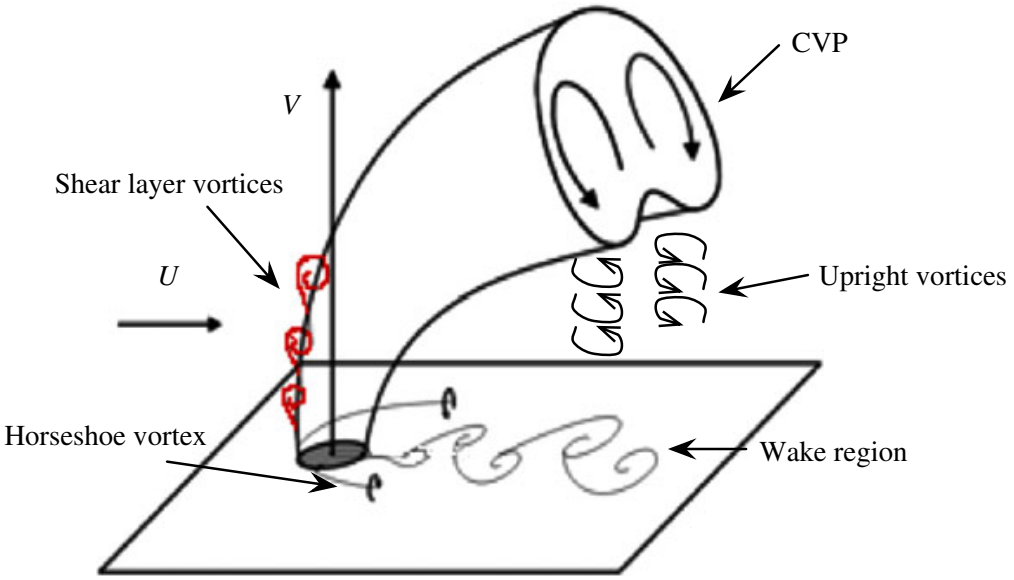

Figure 6.1 – Schematic of a transverse jet in cross-flow over a flat plate; a typical interpretation and presentation of the main vortical structures including the characteristic counter-rotating vortex pair (here noted CVP, but referred to as CRVP throughout this document) that may typically be identified in the flow, from Ilak et al. (2012).

in cross-flow, which forms just behind the jet centreline – on the leeward (downstream) side of the jet;

(b) the horseshoe vortex which forms as the cross-flow separates from the wall in the high pressure region immediately upstream of the jet exit wrapping around the base of the jet in the characteristic shape with the vorticity being swept downstream with the cross-flow (see Kelso and Smits, 1995 for a detailed study);

(c) shear layer instability – found on the windward (upstream) side of the jet-cross-flow shear layer and is a result of the Kelvin-Helmholtz instability of the annular shear layer that separates from the edge of the jet orifice (Fric and Roshko, 1994). Vortices are shed with consistency and regularity downstream

to enhance mixing of the shear layer (Salewski et al., 2008);

(d) vortex shedding in the wake of the jet – particularly for high values of R – which has been compared in numerous studies with that of a bluff-body and most commonly a cylinder of equivalent diameter (e.g. McMahon et al., 1971; Moussa et al., 1977). However, the method of formation of these wake vortices is thought to differ from the way a typical Kármán vortex street develops (see Fric and Roshko, 1994).

6.2 Estimation of cross-flow velocity

In order to provide a relevant comparison with the literature, an estimation of the mean cross-flow velocity, $\overline{U}_{cf}$, at the jet location is required. With the jets positioned on a cylinder surface at $\phi = \pm 65^{\circ}$, they are located in a favourable pressure gradient and hence region of accelerating flow. The introduction of jet fluid from the cylinder surface at this point disturbs the local pressure; Foss (1980) pointed out that, even for very low R, the transverse introduction of fluid into cross-flow is sufficient to create a pressure rise forward of the jet exit hole, altering the jet velocity profile prior to emission into the cross-flow. This pressure rise signifies a retardation of the cross-flow immediately upstream of the jet exit hole, however, as illustrated by the plots of average Reynolds number in the region of $\phi = 65^{\circ}$ (Figure G.1, in Appendix G), the interaction of the jet and cross-flow also leads to an increase in the cross-flow velocity relative to the span-wise position between two jets.

Pressure measurements of the internal cylinder volume were acquired over the full Re_D testing range, however the complex nature of the jet-cross-flow interaction and pressure losses associated with the passive jet supply made it very difficult to

accurately extract the pressure coefficient, C_p, at the surface of the cylinder from this data. The cross-flow velocity at the edge of the boundary layer was not measured over the full Re_D testing range for this research and hence an estimate of the cross-flow velocity has been made from the available data.

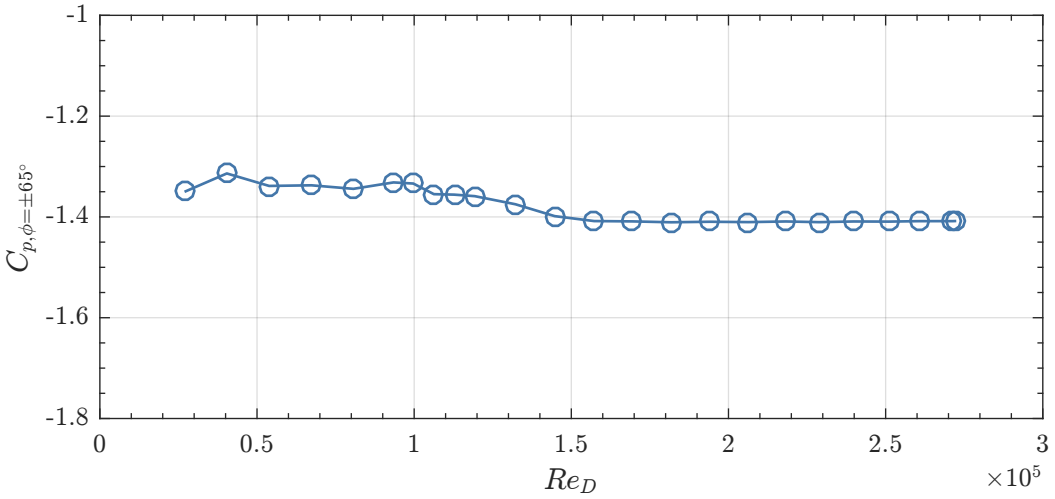

Figure 6.2 – Estimated variation of static pressure coefficient at the cylinder surface where the passive jets are positioned, $C_{p,\phi=\pm65^\circ}$, with free-stream Reynolds number, Re_D.

Using a combination of PIV and pressure measurements, the cross-flow velocity at $\phi = \pm65^\circ$ was estimated by first acquiring the trend of the static pressure coefficient, $C_{p,\phi=65^\circ}$ from the pressure measurements of the internal cylinder volume over the Re_D testing range for the passive jets setup; this assumes that the pressure losses between the air inlet and outlet are linear and the inlet holes are positioned accurately at the frontal stagnation point of the cylinder. The pressure increase at the air supply holes should then correlate simply with the dynamic pressure increase ($C_p = 1$) and thus any variation in $C_{p,(int)}$ is assumed simply to reflect the variation in $C_{p,\phi=65^\circ}$ at the cylinder surface. This assumption also neglects the impact of the local pressure disturbance owing to the jet issuing into the cross-flow.

Local cross-flow velocity measurements were taken from PIV data (discussed later in chapter 8), taken in a 2D (x, y)-plane in-line with a jet exit hole, as a reference to calculate $C_{p,\phi=\pm65^\circ}$ at $Re_D = 1.5 \times 10^5$. This reference point was then used to anchor the $C_{p,(int)}$ trend extracted from the internal cylinder pressure to provide an estimate of $C_{p,\phi=65^\circ}$ v. Re_D, as shown in Figure 6.2.

From Bernoulli's relation for incompressible flow (see, for example, White, 2011), the values of $C_{p,\phi=65^\circ}$ were then used to extract the ratio of jet cross-flow velocity, $U_{cf} \equiv U_{\phi=65^\circ}$, to free-stream velocity, U_∞, using Equation 6.4.

$$\frac{U_{cf}}{U_\infty} = \sqrt{1 - C_{p,\phi=65^\circ}} \tag{6.4}$$

The cross-flow velocity estimates were corroborated with published surface pressure distributions for similar drag coefficient values (Cantwell, 1976; Cantwell and Coles, 1983; Higuchi et al., 1989; James et al., 1980; Zdravkovich, 1997); there is considerable variation throughout the literature on the C_p values found – and indeed there are numerous papers which either correlate closely or differ wildly from the values extracted here – but it is emphasised that U_{cf} is not a directly measured quantity here, and thus provides only a qualitative comparison with the literature.

The estimated values of $C_{p,\phi=65^\circ}$ appear to be at the higher end of comparable values – more commonly found in the pre-critical regime for a plain cylinder – but given the reasonable correlation with many other published papers it was decided to work with these values rather than subjectively altering to another set of values. On the $C_{p,\phi=\pm65^\circ}$ v. Re_D trend, it is interesting to note that $C_{p,\phi=65^\circ}$ varies little throughout the Re_D testing range, even though there is a large change in C_D with the inducement of the critical regime; this is in contrast to the much greater variation

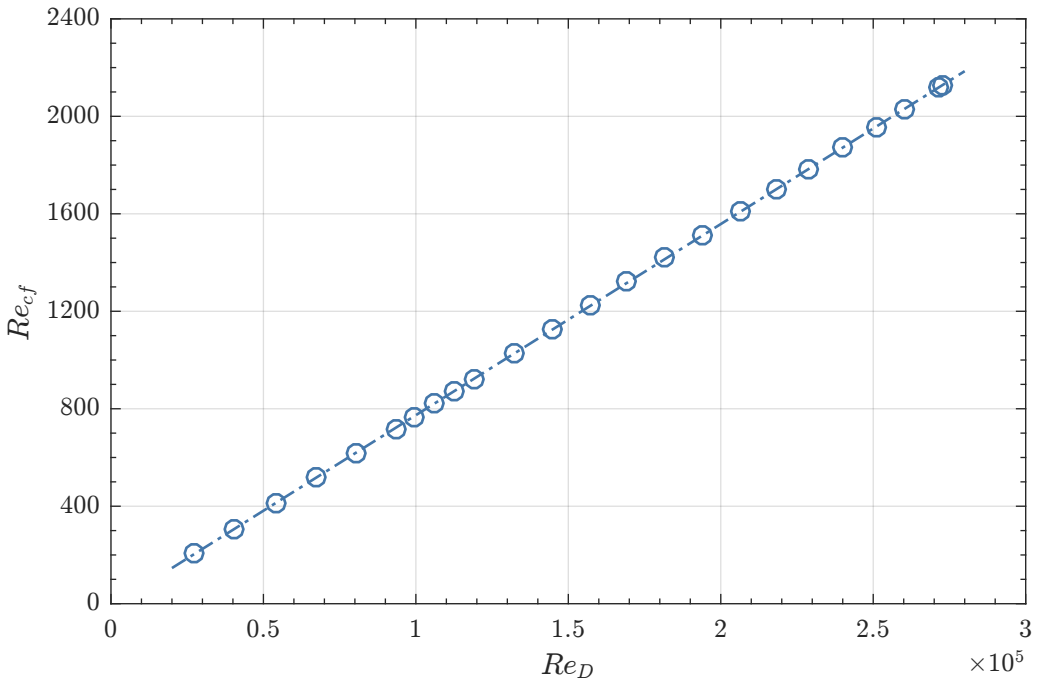

Figure 6.3 – Plot of estimated Re_{cf} at $\phi = \pm 65°$ (the passive jet location) with free-stream Reynolds number, Re_D, overlaid with a linear trend-line.

in surface pressure distribution with Re_D for a plain cylinder, from the pre-critical through critical regimes, found by several researchers (see, for example, Achenbach, 1968; Fage, 1929). Roshko (1961) found for supercritical and post-critical Re_D that there was no significant effect on surface C_p distribution with Re_D or the introduction of a splitter plate and suppression of vortex shedding – the main influence was on the base pressure, commensurate with the change in C_D. Achenbach (1971) also found only small variations in the C_p distribution – from the stagnation point to $\phi \leqslant \pm 65°$ – throughout the pre-critical and critical regimes due to surface roughening of the cylinder to induce the critical regime at lower Re_D. Zdravkovich (2003) pointed out that Fage and Warsap's (1930) surface C_p distribution results for tripping wires all collapsed to the same curve in the range $9.0 \times 10^4 \leqslant Re_D \leqslant 2.6 \times 10^5$ (with higher values than a plain cylinder at the same Re_D) because the addition of tripping wires

meant the flow was equivalent to the TrBL4 or supercritical regime.

$$Re_{cf} = Re_D \frac{U_{cf}}{U_\infty} \frac{d_J}{D} \tag{6.5}$$

With the cross-flow to free-stream velocity ratio established, the cross-flow Reynolds number, Re_{cf}, based on the diameter of the jet exit hole (as is customary in the literature for jets in cross-flow), is simply derived by Equation 6.5. The resulting variation with free-stream Reynolds number, based on the cylinder diameter, is plotted in Figure 6.3, with the remarkably linear relationship emphasising the small variation in C_p with Re_D.

6.3 Transverse jet velocity

During the passive jets feasibility study (see section 5.2) calculations were made to estimate the jet velocity of the proposed design to ensure that the passive supply generated a sufficient amount of pressure, accounting for losses in the system, relative to the static pressure at the cylinder surface where the jet was introduced to the cross-flow (see Appendix A for calculation details). After the passive jets model was made, the cylinder throughput (volume flow-rate of air supply to all jet exit holes) was measured in order to quantify the average individual jet flow-rate and hence calculate the actual jet to cross-flow velocity ratio, R, during experiments.

As detailed in section 3.5, the cylinder stagnation point holes were sealed and compressed air – controlled by matching cylinder pressures obtained with passive jets – was supplied to the cylinder via simple ball-float flow-meters. This method was preferred to, for example, hot wire anemometry (HWA) or particle image velocimetry (PIV) measurements in the immediate vicinity of the jet exit at the cylinder surface

due to the difficulty of accurately measuring the jet profile when: the exit hole diameter was $d = 0.5mm$; the cross-flow boundary layer was as little as $\delta = 1.5mm$; and, the free-stream velocity at the upper-end of the Re_D test range would have transmitted considerable forcing to any sensitive traverse-mounted equipment.

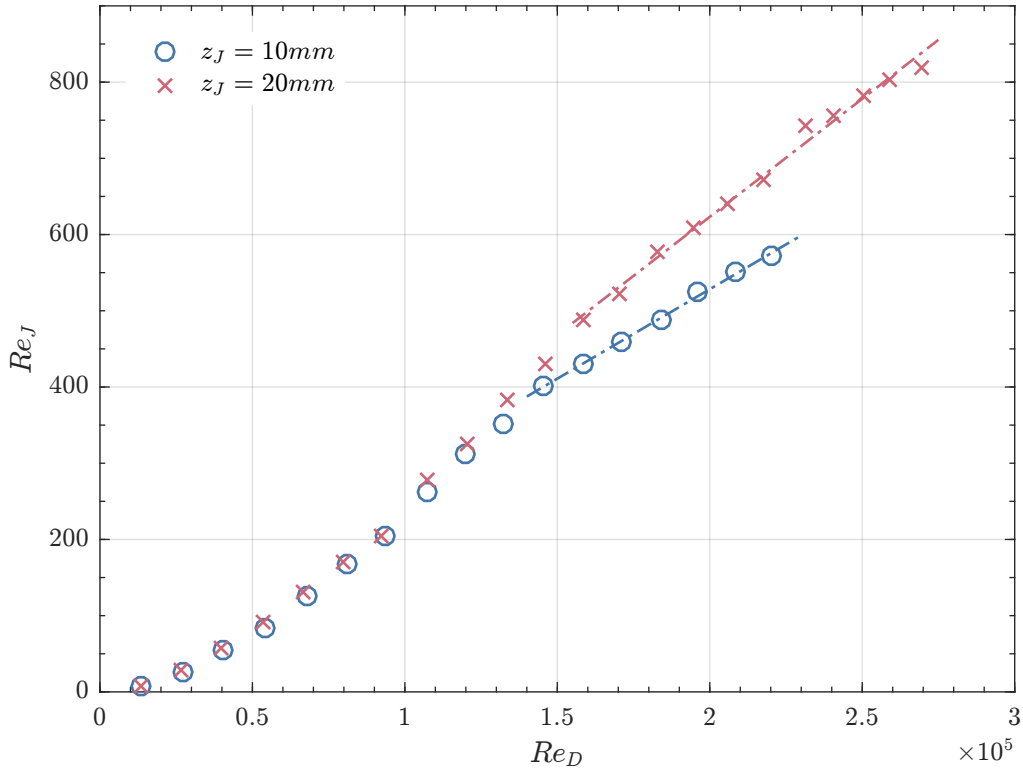

Figure 6.4 – Variation of jet Reynolds number, Re_J, with cylinder Reynolds number, Re_D, for passive jets with span-wise jet spacing of $z_J = 10mm$ and $z_J = 20mm$. The trend-lines highlight the range of Re_D for which the relationship with Re_J is approximately linear for each jet spacing. *Simulated by matching passive jet cylinder pressures with a closely controlled compressed air supply.

With the mean pressure of the cylinder volume matched to passive conditions, the value for the total cylinder throughput was measured over the Re_D testing range. This value was then divided by the total number of jet exit holes to get an average value of a single, continuous jet flow-rate. From the area of a jet exit hole, the mean

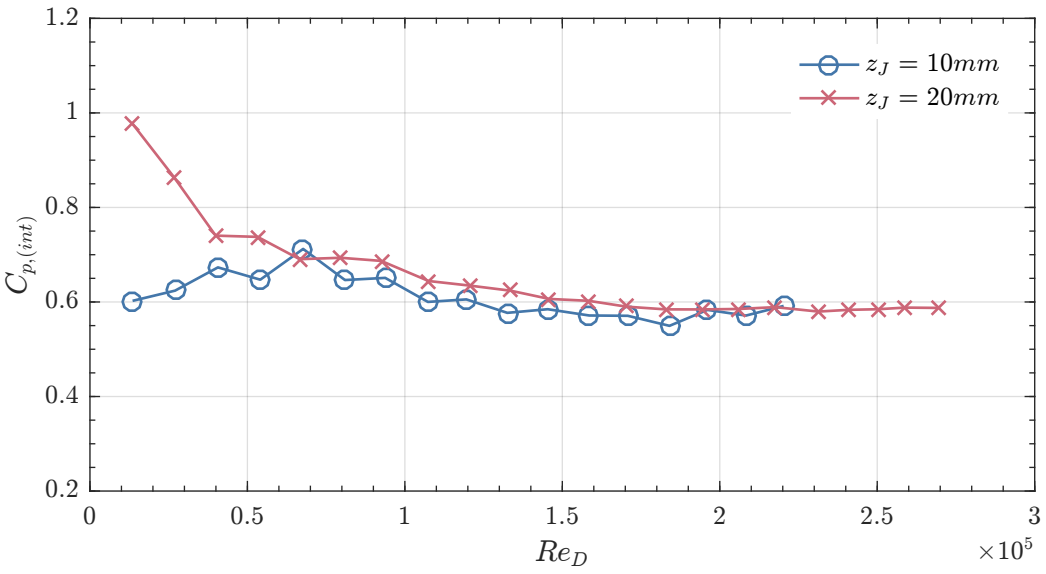

Figure 6.5 – Variation of internal cylinder pressure coefficient, $C_{p,(int)}$, with cylinder Reynolds number, Re_D, from passive* jets flow-rates tests, for span-wise jet spacings of $z_J = 10mm$ and $z_J = 20mm$. *Simulated by matching passive jet cylinder pressures with a closely controlled compressed air supply.

velocity of each individual jet, $\overline{V}_J$, and hence Reynolds number, Re_J, was obtained.

Figure 6.4 plots the variation of Re_J with the free-stream Reynolds number, Re_D. The smoothly increasing gradient of dRe_J/dRe_D is almost indistinguishable at low Re_D for both span-wise jet spacings, $z_J = 10mm$ and $z_J = 20mm$, however there is a distinct dislocation at $Re_D = 1.4 \times 10^5$ where the trends deviate. For $z_J = 10mm$ the trend of dRe_J/dRe_D becomes linear – the rate of increase of Re_J with respect to Re_D is reduced – whereas $z_J = 20mm$ continues as previously up to $Re_D = 1.6 \times 10^5$. From here, with increasing Re_D, the trend of for $z_J = 20mm$ is also approximately linear but with Re_J increasing at a faster rate with Re_D than $z_J = 10mm$. The flow-rate measurements for $z_J = 10mm$ were curtailed at $Re_D = 2.2 \times 10^5$ due to reaching the range limit of the flow-meters used.

The branching of Re_J for the two span-wise jet spacings is interesting because

pressure measurements of the cylinder volume during the tests indicated very close agreement for both setups at the same free-stream Reynolds numbers. Figure 6.5 shows the variation of cylinder internal pressure coefficient, $C_{p,(int)}$, with Re_D for both jet spacing setups during these tests. The disparity in $C_{p,(int)}$ at low Re_D is due to the proportionally larger errors created by the uncertainty of pressure measurements at low speeds when calculating C_p (a change of 0.6 Pa would be sufficient to change the $C_{p,(int)}$ at $Re_D = 1.3 \times 10^4$ for $z_J = 20mm$ from 0.98 to 0.74). The fact that $C_{p,(int)}$ is so closely matched – particularly at higher Re_D – clearly indicates higher losses in the setup of the $z_J = 10mm$ cylinder, since, from $Re_D > 1.4 \times 10^5$, for the same internal cylinder pressures the $z_J = 20mm$ cylinder outputs faster jets (higher Re_J), as shown in Figure 6.4. Plainly, however – by virtue of almost double the number of jets – the total mass flux of the $z_J = 10mm$ cylinder is still much greater throughout the Re_D testing range (see Figure C.1 of Appendix C).

The subject of higher losses in the $z_J = 10mm$ cylinder was first briefly discussed in section 5.3, and here again there seems to be additional losses compared to the $z_J = 20mm$ cylinder setup. Figure 6.6 plots the relationship of the jet-to-cross-flow velocity ratio, R, with Re_D to give another perspective on the differences in jet velocity of the two cylinder arrangements. Because the correlation between $U_{\phi=\pm65^\circ}$ and U_∞ is approximately linear in this range of Re_D, R is approximately constant with Re_D when dRe_J/dRe_D is linear. That R eventually plateaus with increasing Re_D for both cylinder setups, $z_J = 10mm$ and $z_J = 20mm$, naturally displays a limiting condition of the jet velocity with respect to an increase of the free-stream velocity – the resistance of the conduit through which jet air enters and exits the cylinder. From Figure 6.4 and Figure 6.6 it is clear that the $z_J = 10mm$

cylinder reaches this condition sooner – with respect to increasing Re_D – than the $z_J = 20mm$ cylinder. It is possibly the case, viewing Figure 6.6 closely, that rather than plateauing, R is beginning to decline with increasing Re_D for both jet spacings; the incongruous sudden increase in R for $z_J = 20mm$ at $Re_D = 2.3 \times 10^5$ occurs due to a switch over in flow-meters – the new meter appearing to read higher than the previous – with R appearing to drop very gradually.

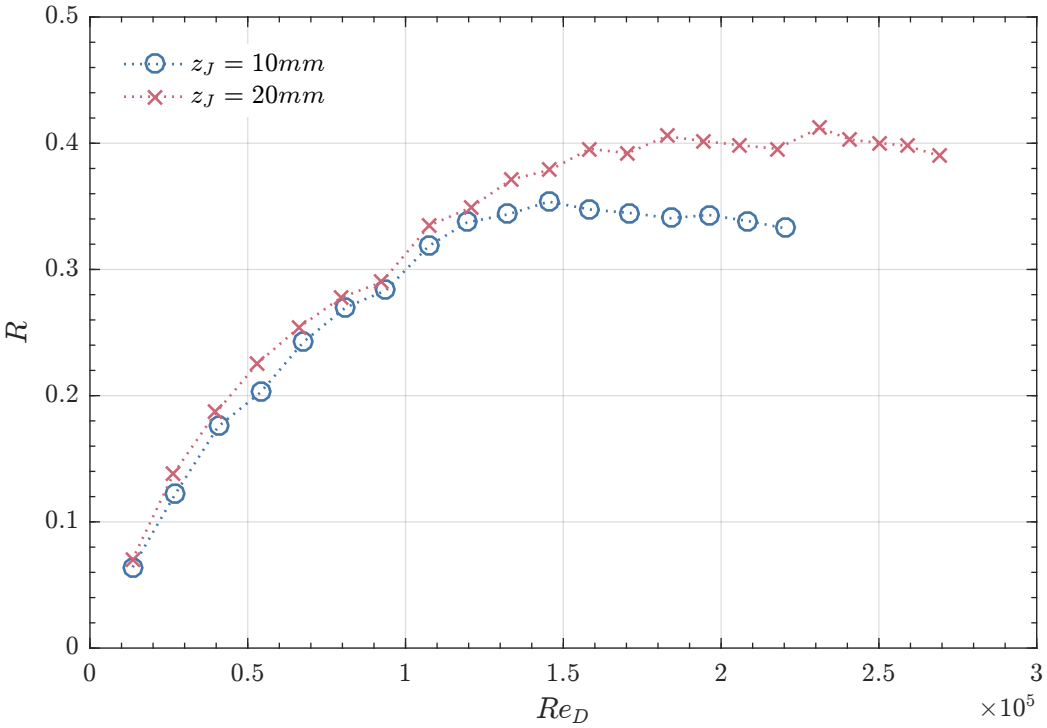

Figure 6.6 – Variation of jet to cross-flow* velocity ratio, R, with free-stream Reynolds number, Re_D. *Cross-flow velocity estimated as detailed in section 6.2.

It had been mooted in several previous tests that a possible reason for unexpected data or the discrepancy between the two cylinder setups was a pressure leak somewhere in the system – and this could similarly be responsible for a gradual decline in R with increasing Re_D for the $z_J = 20mm$ cylinder. Particular attention was paid, however, in these particular flow-rate experiments to ensure each setup was

rigorously leak tested – and where leaks did occur they were repaired and re-tested. The leak test included pressurising the cylinder volume to over twice the level experienced during the experiments and taking periodic pressure measurements to ensure that it was maintained for at least 15 minutes. During the flow-rates experiments, with the passive air entry holes at the stagnation point of the cylinder sealed over and the cylinder pressure controlled by a compressed air supply via a flow-meter, it was clear that at high Re_D for the same testing conditions, the $z_J = 10mm$ cylinder required a lower flow-rate of air supply (per jet exit hole) than the $z_J = 20mm$ cylinder to maintain the same internal cylinder pressure. If the path of least resistance for the air to escape from the cylinder was through the jet exit holes, it can be assumed that the pathways offered by the $z_J = 10mm$ cylinder are more resistive than those of the $z_J = 20mm$ cylinder. The reason for this was not clear – care was taken, for example, to ensure all jet exit holes were clear prior to testing. It has been speculated that slight manufacturing differences between the cylinders could be responsible for additional air resistance – for example wall thickness (affecting 'pipe' length, which could be significant for the additional losses for under-developed flow given the increase in entry length with increasing Re_J (Fargie and Martin, 1971) or additional burring at the junction between the cylinder volume (plenum) and jet exit pipe generating higher entry losses.

Viewing Figure 6.6 in more detail, between $8 \times 10^4 \leqslant Re_D \leqslant 1.1 \times 10^5$ and before the trend of R v. Re_D diverges for each jet spacing arrangement, there is a distinct kink in the curve. This coincides with the initiation of the critical regime – for both cylinders – when the drag coefficient, C_D suddenly and steeply drops for the first time from pre-critical C_D levels (Figure 5.7). It is thought that the drop in C_D from $Re_D = 8 \times 10^4$ results from a sudden increase in the local flow velocity

relative to the jet velocity to produce a dip in R as the flow regime changes. This appears to correlate with a slightly steeper drop in $C_{p,(int)}$ (Figure 6.5). The rate of dR/dRe_D recovers to the previous trend with increasing Re_D as C_D continues to fall incrementally, indicating that the mechanism of drag reduction does not have a significant impact on the rate of change of local U_{cf} with increasing Re_D.

6.4 Low velocity-ratio jets in cross-flow

The estimation of cross-flow velocity, local to the jet exit at the surface of the cylinder, in section 6.2 provides a reasonable basis to compare results here with published studies of jets in cross-flow over flat plates, primarily by quantifying the jet-to-cross-flow velocity ratio, R. As shown in Figure 6.6, the passive jets of this research operate with a jet-to-cross-flow velocity ratio varying in the range $0.07 \leqslant R \leqslant 0.41$, where $R < 1$ is considered low in this field of study (e.g. Mahesh, 2013). As will be discussed further in the following section (section 6.5), compared with higher values ($R \geqslant 2$), jets in cross-flow with low R can have a profound impact on the characteristics of the jet-cross-flow interaction leading to a vastly different set of flow features which translate downstream. Gaining an understanding of these differences and their impact is essential to the use and optimisation of jets in cross-flow for any application.

Cambonie et al. (2013) plotted CRVP trajectories of jets in cross-flow with velocity ratios, $R < 1$ by computing the maxima of mean swirling strength in (y, z) cross-sections of their experimental results (Figure 6.7). They show that for $R \leqslant 0.54$ the trajectory of the CRVP appears to asymptote to a height above the wall which is less than the thickness of the cross-flow boundary layer, δ, i.e. the dominant fea-

ture of the jet flow remains entirely contained within the cross-flow boundary layer at least 12 jet diameters, d_J, downstream of exit with a boundary layer thickness varying in the range $1.78 \leqslant \delta/d_J \leqslant 1.83$. The local boundary layer thickness was not measured during this research, but from Zdravkovich (1997) it is estimated that the cross-flow boundary layer varies in the range $5 \geqslant \delta/d_J \geqslant 3$ over the Reynolds number testing range of $4 \times 10^4 \leqslant Re_D \leqslant 2.8 \times 10^5$. It is thought that maintaining the jet flow within the boundary layer would be particularly desirable for this application, where the aim is to energise the boundary layer by entraining higher momentum fluid from the free stream towards the wall to delay separation. A jet which bursts straight through the boundary layer into the free stream is likely have a reduced benefit to imparting momentum to the region close to the wall. Cambonie et al. note that a significant difference between high and low velocity ratios is the increased jet interaction with the boundary layer at low R, leading to a profound modification of the flow structure.

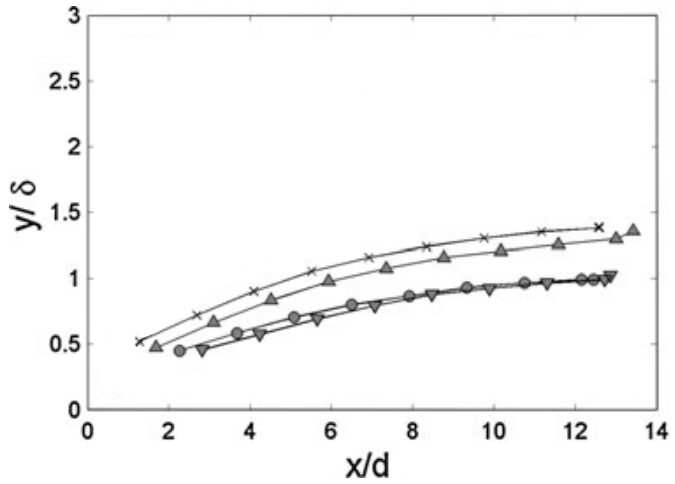

Figure 6.7 – Trajectory of 'CRVP' for jets in cross-flow with varying R and boundary layer thickness for a jet supply 'pipe' length of $l_J = 1.25d_J$, adapted from Cambonie et al. (2013), where: ▼ $R = 0.51$, $\delta/d_J = 1.78$; ● $R = 0.54$, $\delta/d_J = 1.83$; × $R = 0.74$, $\delta/d_J = 1.96$; ▲ $R = 0.83$, $\delta/d_J = 1.78$.

Jets in cross-flow are often studied due to their application in film-cooling – notably turbine blades – which has lead to research in optimising their effectiveness in this regard (Foss, 1980). An effective film-cooling jet provides a large ratio of jet fluid to mix with the boundary layer and thus be brought into contact with the bounded wall of cross-flow containing the jet orifice to affect cooling. A velocity ratio which is too low will not provide sufficient coolant to the surface, but jet fluid emitted with a velocity ratio which is too high will fail to mix with the boundary layer or come into contact with the surface at all. Ramsey and Goldstein (1971) found that the optimum jet to cross-flow velocity ratio in this application was $R \leqslant 0.5$ whereas Bergeles et al. (1976) considered momentum flux ratios of $M > 0.2$ to be beyond a reasonable limit to prevent the jet from lifting away from the surface and adversely affecting the aerodynamic and cooling effectiveness characteristics of the turbine blade. Bergeles et al. noted that the preferred route to improved cooling effectiveness is to reduce the jet velocity ratio and increase the number of jet holes, thus introducing and mixing sufficient quantities of coolant in the boundary layer while keeping injection velocities at acceptably low levels.

6.5 Spectral analysis of jet instability

6.5.1 The shear layer instability

The shear layer instability – commonly referred to by the shedding of shear layer vortices – is not a ubiquitous feature in the literature and opinion is somewhat divided on the mechanism of its formation – which varies according to several flow parameters – but it is a distinct flow feature and focus of many studies (e.g. Davitian

et al., 2010; de B. Alves et al., 2008; Ilak et al., 2012; Kelso et al., 1996; Megerian et al., 2007; Sau and Mahesh, 2008). It appears as a dominant feature of this study and is therefore the subject of attention in this section.

The way in which the shear layer vortices are formed, in equidensity jets in cross-flow, varies according to the following parameters:

1. The jet to cross-flow velocity ratio, R;
2. Reynolds number, Re, of the cross-flow;
3. ...and corresponding boundary layer thickness immediately upstream of the jet exit, δ;
4. The stroke ratio, l/d_J, where l is the straight 'pipe' or 'stroke' length immediately prior to jet exit and d_J is the jet exit hole diameter;
5. ...and corresponding jet velocity profile prior entrance into the cross-flow;
6. The stream-wise pressure gradient.

A brief discussion of the specific effect of each of these parameters on the formation of the shear layer instability follows in section section 6.5.3.

A review of the literature reveals a clear distinction in the type of shear layer instability generated depending on the above listed parameters. Kelso et al. (1996) produced a succinct graphical summary of the occurrence of a selection of phenomena associated with jets in cross-flow (Figure 6.8), relating them to the jet to cross-flow ratio, R, and cross-flow Reynolds number, Re. The highlighted boxes indicate the different types of shear layer instability which can form; the most common type discussed in the literature is marked (a), and the formation mechanism of

interest in this study is marked (b) in Figure 6.8. The shear layer instability marked (c) produces a vortex shedding cycle fundamentally similar to (a) and will not be discussed further here. Type (a) and (b) are outlined below:

(a) The shear layer instability most commonly described in the literature is that of the roll-up and shedding of Kelvin-Helmholtz type vortices on the windward (upstream) side of the jet shear layer (as depicted in Figure 6.1, highlighted in red). This phenomena is induced primarily as a result of 'high' values of R, nominally $R > 1$;

(b) Lim et al. (1992) show that for low R, nominally $R \leqslant 1$, the roll up of the upstream shear layer ceases. Vorticity generated at the downstream edge of the jet exit hole rolls-up to form hairpin vortices (Figure 6.9) which are shed from the leeward side of the jet shear layer (Ilak et al., 2012; Sau and Mahesh, 2008).

It appears that the shedding of vortices from the windward (upstream) side of the shear layer – as is widely reported in the literature (see, for example, Fric and Roshko, 1994; Mahesh, 2013; Rivero et al., 2001) – occurs only for jets in cross-flow with $R > 1$. The experimental studies by Lim et al. (1992) and Kelso et al. (1996), and the detailed analysis of direct numerical simulations (DNS) by Sau and Mahesh (2008) and Ilak et al. (2012), however, clearly indicate the formation and shedding of hairpin vortices on the leeward (downstream) side of the shear layer for jets in cross-flow with $R \leqslant 1$.

As Lim et al. (1992) demonstrate in their experiments, there is a drastic change in the flow structure for $R \leqslant 1$ compared to $R > 1$. The schematics typically presented of the flow structure and vortical systems of a jet in cross-flow (e.g. Figure 6.1),

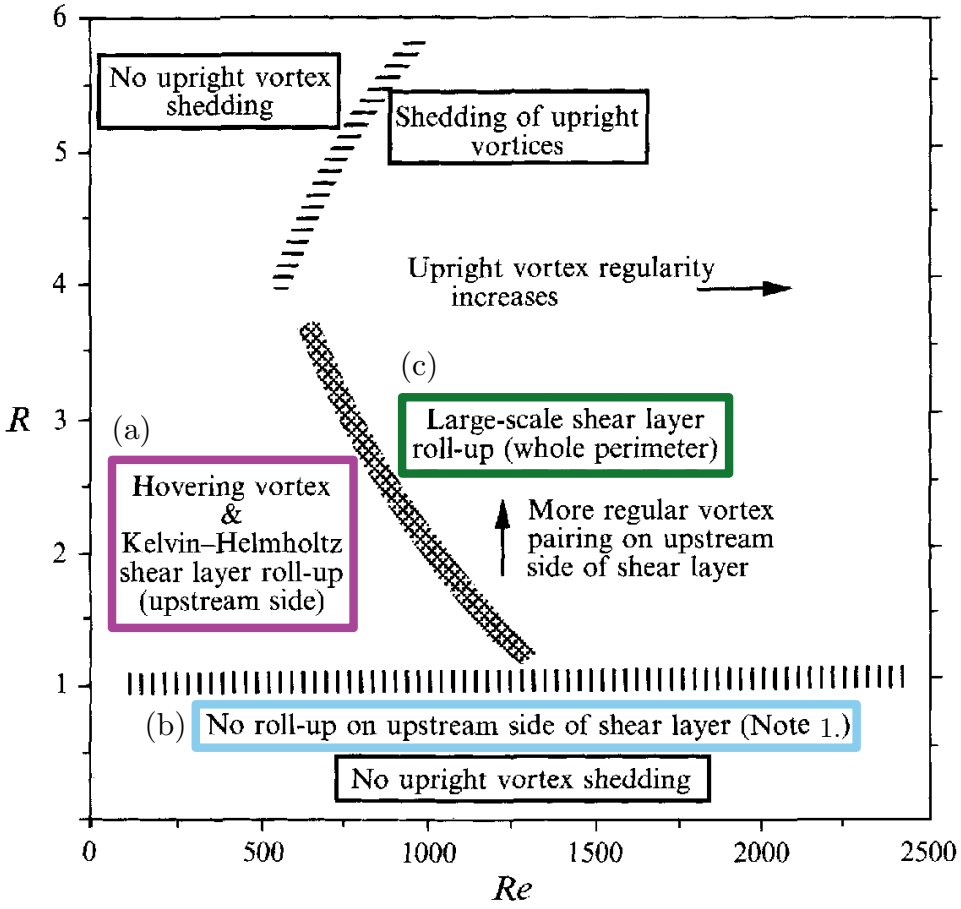

Figure 6.8 – Graphical summary of jet in cross-flow phenomena, adapted from Kelso et al. (1996). The highlighted boxes indicate the variation in the type of shear layer instability formed depending on both the jet to cross-flow ratio, R, and also the cross-flow Reynolds number, Re (based here on the jet hole diameter, d_J and free stream velocity, U_∞). Note 1: Referring to Lim et al. (1992), the roll-up on the lee-side of the shear layer still occurs.

with Kelvin-Helmholtz vortices on the windward shear layer, a dominant CRVP, horseshoe vortices and wake vortices, do not represent the structure formed at low velocity ratios ($R \leqslant 1$) which is dominated by hairpin vortices (Mahesh, 2013; Sau and Mahesh, 2008). The wake vortices of Fric and Roshko (1994) – also known as upright vortices (Kelso et al., 1996; Schlatter et al., 2011) – as depicted in Figure 6.1, are not found for low values of R (Ilak et al., 2012), and even the ubiquitous CRVP

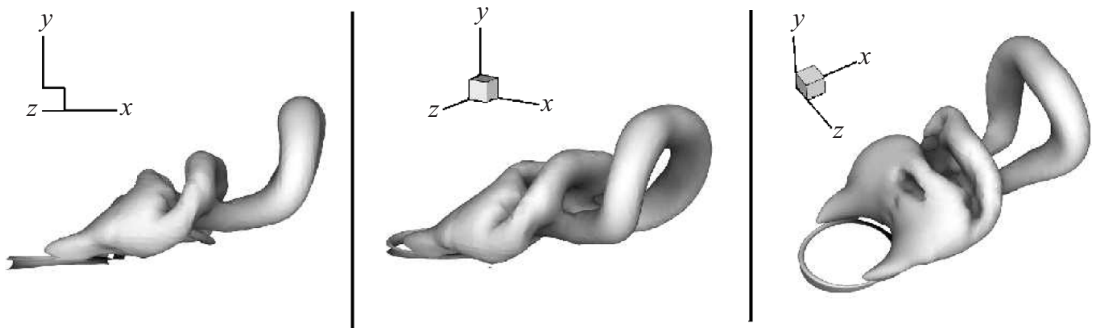

Figure 6.9 – Three-dimensional iso-surface plot of pressure – from three different viewpoints at the same instant in time – depicting hairpin vortex formation and shedding from the leeward edge of the jet exit hole for a jet in cross-flow at $R = 1$ with a stroke ratio, $(l/d_J) = 5$, from the DNS study by Sau and Mahesh (2008).

– the pseudo-appearance of which at low R many still relate to the typical high R examples – has been shown to be part of a completely different vortex structure and formation mechanism (Sau and Mahesh, 2008); the type of flow which develops with $R < 1$ – from the vorticity interaction of the jet and cross-flow boundary layers at the leading edge of the hole, to the low trajectory jets (Figure 6.7) providing increased interaction with the cross-flow boundary layer (Cambonie et al., 2013) immediately downstream of the jet exit – leads to the formation of a fundamentally different set of vortex structures.

Given the findings of the jet velocity measurements (see section 6.3), which confirm the jet to cross-flow velocity ratio of the passive jets is always less than one, it is apparent from a review of the literature that the instability found in this study relates to the shedding of hairpin vortex structures found at low R in jets in cross-flow (see, for example, Acarlar and Smith, 1987*b*; Ilak et al., 2012; Sau and Mahesh, 2008). Interestingly, these structures appear to closely resemble those discovered by Achenbach (1974*b*) for flow around a sphere, Perry and Lim (1978) for a jet emitting from an oscillating pipe into a co-flowing stream and Acarlar and Smith

(1987*a*) for flow over a hemispherical bump. As alluded to earlier, there is a scarcity of studies concentrating on the formation and development of the flow structure, and mixing of jets in cross-flow with $R \leqslant 1$ and large stroke ratios* compared to the many detailed papers covering all aspects of transverse jets with $R > 1$. Two papers which do thoroughly illuminate the structural formation of low velocity ratio jets in cross-flow are those by Sau and Mahesh (2008) and Ilak et al. (2012), and it is assumed that the instability discovered in the present research forms qualitatively according to these analyses.

*It should be noted here that numerous papers do exist for jets in cross-flow with $R < 1$, but with very small stroke ratios – for the simulation of film-cooling applications – issues relating to which are briefly discussed previously in section 6.3 and later in section 6.5.3.

6.5.2 Formation of hairpin vortices

In their DNS simulations of low velocity ratios – in this case values of $R \leqslant 2$ – combined with large stroke ratios, $5 \leqslant (l/d_J) \leqslant 100$ where l is the length of straight 'pipe' leading to the jet exit hole, Sau and Mahesh (2008) show that periodic shedding of coherent hairpin vortices occurs, with the vorticity formed at the trailing edge of the jet exit hole and rolling up the leeward side of the shear layer. At low R, competing vorticity of opposite sign – from the approaching cross-flow boundary layer and the boundary layer formed on the inner surface of the jet supply pipe – weakens and eventually cancels out (Gopalan et al., 2004) at the leading edge of the jet exit hole. Meanwhile, vorticity production continues to grow on the leeward edge, causing the roll-up of hairpin vortices on the leeward shear layer (Figure 6.10).

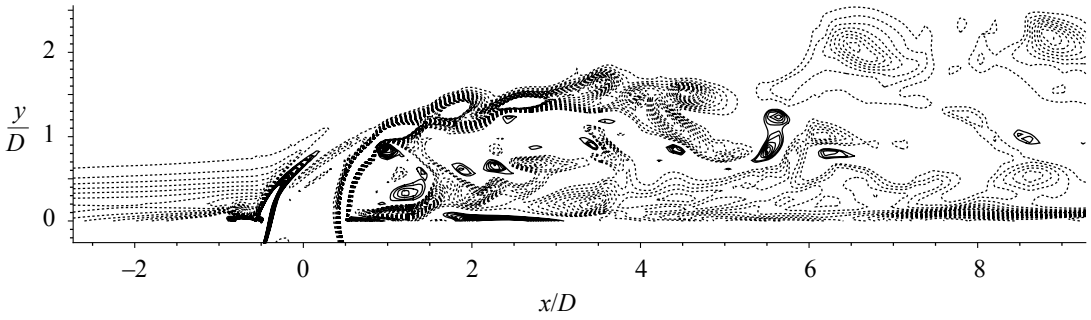

Figure 6.10 – Vorticity contours in the symmetry plane of a jet in cross-flow, showing the cross-section of the 'heads' of the hairpin vortices being shed on the leeward shear layer and the competing vorticity of the approaching cross-flow and jet 'pipe' boundary layers acting to cancel each other out, preventing the roll-up of the windward shear layer. Cross-flow Reynolds number based on jet hole diameter, $Re = 600$, $R = 1$, and stroke ratio, $(l/d_J) = 5$, from the DNS study by Sau and Mahesh (2008).

Sau and Mahesh also noted that the shedding frequency of these vortices depends upon – and increases with – the Reynolds number of the jet, Re_J.

Ilak et al. (2012) state that the global stability analysis they performed (on a jet in cross-flow for $R < 1$) reveals that the first instability at critical R appears to be a Kelvin-Helmholtz roll-up of the *downstream* shear layer, and that by deducing the point at which the direct (global) and adjoint eigenmodes overlap, they identify the location of the so-called "wavemaker" (Chomaz, 2005) which provides the fundamental behaviour of the instability. Ilak et al. argue that immediately downstream of the jet exit, where reverse-flow exists owing to the blockage presented by the jet to the cross-flow, the region of the shear layer on the boundary of the reverse flow is the point of highest sensitivity to instability growth – as postulated in a similar study by Schlatter et al. (2011). From this region, i.e. the aforementioned wavemaker, a localised source of instability waves generates a self-sustained oscillation of the shear layer – which occurs from $R = 0.675$*, where they define R as the ratio of the *peak* inflow velocity to free-stream velocity of the cross-flow boundary layer. This

oscillation of the shear layer results in the periodic shedding of hairpin vortices, and it would appear that this mechanism shares broad similarity with the generation of hairpin vortices by Perry and Lim (1978).

*Since Ilak et al. (2012) used a fully developed laminar (Poiseuille) velocity profile in their simulation and the peak jet velocity, $V_{J(max)}$, in their calculation of R, as demonstrated in Appendix A.4, their values of R can simply be halved to allow comparison with the more commonly used mean jet velocity, $\overline{V}_J$. This brings the critical velocity ratio at which the first instability occurs down to $R = 0.338$.

6.5.3 Parameters which affect formation and structure

There is much concentration throughout the literature on the control that the aforementioned velocity ratios, J, M and R exert on the creation and behaviour of various flow phenomena and topological structures identified. While the velocity ratio provides one of the most significant contributions to the generation of particular types of flow phenomena, there are a number of additional key factors which determine and correlate the parameters of several features associated with these phenomena; indeed, frustration with insufficient correlation has lead some researchers (e.g. Cambonie et al., 2013; Muppidi and Mahesh, 2005) to revise these scaling ratios. The following examples from the literature aim to outline some of the additional factors of influence which are pertinent to the present research.

Megerian et al. (2007) attempt to correlate the shedding frequency of shear layer vortices with the jet to cross-flow velocity ratio for 'high' values of R. Megerian et al. plot the Strouhal number, St, of the jet shear layer instability with $R > 1$ for two different jet Reynolds numbers, Re_J, with St calculated using two different

length scales – the jet diameter, d_J, and the boundary layer momentum thickness, δ_θ, immediately upstream of the jet exit (Figure 6.11). The instability frequency found at values of $R < 3.5$ was acquired from the very strong dominant mode observed to grow almost immediately downstream of the jet exit and along the windward (upstream) side of the jet shear layer. For $R > 3.5$ the instability became weaker and more diffuse. The plot of St_{d_J} in Figure 6.11 (a) shows a general trend for both jet Reynolds numbers of steeply increasing St with R, peaking around $St = 1.0$ and $St = 0.9$ at $R = 3.5$ for $Re_J = 2,000$ and $Re_J = 3,000$ respectively, before St gradually decreases with increasing R to a plateau of $St = 0.7$ for $R > 10$. As McMahon et al. (1971) and Foss (1980) point out, a systematic decrease in St observed for increasing R is an indication that the effective diameter of the jet – upon which the St depends – increases with R.

When δ_θ of the cross-flow boundary layer is used as the St length scale (Figure 6.11 (b)), a more consistent trend appears for $R \geqslant 2$; for constant Re_J there is a fairly smooth curve of decreasing St with increasing R with $Re_J = 3,000$ providing consistently higher St than $Re_J = 2,000$ for the same R up to $R = 8$ where they converge and plateau. However, there is a distinct break with the trend and jump to lower St_{δ_θ} for the small cluster of data points for $R < 2$. Megerian et al. note that as R was reduced below 2.0 a strengthening of strong dominant modes and harmonics occurred even closer to the jet exit. This study explicitly shows that the formation of instabilities in the jet shear layer are affected by Re_J and the characteristics of the cross-flow boundary layer in addition to R, but there is clearly a strong dependence on R for the *type* of flow topology generated as shown by the distinct change in the properties of the shear layer instability for $R < 2$.

The experiments of Peterson and Plesniak (2004) show the significant impact

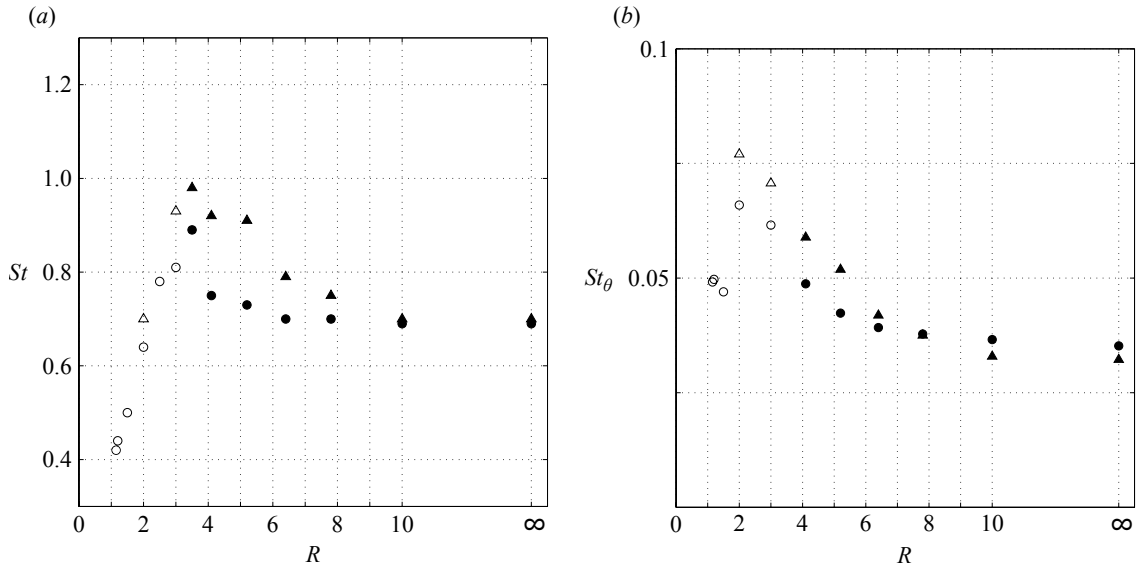

Figure 6.11 – Variation in Strouhal number, St, from the dominant instability first observed to occur along the upstream jet shear layer, with jet-to-cross-flow velocity ratio, R, plotted for two jet Reynolds numbers, Re_J. The Strouhal number is calculated with the characteristic length set to: (a) the jet diameter, St_{d_J}; and, (b) the boundary layer momentum thickness upstream of the jet, St_{δ_θ}, adapted from Megerian et al. (2007). ● $Re_J = 2,000$; ▲ $Re_J = 3,000$. Megerian et al. state that "the open symbols represent dominant Strouhal numbers associated with very strong instabilities generated very close to the jet exit."

that the stroke ratio, l/d_J, and jet velocity profile can have on the jet trajectory and flow structure. To simulate a turbine blade cooling system, Peterson and Plesniak studies arrays of jets in cross-flow with a short stroke length, $l/d_J = 0.66$, connected perpendicularly to a slender air supply plenum of height, $h = d_J$, which provide either a co-flowing or counter-flowing supply relative to the cross-flow direction; the orientation of the supply channel alters the development and sign of rotation of a CRVP within the jet supply. Because the stroke length is so short, the vorticity generated by the interaction of the supply channel and jet 'pipe' exerts considerable influence on the jet flow and the effects of separation at the channel-pipe junction have little chance to attenuate prior to exiting into the cross-flow Walters and Leylek

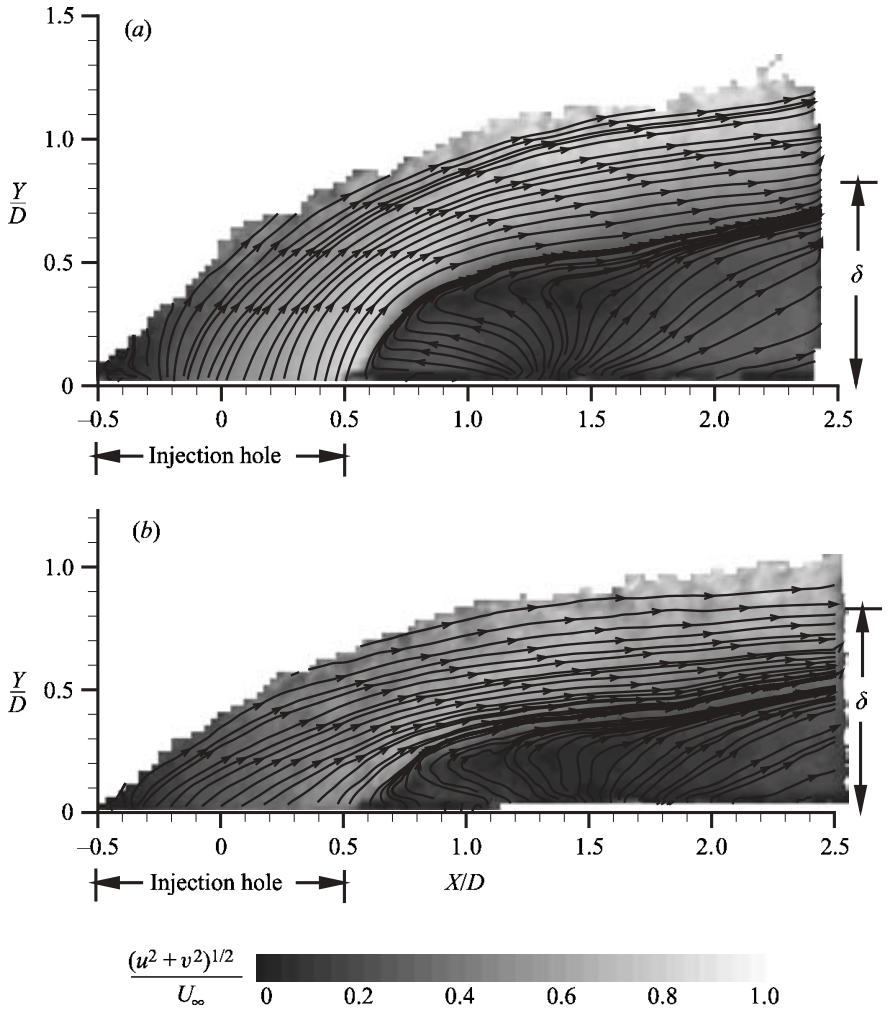

Figure 6.12 – Trajectory of two different supply configurations of jets in cross-flow with $R = 0.5$, from Peterson and Plesniak (2004). The jets are emitted from a 'short' hole – of length $l = 0.66d_J$ such that fully developed flow is not established in the supply 'pipe' – with the direction of flow of the underlying supply channel having a marked effect on trajectory. Figure (a) is supplied by a co-flowing channel; and, figure (b) is supplied by a counter-flowing channel with respect to the free stream direction. The cross-flow boundary layer height, δ, is marked, where $\delta/d_J = 0.83$.

(1997). These effects become more significant with decreasing stroke ratio Walters and Leylek (1997).

Figure 6.12 provides a comparison of the jet trajectory and velocity fields for the two orientations of supply channel for $R = 0.5$. In plot (a) – the co-flowing

case, the vertical velocity component is much stronger, consistent with a stronger CRVP within the jet pipe, which translates to higher trajectory compared to the counter-flowing case in plot (b). Thus, the configuration of the jet supply – particularly the stroke ratio – directly influences the jet structure and trajectory, which in turn determine the levels of jet to cross-flow boundary layer interaction and hence entrainment of fluid close to the wall.

Studies of the influence of jet velocity profiles on the jet to cross-flow interaction (see, for example, Cambonie et al., 2013; Muppidi and Mahesh, 2005; New et al., 2006) provide contrasting results. New et al. (2006) report that for $J = 2.3$, the parabolic profile has weak penetration into the cross-flow and the formation of shear layer vortices occurred only on the leeward shear layer; in contrast, the top-hat profile had greater free stream penetration and shear layer vortices formed both on the windward and leeward shear layers for the same velocity ratio. New et al. relate these findings to the thickness of the jet boundary layer and consequent levels of vorticity formed in each profile. However, Muppidi and Mahesh (2005) find that for jets with same velocity ratio (the two cases presented were for $R = 1.5$ and $R = 5.7$), parabolic profiles penetrate further into the cross-flow than top-hat profiles. Muppidi and Mahesh (2005) and Cambonie et al. (2013) also compared jet trajectories with varying cross-flow boundary layer thickness for constant velocity ratios and found that when the boundary layer is thicker the jet penetrates deeper into the cross-flow and vice versa. Muppidi and Mahesh attributes this behaviour to the fact that thinner boundary layers have more momentum close to the jet exit which acts to increase the curvature of the jet trajectory.

This author has yet to discover a study of jets in cross-flow over a surface with explicitly imposes either a favourable or adverse stream-wise pressure gradient. If

any mention is made of the pressure gradient of the investigation (e.g. Fric and Roshko, 1994; Moussa et al., 1977) then it is to state that the experiment was performed with a zero or near-zero pressure gradient setup. Because the present study is somewhat unique in its application of jets in cross-flow to the non-linear variation in static pressure on the surface of a circular cylinder, it is difficult to avoid addressing this point. The jet location, $\phi = \pm 65°$, marks the angular position on the cylinder surface just prior to point at which the minimum static pressure is experienced. In that sense it enters a favourable pressure gradient, however a short distance downstream of approximately $5° \leqslant \phi \leqslant 10°$, equivalent to $8.7d \leqslant x \leqslant 17.4d$, the static pressure begins to rise (see, for example, Achenbach, 1968) and, as the interacting jet and cross-flow fluid is swept downstream, it will enter an adverse pressure gradient until finally separating from the cylinder surface. With reference more broadly to the literature on hydrodynamic stability (e.g. Drazin and Reid, 2004; Stuart, 1963), it is assumed that the initial phase of the jet and cross-flow interaction is somewhat stabilised by the favourable pressure gradient and in the short region after entering the cross-flow, the topological formation would be analogous to the widely reported studies in the literature. It can similarly be assumed that as the flow progresses through the adverse pressure gradient, the destabilising effect on the flow would alter the structural and mixing properties of the jet and cross-flow fluid interaction – making it increasingly likely for coherent structures to breakdown and lead to laminar-turbulent transition of the flow.

6.5.4 Outline of experimental approach

A hot-wire analysis was conducted on the $z_J = 20mm$ cylinder to establish some characteristics of the perturbation imparted on the flow by the passive jets and to ascertain whether similarities could be found in this specific case – from a transverse jet located in a favourable pressure gradient on the circumference of a circular cylinder – in comparison to the literature for jets in cross-flow on flat plate. Identifying and characterising an upstream instability – arising from the introduction of jet fluid into the boundary layer – could enable it to be traced to an influence on boundary layer dynamics downstream, which may provide further insight into the effectiveness and considered application of passive jets as a drag reducing method.

As was established in section 6.3 with the acquisition of the jet flow velocity, the approximate jet-to-cross-flow velocity ratio for the passive jets was in the range $0.07 \leqslant R \leqslant 0.41$. While acknowledging that the instability sampled by Megerian et al. could be very different from that anticipated in the present study (as discussed in section 6.5.1), as a starting point the data of Megerian et al. (2007) was extrapolated to provide an estimate of the shear layer instability frequency for the present experimental setup. The data of Megerian et al. was for $R > 1$, however, extrapolating the consistent trend of St v. R for $1.0 < R < 3.5$ would suggest an equivalent Strouhal number for $R = 0.5$ in the range $0.3 < St < 0.4$.

The hot-wire was positioned very precisely using a three component traverse capable of moving with a spatial resolution of $0.1mm$. An oscilloscope display of the hot-wire signal was used to help position the wire in locations where the signal of interest could be identified. The instability was to be found very close to the cylinder surface, above and slightly downstream of the trailing edge of the jet exit

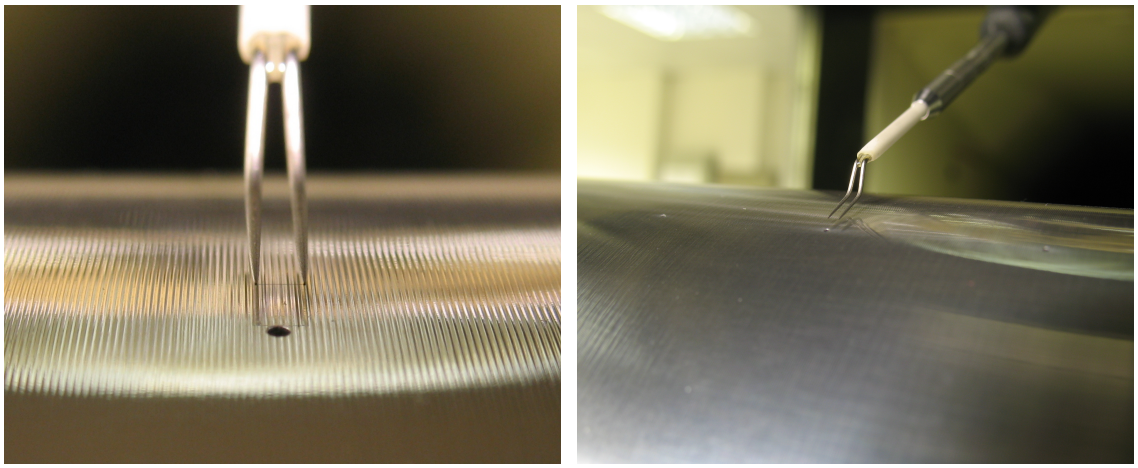

Figure 6.13 – Photos taken from experimental setup showing the approximate acquisition position of the boundary layer hot-wire probe used to detect the shear layer instability emanating from the jet exit hole.

hole (see Figure 6.13).

As the flow speed was increased or decreased, very small adjustments were made to the hot-wire position to maintain signal detection. It became particularly difficult to obtain a strong and consistent signal detection in the higher ranges of Reynolds number; the reduced thickness of the boundary layer (within which the jet emission was assumed to be contained – see Figure 6.7) and increased dynamic pressure on the hot-wire probe made it very difficult to position the hot-wire within the detection region of the jet instability and prevent it from touching the cylinder surface.

As shown in Figure 3.4, the wall thickness of the cylinder was $12mm$, providing a stroke ratio for the passive jets of $l/d_J = 24$. The spectral analysis was conducted over the testing range of Reynolds number outlined in section 2.1.3. For further details of the experimental setup used to acquire the data in this section see section 3.7.2.

6.5.5 Results and discussion

The hot-wire experiments performed in the immediate vicinity of a jet exit hole identified a very high frequency flow instability. This high frequency instability was first detected at $Re_D = 1.03 \times 10^5$, as shown in the periodogram (plot of power spectral density (PSD)) in Figure 6.14(a). The PSD estimate was calculated using the method of Welch (1967) and reveals a periodic instability of $10,664Hz$ followed by a standing wave at $\approx 12kHz$. This standing wave appears consistently in the PSD calculation of all datasets acquired during these experiments. With increasing free stream velocity, there is an increase in appearance and prominence of this and further standing waves – found at approximately $29kHz$, $48kHz$ and $57kHz$ – in the PSD trace as additional modes ($48kHz$ appears as a fourth harmonic of $12kHz$, and $57kHz$ as a second harmonic of $29kHz$) are excited (see Figure 6.15, Figure E.1, and Figure E.2). The source of these standing waves is thought to be attributable to the natural harmonics of the jet supply and exit holes which, as a cylindrical channels drilled through solid aluminium walls, effectively take the form of open ended 'pipes' to produce very high frequency standing waves. Applying the geometry of the jet 'pipes' to the calculation of harmonics for open-ended cylindrical pipes (which can be found, for example, in Benade, 1959), and allowing for additional end-effect corrections (see Benade, 1960; Wolfe and Smith, 2003), numbers very close to these standing waves are found. The influence of these standing waves made extracting the instability frequency of interest from the data somewhat problematic where the the two frequencies would closely coincide and unfortunately a solution to attenuating these standing waves during acquisition was not found.

Figure 6.14(b) presents the the periodogram of the instability found at $Re_D =$

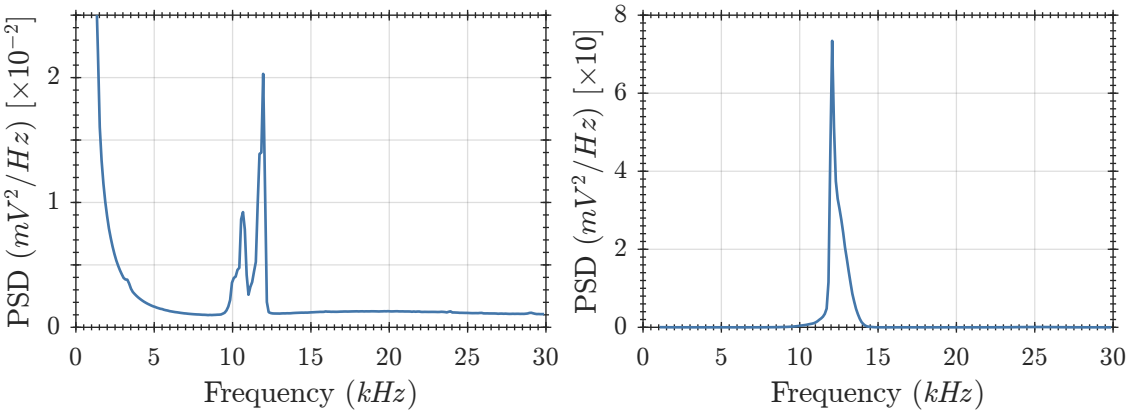

Figure 6.14 – Periodogram of the lowest Reynolds numbers (uncorrected for blockage) for which the jet instability was detected: (a) $Re_D = 1.03 \times 10^5$, the PSD peak at $10.7kHz$ represents the lowest Re_D for which the instability was detected, coupled here with a standing wave of $12kHz$; (b) $Re_D = 1.16 \times 10^5$, the power of the periodic jet instability is overshadowed by the same standing wave of $12kHz$ observed in figure (a).

1.16×10^5 – note that as the trace descends to the right of the peak there is a slight bulge and change of gradient, leading to a buttress-shaped broadening at the base of the spike. Here the sharp peak of the $12kHz$ standing wave found in Figure 6.14(a) and the broader-band peak generated by the shear layer instability – which occurs at a slightly higher frequency – agglomerate to form a single spike in spectral power, covering a wider band of frequencies. This occurs because the method used to calculate the PSD reduces the variance of the periodogram at the expense of spectral resolution to effectively smooth the PSD output. This involves sectioning the time-series data signal into discrete segments which are multiplied by a symmetrical Hamming window to reduce discontinuities in the finite time-series and overlapped to prevent the loss of signal information; periodograms are taken of each overlapped, windowed segment and these modified periodograms are averaged

to produce the final PSD estimate (Welch, 1967). The algorithm used to identify peaks in the PSD trace does so on the basis of gradient change and as such, when a periodic instability has a frequency close to that of a standing wave, the averaged PSD output is effectively biased towards standing wave. The broadband nature of the signals generated by the shear layer instability meant that reduced segmentation of the time-series improved separation of the standing waves from the instability but the increased variance made it difficult to isolate the instability from a noisy spectrum. Fortunately, in all the datasets collected during these experiments, the standing waves interfered in the estimation of only two instability frequencies which were necessarily omitted from trend analyses (as shown in Figure 6.18).

Confirmation that the instability emanated only from the jet exit holes was established by acquiring data between the jet exit holes where only the resonant frequencies of the standing waves produced by the jet exit holes were found on the Fourier transform trace (Figure 6.15). The hot-wire was positioned such that all spatial coordinates were identical to those used to acquire the instabilities found to emanate from the jet exit hole, except for the span-wise (z) coordinate. The hot-wire was traversed in z until it reached a position equidistant from two adjacent jet exit holes and data was acquired using the same procedure. Figure 6.15 shows that the standing waves found above the jet exit holes are also found between the jet exit holes, however the periodogram does not provide any notable evidence of another regular fluctuation in the flow velocity – as is found in the signal acquired within the immediate vicinity of the jet exit holes. It can therefore be concluded that the broadband frequency peaks – found in the PSD of the hot-wire signal acquired above the jet exit holes – are as a direct result of the instability generated by the interaction of the passive jets and cylinder cross-flow.

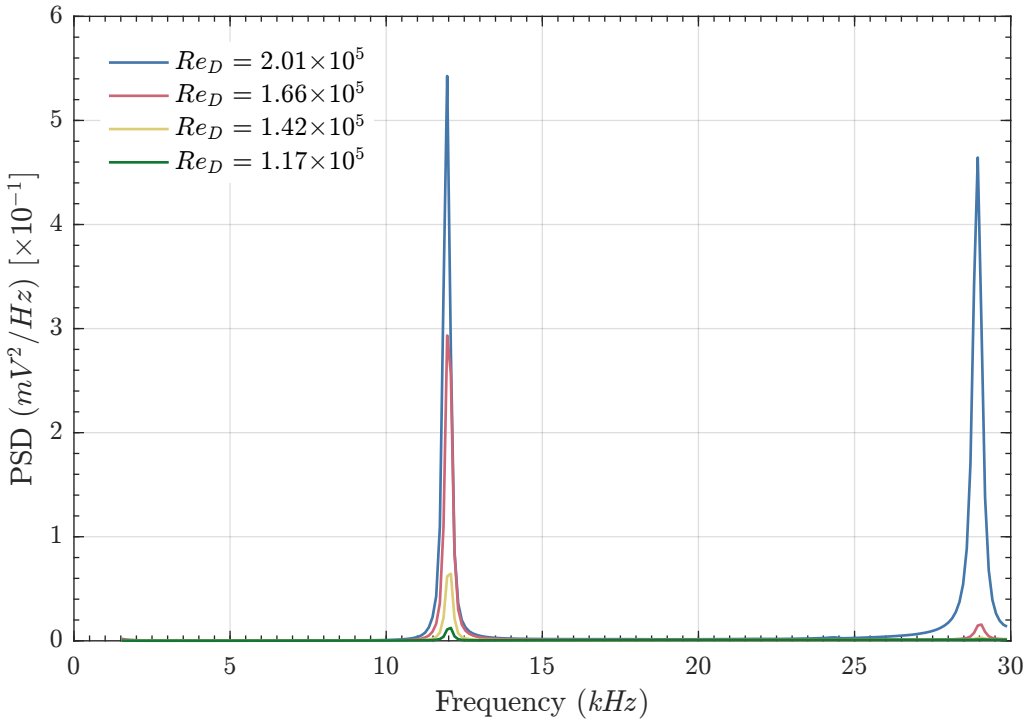

Figure 6.15 – Periodogram of hot-wire signal acquired at a span-wise location between two jet exit holes, just above the surface of the cylinder.

Figure 6.15 also clearly indicates the relationship of increasing Re_D with the appearance and rising prominence of the standing waves; the standing wave at $29kHz$ only appears with $Re_D \geqslant 1.66 \times 10^5$ and dramatically increases in prominence with increasing Re_D through the range $1.66 \times 10^5 \leqslant Re_D \leqslant 2.01 \times 10^5$. This correlation adds to the difficulty of identifying and extracting the instability frequencies of interest since the ability to pick up a strong signal from the jet instability diminishes with increasing Re_D; the reduction in thickness of the boundary layer (within which the jet emission was largely contained) and increased dynamic pressure on the hot-wire probe made it very difficult to position the hot-wire within the detection region of the jet instability at high Re_D. The data collected at higher flow speeds therefore resulted in periodograms where the standing waves would dominate the PSD in

comparison to the weak signals for periodic vortex shedding. This issue is highlighted by the periodograms of Figure E.1 and Figure E.2 which can be found in Appendix E.

Figure 6.16 collates periodograms of the hot-wire data acquired in the immediate vicinity of the passive jet showing a clear trend of increasing hairpin-vortex shedding frequency with increasing Re_D in the range $1.28 \times 10^5 \leqslant Re_D \leqslant 2.36 \times 10^5$. The previously referenced periodograms of Figure E.1 and Figure E.2 were omitted from this figure due to the lack of clarity in the PSD brought about by the dominance of the aforementioned standing waves, however they still contain valid data which correlates with the trend shown in Figure 6.16 and can be viewed in Appendix E. An evident feature of the periodograms of Figure 6.16 is that they all produce broadband PSD peaks which are in contrast to the sharp spikes generated by the standing waves (Figure 6.16(a), Figure 6.16(b)). This indicates that the periodicity of the hairpin vortex shedding was somewhat inconsistent – varying over a frequency band above and below the most consistently detected (PSD peak) value – over the duration of the data acquisition period.

Investigating this aspect further, repeat datasets of two different flow speeds – which were repeated with identical setup and acquisition parameters on different days – were plotted together. Due to a change in atmospheric pressure, the repeat experiments were conducted with different air densities, thus affecting Re_D where all other parameters remained largely unchanged. The resulting plot (Figure 6.17) appears to suggest that the jet instability frequency correlates with Reynolds number, Re_D, rather than flow velocity, U_∞. As shown in Figure 6.4 the relationship between $\overline{Re}_J$ and Re_D is linear through $1.6 \times 10^5 \leqslant Re_D \leqslant 2.7 \times 10^5$ which covers the Re_D range of hairpin vortex detection. Accordingly, it can be postulated that for passive transverse jets positioned $\phi = \pm 65^\circ$ on a circular cylinder, the shedding

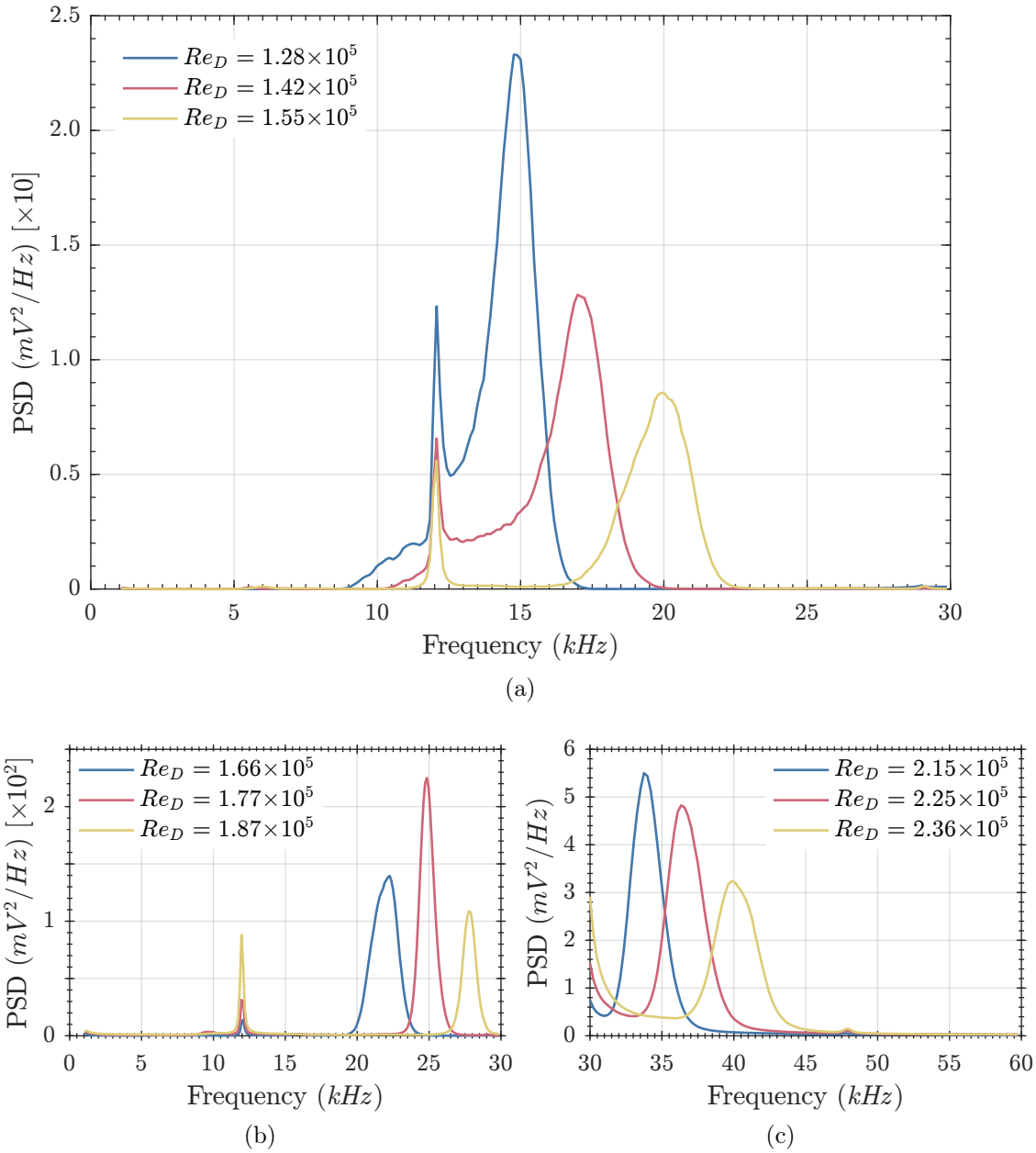

Figure 6.16 – Periodograms of hot-wire signals acquired in immediate vicinity of a passive jet exit hole, indicating the frequency bands of shear layer instabilities detected over the range: (a) $1.28\times10^5 \leqslant Re_D \leqslant 1.55\times10^5$; (b) $1.66\times10^5 \leqslant Re_D \leqslant 1.87\times10^5$; (c) $2.15\times10^5 \leqslant Re_D \leqslant 2.36\times10^5$.

frequency of hairpin vortices correlates with the jet Reynolds number – as found by Sau and Mahesh (2008) for jets in cross-flow at low R.

For these experiments, the PID controller for the wind tunnel was set to control and maintain U_∞, rather than Re_D. The acquisition duration for each of these experiments was 4min:40sec and so it was checked whether, over the course of one test run, a change in flow temperature might affect Re_D sufficiently to be responsible for the wide spread in shedding frequencies. An analysis of the datasets showed that for each run there is a consistent drop in Re_D throughout the duration of data acquisition, but that this drop (owing to an increase in flow temperature) was insignificant in low velocity runs ($\Delta Re_D = 0.02\%$ for $Re_D = 1.28 \times 10^5$, Figure 6.16(a)) and relatively small in high velocity runs ($\Delta Re_D = 0.61\%$ for $Re_D = 2.36 \times 10^5$, Figure 6.16(c)). This compares with $\Delta Re_D = 2.77\%$ and $\Delta Re_D = 2.89\%$ accounting for the mean shedding frequency discrepancies of $\Delta f = 3.77\%$ and $\Delta f = 2.11\%$ for $U_\infty = 28m/s$ and $U_\infty = 30m/s$, respectively, in the datasets plotted in Figure 6.17. While viewing Figure 6.16(b) it is interesting to note, however, that noticeably narrower-band peaks such as those for $Re_D = 1.77 \times 10^5$ and $Re_D = 1.77 \times 10^5$ have a lower drift of Re_D during acquisition ($\Delta Re_D = 0.20\%$ and $\Delta Re_D = 0.16\%$, respectively) compared to a broader-band peak such as that for $Re_D = 1.66 \times 10^5$ ($\Delta Re_D = 0.39\%$). It is therefore likely that the way the data was collected in these experiments has lead to a slightly larger spread (broader frequency band) of the PSD peaks found for the shear layer instability than would be obtained by fixing Re_D to compensate for temperature or atmospheric changes during acquisition. Future experiments aiming to capture this phenomena should design the wind tunnel speed controller accordingly, however the changes in Re_D found here over the course of acquisition clearly do not account for the entire spread in the frequency band of the

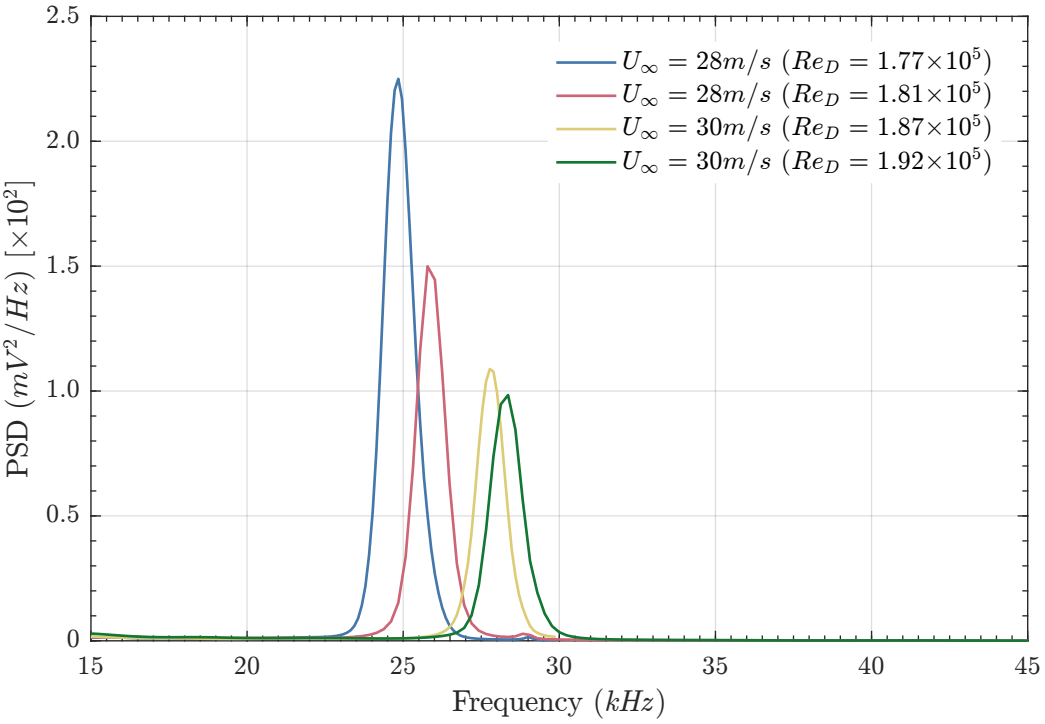

Figure 6.17 – Periodogram showing variation of jet instability frequency found at constant free stream velocity, U_∞, but varying Reynolds number, Re_D.

detected instability.

In section 5.2 it was mentioned that a periodic pressure oscillation occurs around the surface of a cylinder subject to the typical Kármán vortex shedding of a pre-critical flow regime. It is also true of a plain circular cylinder from the TrSL regime through the post-critical regime that regular static pressure fluctuations occur on the cylinder surface, even when Kármán vortex shedding ceases, however the magnitude of Cp' reduces with increasing Re_D with the onset of the critical regime (see, for example, James et al., 1980; Norberg, 2003). In the case of a cylinder modified to disrupt or suppress vortex shedding such as the model studied here, there will similarly still exist pressure fluctuations in the near wake which will translate to static pressure fluctuations around the surface of the cylinder where the flow re-

mains attached – and particularly in the region $50^\circ \leqslant \phi \leqslant \phi_s$ (where ϕ_s is the angle of separation) for $Re_D \leqslant 2.7 \times 10^6$, as shown by James et al. (1980). It is likely, therefore, that the pressure difference, ΔC_p, between $\phi = 0^\circ$ and $\phi = \pm 65^\circ$ continually fluctuates with constant Re_D. This pressure difference controls the jet velocity and thus it can be assumed that there is a fluctuating component of jet Reynolds number, Re'_J, around the mean jet Reynolds number, $\overline{Re}_J$. Further assuming that the shedding frequency of the hairpin vortices is fairly constant for a fixed Re_J, it is proposed that Re'_J reasonably accounts for the resulting fluctuation and spread in hairpin vortex shedding frequency; hence the broadband PSD peaks found in the periodograms.

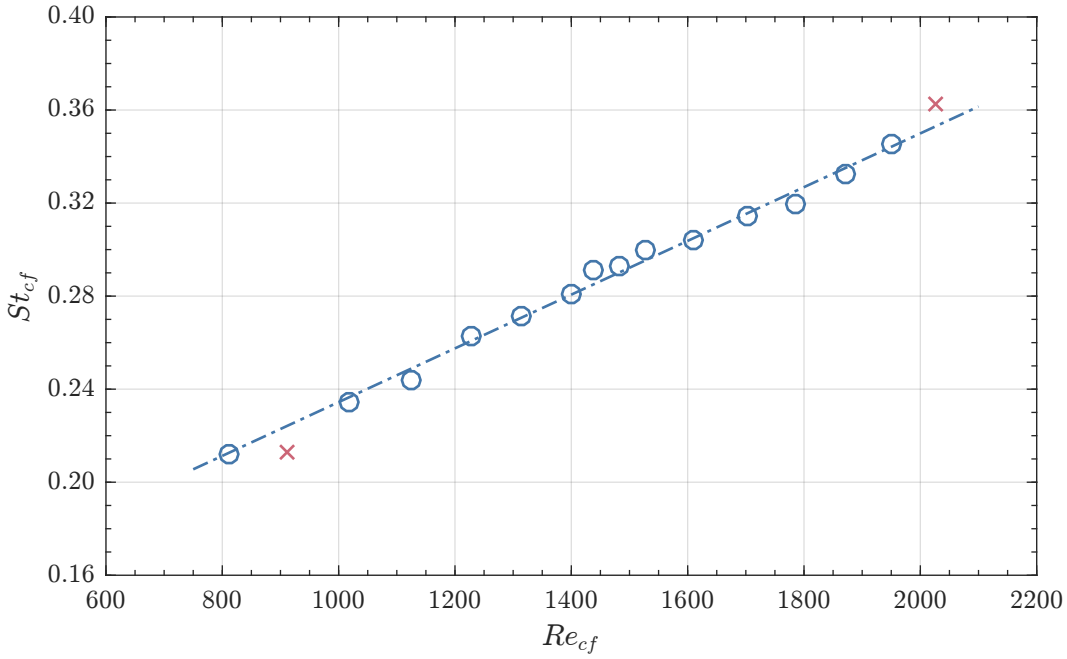

Figure 6.18 – Variation of Strouhal number, St_{cf} (based on the mean cross-flow velocity, U_{cf}, at $\phi = \pm 65^\circ$), for the detected passive jet instability with cross-flow Reynolds number, Re_{cf}. The second and last values of the recorded instability frequency – shown as red crosses, at $Re_{cf} \approx 910$ and $Re_{cf} \approx 2,030$ respectively – were omitted from the linear trend line calculation due to the interference of standing waves which bias the PSD power towards the frequencies at which they occur.

The shear layer instability frequency appears to increase linearly with Re_D and consequently, from Figure 6.3, also with Re_{cf} – as shown in Figure 6.18. The linear trend line added to Figure 6.18 was calculated using all but the second and last values (with respect to increasing Re_{cf}) of the recorded jet instability frequencies – owing to the bias created by the standing waves at $12kHz$ and $48kHz$ (as shown in Figure 6.14(b) and Figure E.2) – but these values have been included on the plot (red crosses) to show that it is likely that without the skewing of the PSD output they would continue the linear trend established by the rest of the dataset. When scaled with the jet hole diameter, d_J, and either the local cross-flow or jet velocity, U_{cf} or v_J respectively, the values found here for the non-dimensional frequency (Strouhal number) of the detected instability appear to correlate well with those found in the literature for hairpin vortex shedding from jets in cross-flow over flat plates (see, for example, Ilak et al., 2012; Lim et al., 1992), and also seem to fall reasonably into the aforementioned range of values extrapolated from Megerian et al. (2007) for shear layer instabilities at higher R.

In contrast, the relationship between the Strouhal number of the shear layer instability, St_{v_J}, (based on mean jet velocity, v_J, and jet exit diameter, d) and jet Reynolds number, Re_J, is not so cogent, as shown in Figure 6.19. As Re_J increases there appears to be a general trend of increasing St_{v_J}, however the trend is discontinuous and inconsistent; there are several pairs of points for which an increase in Re_J corresponds either with an insignificant rise or drop in St_{v_J}. It should be noted at this point that for the passive jets of these experiments it is impossible to decouple Re_J from Re_{cf}; as Re_{cf} increases so too must Re_J, but as has already been shown (Figure 6.4), the relationship is not strictly linear – the range of Re_J which conforms most closely to a linear trend with Re_{cf} may alternatively be perceived

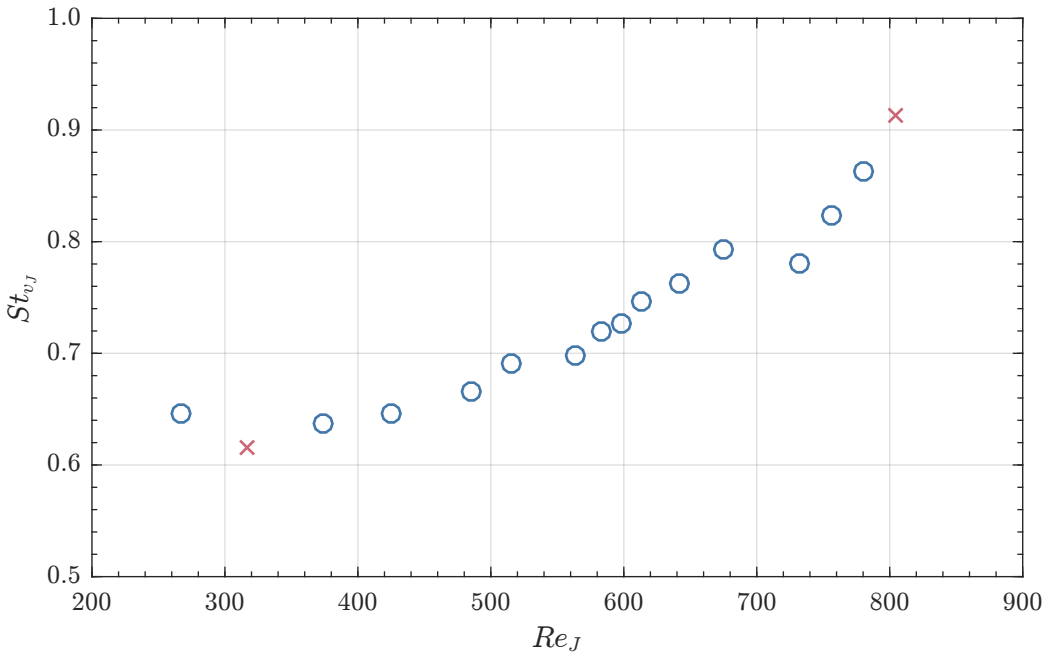

Figure 6.19 – Variation of Strouhal number, St_{v_J} (based on the mean jet velocity, $\overline{v}_J$, and jet exit hole diameter, d) for the detected passive jet instability with jet Reynolds number, Re_J. Red crosses refer to acquisitions of instability frequency which were subject to standing wave interference.

as a curve with a gradually declining gradient (see Figure 6.6 and discussion in section 6.3). As such, an increase in Re_J corresponds with a non-linear change in the jet to cross-flow velocity ratio, R, which many previous studies have shown to have had a significant impact on the shear layer instability.

As mentioned in section 6.5.2, the stability analysis of a DNS simulation of jets in cross-flow at low R by Ilak et al. (2012) first found evidence of a sustained, periodic hairpin vortex shedding cycle at $R = 0.338$. Plotting St_{cf} v. R for this research (Figure 6.20) reveals a remarkably similar value of R for the first detection of the jet shear layer instability, at $R = 0.329$. It should be noted here again that the value for the cross-flow velocity – used to calculate R – is an estimation based on the extrapolation of data acquired in these experiments, rather than a directly

measured value. Limited by the jet 'pipe' inflow profile (Poiseuille flow at the jet exit without any inlet 'pipe' geometry considerations) and length of calculation domain, Ilak et al. (2012) were also candid on the exactitude of their experimental modelling; they state a number of times that their analysis of the shedding mechanism should prove to be correct qualitatively, but perhaps not precise quantitatively. Thus, the coincidental matching of values here does not preclude the hairpin vortex shedding phenomena from occurring, for example, at lower values of R – as in the study of $R < 0.2$ jets in cross-flow from rectangular slots by Acarlar and Smith (1987*b*).

Ilak et al. (2012) also note the development of hairpin vortices as transient features which occur when $R < 0.338$, and may persist for some time, but ultimately decay to leave a stable, steady vortex system. The fact that the signal detected for $R = 0.329$ was very weak in comparison with the that of the next acquired signal at $R = 0.347$ (see Figure 6.14) may indicate that the shedding is periodic but transient and that increasingly persistent shedding occurs at slightly higher R where the signal detection is stronger and more closely matches the limit cycle definition of Ilak et al. (2012).

Figure 6.20 shows that, unlike Megerian et al. (2007) for jets in cross-flow with $R \geqslant 2$, the data in this study does not produce a coherent correlation between the frequency of the shear layer instability and the jet to cross-flow velocity ratio. There was no data for the boundary layer momentum thickness to use as a scaling factor and make a more considered comparison with Megerian et al.'s (2007) findings, however it is thought that the variation in δ_θ for the cluster of data points around $R = 0.40 \pm 0.01$ – for which there is such disparity for relatively small variations in Re_{cf} – would unlikely be enough to realign the data into a compelling trend. Further work is requied to confirm this, but it would not be unexpected given the

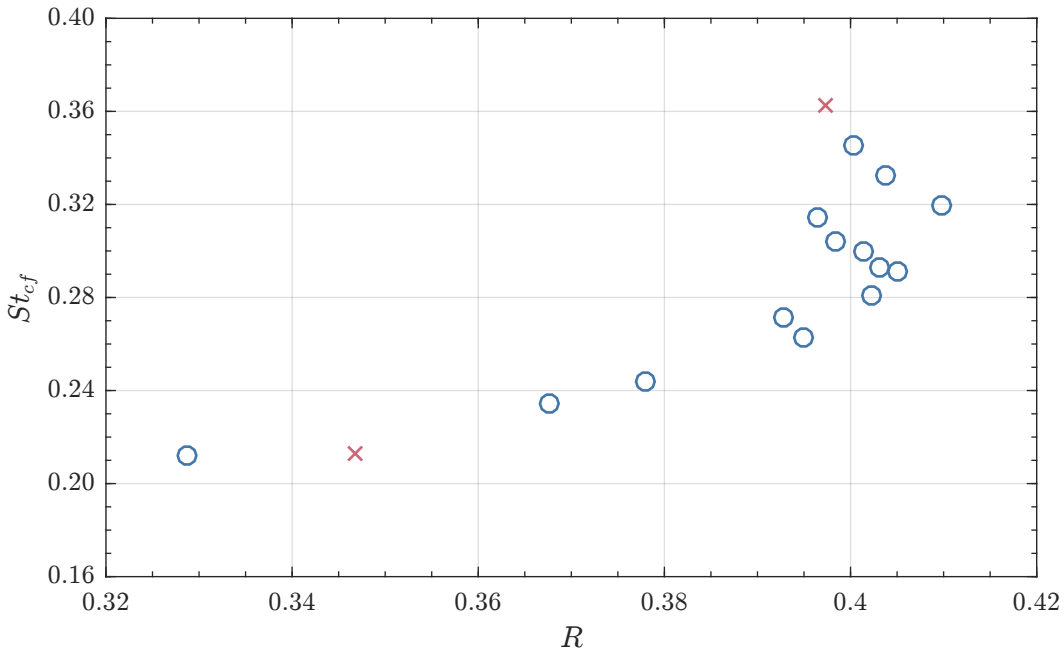

Figure 6.20 – Variation of Strouhal number, St_{cf} (based on the mean cross-flow velocity, U_{cf}, at $\phi = \pm 65°$ and the jet exit hole diameter), for the detected passive jet instability with jet to cross-flow velocity ratio, R. The first detection of the jet shear layer instability occurred at $R = 0.335$, with a Strouhal number of $St_{cf} = 0.212$. Red crosses refer to acquisitions of instability frequency which were subject to standing wave interference.

differences in flow mechanisms between high and low R jets in cross-flow already discussed in section 6.5.1.

The findings of this set of experiments on the instability of the jet shear layer suggest that, as per Ilak et al. (2012), a minimum or critical value of R must first be met before a periodic instability is generated by the jet and cross-flow interaction, namely the formation of hairpin vortices through the interaction of vorticity generated in the boundary layers of the jet 'pipe' and oncoming cross-flow. Raising the value of R slightly again reinforces the hairpin shedding process so that it becomes more persistent and a regular, periodic shedding of hairpin vortices becomes the dominant feature of the jet-cross-flow interaction. With the hairpin vortex

formation and shedding process established, and the value of R maintained above the critical level (in the range $0.329 \leqslant R \leqslant 0.410$ for this set of experiments), the Strouhal number of the vortex shedding is a linear function of the cross-flow Reynolds number, Re_{cf}. In other words, the jet to cross-flow velocity ratio controls the condition by which the hairpin vortices are formed – by adjusting the ratio of vorticity generated at the boundaries of the jet and cross-flow, respectively – and the Reynolds number of the cross-flow determines the rate at which these vortices are shed downstream. This contrasts with the findings by Sau and Mahesh (2008) who state that the hairpin shedding frequency was dependent on Re_J, though no presentation of this data is given. The findings here concur somewhat with the findings of Acarlar and Smith (1987*b*); they show that the roll-up frequency is linked to the cross-flow Reynolds number, but they also find that for constant cross-flow velocity an increase in jet velocity (i.e. an increase in R) also provides a linear increase in the frequency of hairpin formation. The influence of Re_J on shedding frequency cannot be discounted completely here because of the inherent coupling with Re_{cf}, but St formed a far more cogent relationship with Re_{cf} throughout these experiments and therefore appears to exert a more direct influence on shedding frequency.

With the low values of R found in these experiments, it is expected that the jet trajectory is sufficiently shallow for the majority of jet fluid to be maintained within the boundary layer for several jet diameters downstream of exit into the cross-flow (Figure 6.7). Once a critical value of R is reached, the jet to cross-flow interaction provides a continuous supply of hairpin vortices within the boundary layer which are swept downstream, stimulating mixing between the high-momentum fluid of the outer-flow and the retarded boundary layer flow; thus, by entrainment of high momentum fluid towards the wall, the boundary layer is energised and local flow

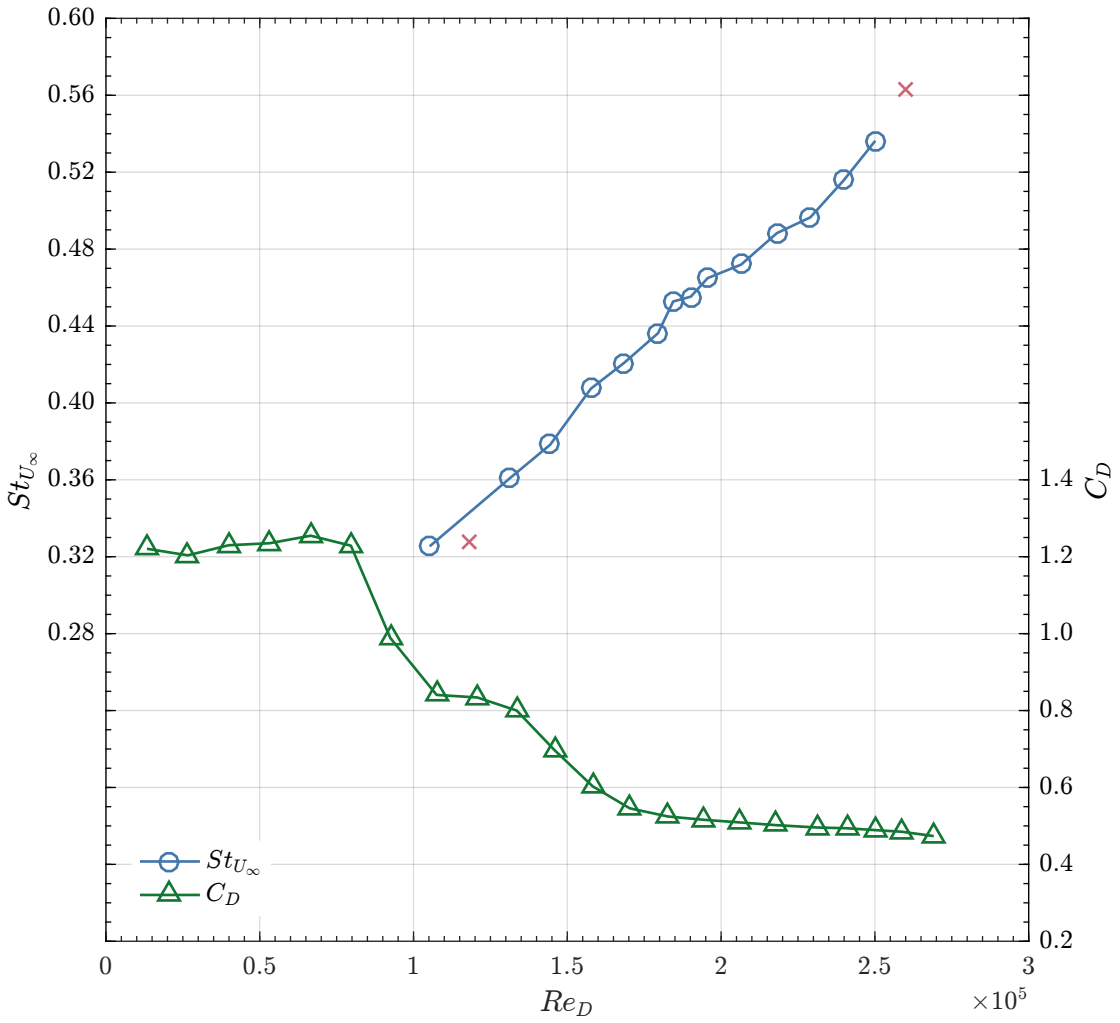

Figure 6.21 – Variation of jet instability Strouhal number, St_{U_∞} (based on the mean free-stream velocity, U_∞, and the jet exit hole diameter), and cylinder drag coefficient, C_D, with free-stream Reynolds number, Re_D. All detections of hairpin vortex shedding from the jet-cross-flow interaction coincide with a reduction in C_D. As in previous plots of St, red crosses refer to acquisitions of instability frequency which were subject to standing wave interference.

separation is delayed.

Figure 6.21 displays the correlation between the detected occurrences of hairpin vortex shedding and drag coefficient of the cylinder, C_D, throughout the testing range of free-stream Reynolds number, Re_D. For every detection of the shear layer

instability there coincides a drop in C_D, however the opposite is not the case; for the initial drop in C_D between $8 \times 10^4 < Re_D < 9 \times 10^4$, there was no detection of the dominant instability found for $Re_D \geqslant 1.05 \times 10^5$. This indicates that, with the application of passive jets, a drop in C_D does not presuppose the shedding of hairpin vortices from the jet to cross-flow interaction, and hence there is a modification of the flow prior to the generation of hairpin vortices which precipitates the initial C_D reduction. Alternatively, with the data available, it cannot be disputed that the drop in C_D simply occurs prior to the first detection of an instability emanating from the jet to cross-flow interaction on that particular side of the cylinder. As was shown previously in Figure 5.8(b), a change in C_L consistently occurs with the onset of C_D reduction; this asymmetry may be, for example, as a result of hairpin vortices being shed from jet holes on one side of the cylinder prior to the side over which the hot-wire was placed.

Without a more extensive investigation of the instabilities arising from the jet and cross-flow interaction in the Re_D range coinciding with the onset of C_D reduction, it cannot be said with certainty from these investigations that weak or intermittent hairpin vortex formation does not occur for $Re_D < 1 \times 10^5$. It is possibly the case, however, that prior to the generation of the dominant shear layer instability with a critical value of R, the local disturbance created by the jet emission into the cross-flow – at the sensitive location of $\phi = \pm 65^\circ$ – may engender a local acceleration of the flow (Andreopoulos and Rodi, 1984) and hence slight span-wise variations in velocity even for very low v_J; encouraging small span-wise variations in flow separation may be the factor which precipitates the drop in C_D prior to the subsequent amplification of C_D reducing mechanisms by the generation of hairpin vortices.

Chapter 7

Transverse jets: Flow topology

7.1 Introduction

To gain a better insight into the mechanisms of the drag reduction generated by the passive jets, the flow visualisation method variously known as oil-streak, oil-film and here denoted surface-oil (SOFV), was employed around the region of flow separation. A mixture of oils and tracer particles are applied to the surface of the test model and the shear force of the flow acts on the mixture to form a time-averaged pattern of the unsteady flow by revealing the skin friction lines, which are tangent at each of their points to the local skin friction vector (Delery, 2011; JSME, 1988). From these patterns, the mean flow direction, vortex structures and lines of transition, separation and reattachment can be revealed. It is a technique which is particularly suited to high speed flows which generate a level of surface shear sufficient to move and shape the film of oil mixture at the surface. Higher speed flows also tend to aid evaporation of the oils and hence setting of the tracer particle patterns for photographing once the wind tunnel is switched off. For this

reason the analyses were conducted primarily at the upper end of the Re_D range of interest. For more details of the experimental setup and SOFV techniques used in this section, see section 3.6.

From the photographs and videos taken of the SOFV tests, schematics were produced to more clearly illustrate the skin friction line topology. These schematics were then interpreted using Critical Point Theory to determine the impact of the passive jets on the development of the boundary layer and flow separation.

According to Delery (2001), it was Legendre (1956) who introduced the basic concepts of Critical Point Theory to provide a rational framework to describe three-dimensional separation in the 1950s, however Perry and Chong (1986) state that Oswatitsch (1958) was the first to provide a systematic analysis of Critical Point Theory to determine three dimensional separation and reattachment. Lighthill (1963) clarified that the application of Critical Point Theory to viscous flows associates the continuous vector field to skin friction lines rather than streamlines lying just above the surface and Hunt et al. (1978) extended the application of Critical Point Theory to flow above the surface by applying the topological classification of critical points in three-dimensions. By examining the skin friction line pattern with Critical Point Theory, one is able to elicit possible solutions of the outer-flow topology and thus obtain a three-dimensional visualisation and better understanding of the flow physics. The analysis of skin-friction line patterns here, and the application of Critical Point Theory, was on the basis of following the topological rules as set out in the review papers by Tobak and Peake (1982), Perry and Chong (1987) and Delery (2001) which provide a thorough treatment of both the theoretical and mathematical principles. A detailed description of Critical Point Theory will not be covered here – the reader is referred to the aforementioned review papers – however, in order to

follow the schematics and descriptions of the SOFV tests found here, the following provides a basic overview of the relevant critical points and topological rules.

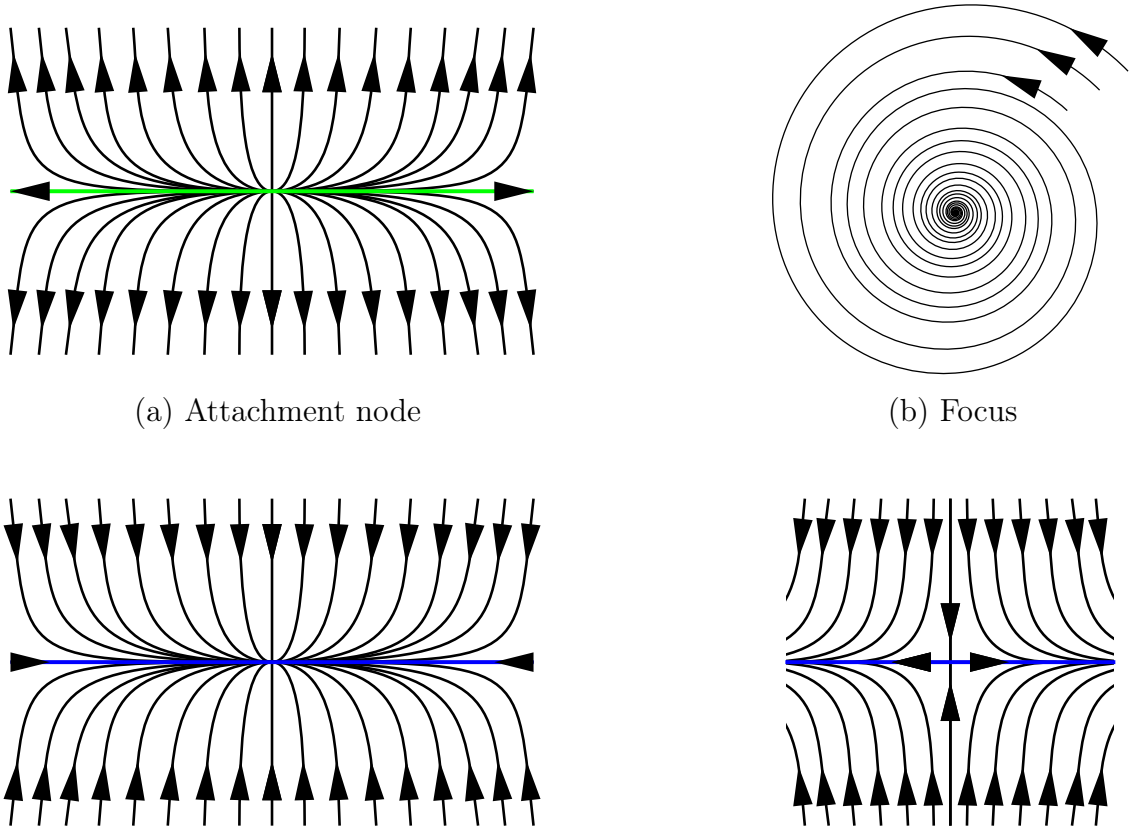

(a) Attachment node

(b) Focus

(c) Separation node

(d) Saddle point

Figure 7.1 – Classification of a selection of critical points; attachment line shown in green, separation lines (separatrices) shown in blue. Nodes and foci are topologically equivalent (they are either sources or sinks of skin friction lines); (b) is a focus of separation but line colouring is omitted here for illustrative clarity.

The type and number of critical points characterise the skin friction line pattern and therefore the three-dimensional flow topology above the body surface. Figure 7.1 provides illustration and classification of the different critical points. Nodal points, (a) and (c), are common to an infinite number of skin-friction lines which either diverge from it (attachment node, (a)) or converge upon it (separation node, (c)).

A nodal point of attachment, (a), is found at the stagnation point of a body and, for example, in areas of flow re-attachment. All but a single perpendicular skin friction line are tangential to a particular line which bisects a nodal point. For an attachment node, this is often described as an attachment line – a line from which all other skin friction lines diverge, and is shown in green. For a separation node, this is a line of separation and is also known as a separator or separatrix and these are shown in blue. A necessary condition for flow separation is the existence of a particular skin-friction line on which other lines converge (Tobak and Peake, 1982). The focus shown in Figure 7.1 (b), therefore also provides a point of flow separation; as explained by Perry and Chong (1982), the spiralling out of fluid from foci is necessary for continuity – any fluid which finds its way into the focus will be lifted from the surface. A saddle point, (d), comprises two perpendicular lines which pass through the critical point, with directions inward on one line and outward from the point on the other. The line whose direction is outwards from the critical point is a separatrix, the line upon which all other skin-friction lines converge. Apart from the two perpendicular lines, all other skin friction lines deviate from the saddle point in the direction of the adjacent perpendicular lines.

To create a topologically consistent skin friction pattern, skin friction lines must originate at a node and terminate either at a node or a focus (Delery, 2001). The topological rule for a three-dimensional body immersed in a flowing stream is that the sum of nodal points (which include foci) must exceed saddle points by two (Lighthill, 1963). It should be noted, therefore, that in the schematics presented in this section the nodal points of attachment far upstream and downstream of the area of analysis are omitted due to space constraints; however, when these points are included the schematics comply with the topological rules of Critical Point Theory.

7.2 Passive jets, $z_J = 20mm$

7.2.1 SOFV results

The photograph of an SOFV test of the $z_J = 20mm$ cylinder shown in Figure 7.2 clearly demonstrates that the passive jets have a profound influence on the boundary layer development and, consequently, on the cylinder wake formation. For this particular image $Re_D = 2.70 \times 10^5$ and the flow direction is approximately right to left – the jet emission holes on the right hand side of the cylinder surface, indicating the upstream portion of the cylinder surface, are clearly visible.

The bright white span-wise band downstream of the jet holes does not signify a feature of the flow; it appears as a result of the oil mixture overlapping onto an area of the cylinder surface which was untreated for viewing the SOFV (see section 3.6 for details); this simply means that there is a much higher reflectivity here compared to the treated viewing area immediately downstream. The foremost boundary layer separation occurs just downstream of the white band in gently sweeping lines between the jet exit holes, with a separation angle consistent with the laminar separation line of a plain cylinder tested separately at equivalent Re_D.

Flow separation downstream of the jet holes is significantly delayed, essentially partitioning the laminar separation line, and a repeating pattern of distinctive counter-rotating vortex pairs (CRVP) forms. Immediately downstream of these primary, strongly defined CRVP are a secondary set of repeating CRVP which appear more faintly and are less well-defined compared with the primary CRVP. When looking closely at Figure 7.2, one can make out the faint trace of reverse flow being funnelled towards the inner region between the two vortices of the secondary CRVP.

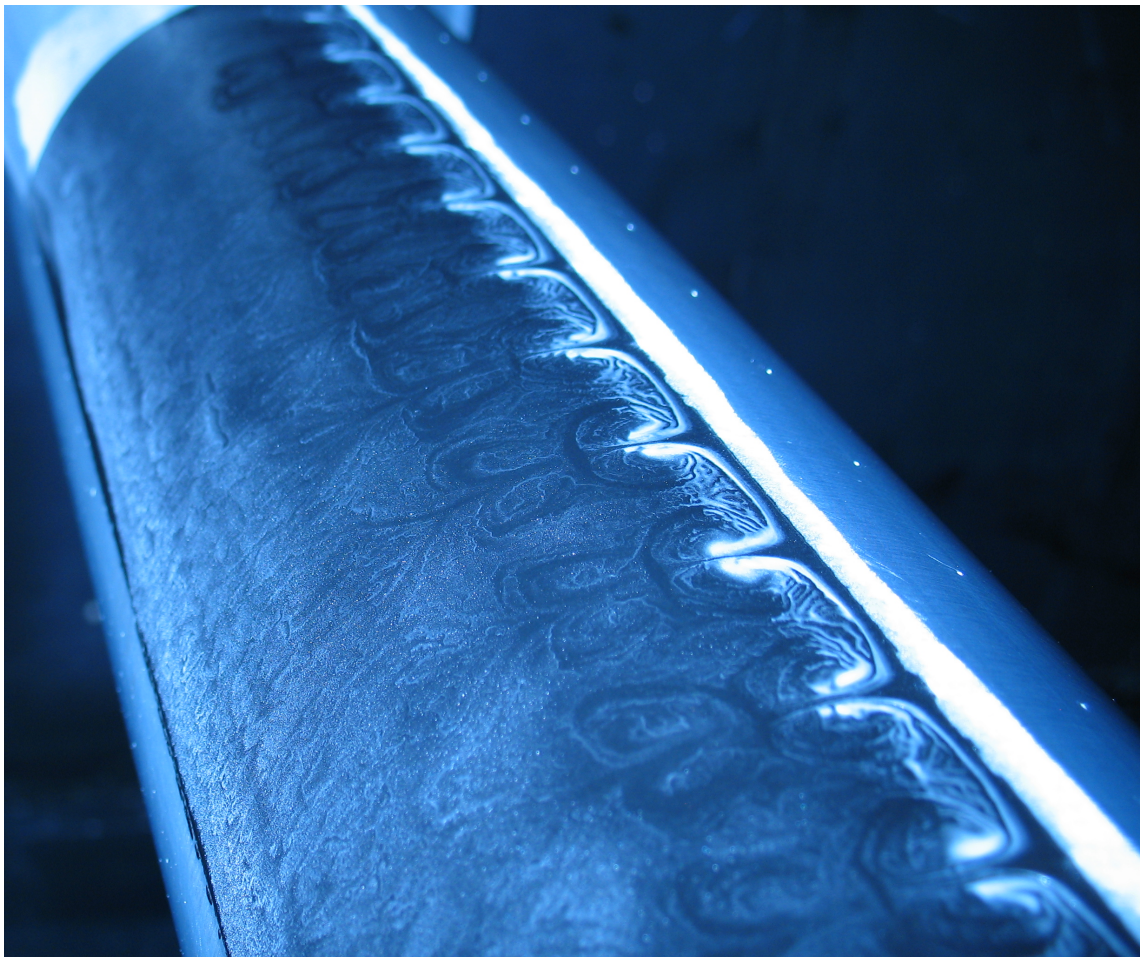

Figure 7.2 – Photograph of surface oil flow visualisation test showing time averaged surface streaklines downstream of the jet exit holes. A repeating pattern of counter-rotating vortex quartets (CRVQ) are clearly observed across the span. Test cylinder was the $z_J = 20mm$ spaced passive jets at $Re = 2.7{\times}10^5$. Free-stream flow direction is right to left.

Figure 7.3 clarifies this reverse flow region and also helps to illuminate some important characteristics of the flow; this photograph was taken after conducting a SOFV test at the same Re_D as Figure 7.2 but with only the rear-most (downstream) portion of the SOFV viewing area covered with oil solution. Once the wind tunnel was up to speed the skin friction of the reverse flow was sufficient to lift the oil mixture upstream and against gravity into the clearly displayed secondary CRVP, which take

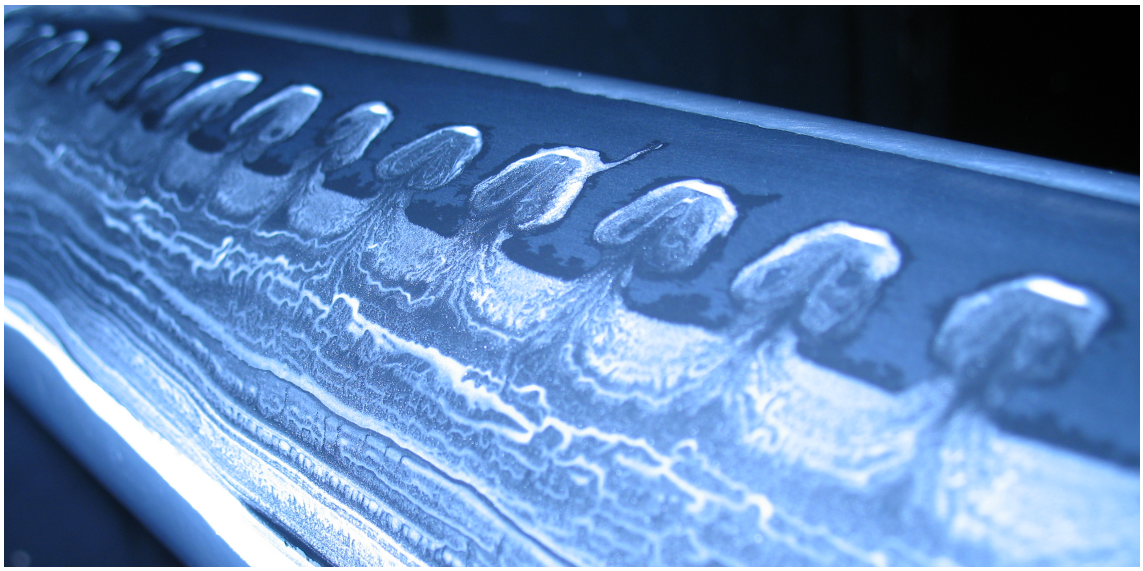

Figure 7.3 – Photograph of surface oil flow visualisation test showing time averaged surface streaklines of the well-defined mushroom-shaped secondary counter-rotating vortex pairs (CRVP) with reverse flow 'stalks' downstream of the jet exit holes. Test cylinder was the $z_J = 20mm$ spaced passive jets at $Re = 2.7{\times}10^5$. Free-stream flow direction is approximately right to left.

a distinctive mushroom-shaped appearance. Downstream of the 'mushroom' heads, the straightish span-wise lines of the upstream edges of the almost semi-circular, somewhat densely powdered, patches linking the 'mushroom' stalks marks the limit of the applied oil mixture prior to starting the wind tunnel. Once fluid from the base region is drawn into the secondary CRVP, it is largely limited from any further movement upstream and with a close look at Figure 7.3, one can identify a regular occurrence of tracer particle accumulation along the upstream edge of the 'mushroom' heads. This provides a clear identification of a point of flow separation. Less clear from this photograph is that the aforementioned semi-circular patches of tracer particle accumulation also identify areas of flow separation and this will be discussed in more detail later.

7.2.2 Interpretation of flow visualisation

From the interpretation of numerous photographs and videos of the surface-oil flow visualisation tests, schematics of the time-averaged skin friction line patterns were created to enable a clearer understanding and presentation of the flow topology above the cylinder surface. The schematics of Figure 7.4 and Figure 7.5 present two simplified arrangements of time-averaged skin friction line patterns for the separation region of the cylinder with passive jets spaced at $z_J = 20mm$ intervals. The schematics were drawn as span-wise repeatable patterns on a flat two-dimensional surface which can be interpreted as the unwrapped cylinder surface. The free stream direction is from the top to the bottom of the page, where the jet holes, marked JH, are at the upstream end of the images. The skin friction lines which enter from the top of the schematic are assumed to originate from an attachment node at the stagnation point of the cylinder, and similarly the reverse flow skin friction lines which appear from the bottom of the schematics emanate from a nodal point of attachment of fluid drawn from the recirculation zone at the rear of the cylinder. For illustrative clarity, the number of skin friction lines have been kept to a minimum to maintain topological coherency; they can therefore be considered as time-averaged guidelines for an infinite number of skin friction lines to fill in the gaps.

The nature of the jet interaction with cylinder cross-flow has already been discussed in section 6.5, but it should here again be noted that the introduction of a continuous shedding cycle of hairpin vortices into the boundary layer is assumed to result in these structures breaking down to precipitate transition from laminar to turbulent flow at some distance downstream of the jet holes. It is further assumed – given the emergence of an adverse pressure gradient $5^\circ \leqslant \phi \leqslant 15^\circ$ downstream from

the jet emission – that this distance to transition would be far less than the distance to the ordinarily anticipated point of laminar separation from a plain cylinder at equivalent Re_D. As such, it can be assumed that the skin friction lines drawn in-line with the jet holes (i.e. the jet-energised flow stream) are from a turbulent boundary layer flow, and are accordingly coloured red to distinguish them from the skin friction lines produced by a laminar boundary layer – from span-wise locations between the holes. The separatrices which emanate from the saddle points, labelled S, are coloured blue to clearly identify the time-averaged lines of separation; each of these terminates at a focus, labelled F. This connection also serves to illustrate that fluid is drawn from the cylinder surface (i.e. in a direction out of the page) and into the wake by the development of vorticity generated at the cylinder surface. Attachment lines (emerging from the nodes of attachment, labelled N, located directly downstream from the foremost saddle points, S_1, between the jet holes) are coloured green, marking the boundary from which the flow close to the wall diverges – in a direction approximately upstream or downstream – after re-attachment.

The difference between the two arrangements, (a) and (b) in Figure 7.4 and Figure 7.5 respectively, is whether the connection of the separatrix emerging from saddle point S_2 bounds the primary CRVP (arrangement (a)), or secondary CRVP, (arrangement (b)). As a consequence, the connection to the dividing line of saddle point S_3 also alternates between skin friction lines derived from the nodal attachment of the recirculated base flow or the oncoming free stream flow. From observations of videos of the SOFV tests, it is particularly noticeable from the behaviour of the primary CRVP that the flow is unsteady. The centres of the primary CRVP foci continuously rove around the local surface area, and the rapidly changing size and shape of the foci themselves leads them to interact with and alter the other

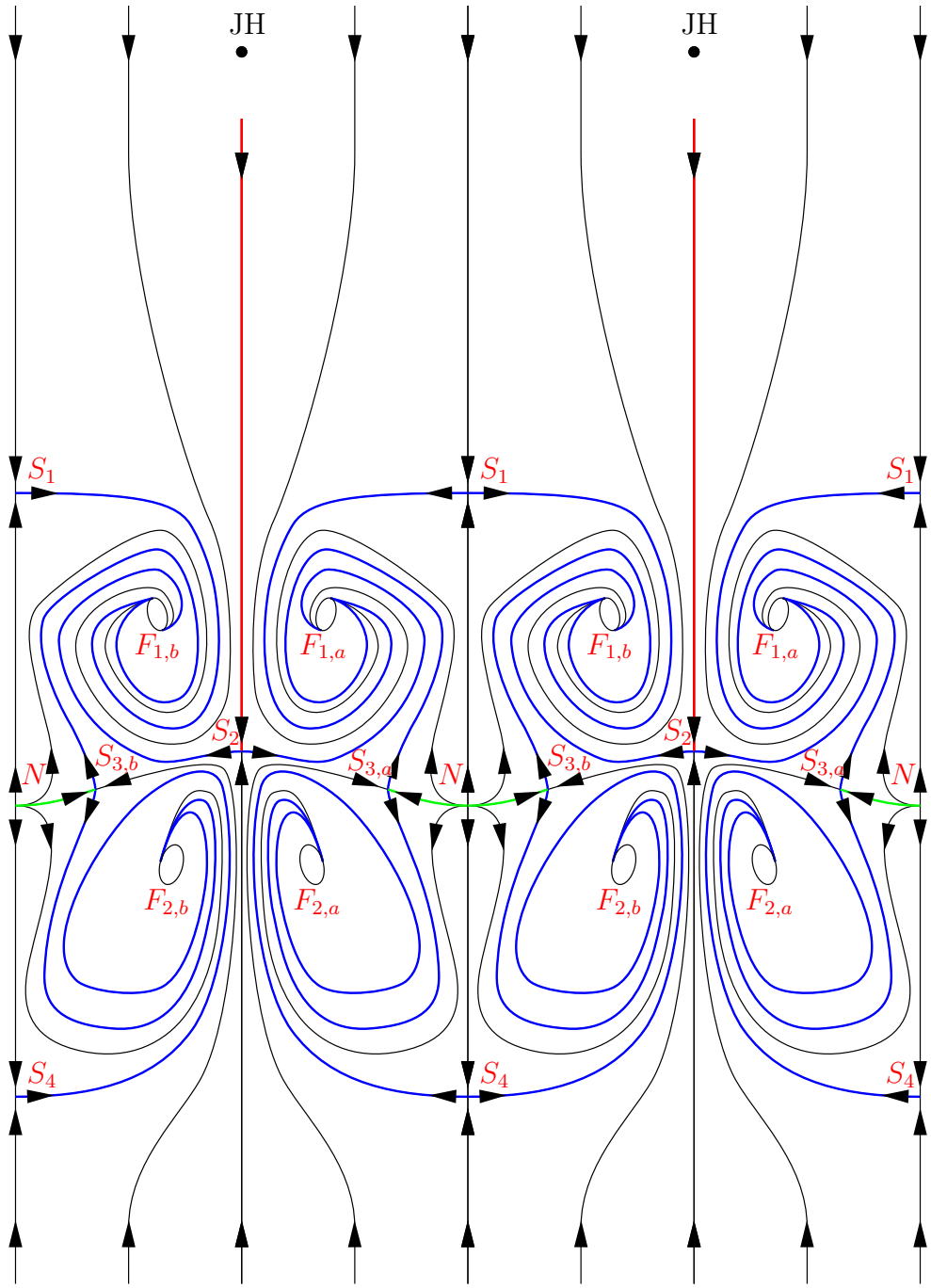

Figure 7.4 – Skin friction line schematic, $z_J = 20mm$, $Re = 2.7{\times}10^5$ – arrangement (a). Red lines represent skin friction lines from turbulent boundary layer flow, blue lines are saddle point separatrices (separation lines) and attachment node tangent lines (attachment lines) are shown in green. Text (black) and critical point (red) labels have the following meanings: JH, jet hole; S, saddle point; N, node; F, focus.

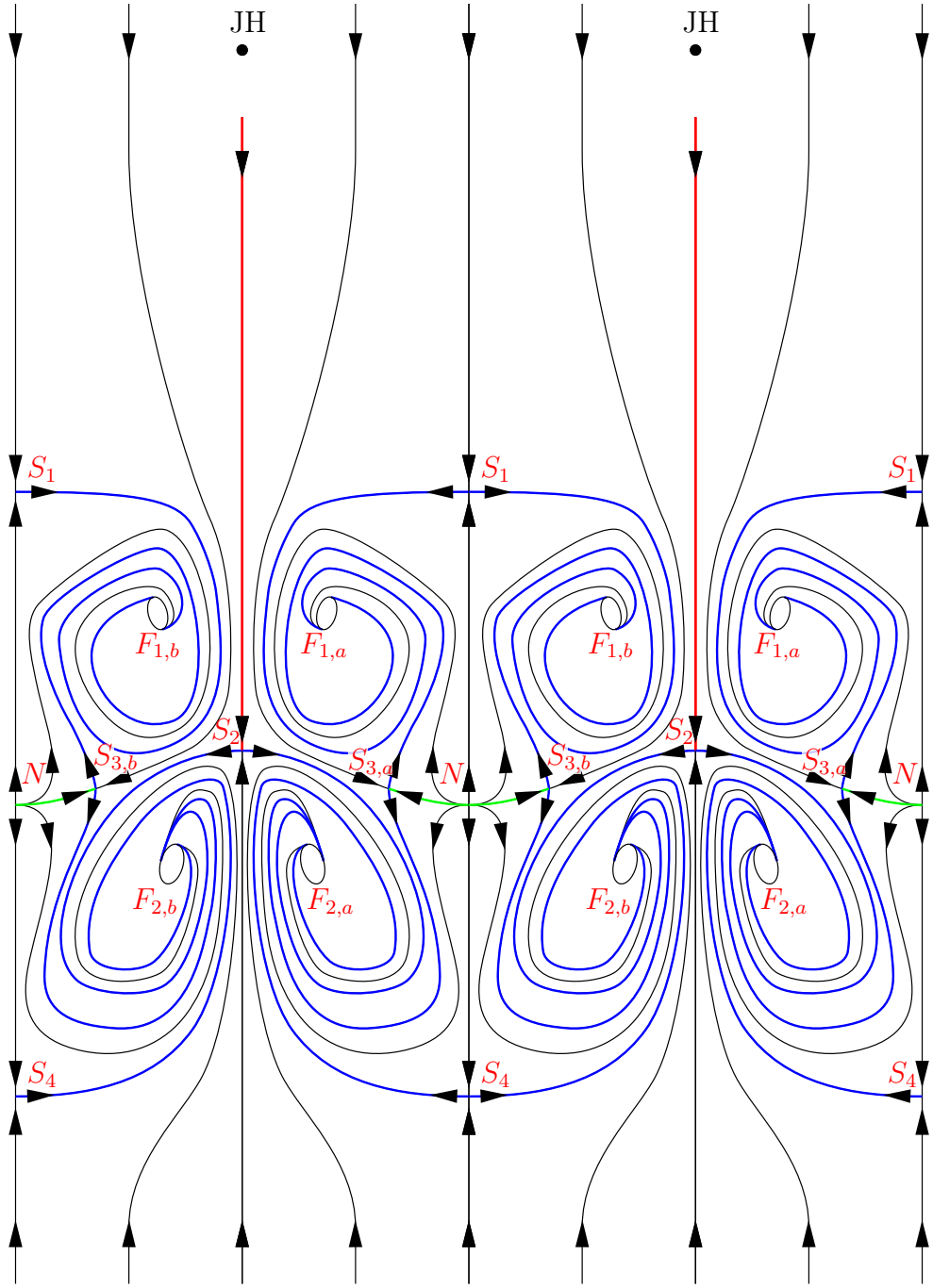

Figure 7.5 – Skin friction line schematic, $z_J = 20mm$, $Re = 2.7{\times}10^5$ – arrangement (b). Red lines represent skin friction lines from turbulent boundary layer flow, blue lines are saddle point separatrices (separation lines) and attachment node tangent lines (attachment lines) are shown in green. Text (black) and critical point (red) labels have the following meanings: JH, jet hole; S, saddle point; N, node; F, focus.

locally identified topological features – and hence the resulting skin friction line patterns on the surface. Observations of SOFV test video footage and analysis of post-test photographs have therefore led to the postulation that the skin friction line patterns typically alternate between these two arrangements, with arrangement (a) appearing more consistently to produce a stronger imprint on the time-averaged SOFV test results. Both schematics, (a) and (b), are topologically stable, however the unsteady nature of the flow appears to enforce numerous changes and variety to the arrangement of the skin friction lines at the surface, and hence flow structure above it.

The process of interpreting the skin friction lines from the SOFV results and reconstructing them into schematic form provided some important insights which were not immediately obvious simply by observing the SOFV photographs. Perhaps the most striking finding was the discovery of an attachment node downstream of the foremost laminar separation lines – which emanate from saddle point S_1 downstream of the span-wise locations between the jet holes. The initial analysis of photographs led to speculation of an attachment node in this location, and so it was proved after conducting specific experiments to investigate this further (see Figure F.2 in Appendix F for photographs of these experiments which help clarify its existence). The logical inference from the existence of an attachment node downstream of a laminar separation line is the existence of a separation bubble between the two. The flow re-attaching at the node is split between that which is recycled back upstream into the bubble, and that which continues downstream until either finally separating along the flanking separatrix lines emerging from saddle points S_3 and S_4, or is drawn into the secondary CRVP (foci $F_{2,a}$ and $F_{2,b}$). In any case, the reattached flow appears to be capable of withstanding an adverse pressure for an extended period

at a location far downstream from the initial laminar separation. This indicates that the reattached flow constitutes a turbulent boundary layer, which therefore implies that subsequent to the laminar separation, the detached laminar shear layer transitions before making a turbulent reattachment in a process analogous to the commonly understood laminar separation bubble.

Unlike the laminar separation bubbles which are found on a plain cylinder in the critical Reynolds number regime, the separation bubbles found here are formed of short, discontinuous span-wise segments – partitioned by the energised boundary layer flow of the jet-cross-flow interaction. The interaction between the locally accelerated, turbulent boundary layer flow of the jets in cross-flow and the adjacent laminar boundary layer between the holes leads to an inextricably three-dimensional flow topology. The jet-energised flow stream reaches the limit of its attachment length at the separatrix of saddle point S_2; the reduced momentum at the edges of this energised flow stream – as it interacts with the adjacent laminar boundary layer – provides an increasing curvature to the (initially) laminar separation line emanating from S_1. On the approach to S_2, as the boundary layer thickness increases and momentum continues to drop, the flow at the edges of this energised stream appears to be swept exclusively into the primary CRVP of foci $F_{1,a}$ and $F_{1,b}$ (for both arrangements, (a) – Figure 7.4 and (b) – Figure 7.5). A central portion of the jet-energised stream, meanwhile, continues in the free stream direction to make a final separation along the separatrix of S_2 (as in (a) – Figure 7.4) or (in the case of (b) – Figure 7.5) either – similarly – makes a final separation along the separatrix of S_2, which now curves downstream to encompass the secondary CRVP of foci F_2, or splits on the approach to saddle S_3 to be swept into both primary and secondary CRVP (foci F_1 and F_2) or separate along the separatrix emanating from

saddle S_3. The action of the shear layer development between the jet-energised flow stream and the adjacent laminar boundary layer is therefore to invoke the roll-up of a counter-rotating vortex pair ($F_{1,a}$ and $F_{1,b}$) at the cylinder surface with the sign of rotation set by the difference in momentum between the two streams – i.e. the faster moving stream wraps around the slower moving stream. Since saddle point S_1, and the separatrix that originates there, appears at approximately the same location as the separation line of a plain cylinder at equivalent Re_D, the development of the separation bubble – the apparent transition and subsequent reattachment of the flow at node N – is a direct consequence of the type of topological changes introduced by the jet-energised flow stream. It would appear that the generation of the primary CRVP gives rise to a sufficient destabilisation of the separated laminar shear layer such that transition and turbulent reattachment to the cylinder surface occurs. However, this CRVP, which may provide the necessary conditions to sustain the separation bubble, also appears to limit the proportion of flow reattachment to the central section downstream of S_1 – in the space between the primary CRVP. The separation bubble is not completely enclosed – it is instead continually being supplied from the oncoming flow – and by continuity must therefore issue fluid from the two foci, $F_{1,a}$ and $F_{1,b}$. This being the case, for topological consistency, the separation bubble would form another vortex as the laminar shear layer rolls over the bubble and this would necessarily be of the opposite sign to the primary CRVP. A sketch of this type of separation bubble, by Perry and Chong (1986), is shown in Figure 7.6, where the two vortex lines have been shown to intertwine with one another. This may not precisely reflect the structure found here for the passive jets setup, but in any case the close proximity of counter-rotating vortices leads to an increased rate of decay of the pair (Leweke et al., 2016) and this may have a bearing

on the relative success of flow reattachment.

The secondary CRVP, formed of foci $F_{2,a}$ and $F_{2,b}$ immediately downstream of the primary CRVP, does not stimulate reattachment of the flow because the flow separating at S_2 already derives from a thickened turbulent boundary layer. The secondary CRVP is also much weaker than the primary CRVP. This is because it is typically supplied only from the recirculating, low-momentum base flow and limited supply of the turbulent, reattached flow emanating from N, as depicted by arrangement (a) – Figure 7.4. Occasionally it will get a boost when a small amount of fluid from the jet-energised stream finds its way between the channel formed by the separatrices emanating from saddles S_2 and S_3 while the topology structured as drawn in arrangement (b) – Figure 7.5. The primary CRVP, by contrast, is always supplied from a combination of the high momentum jet-energised stream and oncoming free-stream flow. A number of factors appear as possible influences on the production of the secondary CRVP; the sign of rotation is opposite to the primary CRVP and it is possible that the emission of the primary CRVP close to the wall results in the formation of secondary vorticity (see, for example, Harris and Williamson, 2012; Leweke et al., 2016). In observations of videos of the SOFV tests, one of the main drivers of the secondary CRVP appears to be the reverse flow generated by the jet-energised stream separating directly into the wake at S_2. This is perhaps supplemented in the opposite direction by the reattached flow between N and S_4. Again, by continuity, vorticity is shed into the wake by foci $F_{2,a}$ and $F_{2,b}$.

It is not possible, without additional three-dimensional flow-field data directly above the cylinder surface, to predict with certainty the time-averaged flow topology from the SOFV tests and their resulting skin friction patterns. Dallmann (1983) points out that there is no unique relationship between the pattern of the wall

skin friction lines and the flow field above; topologically different flow fields may produce the same surface oil flow visualisation results. Lines of separation and the origin of some vortical wake structures may be confidently elucidated, however the behaviour of unsteady, three-dimensional separated flows is difficult to predict – particularly the interaction and formation of vortical structures. From observations of flow visualisations on the cylinder surface – and the resulting skin friction line data – a reasonable estimate can be made, and by acquiring data in the near-wake region a more complete picture can emerge by linking the behaviour of each. A discussion and comparison of wake and SOFV data follows in chapter 8.

It should be emphasised that the skin friction line pattern analysed and discussed here is representative only of the time-averaged flow behaviour. As mentioned previously, from videos of the SOFV tests it is immediately obvious that the primary CRVP in particular is unstable and there is frequent exchange of fluid between the two foci ($F_{1,a}$ and $F_{1,b}$) by crossing the boundary of the line running perpendicular to the separatrix of S_2. Many permutations of the flow topology are possible – and it appears that the instantaneous skin friction pattern changes continuously without settling on any single, stable configuration – but to accurately chart this behaviour requires further investigation which is beyond the current scope of this research.

7.2.3 Similar flow topology in the literature

The skin friction line patterns found here in the SOFV experiments were similar to those found by Fairlie (1980), for a hemisphere capped cylinder inclined to the flow, which can be seen in Figure F.3 of Appendix F, and to the computed topology of Perry and Chong (1986), shown here in Figure 7.6, which both describe possible topological solutions of the so-called 'owl-face of the second kind' (Dallmann, 1983;

Fairlie, 1980; Perry and Chong, 1986) – shortened hereafter to 'owl type-2' – skin friction pattern. The schematics of Fairlie (1980) are referenced here as an example of similar surface skin friction lines providing quite different topological solutions – highlighting the uncertainty which exists in reconstructing three-dimensional flow topology from skin friction patterns alone; the flow topology above the surface is altered by the orientation of the cylinder and separating shear layers, resulting in an arrangement of vortices at odds with the topology generated by the cylinder with passive jets. From an analysis of the data, it is thought that the three-dimensional topology of the separation bubble found here could follow a slightly modified version of the solution produced by Perry and Chong (1986), as shown in Figure 7.6.

The curvature and proportions of the Perry and Chong surface pattern differs somewhat to the cylinder skin friction lines found here – which would of course alter the topology somewhat – but the general arrangement seems an acceptable comparison with the accumulated data of the $z_J = 20mm$ passive jet cylinder setup at high Re_D, and is therefore proposed as a similar time-averaged topological solution. It is important to note here that because the vortex filaments of foci $F_{1,a}$ and $F_{1,b}$ trail downstream, the roll-up of the shear layer after laminar separation immediately downstream of S_1 necessarily generates an additional focus in the (x, y) – plane, labelled F_3 in Figure 7.6, (b), in order to 'close' the separation bubble. The vorticity channelled by this focus wraps around in the free-stream direction, either side of the attachment node, N, to form a horseshoe type vortex with vorticity trailing downstream – in tandem with the tornado-like vortices emanating from the foci of the primary CRVP, $F_{1,a}$ and $F_{1,b}$, but with opposite sign of rotation. Perry and Chong have shown the vortex filaments intertwining with one another as they sweep downstream, and this type of behaviour is predicted to occur on the likely

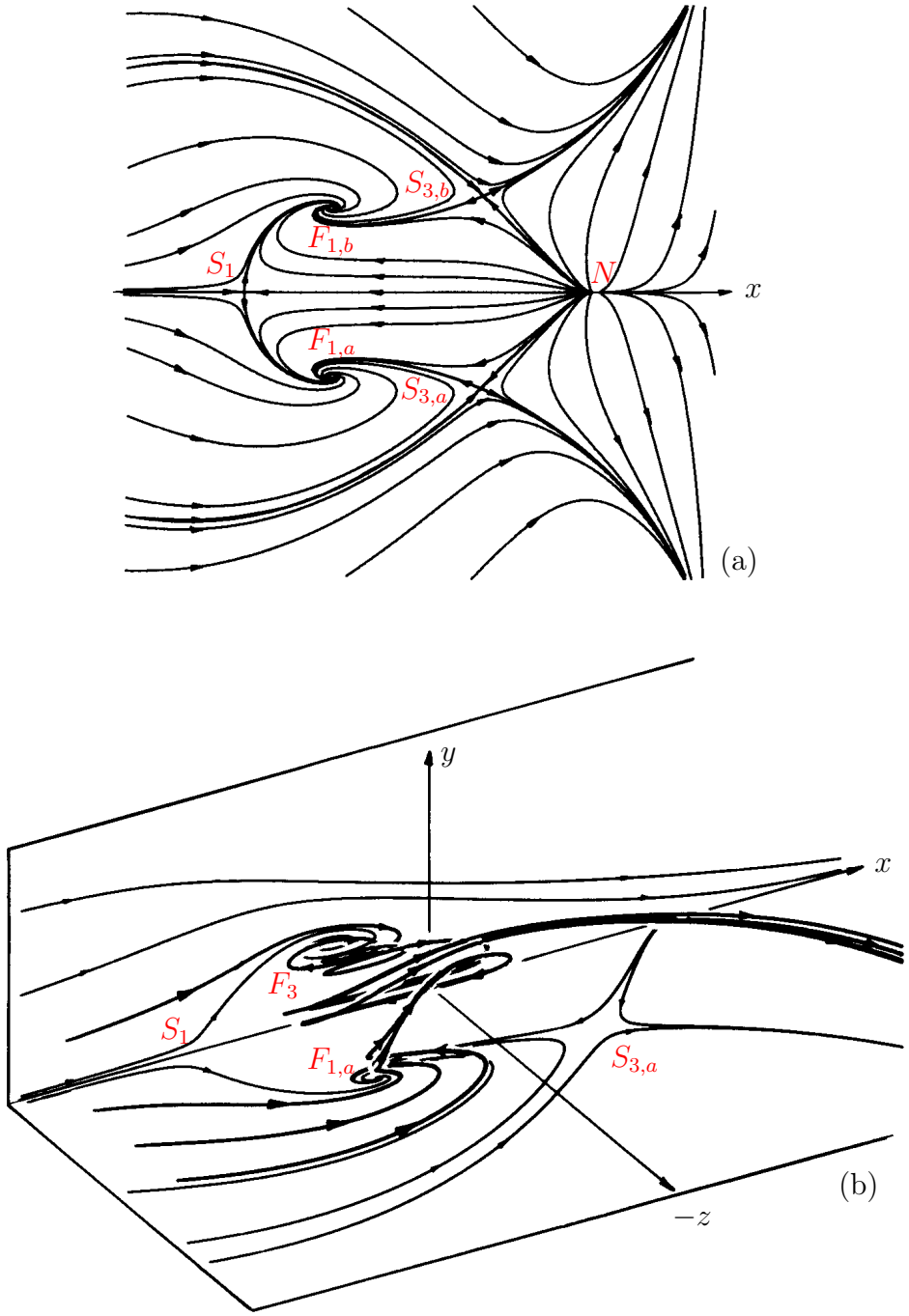

Figure 7.6 – Flow topology schematics of 'owl type-2' separation pattern in three dimensions, adapted from Perry and Chong (1986), where: (a) presents the two-dimensional skin friction lines, and; (b) provides a three-dimensional representation of a topologically consistent solution to the flow topology above the surface. Free stream direction is left to right.

assumption that the vortices are of unequal circulation strength. As shown in Figure 7.6, (b), the central portion of the separation bubble reattaches so it is assumed, in the time-averaged case of the cylinder with $z_J = 20mm$ passive jets at high Re_D, that the topology produced is a repeating array of separation bubbles flanked on either side by counter rotating vortex pairs (F_1 and F_3) which are shed, intertwined, downstream from the cylinder surface into the wake.

It would appear, therefore, that a considerable proportion of the cylinder span is given over to shedding vorticity (with filaments extending in the stream-wise direction) into the wake, leaving only small span-wise segments of reattaching flow; the jet-energised stream arriving at S_2 partitions two sets of CRVP shedding into the wake, meaning that four vortices are shed between each separation bubble – even before the topology of the secondary CRVP is taken into account.

In the same manner of the primary CRVP, the foci of the secondary CRVP ($F_{2,a}$ and $F_{2,b}$) continually lift fluid from the cylinder surface to produce tornado-like vortices which extend downstream into the wake. As mentioned earlier in section 7.2.1, there is a strong reverse flow channelled between $F_{2,a}$ and $F_{2,b}$ towards S_2 underneath the separated flow of the jet-energised stream. Here, however, there are no obvious signs to suggest that there is an additional vortex roll-up similar to the primary CRVP just discussed and it is assumed that the reverse flow is simply drawn from recirculating flow reattaching in the base region. This analysis thus predicts at least six vortex filaments extending downstream into the wake per separation bubble.

7.2.4 Imposing three-dimensional flow topology

It can be demonstrated quite simply by the graphic shown in Figure 7.7 that the introduction of the vortical structures – generated by the interaction of the transverse jets with the boundary layer – into the wake region has a positive effect on drag reduction beyond simply delaying boundary layer separation; the majority of the separation points identified in section 7.2.2 lie upstream of those found on a cylinder with tripping wires, which has a greater C_D at high Reynolds numbers. For the SOFV photos shown in Figure 7.7, the cylinder with tripping wires was tested at $Re_D = 2.85 \times 10^5$ and the cylinder with passive jets was tested at $Re_D = 2.75 \times 10^5$, which correspond to respective drag coefficient values of $C_D = 0.58$ and $C_D = 0.45$, as previously shown in Figure 4.2 and Figure 5.7.

It was mentioned previously in section 5.5 that disrupting straight-line separation can reduce the strength of, or completely obliterate, Kármán vortex shedding. As a consequence, there is an increase in base pressure and, hence, a reduction in drag. Knowing this, the approach to optimising the application of passive drag reducing flow control methods should therefore be to understand the effects of imposing particular forms of three-dimensional topology on the boundary layer – and their subsequent influence on wake formation – aside from the mean span-wise delay in flow separation. This modification of the flow may take many forms (e.g. vortex generators or discrete roughness textures of various kinds) so, along with an appreciation of the operational flow characteristics, the route to optimisation is lead by an understanding of the types of wake formation which are desirable coupled with an understanding of the effects, possibilities and practicalities of applying various flow modifiers. It is not always possible to predict – particularly for high

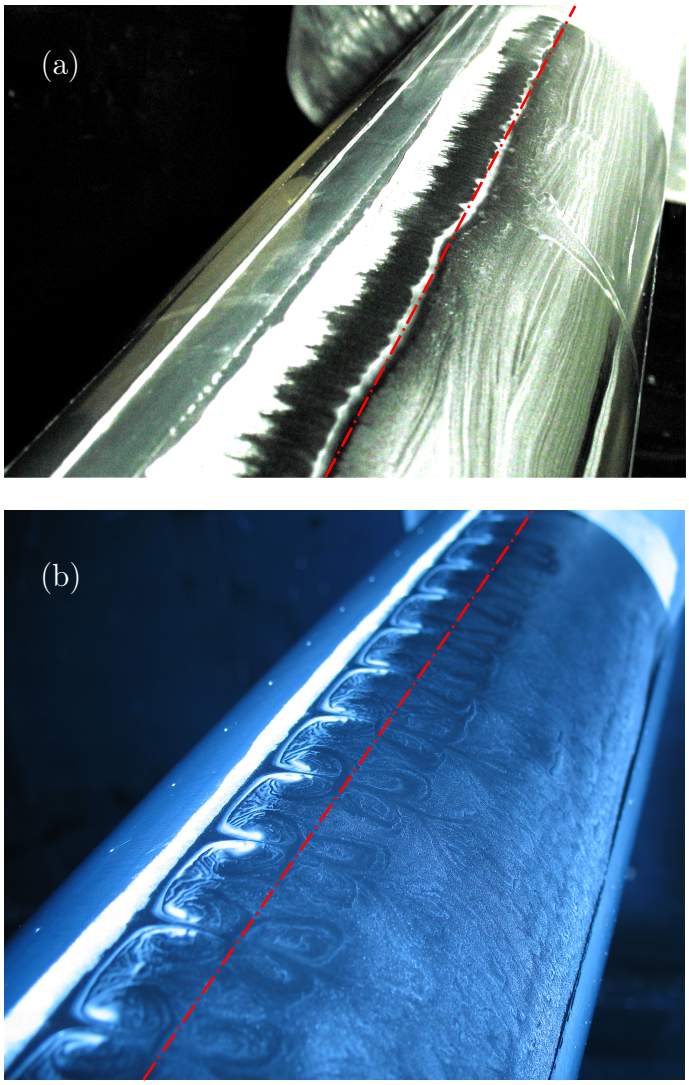

Figure 7.7 – Comparison of separation lines from surface-oil flow visualisations at $Re \approx 2.80 \times 10^5$, for: (a) tripping wires, $C_D = 0.58$; and, (b) passive jets, $C_D = 0.45$. Both images are overlaid with a red dashed line representing the mean angular position of the separation line for the cylinder with tripping wires. Free stream direction is approximately left to right.

Reynolds numbers – the precise characteristics a particular type or arrangement of flow control device may have on boundary layer topology and wake formation. As such, the approach here is to elicit some understanding of the fundamental fluid mechanics which may lead to improved drag reduction and passive flow control design

strategies.

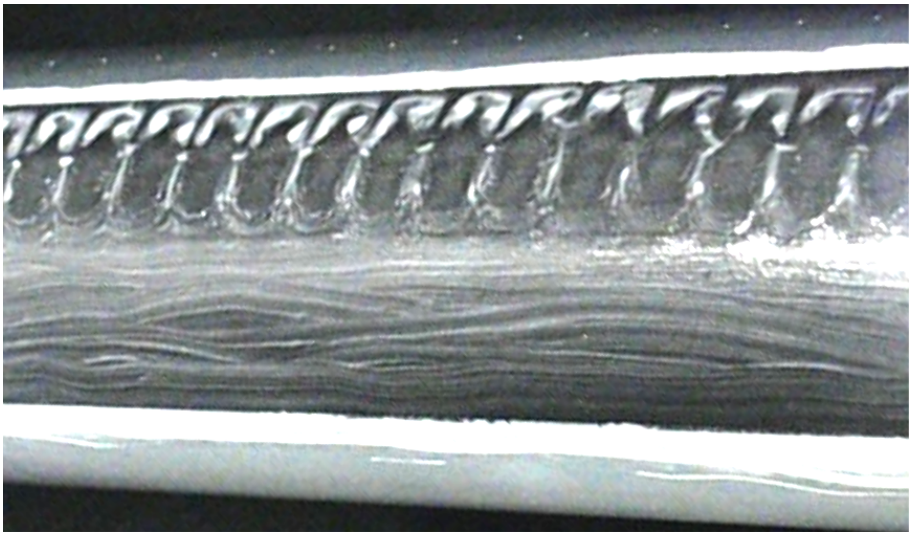

Figure 7.8 – Video still of a SOFV test showing wavy separation line at $Re = 2.80 \times 10^5$. The free stream direction is approximately from top to bottom if the image.

The image in Figure 7.8 is a video-still taken from a SOFV test on the cylinder with 20mm spaced passive jets at $Re = 2.80 \times 10^5$. This screen grab was taken from near the beginning of the SOFV test, just after the wind tunnel had reached the speed set by the PID controller, with the secondary sets of CRVP just about to make a visual appearance in the oil mixture on the cylinder surface. As is quite clearly shown in the image, the accumulation of oil mixture downstream of the primary CRVP provides evidence of a distinctively wavy separation line. With reference to Figure 7.5, these waves are outlined by crests positioned at the S_2 saddle points, with the separation line sweeping down to the S_4 saddle points to form U-shaped troughs. The existence of this wavy separation line helps to corroborate the evidence of a closed separation bubble between the primary CRVP, from which the flow reattaches before separating much further downstream.

The surface flow topology of Figure 7.8 is very similar to that found by Mizuno

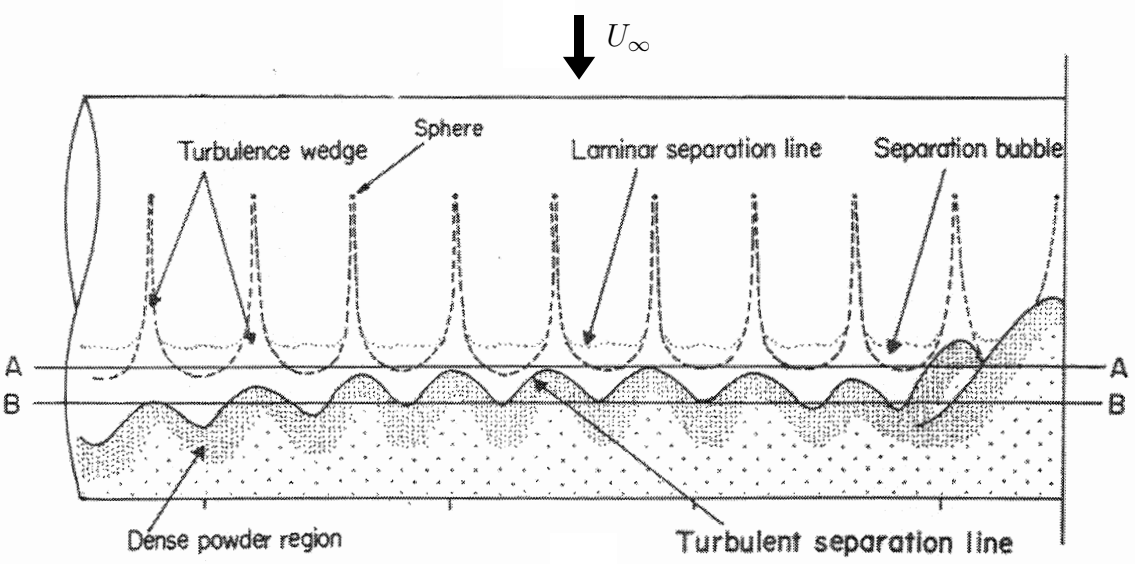

Figure 7.9 – Schematic of surface pattern for a cylinder with discrete protuberances placed at $\phi = \pm 60°$, from Mizuno (1970). The 'turbulence wedge' and wavy separation line are very similar to the topological features found here for passive jets.

(1970), whose paper was discovered after the present body of research was completed. Figure 7.9 shows a schematic produced by Mizuno, interpreted from talc dust flow visualisations, which describes 'turbulence wedges', emanating from the perturbation of the cross-flow caused by the spherical protuberances attached to the cylinder surface. These turbulence wedges spread downstream, slicing through the straight laminar separation line. The laminar separation at the span-wise locations downstream of the inter-sphere positions subsequently forms a laminar separation bubble. The flow from the turbulence wedges then separates finally at a position upstream of the flow originating from the span-wise locations between the spheres; this flow remains attached due to the energising action of the laminar separation bubble formed well downstream of the boundary layer tripping action of the spheres. This difference in span-wise separation points creates a separation line with a clear wave formation across the span. Mizuno also finds that Karman vortex shedding

ceases with the 'cell' formation from $Re_D = 8 \times 10^4$, but does not report any findings of vortical patterns forming on the cylinder surface. This, however, may be due to the method of flow visualisation used; the use of a talc dust dispenser to blow an air-powder mixture into the reverse flow region might inhibit the observation of such structures. Mizuno does however note that some of his findings suggest a pair of longitudinal vortices trail from the sphere protuberances.

7.3 Passive jets, $z_J = 10mm$

For comparison with the $z_J = 20mm$ arrangement, the cylinder with $z_J = 10mm$ passive jet spacing was tested with the SOFV method at a similar Reynolds number; a photograph of one of these test results is presented in Figure 7.10. As was shown in Figure 5.7 of section 5.3, the cylinder with $z_J = 10mm$ passive jet spacing has a C_D v. Re_D profile which noticeably deviates from that of the $z_J = 20mm$ arrangement in the range $1 \times 10^5 < Re_D < 2.2 \times 10^5$, however at Reynolds numbers above and below this range the C_D values were very similar. The skin friction line patterns, and hence flow topology, associated with Figure 7.2 and Figure 7.10 – which were both produced under the same testing conditions at $Re_D = 2.7 \times 10^5$ – are therefore approximately equal in terms of their impact on C_D reduction.

Figure 7.11 provides a photographic comparison of the effect on wall shear stress – and, by direct relation, flow topology – of the two jet spacings. Other than the obvious difference in size of the primary CRVP formation imposed by the jet spacing, the most distinguishable feature of the two SOFV patterns is the relative position of the delayed separation line directly downstream of the jet holes. For the $z_J = 20mm$ arrangement, the time-averaged flow typically produces a continuous line of sepa-

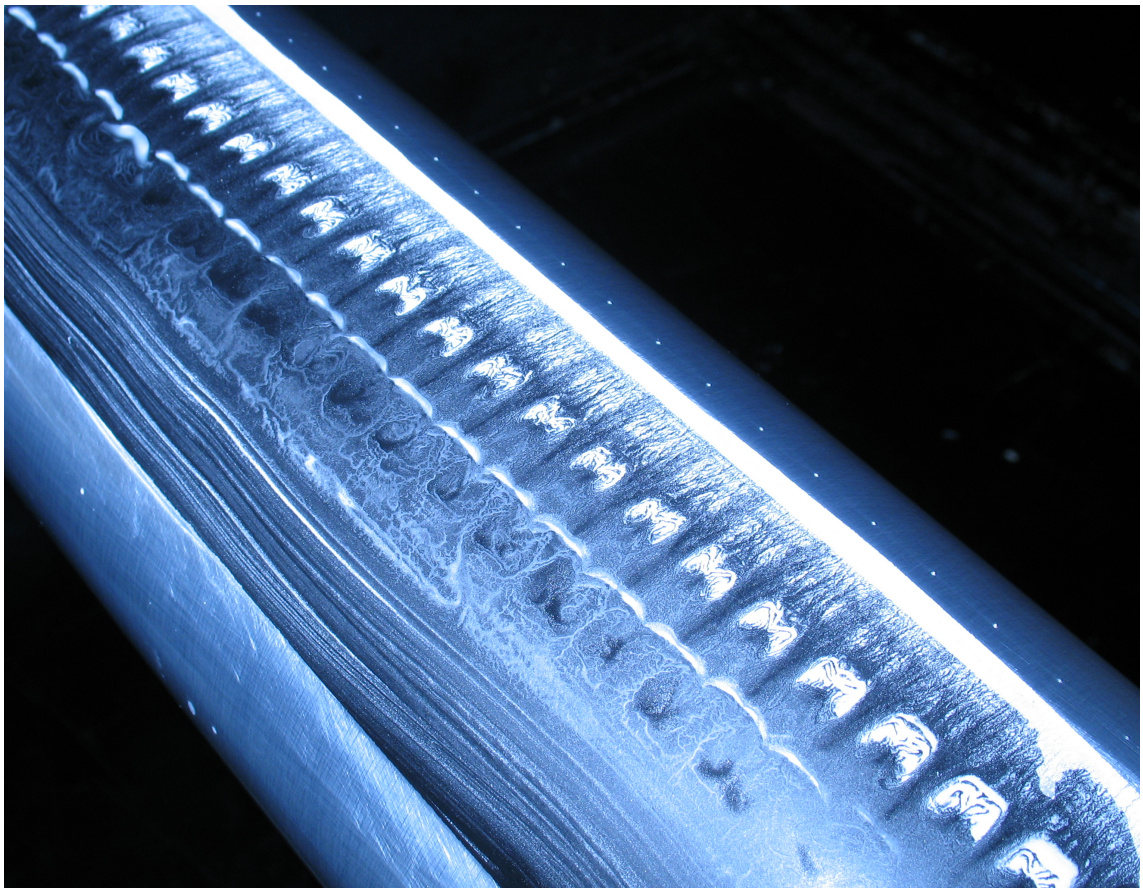

Figure 7.10 – Photograph of surface oil flow visualisation test showing the time averaged skin friction line pattern downstream of the jet exit holes for the $z_J = 10mm$ spaced passive jets at $Re = 2.7{\times}10^5$. With reference to the image frame, free-stream flow direction is approximately top right to bottom left.

ration which diverges symmetrically about the direction of the jet-energised stream and is drawn into the two adjacent foci (of the two separate CRVP which flank that jet-energised stream). In contrast, for the $z_J = 10mm$ spacing there appears to be a dislocation of this delayed separation line from the primary CRVP and instead the formation of a seemingly continuous, span-wise line of separation develops noticeably further downstream. This is depicted schematically in Figure 7.12 where a continuous separation line is marked out by the separatrices from the S_3 saddle

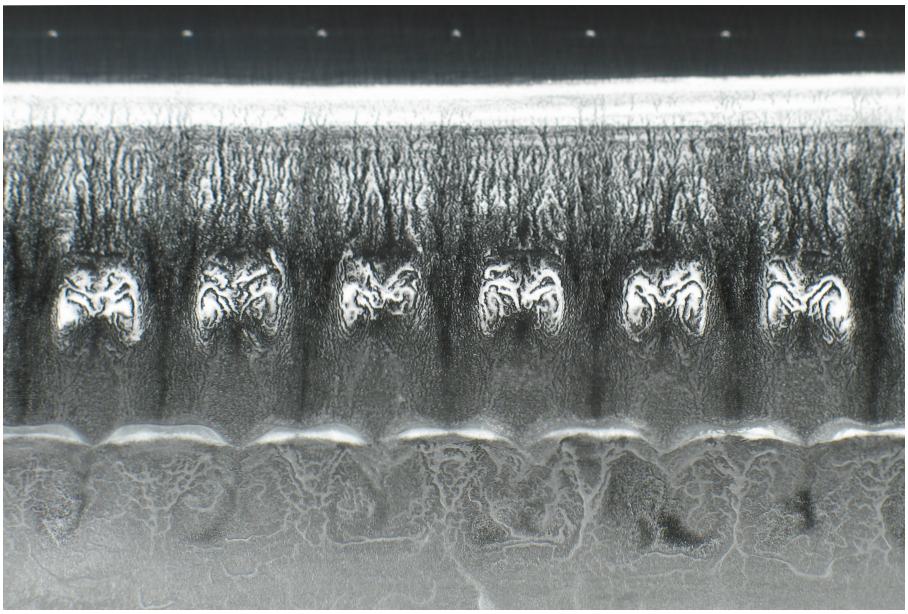

(a)



(b)

Figure 7.11 – Photographic comparison of surface oil flow visualisation test results, showing the time averaged skin friction line patterns for passive jet spacing of: (a) $z_J = 10mm$; and, (b) $z_J = 20mm$. $Re = 2.7{\times}10^5$, free-stream flow direction is approximately top to bottom.

points which join with the N_2 separation nodes to create a typical example of a separation line formed of a node-saddle array. Despite this distance being somewhat exaggerated by the size of the shift relative to the reduced size of the CRVP, there is a measurable change in the mean position of this separation line of approximately $\Delta\phi_s = 2.5°$ further downstream for $z_J = 10mm$ compared to the equivalent position of the S_2 saddle points of the $z_J = 20mm$ separation line (Figure 7.4 and Figure 7.5). This increased delay in separation for the jet-energised stream of the $z_J = 10mm$ setup suggests that a smaller proportion of the jet-energised stream is drawn into the foci of the primary CRVP, allowing a substantial amount of the jet-energised stream to maintain its momentum and continue downstream – thus remaining attached to a greater circumferential angle, ϕ, before finally separating. The wider jet spacing of $z_J = 20mm$, which allows for and generates larger foci – with an assumed increase in swirling strength over those of the $z_J = 10mm$ setup – appears to be able to draw all of the momentum from the jet-energised stream into the primary CRVP and is thus assumed to pass an increased intensity of vorticity into the wake from this source. This point is particularly intriguing given the finding, from section 6.3, that for $Re_D > 1.4 \times 10^5$ the $z_J = 10mm$ cylinder produces a lower jet velocity – and hence volume flow-rate – than the $z_J = 20mm$ arrangement.

At this juncture it should be noted that the result of the SOFV test for the $z_J = 10mm$ setup in Figure 7.11 (a) is not a completely faithful reflection of the characteristics of the mean (delayed) separation line. One is reminded that the application of even a very thinly spread solution of oil and tracer particles represents an intrusive method of flow visualisation, particularly where the action of the surface shear stress is to collect this solution into a small region of the model surface – as is typically the case for lines of separation. The build-up of tracer particles at specific

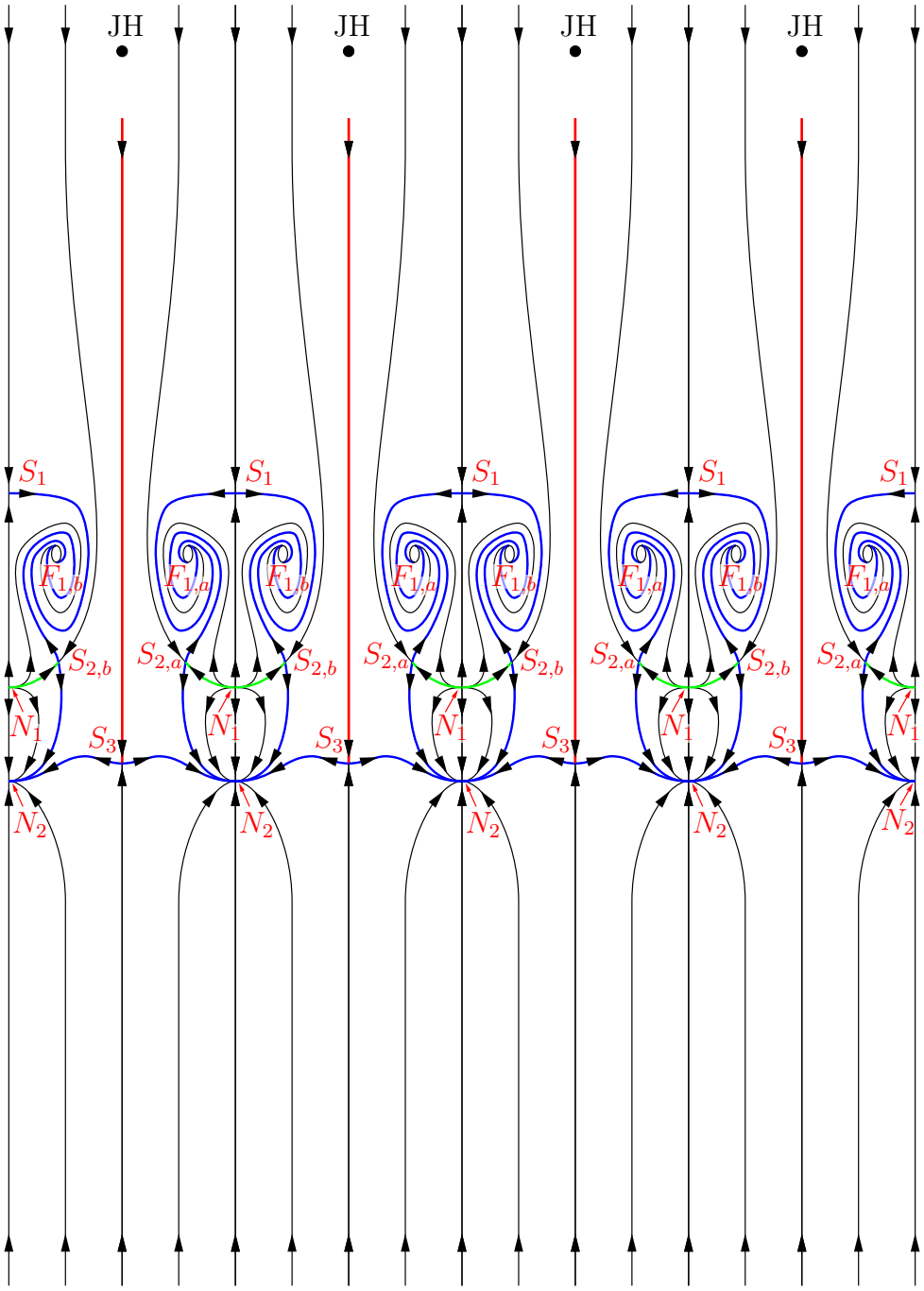

Figure 7.12 – Skin friction line schematic, $z_J = 10mm$, $Re = 2.7{\times}10^5$ – arrangement (a). Red lines represent skin friction lines from turbulent boundary layer flow, blue lines are saddle point separatrices (separation lines) and attachment node tangent lines (attachment lines) are shown in green. Text (black) and critical point (red) labels have the following meanings: JH, jet hole; S, saddle point; N, node; F, focus.

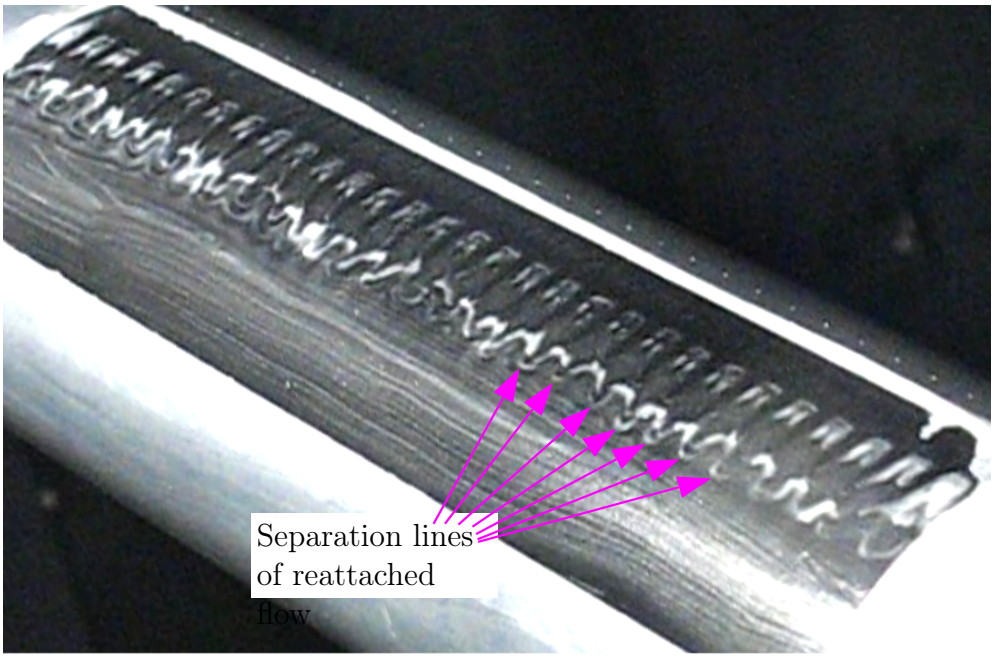

Figure 7.13 – Still from video of a surface oil flow visualisation test of $z_J = 10mm$ spaced passive jets at $Re = 2.7{\times}10^5$. A selection of curved separation lines, of reattached flow downstream of the primary CRVP, are indicated by arrows. With respect to the image frame, free-stream flow direction is approximately top-right to bottom-left.

points on the model surface can effectively produce surface protrusions which – especially for unsteady flows – can alter the local flow topology and promote flow separation. Figure 7.13 shows a video still from a SOFV test on the $z_J = 10mm$ cylinder at $Re = 2.7{\times}10^5$. The still shows an instantaneous skin friction line pattern during the early stages of the test – before the oil mixture had time to dry and was thus still in a low-viscosity state easily moulded by the oncoming flow. Downstream of the primary CRVP, after which the flow reattaches, curved separation lines (a selection of which are indicated by arrows) can be clearly identified to extend beyond the separation lines of the jet-energised streams on either side. As the test progressed and the thinner oils began to evaporate, the protrusions caused by the coagulating

oil/tracer particle mixture began to grow, slowly bridging the gaps between adjacent separation lines generated by the jet-energised streams. The resulting final image of Figure 7.11 (a) is therefore somewhat misleading, however one can trace the extent of the delayed separation lines of the reattached flow by the faint pattern of skin friction lines immediately downstream.

The secondary CRVP is not nearly as clearly defined as is found with the $z_J = 20mm$ spacing cylinder – partly as a consequence of the aforementioned span-wise closing of the separation lines but also because they are fundamentally weaker than those of the $z_J = 20mm$ cylinder. As shown in Figure 7.14 – a schematic representation of the time-averaged skin friction lines before the flow-disturbing impact of the surface clumping of tracer particles takes effect – the secondary CRVP in this arrangement can only be supplied from the reattached flow stream emanating from N_1. The secondary CRVP are still just possible to make out in Figure 7.11 (a), and it is the furthest downstream edge of these CRVP which marks the furthest extent of the delayed separation line of the reattached flow, represented by the separatrix of S_4 of schematic arrangement (b) (Figure 7.14). The circumferential angle, ϕ, for which the furthest downstream edge of the secondary CRVP were measured for both jet spacings turned out to be remarkably similar ($\phi = 113.5°$ and $\phi = 114°$ for $z_J = 10mm$ and $z_J = 20mm$ respectively), however, where this marks the final point of separation for the $z_J = 10mm$ setup, the reattached flow of the $z_J = 20mm$ cylinder appears to be more capable of delaying separation for an increased distance downstream (up to a maximum of $\phi_s = 119°$). It is seems plausible that this difference in angle of the final separation point for the reattached flow is due to the wider jet spacing allowing a reattachment bubble of greater span-wise width.

That both jet spacings produce such distinctly varied flow topology and yet

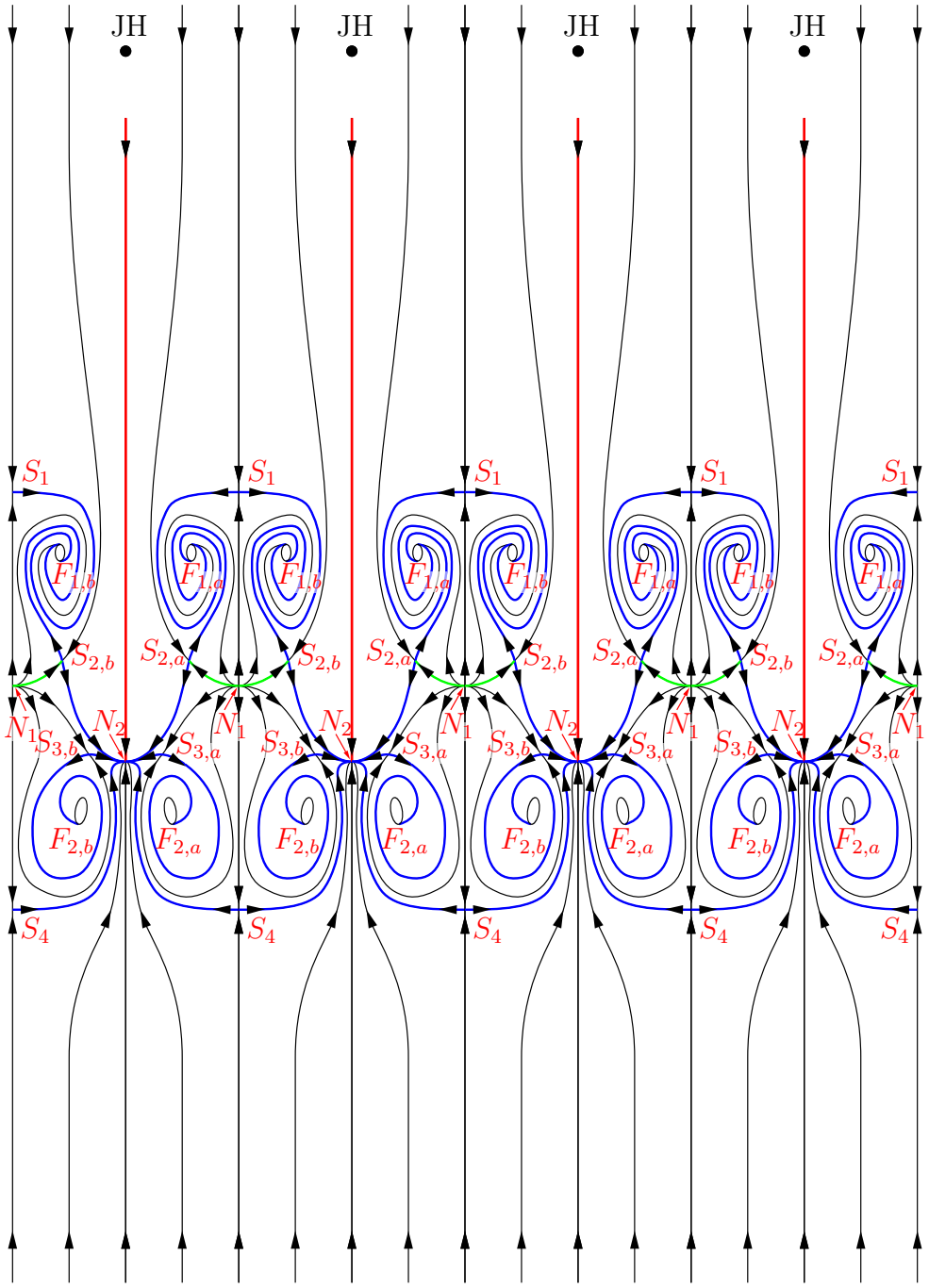

Figure 7.14 – Skin friction line schematic, $z_J = 10mm$, $Re = 2.7{\times}10^5$ – arrangement (b). Red lines represent skin friction lines from turbulent boundary layer flow, blue lines are saddle point separatrices (separation lines) and attachment node tangent lines (attachment lines) are shown in green. Text (black) and critical point (red) labels have the following meanings: JH, jet hole; S, saddle point; N, node; F, focus.

produce almost the same effect on drag reduction at $Re_D = 2.7 \times 10^5$ is remarkable, and is yet more evidence of the multi-faceted approach to inducing a drag reducing flow regime; the $z_J = 10mm$ and $z_J = 20mm$ arrangements appear to produce a specific variety of drag reducing qualities which balance each other out around $Re_D = 2.7 \times 10^5$. The following section attempts to illuminate some of these drag reducing mechanisms further by analysing SOFV tests throughout the Re_D testing range.

7.4 Development of skin friction lines with Re_D

It is observed from Figure 5.7 that rather than a smooth, continuous progression of drag coefficient reduction with increasing Reynolds number, the C_D v. Re_D relationship for both the $z_J = 10mm$ and $z_J = 20mm$ jet spacing arrangements appears to advance through various stages of behaviour before finally reaching a stable gradient at high Re_D. These distinctive step changes in gradient appear to follow a reasonably similar trend for both jet spacing arrangements. With the aim of better understanding this variance, the $z_J = 10mm$ cylinder was tested with the SOFV method throughout the Re_D range of interest in order to analyse the development of time-mean skin friction lines – and hence link these changes in flow topology to their effect on cylinder drag.

The choice of acquisition Re_D corresponded to particular points of interest on the C_D and C_L v. Re_D curves for this cylinder setup; the plot in Figure 7.15 shows how both C_D and C_L vary with Re_D and is overlaid with dashed lines to mark the acquisition Reynolds numbers (from left to right, $Re_D = 0.94; 1.13; 1.38; 1.70$; and 2.74×10^5, respectively) for which the flow topology was recorded using the SOFV

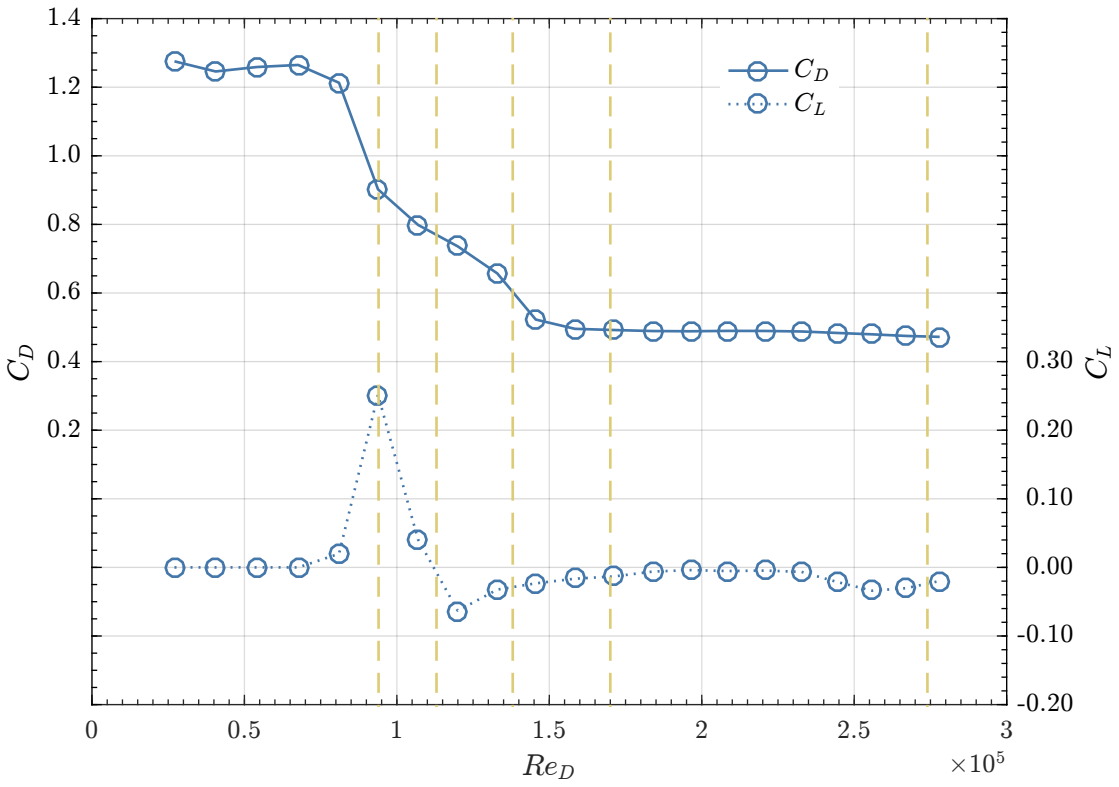

Figure 7.15 – Graphic showing the acquisition Reynolds numbers, Re_D, for the SOFV analysis of surface flow topology as it varies throughout the testing range, with respect to points of interest on the C_D and C_L curves for the for $z_J = 10mm$ passive jets arrangement. The five acquisition Re_D are indicated by the dashed vertical lines.

technique.

The first marker, at $Re_D = 9.4 \times 10^4$, represents the first point on the C_D v. Re_D curve where the cylinder with passive jets deviates significantly from the characteristic curve of a plain cylinder, so it was expected that the first evidence of the flow control method working would be found here. The second marker, at $Re_D = 1.13 \times 10^5$, is placed in the middle of a constant gradient section of the C_D v. Re_D curve, where the rate of C_D reduction has slowed beyond the initial and steeper drop in C_D immediately prior. The third marker is placed at the point where there

is a final significant change in gradient of the C_D v. Re_D curve, at $Re_D = 1.38 \times 10^5$, just before C_D plateaus considerably for the remainder of the Re_D range tested. The final two markers, at $Re_D = 1.70 \times 10^5$ and $Re_D = 2.74 \times 10^5$, represent the beginning and end of the final plateau in the C_D v. Re_D curve respectively – where C_D actually continues to fall but only very gradually, by $\Delta C_D = 0.03$ over $\Delta Re_D = 1.19 \times 10^5$.

From the results of the experiments discussed in section 6.2 and section 6.3, the jet to cross flow ratio for the $z_J = 20mm$ cylinder was found to be $0.07 \leqslant R \leqslant 0.41$. On the basis of the data available, the cross-flow velocity was estimated only for the $z_J = 20mm$ cylinder, however it can be assumed that the variation in the ratio of local cross-flow velocity to free-stream velocity will not vary significantly between $z_J = 10mm$ and $z_J = 20mm$ setups throughout the Re_D testing range. Given that the mean jet velocities of the two arrangements match closely up to $Re_D = 1.2 \times 10^5$ – even after the deviation in C_D between the two – the plot in Figure 6.6 can be considered representative of the variation of R with Re_D for $z_J = 10mm$; thus, the range of jet to cross-flow velcoity ratio for $z_J = 20mm$ is estimated to be $0.06 \leqslant R \leqslant 0.35$.

For the cylinder with passive jets setup, all SOFV tests were carried out to resolve the topological features downstream of the jet exit – around the points of flow separation from the cylinder. SOFV tests conducted around the jet exit holes were considered, however it was decided that these were best avoided due to the difficulty of achieving a detailed analysis at sub-millimetre scale and also to prevent the oil mixture from clogging the small diameter, long stroke-ratio jet exit holes. Foss (1980) is one of only a few researchers to publish a detailed analysis of jets in cross-flow topology at low values of R. As part of his analysis, Foss produced schematics of surface streaking patterns interpreted from SOFV tests in the immediate vicinity

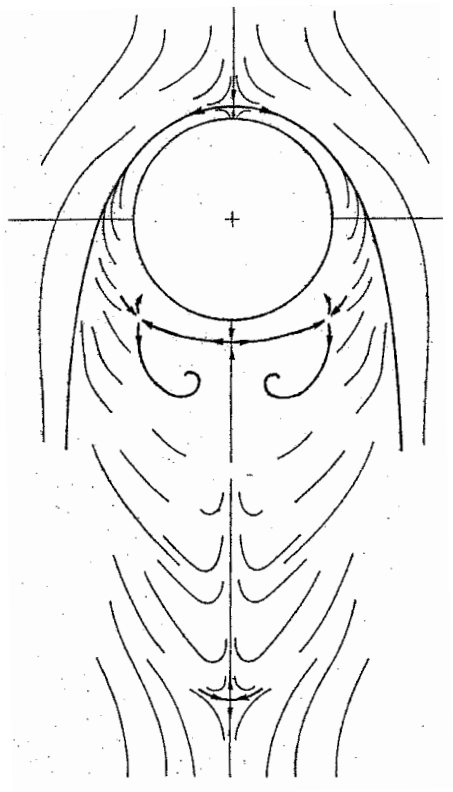

Figure 7.16 – Schematic of wall shear stress and location of critical points – produced by tracing surface streak lines from photographs of a SOFV test – for a jet in cross-flow at $R = 0.3$, from Foss (1980). Free stream direction is top to bottom.

of low R jets in cross-flow to provide an insight into the transformation of the flow topology with incremental changes of R. One such schematic is shown in Figure 7.16, providing Foss' (1980) interpretation of the surface flow topology within the range of interest here – for a jet in cross-flow at $R = 0.3$. Saddle points immediately fore and aft of the jet hole indicate flow separation around the perimeter of the jet exit hole, and both the sign of rotation of the CRVP forming on the leeward side of the jet and the saddle point located further downstream – at the bottom of the schematic – fit well with the expected topology of a hairpin vortex formation above the cross-flow surface.

In addition to the investigation of the jet instability generated by the jet-cross-flow interaction and subsequently studied analyses of Sau and Mahesh (2008) and Ilak et al. (2012) – see section 6.5 – the work by Foss (1980) provides the means to trace the influence of the passive jets' on the cylinder cross-flow and how this interaction develops as it progresses downstream. Further work is required to provide clear evidence of the finer details – for example, as to how the instabilities formed by the passive jets develop and mix with the boundary layer as they are swept downstream – but a reasonably confident picture emerges from the research as to the flow topology and mechanisms prior to flow separation and interaction with the cylinder wake.

7.4.1 $0.94 \times 10^5 \leqslant Re_D \leqslant 1.13 \times 10^5$

Starting from the lowest Reynolds number SOFV tests, the photographs in Figure 7.17(a) and Figure 7.17(b) provide a comparison of surface shear stress patterns found at $Re_D = 0.94 \times 10^5$ and $Re_D = 1.13 \times 10^5$, respectively. There is not a lot of well-defined structure to the surface covering of oil solution of the $Re_D = 0.94 \times 10^5$ test in Figure 7.17(a), but the first immediately recognisable sign of influence from the passive jets are the channels in the oil mixture furrowed by the jet-energised stream as it is swept downstream by the cross-flow – this, perhaps, can be seen more clearly from a wider angle view which can be found in Figure F.1(a) along with wide angled photographs of all other test results of this study in Appendix F. The image frame of the photograph in Figure 7.17(a) was selected as it is one of only a few regions of the cylinder span where there are signs of delayed separation; this is identified here by the evidence of separation lines between the holes which are sliced through by the jet emission directly downstream of, and in line with, the jet

holes. At low Reynolds numbers it is difficult to get a clear pattern of the surface shear stress in the film of oil mixture, however the fact that there are only sporadic signs of delayed separation and pattern formation across the span shows: firstly, some of the effects the passive jets are having in first generating drag reducing flow mechanisms; and secondly, that these effects are not equally spread across the span – or on either side (i.e. from each row of jet holes), as is clear from the C_L profile of Figure 7.15. It is common for flow regimes in cylinder flow to begin sporadically across the span – due, at least in part, to experimental imperfections – however here it may also indicate a preference for increased jet flow from some areas of the span over others.

If one looks very closely at the region immediately downstream of the clearly identified separation lines in the middle of Figure 7.17(a), there is the faintest indication of rotation in the cylinder plane. Taking a slightly broader view of the span it is questionable whether there are larger cell-like formations appearing on the cylinder surface; a semi-circular shaped area of a darker shade can be identified in Figure 7.17(a), roughly spanning the middle six jet holes of the image. A second, very similar formation can be seen to the right of this in Figure F.1(a) which also shows signs of a large counter-rotating vortex structure forming within the cell. This is perhaps additional evidence of the intrinsic three-dimensional nature of even plain cylinder flow, with the cell formation bearing resemblance to the type found and discussed by Humphreys (1960).

At $Re_D = 1.13 \times 10^5$ (Figure 7.17(b)), clearly identifiable and repeating structures are now visible along the entire cylinder span. There still appears, however, to be a variety in the shape and prominence of these patterns, but as a step change from $Re_D = 0.94 \times 10^5$ they are much more regular and increasingly well defined.

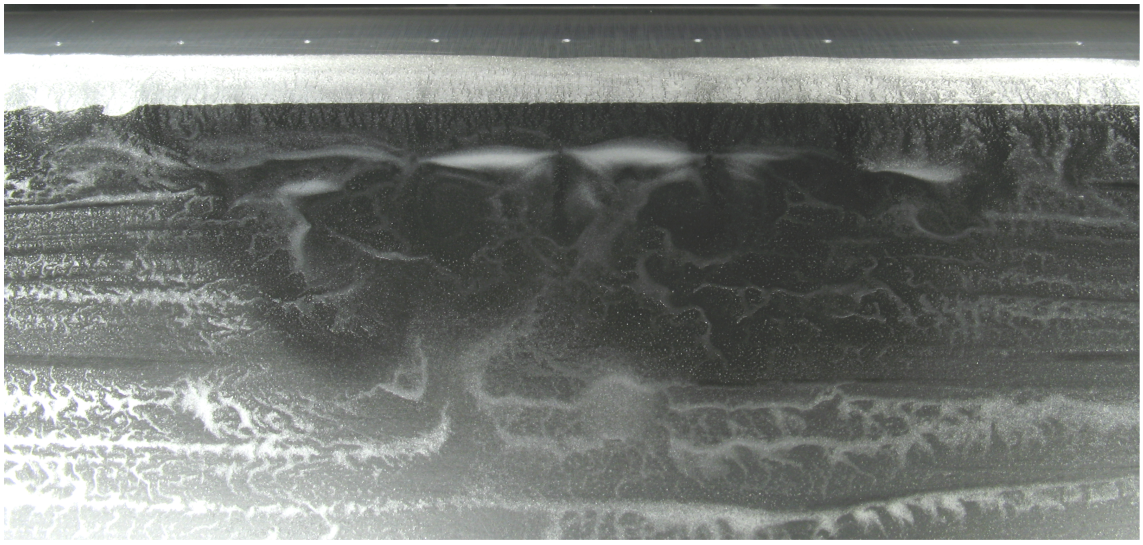

(a)

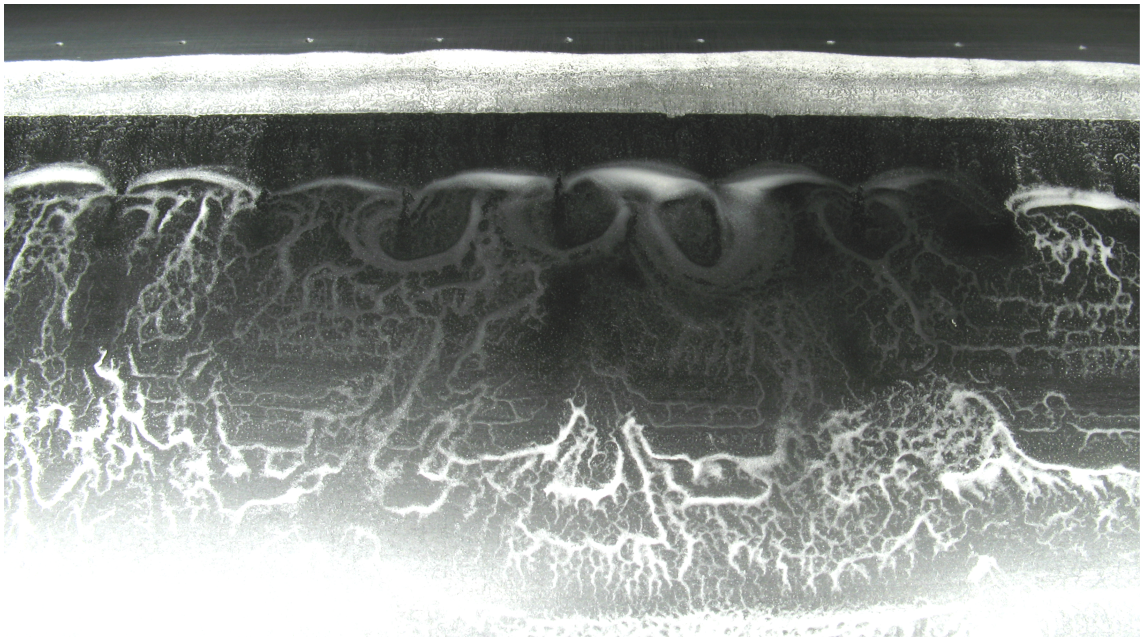

(b)

Figure 7.17 – Photographs of SOFV results on the $z_J = 10mm$ cylinder, at: (a) $Re_D = 0.94 \times 10^5$; and, (b) $Re_D = 1.13 \times 10^5$. Figure continues over the page (full caption follows final photo).

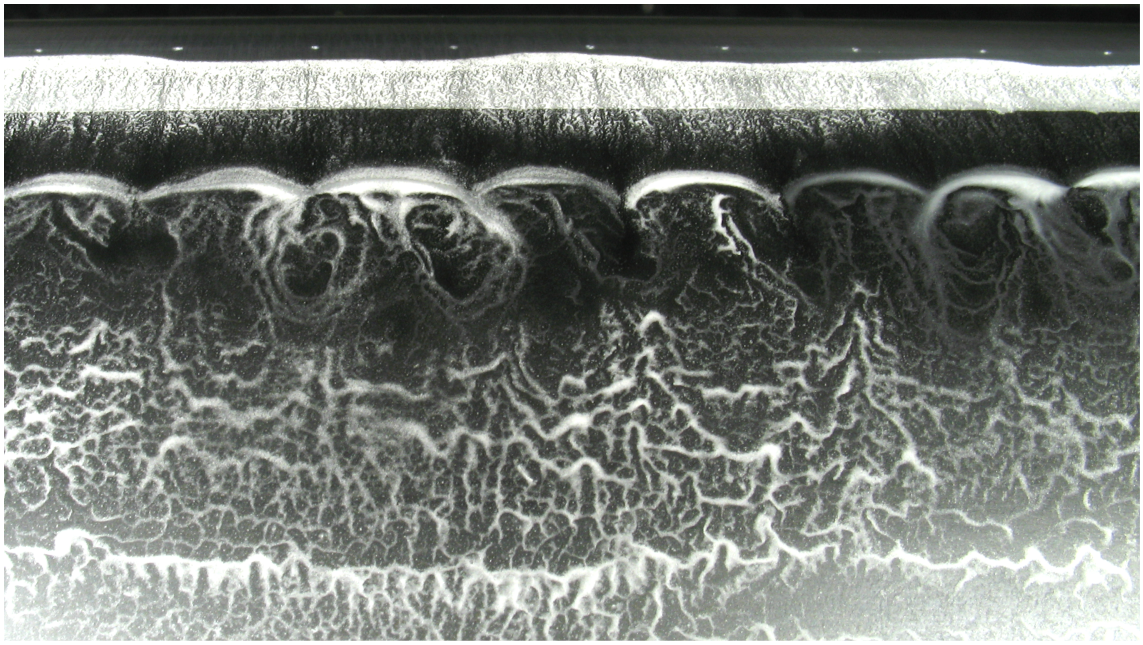

(c)



(d)

Figure 7.17 – Photographs of SOFV results on the $z_J = 10mm$ cylinder, at: (c) $Re_D = 1.38 \times 10^5$; and, (d) $Re_D = 1.70 \times 10^5$. Figure continues over the page (full caption follows final photo).

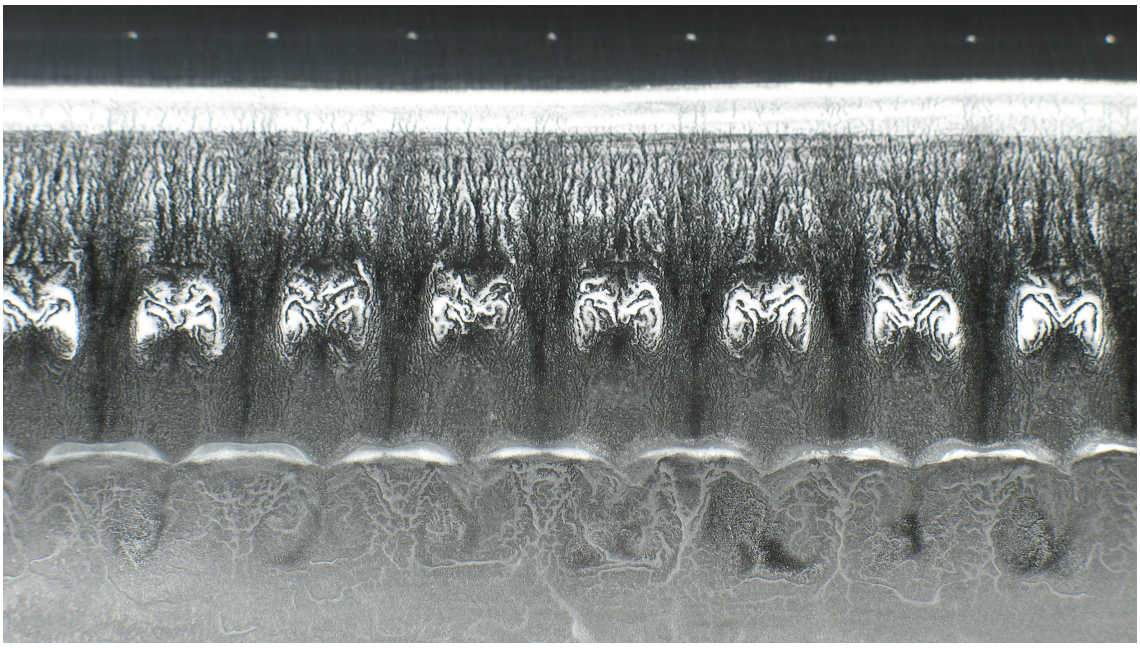

(e)

Figure 7.17 – Photographs of SOFV results on cylinder with passive jets, $z_J = 10mm$, at: (a) $Re_D = 0.94 \times 10^5$; (b) $Re_D = 1.13 \times 10^5$; (c) $Re_D = 1.38 \times 10^5$; (d) $Re_D = 1.70 \times 10^5$; and, (e) $Re_D = 2.74 \times 10^5$. See preceding pages for figures (a) – (d).

This can be attributed in part to the increased flow velocity providing a greater level of surface shear to carve into the oil film, but the effects of the passive jets are also much less sporadic. Apart from a discontinuous separation line cut through by the jet-energised flow, there are now indisputable signs of vorticity and occasionally counter rotating vortex pairs forming on the cylinder surface, immediately downstream of the initial separation.

In an effort to correlate the formation of flow topology with their effect on drag reduction as Reynolds number is varied, the angular position – with respect to the cylinder stagnation point – of separation points, ϕ_s, of selected, commonly identifiable flow streams, have been measured. From an analysis of the skin friction line patterns of these SOFV tests, the evolution of the flow topology allows one to

identify the separation points of three regularly occurring flow streams: (1) the initial (laminar) separation point which occurs downstream of the span-wise location between the jet holes – equivalent to that of a plain cylinder; (2) the jet-energised flow stream – the downstream extent to which flow in-line with the jet holes remains attached; and, (3) the reattached (turbulent) flow stream – which develops at higher Reynolds numbers with the formation of the laminar separation bubble immediately downstream of the initial laminar separation. To supplement the analysis of the SOFV photographs, these points are plotted in Figure 7.18.

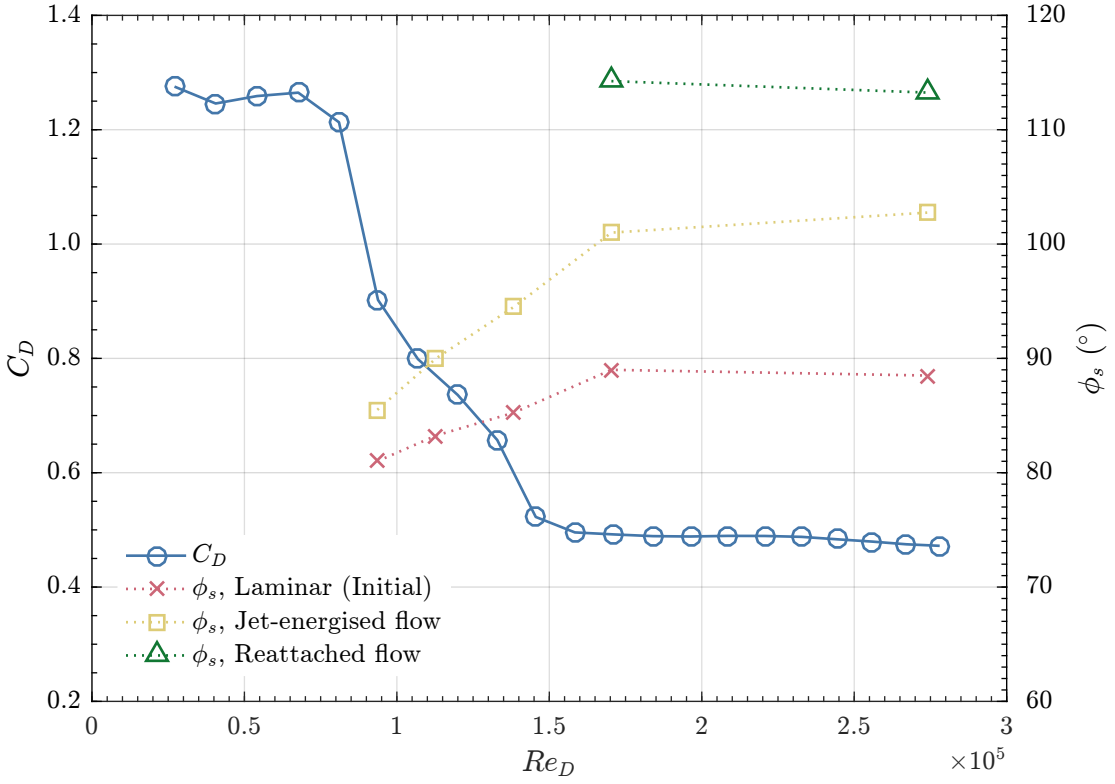

Figure 7.18 – Passive jets, $z_J = 10mm$; plot of C_D v. Re_D overlaid with the variation in time-averaged angles of separation, ϕ_s, of selected flow streams identified on the cylinder surface from skin friction line patterns – measured directly from SOFV tests.

The fact that $Re_D = 0.94 \times 10^5$ is found where there is a significant and steep

drop in C_D is interesting because the introduction of only very small, weak jet flow ($R \approx 0.28$, see section 6.3) is sufficient to: (i) produce channels of delayed flow separation; and, (ii) as shown in section 5.5, prevent von Kármán vortex shedding – which ceases to occur for $Re_D > 0.66 \times 10^5$. As inferred from Figure 7.17(b) and Figure 7.18, both of these processes strengthen with increasing Reynolds number to $Re_D = 1.13 \times 10^5$ where vorticity is now clearly shed into the wake.

7.4.2 $1.38 \times 10^5 \leqslant Re_D \leqslant 1.70 \times 10^5$

The flow topology found at $Re_D = 1.38 \times 10^5$ (Figure 7.17(c)) appears to be much the same as for $Re_D = 1.13 \times 10^5$ in terms of structures found, but again more regular and pronounced along the span. Figure 7.18 shows that the both the initial laminar and jet-energised flow separation points continue in a relatively linear trend to push further downstream. It can be expected that with the increase in jet to cross-flow velocity from $R \approx 0.28$ to $R \approx 0.35$ at $Re_D = 1.38 \times 10^5$ that the strength of vorticity shed into the wake would be increased. Looking again at Figure 7.18, it is perhaps a combination of both of these actions which continues to push C_D down ever more rapidly with increasing Re_D at this point.

With $Re_D = 1.70 \times 10^5$ (Figure 7.17(d)) comes a drastic change in the pattern of skin friction lines; counter rotating vortex pair (CRVP) structures are very intricately and strongly defined, and the initial laminar separation lines wrap neatly around the span-wise repeating CRVP cells. The measured angles of separation continue to increase in much the same linear trend but, compared to the tests at lower Reynolds numbers, the span-wise variation in pattern structure is small. There is now a distinctive extension to the structure in the stream-wise direction where there is an observable influence downstream of the separation points of both the laminar

and jet-energised streams. There now appears to be evidence of a separation line downstream of the initial CRVP – the first evidence of a separation bubble reattachment – in addition to reverse flow channelling between the reattached flow streams, meeting at the separation point of the jet-energised stream. Despite the evidence of this contraflow, there is very little else to suggest that a secondary CRVP forms at this Reynolds number.

It is intriguing to note here the topological arrangement of the delayed separation line (in-line with the jet-energised flow) at $Re_D = 1.70 \times 10^5$ – it is swept into the adjacent foci of the (primary) CRVP in the what appears to be identical fashion to the $z_J = 20mm$ passive jets at $Re_D = 2.70 \times 10^5$ (see, for example, Figure 7.2). This might suggest that increasing Reynolds number beyond $Re_D = 2.70 \times 10^5$ for the $z_J = 20mm$ cylinder may eventually produce a flow topologically similar to that of the $z_J = 10mm$ spaced jets at $Re_D = 2.70 \times 10^5$ – that is an increase in the separation angle of the jet-energised flow stream accompanied with a dislocation from the primary CRVP.

It is also worth noting that the jet to cross-flow velocity has not increased from $Re_D = 1.38 \times 10^5$, staying relatively stable at $R \approx 0.35$ so the sudden transformation in flow topology is not owed to an increase in the velocity differential of jet and cross-flow. Perhaps, therefore, it is simply due to the increase in Reynolds number and hence propensity for instability.

7.4.3 $Re_D = 2.74 \times 10^5$

As the Reynolds number increases to $Re_D = 2.74 \times 10^5$ (Figure 7.17(e)), the tracked points of flow separation plateaued with only relatively small variations from $Re_D = 1.70 \times 10^5$ (see Figure 7.18). The only flow stream to further delay separation was

the jet-energised flow by approximately $\Delta\phi = 2°$. This relative stasis of separation points coincides with the flattening of the C_D v. Re_D profile for $Re_D > 1.6 \times 10^5$.

There is a noticeably different consistency of oil solution for the $Re_D = 2.74 \times 10^5$ SOFV test compared to $Re_D = 1.70 \times 10^5$ – a higher ratio of tracer particles to oils – which makes it difficult to make a direct comparison with some of the flow structure elements found at $Re_D = 1.70 \times 10^5$. The flow structure has, however, changed in much the same way as is discussed in the comparison of the $z_J = 10mm$ and $z_J = 20mm$ SOFV tests at $Re_D = 2.7 \times 10^5$ (see section 7.3), excepting the observation of a secondary CRVP.

Again, compared with the tests at lower Reynolds numbers, an increase in Re_D produces a more strongly defined and regimented set of patterns in the surface oil-film. The secondary CRVP is visibly present for the first time in this study of the topological progression with Re_D, and – taking into account the previous discussion in section 7.3 – it appears to share a similar structure to that of the primary CRVP at lower Re_D, with a secondary delayed separation line immediately following the CRVP.

Another interesting observation between the test results of $Re_D = 1.70 \times 10^5$ and $Re_D = 2.74 \times 10^5$ is that the gaps between the primary CRVP have also grown considerably, despite the likelihood of a decrease in R (see section 6.3) and hence reduced volume of jet emission relative to the cross-flow.

Chapter 8

Transverse jets: Shear layer development and wake dynamics

In order to develop a more in-depth analysis – both qualitative and quantitative – and hence better understanding of the near-wake structure generated by the application of the passive transverse jets concept, investigations were made in two different coordinate planes using two different types of PIV arrangement. The experiments were carried out on cylinder models with and without the flow control concepts in order to provide clear evidence of the effects of these passive devices. The first PIV setup acquired data in the (x, y) plane with a single camera positioned at a series of streamwise (x – coordinate) locations, to provide analyses of the near-wake, shear layer development and boundary layer separation. The second PIV setup acquired data in the (y, z) plane in a stereo camera arrangement – at a fixed location immediately downstream of the cylinder – providing all three components of velocity for the near wake, specifically focusing on the shear layer development. The following sections analyse and discuss the results of these experiments.

Detailed descriptions of the PIV equipment, setup, acquisition and processing procedures can be found in section 3.8.

8.1 Flow separation

Using the (x, y) plane PIV setup, flow separation could be tracked to provide an estimation of the separation angle and hence make a comparison between a plain cylinder and the cylinder with passive jets. The results found here are compared with the measurements taken during surface oil flow visualisation tests – see chapter 7, which enabled direct measurement of time averaged separation points on the cylinder surface. All of the (x, y) plane PIV tests were conducted at $Re_D = 1.5 \times 10^5$ which corresponds to the point on the C_D v. Re_D curve for the 20mm spaced jets at which C_D is still steeply falling with increasing Re_D, the distinctive CRVQ – see chapter 7 – is yet to form and there is still a substantial increase in Re_D required to reach the point where the drop in C_D dramatically slows at around $Re_D = 1.8 \times 10^5$. At $Re_D = 1.5 \times 10^5$, $C_D \approx 0.7$ for $z_J = 20mm$, which is significantly lower than that of a plain cylinder at equivalent Reynolds number. This point in the Re_D range was chosen as it provides a good distinction between the plain and passive jets cases in terms of C_D, but at a Reynolds number in the middle of the range tested in order to build understanding of how the drag reduction mechanisms develop prior to the high Re_D range.

Since these tests were conducted at sub-critical Reynolds numbers for a plain cylinder, the vortex shedding and hence cyclical fluctuations in static pressure over the cylinder circumference lead to a not inconsiderable variation in separation angles over a single vortex shedding period; see, for example, Dwyer and McCroskey (1973)

who found a variation in separation angle, ϕ_s, of 10° for plain cylinder flow at $Re_D = 1.06 \times 10^5$. Even for the cylinder with passive jets – where von Kármán vortex shedding has been shown to cease for $Re_D \geqslant 1 \times 10^5$ (section 5.5) – there is a considerable but sporadic variation in the instantaneous separation angle. The estimations made here of the flow separation angle for each of the cylinder setups are therefore taken from time-mean plots. For the passive jets setup, two span-wise acquisition locations were used; one directly in line with a jet, and another at a location between – and equidistant from – two adjacent jets.

PIV data was taken with a spatial resolution of $\approx 0.5mm$ which allowed fine features of the flow to be observed close to the cylinder surface. The boundary layer of the cylinder could not be resolved, however, due to the difficulty of mitigating reflections of laser light from the cylinder surface. The diffusion of laser light in the immediate vicinity of the reflection (at the cylinder surface) saturates the limited light-intensity scale of the camera CCD (image sensor) such that seeding particles in this area of the image can no longer be distinguished. During image pre-processing, masking of the cylinder and areas of reflection necessarily overlapped areas of the boundary layer and hence the points of flow separation were estimated without precise measurement from within the boundary layer. Here, because flow separation occurs close to $\phi = 90°$ on the cylinder surface, the error of equating the local stream-wise velocity component, u_x, with the tangential velocity at the point of separation, $u_{x,y}$, is small. From the time averaged velocity vector field, the line of $\bar{u}_x = 0$ is plotted; as this line approaches the cylinder surface, the separation angle is estimated from the extrapolated point where this line touches the cylinder surface, with an approximate uncertainty of ±1.5°.

In Figure 8.1, a vector field plot in the (x, y) plane is set on a colourmap of local

velocity in the free-stream direction, u_x, and is overlaid with a schematic of the cylinder (green line) and a marker (black line, inset) to indicate the estimated time mean separation angle for a plain cylinder at $Re_D = 1.5{\times}10^5$. The separation angle was estimated to be $86^\circ \leqslant \phi_s \leqslant 89^\circ$ which matches well with the previous SOFV tests (for both the plain cylinder and the initial laminar separation lines which form between jets – see Figure 7.18) and quite well with, for example Fage (1929), but is somewhat higher than the values measured by Achenbach (1968), who measured a very low value of $\phi_s = 75^\circ$ for a plain cylinder without end plates at $Re_D = 1.5{\times}10^5$.

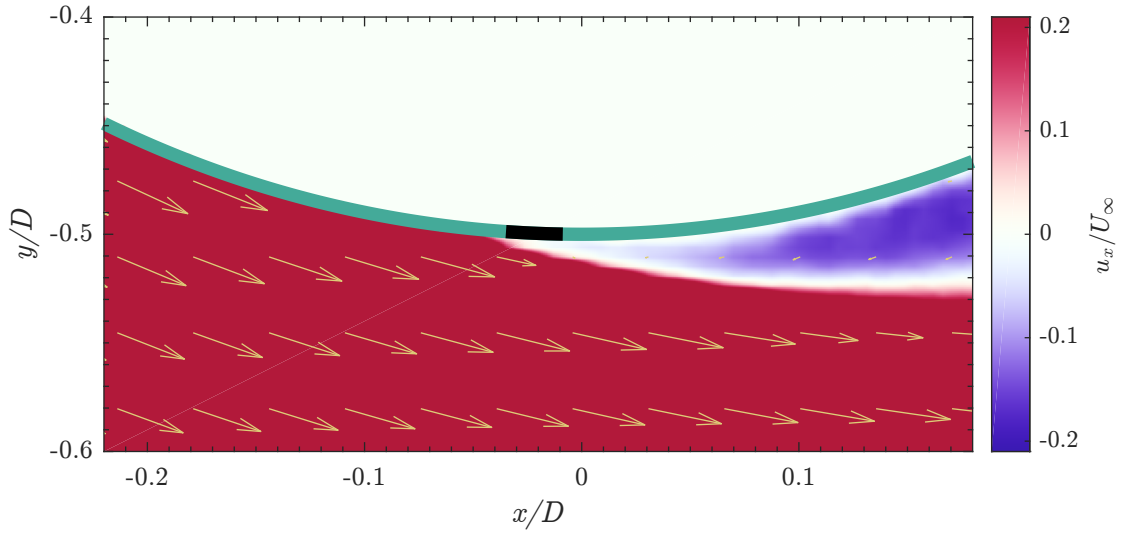

Figure 8.1 – Mean range of flow separation, measured with respect to the mean cylinder stagnation point (designated $\phi = 0^\circ$), for a plain cylinder at $Re_D = 1.5{\times}10^5$. The range of separation angles is represented by the black segment of the cylinder circumference (drawn in green) and was found to be $86^\circ \leqslant \phi_s \leqslant 89^\circ$.

Time-mean vector fields overlaid on plots of local velocity in the free-stream direction, u_x, are shown in the (x, y) plane for the two span-wise acquisition locations of the cylinder with passive jets in Figure 8.2, where the span-wise locations are: (a) in-line with a jet hole; and, (b) in the middle between two adjacent jet exit holes. Figure 8.2 provides a means of comparison of the flow separation angles for these

two span-wise locations at $Re_D = 1.5{\times}10^5$, where, as in Figure 8.1, the cylinder is outlined in green and the estimated separation angle ($\phi_s \pm 1.5°$) is marked by a black segment inset into the green line.

The first thing to notice is that there is clear difference in the time-mean separation point at these two locations of the span, measured here to be about $\Delta\phi_s = 4°$. With reference to the SOFV tests in section 7.4 and skin-friction line patterns discussed in section 7.2.2, this is to be expected as for $z_J = 10mm$ from $Re_D \geqslant 1.13{\times}10^5$ there is a discontinuous separation line – well marked by the curved separtrices of saddle points along the span – regularly broken by the jet-energised streams to indicate a clear angular variation in separation points. There were no SOFV measurements at $Re_D = 1.5 \times 10^5$ for the $z_J = 20mm$ cylinder to compare with, but a reasonable comparison can be made with the $z_J = 10mm$ cylinder at $Re_D = 1.13 \times 10^5$, where the drag coefficient is similar at $C_D \approx 0.76$ compared to $C_D \approx 0.70$ for the 20mm spaced jets. As can be seen in section section 7.4, the measurement of $\Delta\phi_s$ between the initial laminar separation and the delayed separation of the jet-energised stream for the $z_J = 10mm$ cylinder at $Re_D = 1.13{\times}10^5$ was approximately $\Delta\phi_s = 6.5°$. By comparison, the estimation from the PIV data for the $z_J = 20mm$ cylinder at $Re_D = 1.5 \times 10^5$ was a mean value of $\Delta\phi = 4°$.

The SOFV measurements were somewhat larger than that shown in the PIV data but there is a clear correlation between the initial separation point found between the jets and the delayed separation in line with the jets. Without a direct comparison of an SOFV test for the $z_J = 20mm$ cylinder $Re_D = 1.5{\times}10^5$, it is difficult to make firm conclusions, however a number of factors may have contributed to the discrepancy. Comparing the angles of the delayed separation lines for the jet-energised streams of both $z_J = 10mm$ and $z_J = 20mm$ cylinders at $Re_D = 2.7 \times 10^5$, the angles of

separation for the $z_J = 10mm$ cylinder is $\Delta\phi = 2.5°$ greater and, hence, perhaps it is the case that this trend is replicated for lower Re_D. Since the test here for the $z_J = 20mm$ cylinder is at a higher Reynolds number than the equivalent C_D test of the $z_J = 10mm$ cylinder, there will be a difference in the jet to cross-flow velocity ratio, R, which may impact on the relative difference between the initial laminar separation and the delayed separation of the jet-energised stream. In addition, as shown in the photograph of the SOFV test result for the $z_J = 10mm$ cylinder at $Re_D = 1.13 \times 10^5$ in Figure 7.17 and more broadly in Figure F.1 of Appendix F, at the lower end of the test-speed range there is an inconsistency in the effectiveness of the jets across the span – leading to a variation in the delayed separation points achieved by the jet-energised streams – and there can be significant differences in separation due to very small changes in span-wise location along the cylinder surface. The light-sheet of the experiment was very accurately aligned with a jet exit hole in the (x, y) plane, however it is clear – again particularly at lower speeds – that the topological features made visible on the cylinder surface by the SOFV tests often do not align exactly (downstream) with the jet holes.

Curiously, there is a noticeable difference between the time-mean separation angles measured on the the plain cylinder and the foremost separation angle found for the cylinder with passive jets, at the span-wise position between two adjacent jets. It was expected that these values should be very similar, but there is a substantial discrepancy of $\Delta\phi_s \approx 6°$. That the PIV data for separation angles for the plain cylinder match well with both the literature and also the laminar separation points found between jets in SOFV tests indicates the discrepancy lies with the PIV data of the cylinder with passive jets. As shown in Figure 5.8(b), at this Reynolds number there is not likely to be an asymmetrical pressure distribution caused by an uneven

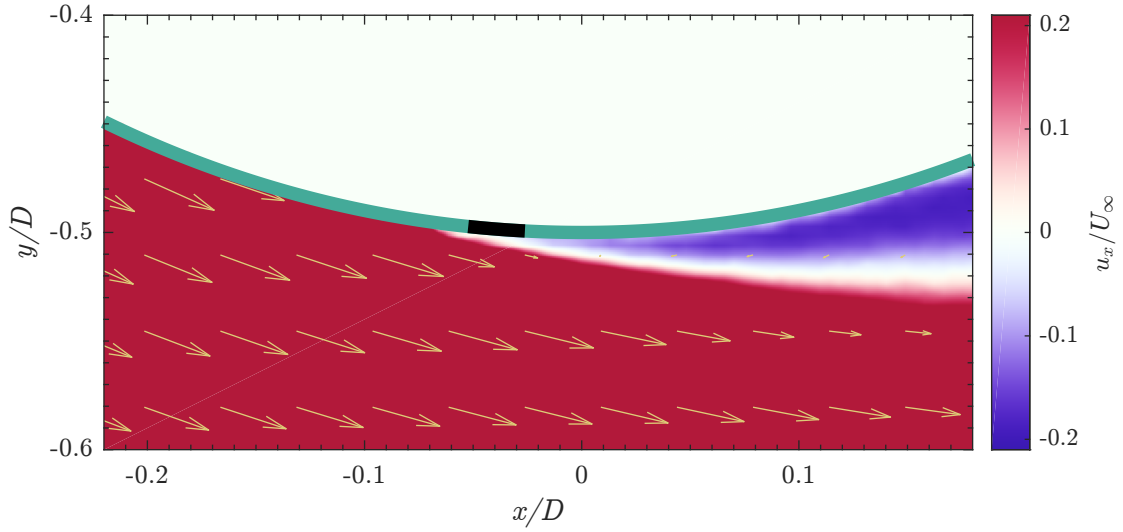

(a)

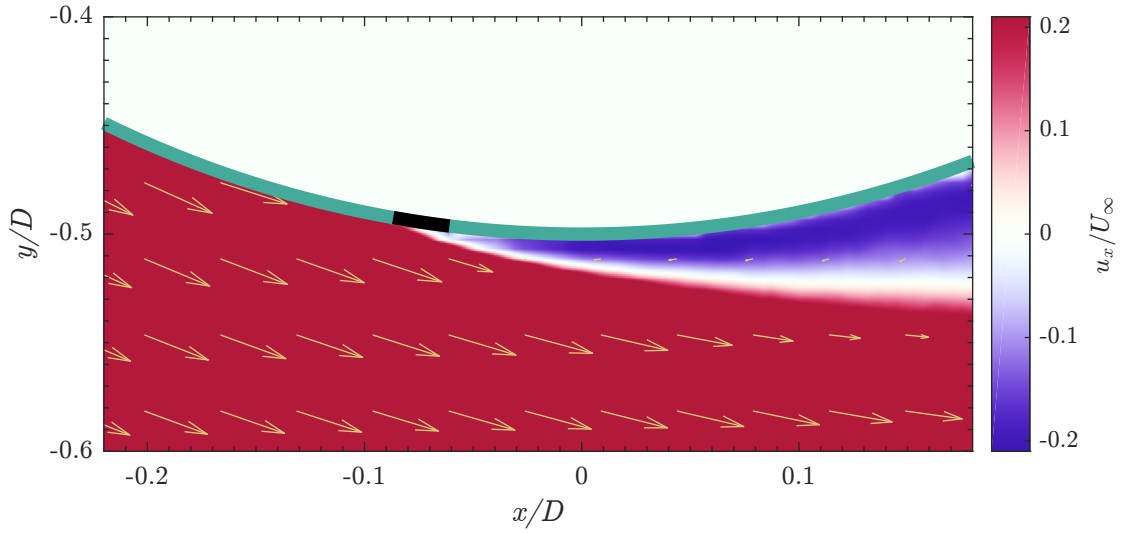

(b)

Figure 8.2 – Mean range of flow separation, measured with respect to the mean cylinder stagnation point (designated $\phi = 0°$), for $z_J = 20mm$ passive jets at $Re_D = 1.5 \times 10^5$. The range of separation angles is represented by the black segment of the cylinder schematic (drawn in green), where: (a) Span-wise position in line with a jet, $84° \leqslant \phi_s \leqslant 87°$ as shown (subsequently revised to $90° \leqslant \phi_s \leqslant 93°$); and, (b) Span-wise position between two adjacent jets $80° \leqslant \phi_s \leqslant 83°$ as shown (subsequently revised to $86° \leqslant \phi_s \leqslant 89°$).

jet distribution between the two sides of the cylinder. The experimental setup and procedure for both plain and passive-jet cylinder arrangements were identical so it is difficult to attribute the difference to a possible experimental error, however this discrepancy is also found in the analysis of wake data in the (x, y) plane, and is discussed in the following section (section 8.2). Even in the case of a substantial cylinder misalignment of the jet holes (either upstream or downstream), the initial laminar separation line – which could still be expected to form downstream of a location between adjacent jets – should still be expected to form at approximately the same angle as a plain cylinder (and indeed the same angle as the laminar separation points measured from the SOFV tests for the cylinder with passive jets). Unfortunately, it has not been possible – with the data available – to confirm whether there was an alteration of the frame of reference between the two tests, but the discrepancies in separation angles and wake formation suggest that the field of view (FOV) of the PIV camera was tilted slightly relative to the plain cylinder tests.

Assuming this to be the case, and revising the separation angles accordingly – by matching the initial separation line of the passive jets between the holes to the that of the plain cylinder – the values for the cylinder with passive jets at $Re_D = 1.5 \times 10^5$, with reference to Figure 8.2, become: (a) at a span-wise position in line with a jet, $90^\circ \leqslant \phi_s \leqslant 93^\circ$; and, (b) at a span-wise position between two adjacent jets $86^\circ \leqslant \phi_s \leqslant 89^\circ$. The revision of these values now provides a very good correlation with the findings of the the SOFV tests for the $z_J = 10mm$ (where the delayed separation of the jet-energised flow for $1.13 \times 10^5 \leqslant Re_D \leqslant 1.38 \times 10^5$ was $90.0^\circ \leqslant \phi_s \leqslant 94.5^\circ$ and the initial laminar separation for $1.38 \times 10^5 \leqslant Re_D \leqslant 1.70 \times 10^5$ was $85.5^\circ \leqslant \phi_s \leqslant 89.0^\circ$ – see section 7.4), and it is reasonable to assume that a realignment of this data provides a good estimate of the separation angles

and wake formation, however further work is required to provide a more conclusive study of these features.

8.2 Shear layer development/mixing

Taking a broader view of the cylinder wake from the time-mean PIV data, a clear distinction can be made between the shape and development of the shear layer in each case. Comparing the time-mean plot of u_x/U_∞ at $Re_D = 1.5 \times 10^5$ for the plain cylinder in Figure 8.3 with those of the $z_J = 20mm$ jets setup in figure Figure 8.4(a) and Figure 8.4(b) – representing the span-wise locations in-line with, and between, jets respectively – the curvature of the shear layer behind the plain cylinder is much higher than the two plots of the jets setup. The higher curvature of the time-mean position of the shear layer leads to a shorter length of the recirculation zone (the furthest distance downstream where the stream-wise velocity goes to zero). By tracing the line of $\bar{u}_x = 0$, the boundary of the mean recirculation can be identified and measured for comparison. For the plain cylinder, $\bar{u}_x = 0$ extends downstream to $x/D = 1.24$, which is somewhat larger than that found by Cantwell and Coles (1983) – who were surprised by the small size of the recirculation bubble – which had a mean closure point "slightly more than" $x/D = 1$ for a plain cylinder at $Re_D = 1.4 \times 10^5$ with a mean separation point of $\phi_s = 77°$. Cantwell and Coles used a "flying" pair of hot-wires (see Coles et al., 1978) to acquire velocity vector data of the wake region and stated some difficulties acquiring good quality data in and near the zone of recirculating mean flow owing to the directional sensitivity of the hot-wire probes.

For the cylinder with passive jets, the length of the recirculation zone extends

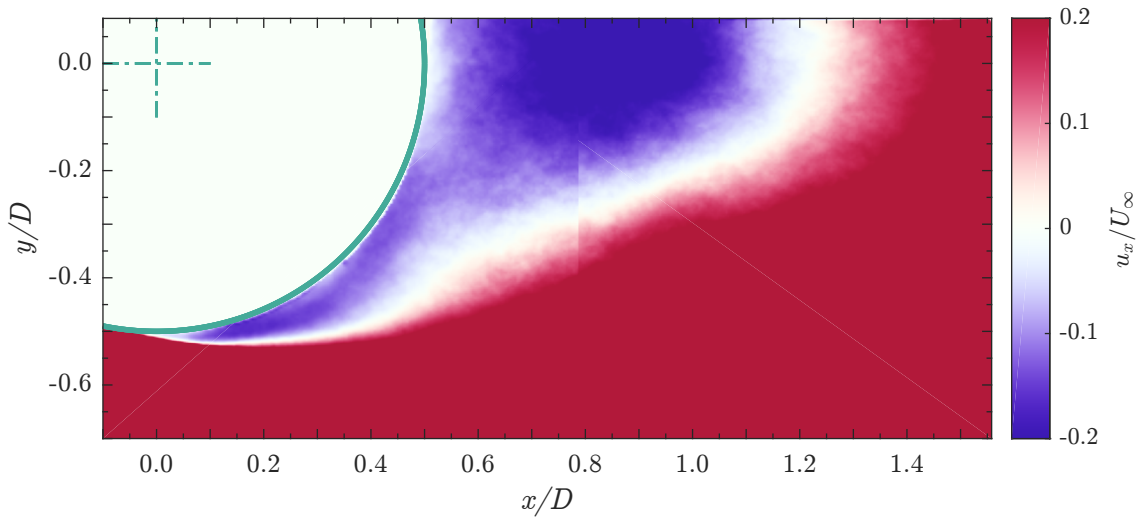

Figure 8.3 – Plot of u_x/U_∞ showing the time-mean length of the recirculation region for a plain cylinder at $Re_D = 1.5{\times}10^5$. The furthest downstream extent of the line traced by $\bar{u}_x = 0$ occurs at $x/D = 1.24$. The colourbar scale for u_x/U_∞ is clipped to ± 0.2 in order to accentuate velocity gradients within shear layer and wake – see Appendix G.1.2 for full velocity scale plots. This plot has been formed by stitching together the mean vector fields of two datasets taken separately at overlapping stream-wise locations.

to $x/D = 1.49$ at the span-wise position in-line with a jet. For the span-wise position between two adjacent jets, the boundary of $\bar{u}_x = 0$ extends even further downstream, however, unfortunately this line continues beyond the FOV for this experiment. Based on an approximation of the line's trajectory, it is estimated that the recirculation region extends to $x/D \approx 1.63$.

Schiller and Linke (1933) have shown – in the transition in shear layer (TrSL) regime – that as the length of the mean recirculation region decreases, there is a reduction in base pressure and consequent increase in drag. As discussed by Tombazis and Bearman (1997), this holds true so long as the wake width at the points of formation of the shear layer are equivalent and for this case any differences according to the mean point of flow separation have little significance compared to

the relative extension of the mean recirculation length. That there is a difference in drag coefficient of approximately $\Delta C_D \approx 0.5$ between the plain cylinder and the cylinder with passive jets at this Reynolds number, this observation correlates well with Schiller and Linke's (1933) findings and clearly shows that – at this Reynolds number – the passive jets flow control concept develops a significant increase in base pressure without a narrowing of the wake width.

Comparing the two plots in Figure 8.4 there is also an obvious difference between the shear layer curvature and length of the recirculation region for the two span-wise acquisition positions of the jets setup; the position directly downstream of a jet exit hole Figure 8.4(a) has noticeably stronger curvature of the shear layer and hence shorter recirculation zone than that of the span-wise position between two jet exit holes, shown in Figure 8.4(b). This indicates a regular variation in base pressure along the span, according to the distance between adjacent jets, and this being the case, one would expect to observe a span-wise 'waviness' to the separated shear layer. The span-wise variation in both the formation of the shear layer and pressure within the wake, plus the suppression of Kármán vortex shedding along with the overall increase in length of the recirculation zone and base pressure, may all be interconnected with the counter-rotating vortices which are thought to be shed into the wake through the interaction of the passive jets and cross-flow boundary layer – as discussed in chapter 7. That there is time-mean evidence – as a result of introducing transverse jets to the cylinder surface – both of counter-rotating vortices, with filaments extending downstream from the cylinder surface, and a span-wise waviness to the separated shear layer, suggests that vorticity in a plane tangent to the cylinder surface (with rotation observable in either the (x, z) or (y, z) plane) exists in the wake.

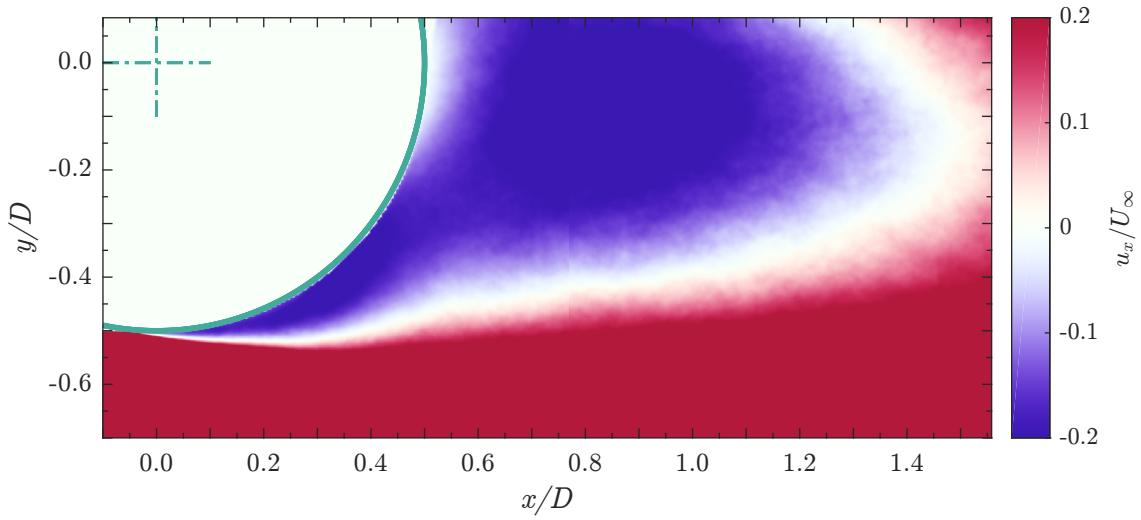

(a)

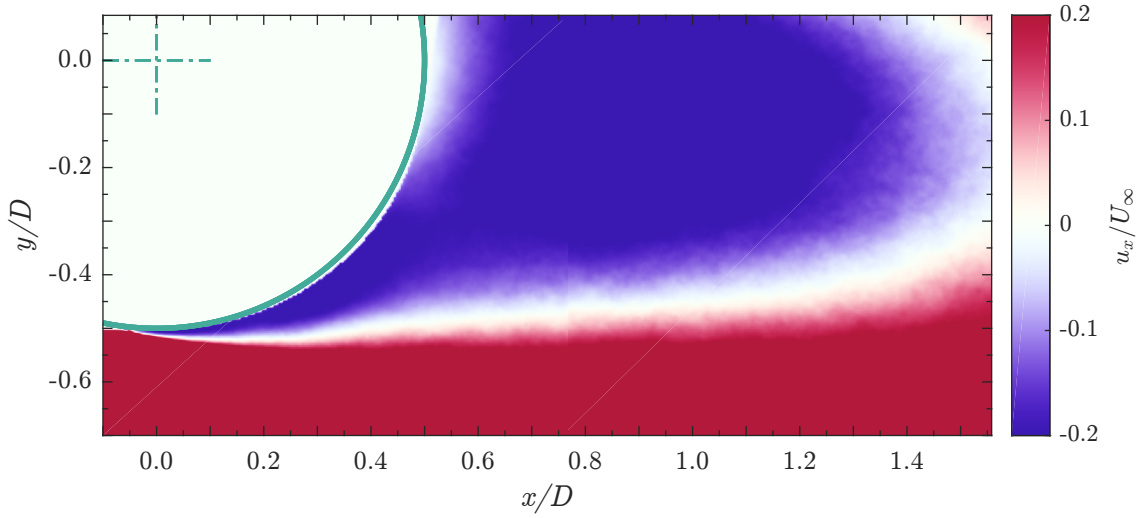

(b)

Figure 8.4 – Plot of u_x/U_∞ showing the time-mean length of the recirculation region for the cylinder with passive jets; $z_J = 20mm$, $Re_D = 1.5{\times}10^5$, at two different span-wise locations. The plot was formed by stitching together the mean vector fields of two datasets taken separately at overlapping stream-wise locations and the colourbar scale for u_x/U_∞ is clipped to ± 0.2 in order to accentuate velocity gradients within shear layer and wake – see Appendix G.1.2 for full velocity scale plots. Span-wise locations were: (a) in-line with a jet hole – the furthest downstream extent of the line traced by $\bar{u}_x = 0$ occurs at $x/D = 1.49$; and, (b) between two adjacent jets – where $\bar{u}_x = 0$ is estimated to extend to $x/D \approx 1.63$.

Adding to the discussion started in section 8.1 on the revision of the separation angles found for the cylinder with passive jets; looking closely at the shape of the wake for the two span-wise positions of the jets setup (Figure 8.4), and judging by the angle of the wake line of symmetry – extending from cylinder centreline (dashed cross-hairs overlaid in green) to the downstream tip of the recirculation region – it would appear that the formation of the wake is off-centre relative to the free-stream (x) direction. The time averaged asymmetry of the wake about the free-stream direction ordinarily indicates a variation in both the angle of flow separation and, hence, boundary layer formation on each side of the cylinder. But as has already been argued (see section 8.1) the FOV of these plots is offset by approximately $\Delta\phi = 6^{\circ}$ and at this Re_D time-mean lift has been measured to be negligible. Measuring the location of the downstream tip of the recirculation zone to be approximately $x/D = 1.5$, $y/D = 0.15$ relative to the origin of the cylinder, the resulting offset is $\Delta\phi = tan^{-1}(0.1) = 5.7^{\circ}$. It can therefore be concluded that the relative shape of wake formation is correct and the FOV of the existing data could be realigned to match the free-stream direction.

8.3 Mean-flow correlation with jet spacing

In order to get a clearer indication of the drag reduction mechanisms of the passive jets flow control concept, in particular how the tornado-like vortices found in the SOFV experiments (see chapter 7) influence the shear layer dynamics and consequently the formation of the wake, further PIV tests were conducted. These experiments acquired data in the (y, z) plane, $\Delta x = 7mm$ immediately downstream of the $\phi = 180^{\circ}$ point of the cylinder, with the intention of capturing the shear layer

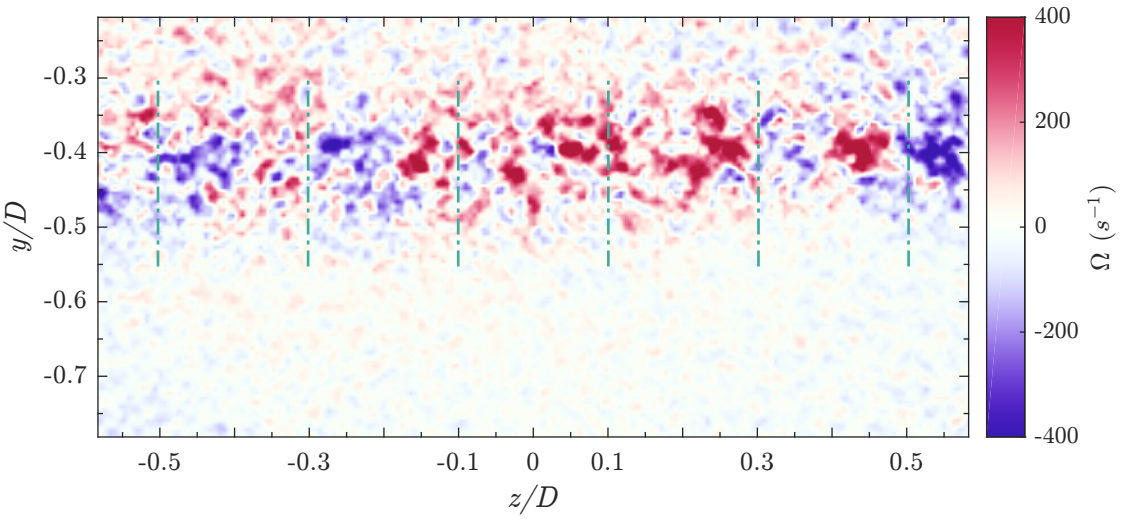

Figure 8.5 – Time-mean vorticity, Ω, in (y, z) plane, $z_J = 20mm$, $Re_D = 2.5 \times 10^5$ (uncorrected for blockage). $D/U_\infty = 2.57 \times 10^{-3}$.

dynamics as they passed through this plane. The FOV coordinates were aligned with reference to the cylinder central axis and centre-span – such that $y/D = 0$ and $z/D = 0$ coincide with the point where the cylinder central axis and a vertical line passing through the mid-span meet – and the horizontal centreline of the FOV was aligned with the bottom of the cylinder ($y/D = -0.5$). Two cameras in stereo were used to acquire all three components of velocity in a single plane. For details of the experimental setup, see section 3.8.2.

Figure 8.5 presents the time-mean vorticity, Ω, in the (y, z) plane of the near wake of the cylinder with $z_J = 20mm$ passive jets at $Re_D = 2.5 \times 10^5$ (uncorrected for blockage – drag measurements were not taken during the PIV tests due to the limitations of the setup, however, extrapolating from previous tests the corrected Reynolds number is approximately $Re_D = 2.54 \times 10^5$), where vorticity is defined by Equation 8.1.

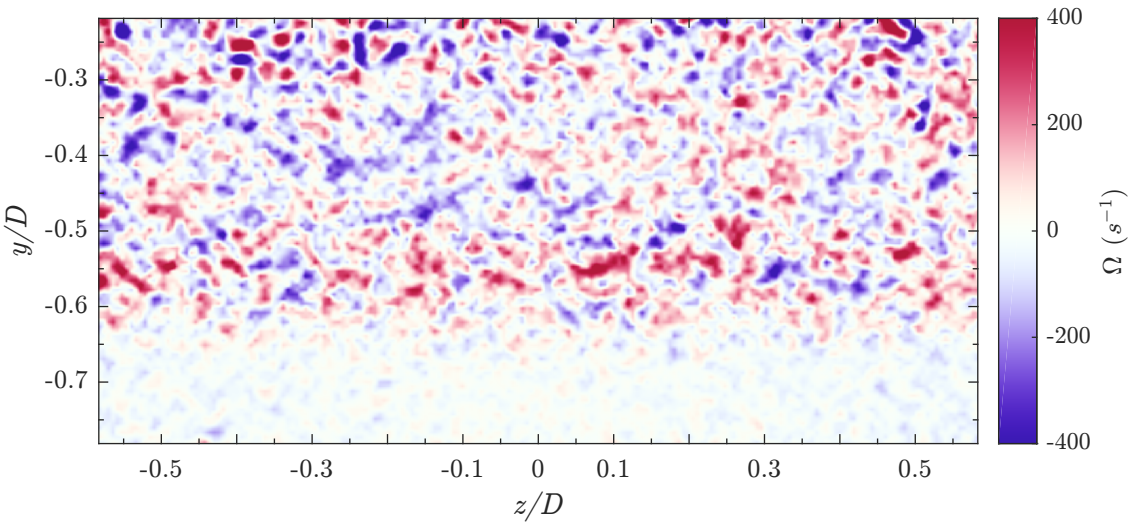

Figure 8.6 – Vorticity in (y, z) plane, plain cylinder, $Re_D = 2.5 \times 10^5$ (uncorrected for blockage). $D/U_\infty = 2.54 \times 10^{-3}$.

$$\Omega = \left(\frac{\partial u_y}{\partial z} - \frac{\partial u_z}{\partial y} \right) \tag{8.1}$$

For each vorticity plot presented throughout the thesis, a D/U_∞ scaling factor – based on the free stream velocity, U_∞, and cylinder diameter, D – is provided in the caption.

Figure 8.5 depicts the shear layer separated from the bottom surface of the cylinder and is overlaid with green dashed lines which align with the span-wise position of the jet holes. One of the first impressions is that there appears to be a relatively neat span-wise band of counter-rotating vorticity between $-0.5 \leqslant y/D \leqslant -0.3$. A closer inspection appears to suggest that there is a fairly regular organisation of this counter-rotating vorticity which may be consistent with the jet spacing. Other than the segment banded between $0.1 \leqslant z/D \leqslant 0.3$ the vorticity is quite uniformly distributed between clumps of anti-clockwise rotating fluid (red) and clockwise rotating fluid (blue).

By way of confirmation that the time-mean vorticity found in Figure 8.5 was particular to the effect of the passive jets on the cylinder flow, a comparison is made with an equivalent test of a plain cylinder – as shown in Figure 8.6.

It is clear from Figure 8.6 that the time-mean vorticity found in the wake of the plain cylinder has nothing of the coherent structure found for the cylinder with $z_J = 20mm$ passive jets. There is a broadly homogeneous spread of scattered vorticity without any of the distinctly concentrated regions of vorticity found with the passive jets. A clear difference is observed in the wake width, where the time-mean extent of the spread (in the y-direction) of wake vorticity is – as expected – greater for the plain cylinder at $y/D \approx -0.6$, than that of the cylinder with passive jets at $y/D \approx 0.5$. It is also evident that there is not so much movement in the y-axis of the shear layer for the passive jets since the band of vorticity is kept mainly within a $\Delta y/D = 0.2$ whereas for the plain cylinder a greater 'flapping' movement of the shear layer – from the continued presence of von Kármán vortex shedding – produces a much greater spread of wake vorticity to beyond the bounds of the FOV at $y/D = -0.22$.

8.4 Correlation with skin friction line patterns and flow topology

A composite of the $z_J = 20mm$ cylinder skin friction pattern schematic (see chapter 7) aligned with the corresponding vorticity plot of a (y, z) – plane slice of the shear layer, as it is swept downstream (out of the picture), is presented in Figure 8.7. The span-wise locations of the jet holes (marked 'J') are matched with the dashed green lines of the vorticity plot, representing the same span-wise coordinate of the

near-wake. The sign of rotation of both the primary (upper), and secondary (lower) CRVP are marked by coordinating the colour of the foci with the vorticity colourbar to represent either positive (anti-clockwise) vorticity – red; or, negative (clockwise) vorticity – blue). The vorticity plot of Figure 8.7 is essentially the reverse of that shown in Figure 8.5; it has been plotted in this way to reflect the vorticity of the top shear layer (i.e. that which separates from the top surface of the cylinder) so that it is coherent with the schematic of the skin friction pattern which represents that found on the top surface of the cylinder. The flow direction is therefore from top to bottom, over the schematic (as though it has been unwrapped from the top cylinder surface) and when the top shear layer separates it flows out of the page, through the vorticity plot.

Other than the aforementioned segment between $0.1 \leqslant z/D \leqslant 0.3$ – within which negative vorticity predominantly resides – the clumps of time-mean vorticity, in the (y, z) plane within the shear layer, appear to correlate quite well – both in terms of relative span-wise location and in terms of sign of rotation – with the primary CRVP. On this basis, it would appear that the vortices found in the (y, z) plane are shed into the shear layer of the cylinder wake as a direct result of the passive jet flow control, and that despite observations in the experiments of fluctuating, unstable boundary layer and wake dynamics, a time-mean structure – likely formed of tornado-like vortices shed downstream from the primary CRVP – is found.

The secondary CRVP were coloured accordingly to display the fact that these foci too lift fluid from the cylinder surface and project it downstream in the form of tornado-like vortices. These secondary CRVP vortices are considerably weaker than those of the primary CRVP, however analysis of frame by frame instantaneous vorticity plots of the shear layer in the (y, z) plane suggests that these vortices, and

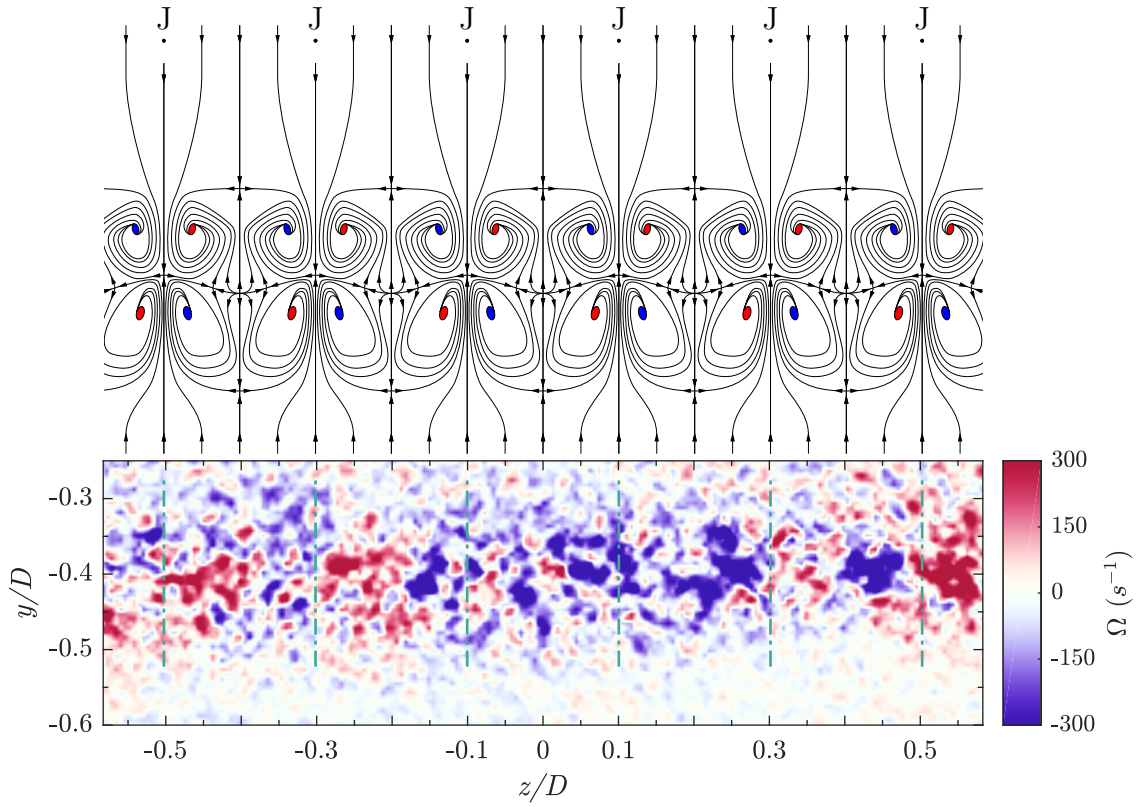

Figure 8.7 – Composite graphic of time-averaged skin-friction line pattern schematic (see section 7.2.2) with time-mean wake vorticity for passive jets, $z_J = 20mm$, at $Re_D = 2.7 \times 10^5$. Jet holes are labelled 'J' and downstream wake positions in-line with holes are marked by green dashed lines. The foci of the CRVQ are coloured according to the vorticity colourbar scale, where positive vorticity – corresponding to anticlockwise rotation – is coloured red, negative is blue. Vorticity scaling factor, $D/U_\infty = 2.57 \times 10^{-3}$.

others, interweave with, merge or weaken those of the primary CRVP in what seems like a rather erratic, non-periodic, fashion – hence the rather diffuse plot of time-mean vorticity. Unfortunately, time-resolved PIV measurements were not possible here for this particular configuration of the experiment to analyse the (y, z) plane of the shear layer; measurement of this kind would provide invaluable insight into linking the shear layer dynamics with the flow topology interpreted from observations at the cylinder surface around the area of flow separation.

As discussed initially in section 7.2.4, the drop in C_D for a cylinder with an array of transverse jets cannot be due only to a delay in flow separation and must therefore be due to the mechanisms which impart vorticity – observed as CRVP at the cylinder surface, from the interaction of the jets and cross-flow, which is subsequently shed with the separating shear layer – into the wake, and the way this impacts on the breakdown of von Kármán vortex shedding and wake formation more generally. That drag is reduced in this way – without significantly narrowing the near-wake by delaying flow separation – indicates that the base pressure is increased by mechanisms which help extend the length of the recirculation zone by preventing the formation of von Kármán vortex shedding. It is thought that introducing streamwise vorticity in the (y, z) plane of the separating shear layer could be particularly beneficial to mitigating large-scale, alternating vortex formation in the (x, y) plane (i.e. a von Kármán type vortex street) and effectively extending the length of the time-mean recirculation region.

8.5 Development of vorticity with Reynolds number

With the aim of better understanding how developments in the wake of the cylinder with passive jets can be linked to drag reducing mechanisms throughout the Reynolds number range of testing, PIV data in the (y, z) plane was acquired at five selected Re_D values based on points of interest along the C_D v. Re_D curve. A plot of the C_D v. Re_D curve, overlaid with vertical dashed lines to indicate the acquisition Re_D, is displayed in Figure 8.8. In ascending order, the acquisition Reynolds numbers (corrected for blockage) were: $Re_D = 0.26; 0.52; 1.02; 1.53$; and, 2.54×10^5, respectively.

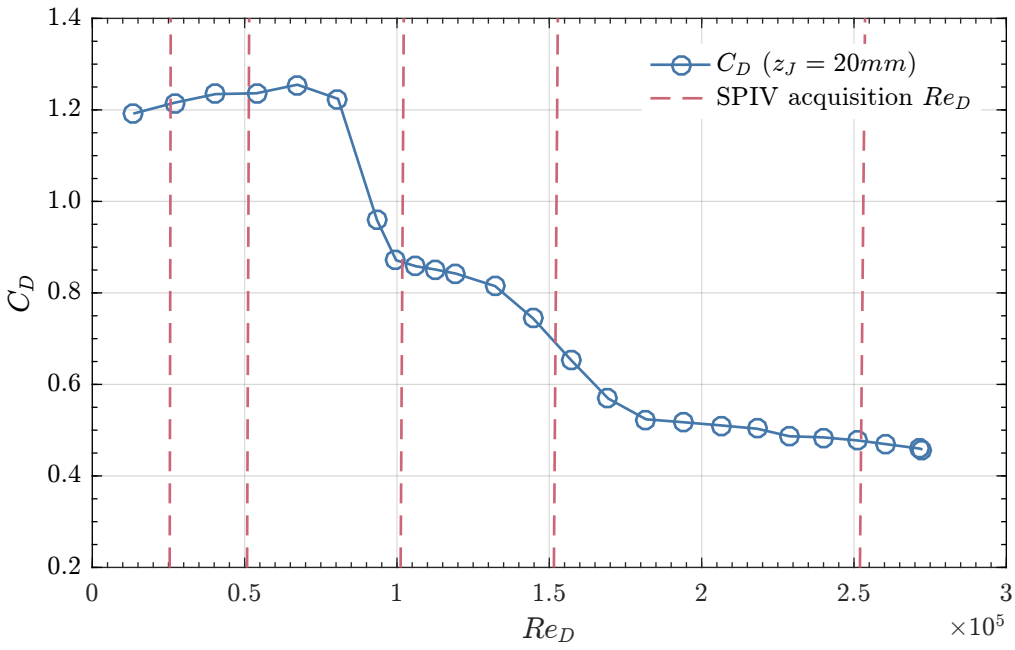

Figure 8.8 – C_D profile for $z_J = 20mm$ passive jets overlaid with vertical dashed lines to indicate the acquisition Re_D for the SPIV measurements in the (y, z) plane.

Figure 8.9 on the following pages provides a collection of plots to chart the development of time-mean near-wake vorticity with increasing Reynolds number. The FOV is of the bottom shear layer, where the $y/D = -0.5$ approximately represents the bottom-most ($\phi = 90°$) edge of the cylinder, and the central axis is at $y/D = 0$ (above the top of the plot). For the purposes of clarifying the findings as a result of the passive jets flow control concept, a full supplement of equivalent data is plotted for a plain cylinder and can be viewed in Appendix G.2.

As one would expect, with reference to Figure 8.8, the pre-critical Reynolds numbers of Figure 8.9(a) and Figure 8.9(b) show a fairly homogeneous spread of vorticity, from around $-0.65 \leqslant y/D \leqslant -0.6$ to beyond the top limit of the FOV – indicating a significant oscillation of the shear layer.

With increasing Re_D, a drastic departure from the stochastic, but evenly spread,

near-wake vorticity is observed from $Re_D = 1.02 \times 10^5$ (Figure 8.9(c)). Distinct arrangements of counter-rotating vorticity are found in the time-mean plots of Ω for both $Re_D = 1.02 \times 10^5$ and $Re_D = 1.53 \times 10^5$ (Figure 8.9(d)), where relatively large-scale (of the approximate order $0.6 \leqslant z/D \leqslant 0.7$) clumps of vorticity are arranged in a span-wise and somewhat orderly fashion. The spread of this organised wake vorticity is still fairly broad – indicating that there is still some significant vertical oscillation of the shear layer – but this can be seen to reduce in Figure 8.9(d) with the increase in Reynolds number and corresponding drop in C_D at $Re_D = 1.53 \times 10^5$.

Looking back to section 7.4, there is not an immediately obvious answer to the reason for this larger-scale clumping of vorticity. The patterns may be ascribed to the possibility of a repeated coalescence of co-rotating vortices shed from the cylinder surface, however it is thought that the reason for these vortical arrangements may be more closely associated with three-dimensional wake modes of the cylinder, of the type briefly discussed in section 7.4.1. A closer analysis of the wide-angled photos of SOFV results throughout the Re_D testing range (see Appendix F), suggests regular span-wise structures of a similar scale to those found in the time-mean vorticity plots for $Re_D = 1.02 \times 10^5$ and $Re_D = 1.53 \times 10^5$ – observable by the darker patches of often less well formed skin-friction line patterns at the cylinder surface. Williamson (1996*b*) shows that three dimensional flow features are inherent in the wake formation of cylinder flows from around $Re_D > 180$, and it is well known that the wake regime goes through several distinctive regimes with varying wake modes as Reynolds number is increased. Two particular wake instability modes (for the 'natural' wake of a plain cylinder), termed 'mode A' and 'mode B' are well known to occur from very low Reynolds numbers with wavelengths ranging from approximately $3D - 4D$ for mode A down to $1D$ for mode B (Williamson, 1996*a*).

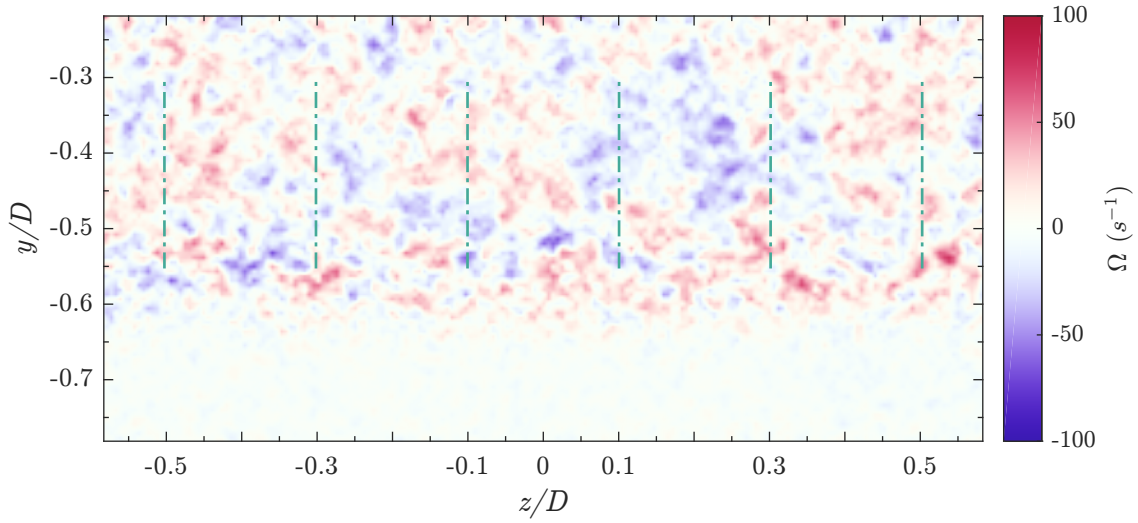

(a)

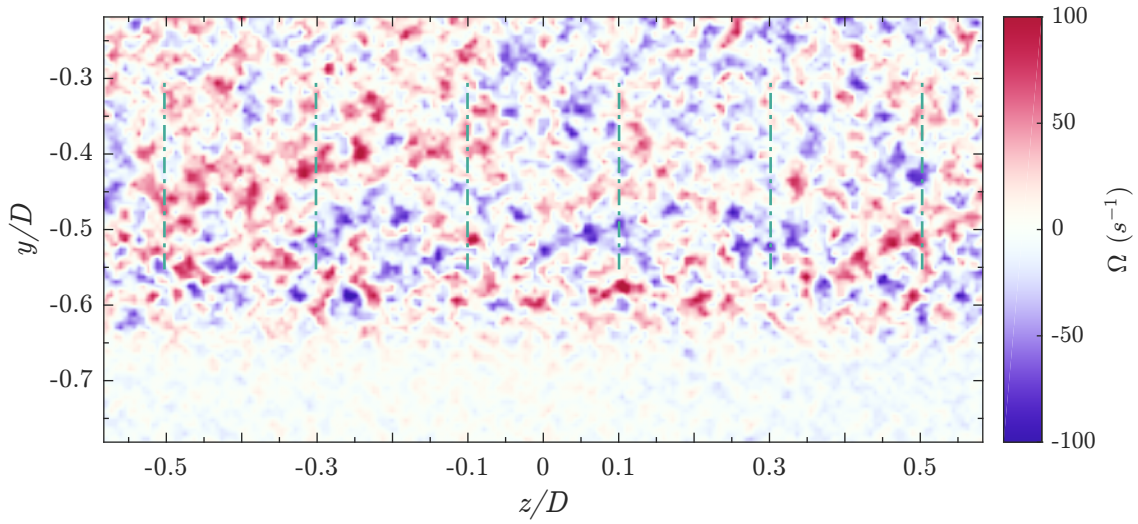

(b)

Figure 8.9 – Wake vorticity, Ω, for $z_J = 20mm$ cylinder at: (a) $Re_D = 2.6 \times 10^4$; and, (b) $Re_D = 5.2 \times 10^4$. Figure continues on following pages – full caption follows final plot.

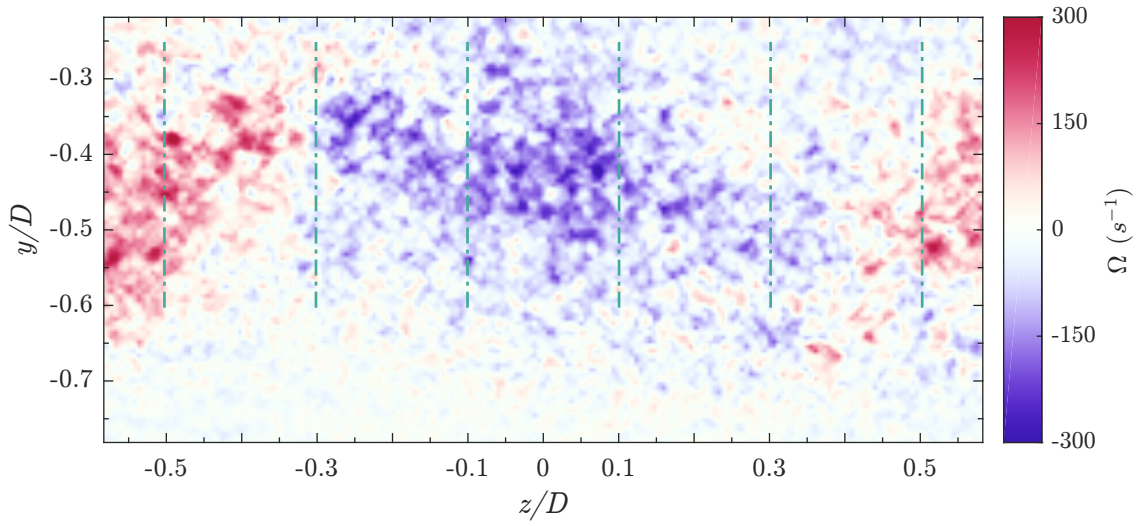

(c)

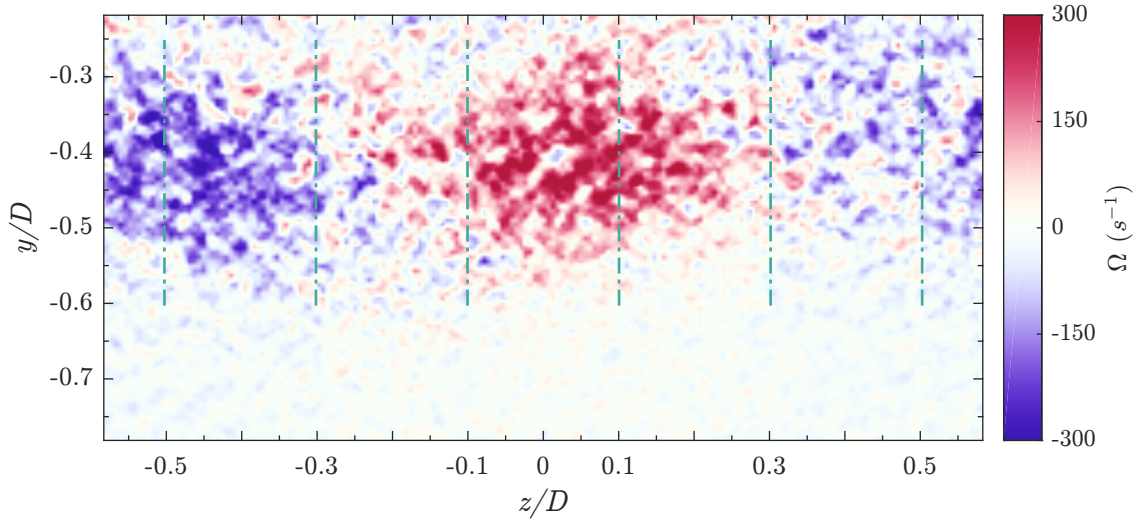

(d)

Figure 8.9 – Wake vorticity, Ω, for $z_J = 20mm$ cylinder at: (c) $Re_D = 1.02 \times 10^5$; and, (d) $Re_D = 1.53 \times 10^5$. Figure continues with full caption on following page.

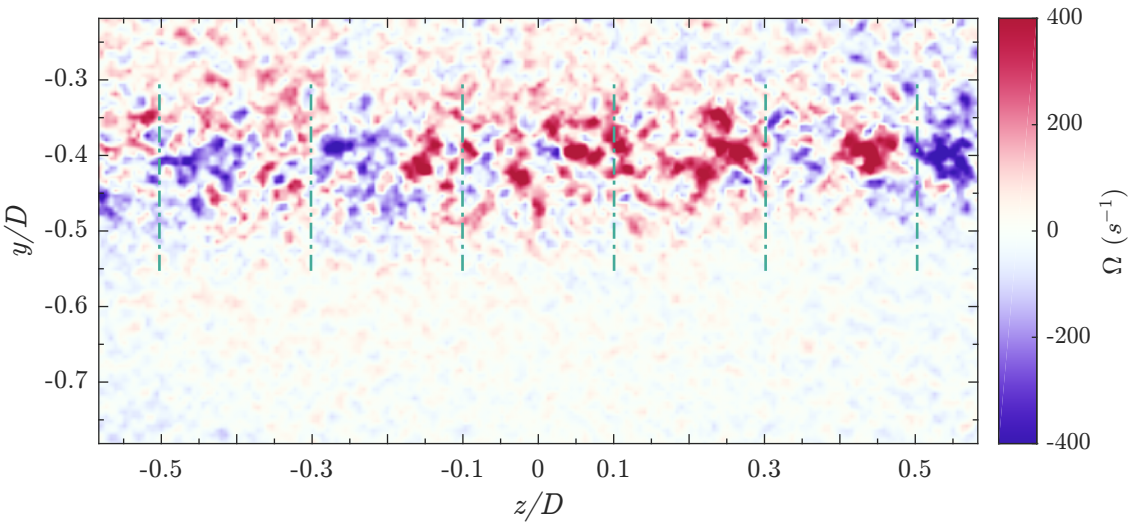

(e)

Figure 8.9 – See preceding pages for figures (a) – (d). Time-mean vorticity, Ω, in the (y, z) plane of the near wake for the cylinder with passive jets, $z_J = 20mm$, at: (a) $Re_D = 2.6\times10^4$, $D/U_\infty = 25.9\times10^{-3}$; (b) $Re_D = 5.2\times10^4$, $D/U_\infty = 12.9\times10^{-3}$; (c) $Re_D = 1.02\times10^5$, $D/U_\infty = 6.46\times10^{-3}$; (d) $Re_D = 1.53\times10^5$, $D/U_\infty = 4.30\times10^{-3}$; and, (e) $Re_D = 2.54\times10^5$, $D/U_\infty = 2.57\times10^{-3}$. Green dashed lines represent the vertical (x, y) plane which aligns with the jet holes.

Stream-wise vorticity is generated in both modes, however mode B also tends to result in regular arrays of counter-rotating span-wise vorticity in the wake (see, for example, Scarano and Poelma, 2009; Williamson, 1996*b*), and it is thought that the passive jets, between $1.02\times10^5 \leqslant Re_D \leqslant 1.53\times10^5$ may excite this instability mode to form the time-mean vorticity structures shown in Figure 8.9(c) and Figure 8.9(d).

With a further increase in Reynolds number to $Re_D = 2.54\times10^5$, where C_D is close to the minimum value tested here, there is again a distinct change in the organisation of the vorticity in the shear layer. From the relatively large regions of counter rotating vorticity in the range $1.02\times10^5 \leqslant Re_D \leqslant 1.53\times10^5$ to a concentrated, narrow band array of counter-rotating vorticity, which now appears to correlate with the jet spacing. The vertical position of the shear layer has also

moved noticeably closer to the cylinder centre, indicating a narrowing of the near wake commensurate with the low value of C_D.

The development of the transfer of vorticity from the separated shear layer to the near wake with increasing Reynolds number would appear to indicate a correlation between the level – and scale – of stream-wise vorticity found in the wake, and the reduction in drag coefficient. The reduction in C_D is initially accompanied by the introduction of large-scale regions of stream-wise counter-rotating vorticity in the near wake, and as vorticity increases with Reynolds number, these patches become more closely ordered and compact, coinciding with a narrowing of the wake and a reduction in the vertical fluctuation (flapping) of the shear layer. It is thought likely that there is also a corresponding increase in the time-mean formation length (see section 8.2) with increasing stream-wise vorticity. All of these factors lead to an increase in the base pressure with increasing Re_D and, hence, reduction in C_D.

8.6 Shear layer span-wise waviness and correlation with wake vorticity

Further insight into the impact of the passive jets on shear layer and wake development is elicited by observation of the time-mean stream-wise velocity component, u_x/U_∞, plotted in the (y, z) plane of the near wake to provide a clear representation of the time-mean shape and position of the separated shear layer. Figure 8.10 provides comparisons of u_x/U_∞ with the equivalent plot of time-mean vorticity, Ω, through the range of SPIV acquisition Reynolds numbers (Figure 8.8). Equivalent plots of u_x/U_∞ for a plain cylinder can be seen in Appendix G.2.

For completeness, comparisons of u_x/U_∞ and Ω for $Re_D = 2.6 \times 10^4$ (Fig-

ure 8.10(a) – (b)) and $Re_D = 5.2 \times 10^4$ (Figure 8.10(c) – (d)) are shown here, and it is again made clear from the plots of u_x/U_∞ that the position of the shear layer is unsteady and the wake-width is relatively large – in-keeping with the pre-critical C_D values observed.

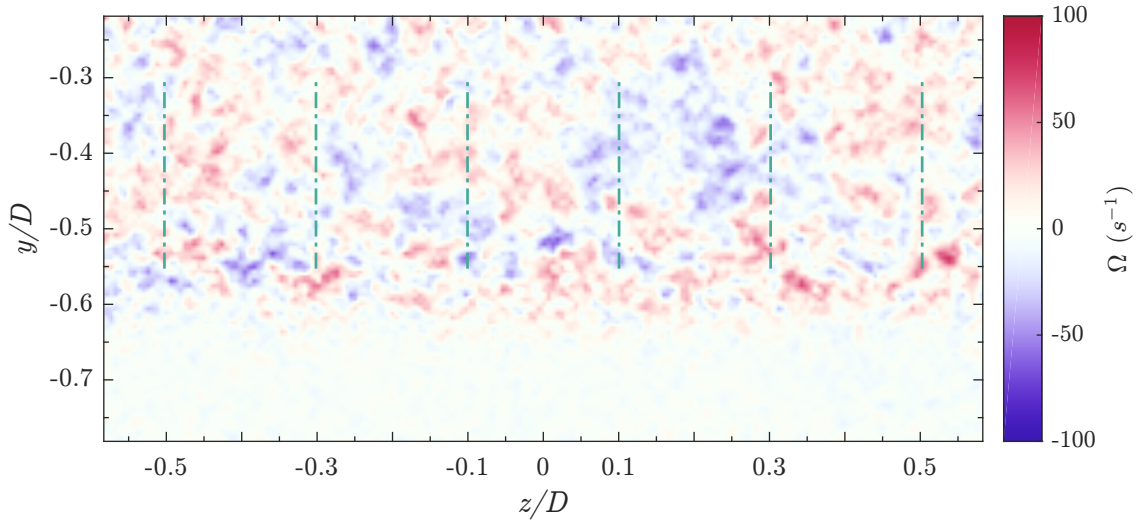

(a)

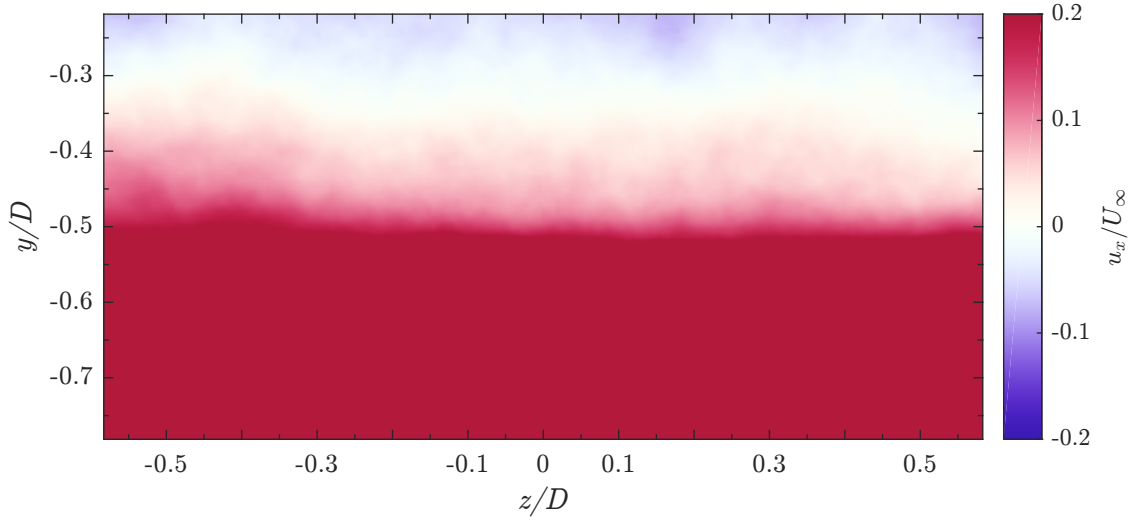

(b)

Figure 8.10 – (a) Vorticity, Ω; and, (b) Stream-wise velocity, u_x/U_∞, at $Re_D = 2.6 \times 10^4$. Figure continues on following pages – full caption follows final plot.

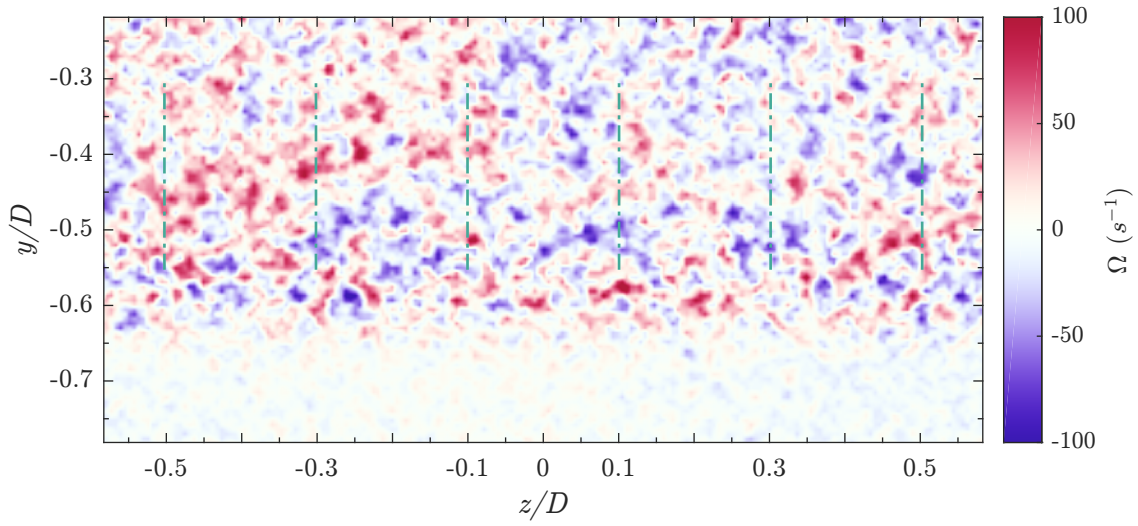

(c)

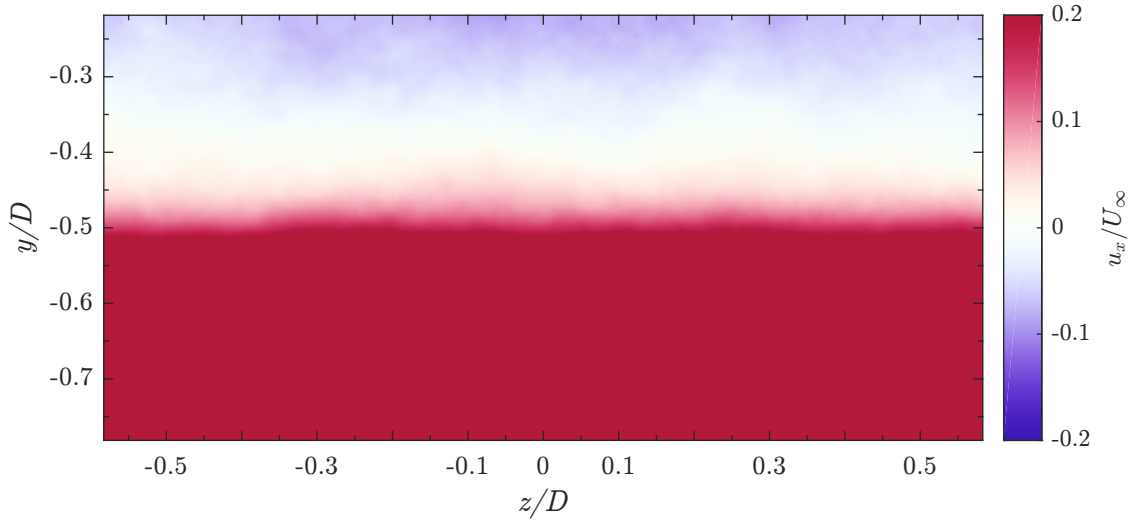

(d)

Figure 8.10 – (c) Vorticity, Ω; and, (d) Stream-wise velocity, u_x/U_∞, at $Re_D = 5.2 \times 10^4$. Figure continues on following pages – full caption follows final plot.

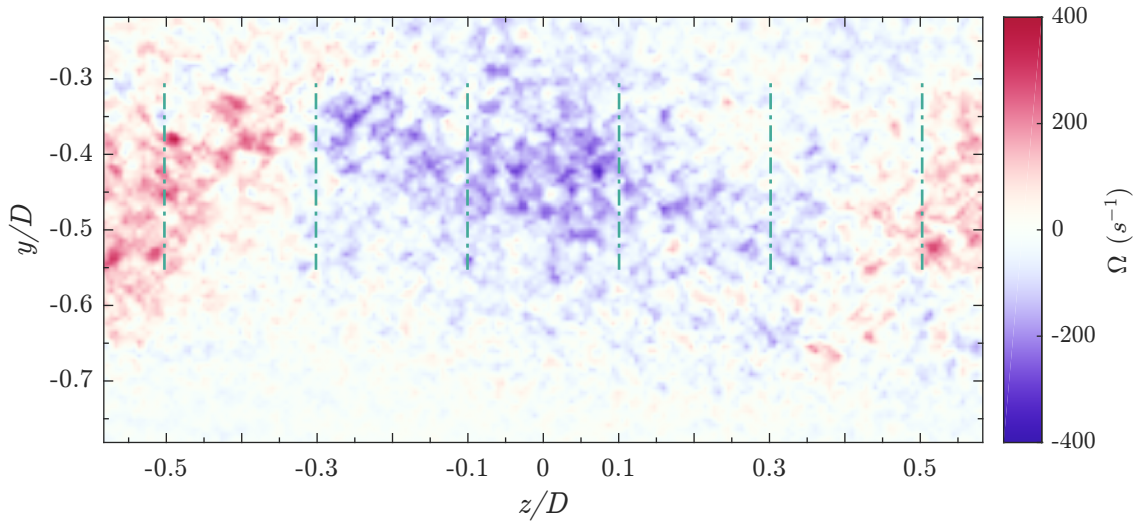

(e)

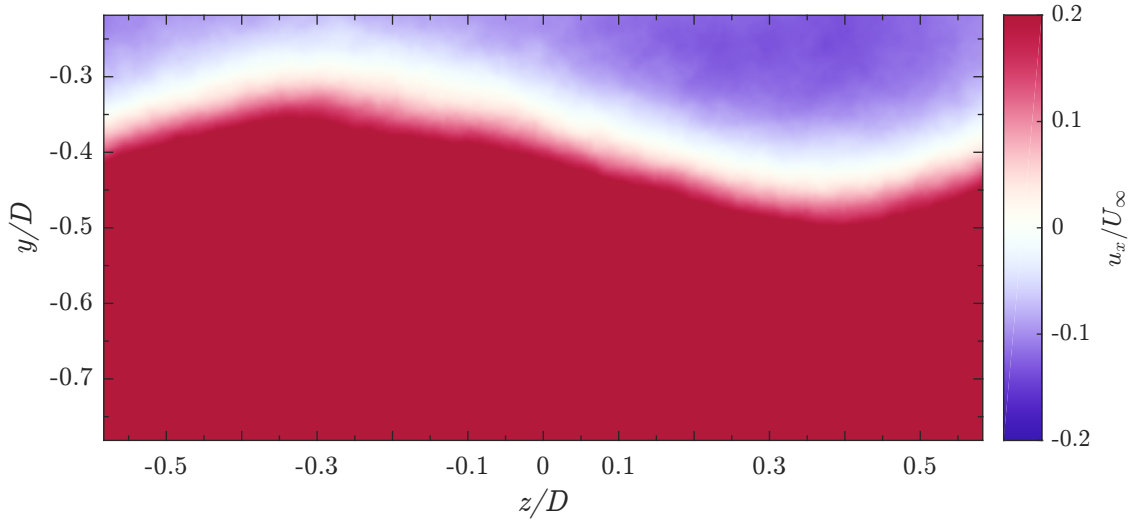

(f)

Figure 8.10 – (e) Vorticity, Ω; and, (f) Stream-wise velocity, u_x/U_∞, at $Re_D = 1.02 \times 10^5$. Figure continues on following pages – full caption follows final plot.

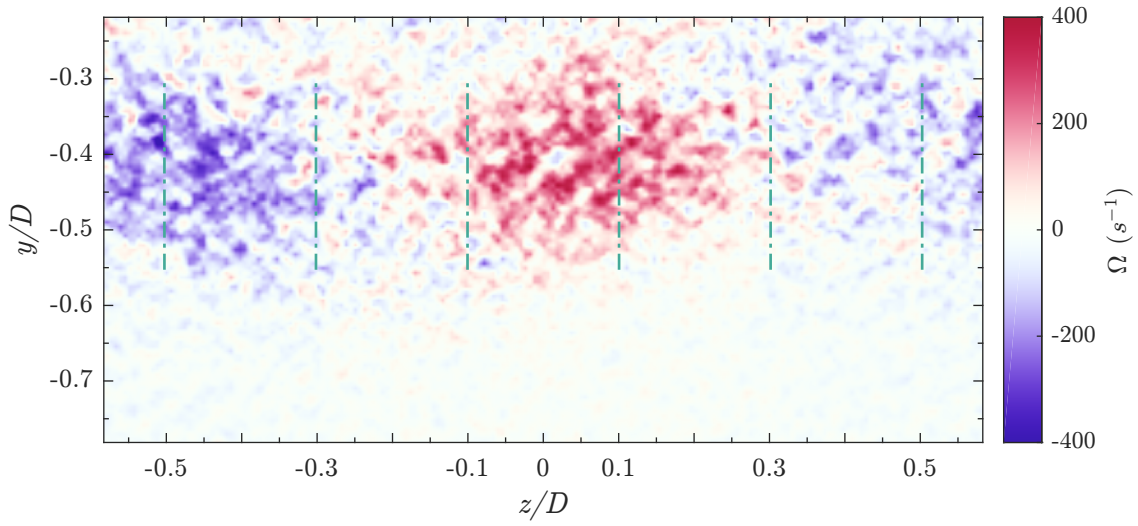

(g)

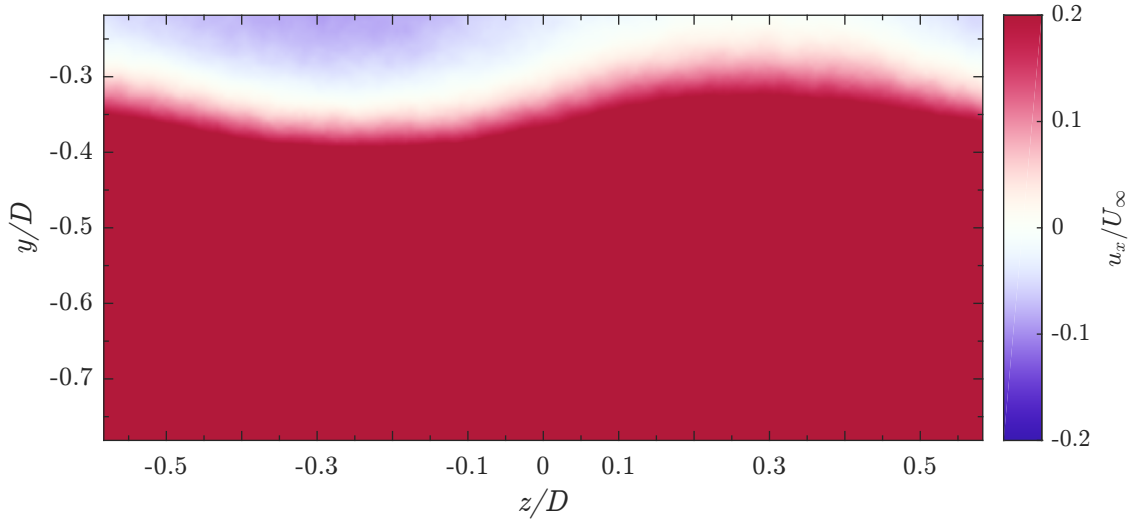

(h)

Figure 8.10 – (g) Vorticity, Ω; and, (h) Stream-wise velocity, u_x/U_∞, at $Re_D = 1.53 \times 10^4$. Figure continues on following pages – full caption follows final plot.

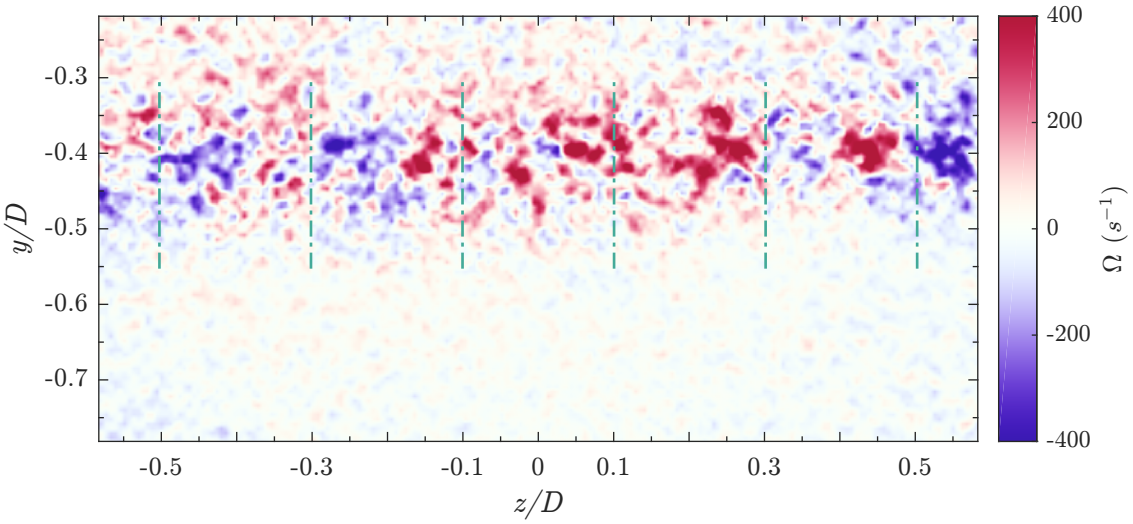

(i)

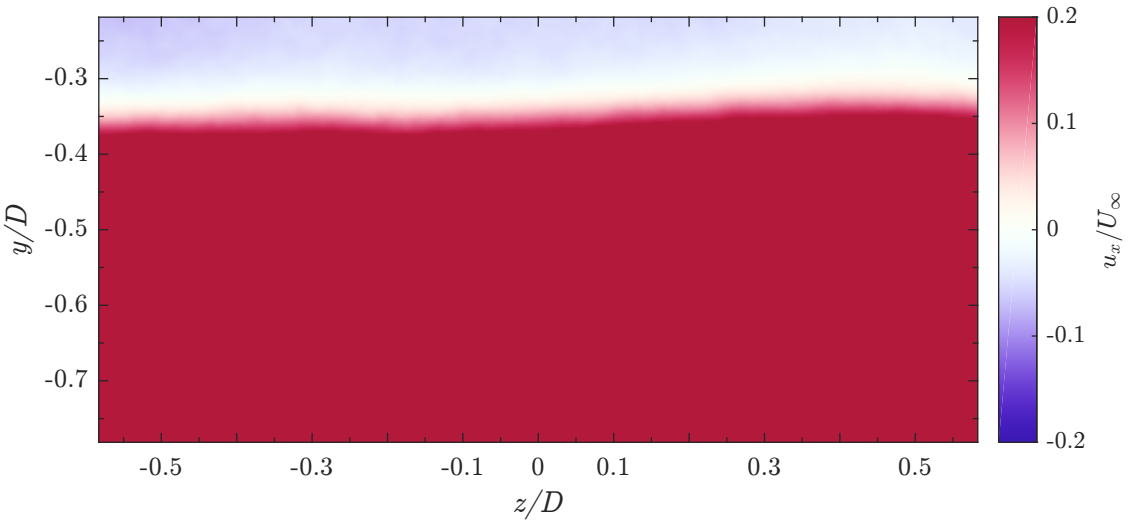

(j)

Figure 8.10 – See preceding pages for figures (a) – (h). Comparisons of time-mean vorticity, Ω, and stream-wise component of velocity, u_x/U_∞, in the (y, z) plane of the near wake for the cylinder with passive jets, $z_J = 20mm$, at: (a), (b) $Re_D = 2.6\times10^4$, $D/U_\infty = 25.9\times10^{-3}$; (c), (d) $Re_D = 5.2\times10^4$, $D/U_\infty = 12.9\times10^{-3}$; (e), (f) $Re_D = 1.02\times10^5$, $D/U_\infty = 6.46\times10^{-3}$; (g), (h) $Re_D = 1.53\times10^5$, $D/U_\infty = 4.30\times10^{-3}$; and, (i), (j) $Re_D = 2.54\times10^5$, $D/U_\infty = 2.57\times10^{-3}$.

Clarification of a time-mean span-wise waviness to the shear layer is provided by the plots of u_x/U_∞ for $Re_D = 1.02 \times 10^5$ (Figure 8.10(f)) and $Re_D = 1.53 \times 10^5$ (Figure 8.10(h)). There is a striking correlation of the wave formation with the size and position of the time-mean patches of vorticity; the left side of a patch of positive (anti-clockwise) vorticity serves to push the shear layer down while the right-side pulls the shear layer up – and vice-versa for the patches of negative (clockwise) vorticity. That the observed wavy shear layer form at these Re_D is a time-mean feature is particularly interesting since it suggests that the flow regime of the wake passes through several different mode shapes which may be excited with increasing Reynolds number (of both the free-stream and jets). It is also intriguing from the point of view of the shorter wavelength (associated with the jet spacing) of the wavy – or at least broken – separation line which appears to form at the cylinder surface in the SOFV tests (see chapter 7). Until these features become dominant in shaping the development of the separating shear layer, one could assume that there is considerable interaction and reformation of the topological features observed in the SOFV tests when they are shed into the wake.

With the increase in Reynolds number to $Re_D = 2.54 \times 10^5$ comes a flattening of the shear layer form as the vorticity is compacted into the aforementioned narrow span-wise band. It is apparent from the plot of u_x/U_∞ that the form of the shear layer is not completely straight across the span, with the left side edge slightly lower than the right. There also appears to be a gentle crest at approximately $z/D = 0.5$ before beginning to drop again with increasing z/D, raising the possibility of additional, longer-wavelength modes which exist in the wake.

Chapter 9

Discrete boundary layer protrusions – "Pins"

For the passive jets system to work effectively, the supply of air needs to be very efficient at low Reynolds numbers in order to provide a suitably high jet flow rate to initiate the critical regime. As Re_D increases, so too does the pressure head available to supply the jets and hence mean jet velocity, $\overline{u}_J$, increases with Re_D. This is only useful in a limited range of low-to-mid-range Re_D, beyond which it is beneficial to reduce the jet flow rate – and hence internal cylinder pressure – in terms of drag reduction. This could be achieved, for example, with a (passive) self-attenuating valve, but this added complexity would inevitably add design and reliability issues. As demonstrated by the application of tripping wires and vortex generators (see section 2.4.3 and section 2.4.4), a simple way of introducing a strong perturbation into the flow at low Re_D is placing a solid surface-mounted protrusion in the boundary layer. In order to address the shortcomings of the passive jets at low Re_D, and to provide a comparison of the downstream effects that the differing

influence of jets and equivalently sized cylinders have on boundary layer transition and separation, a new passive flow control arrangement was devised whereby the jets would simply be replaced by solid cylindrical protrusions – henceforth referred to as "pins".

Stiff plastic inserts were developed to fix into the jet exit holes such that $\varnothing 0.5mm$ cylinders protrude approximately $l_P = 2.5 \pm 0.5mm$ from the cylinder surface in place of the jets. As such, these pins were positioned at precisely the same location as the jet exit holes of the test cylinder to provide a direct comparison with the passive jets as a means of passive drag reduction. The pins were all manufactured to be identical, however, owing to slight manufacturing variability of the cylinder holes and plastic insert pins, the protrusion height along the cylinder span was somewhat inconsistent, with the maximum and minimum protrusions measuring $l_{P(max)}3mm$ and $l_{P(min)}2mm$ respectively. Care was taken to ensure, as far as possible, that the pins in the central span region of the cylinder – around which most of the experimental measurements were acquired – were of an equal protrusion height. The selection of pin height was based on the calculated boundary layer thickness (Zdravkovich, 1997) throughout the Re_D test range, which was found vary in the range $3.0mm \leqslant \delta \leqslant 1.5mm$ over the Reynolds number test range of $3 \times 10^4 \leqslant Re_D \leqslant 2.8 \times 10^5$. This ensured that the mean pin height, l_P, would reach or exceed the boundary layer thickness from $Re_D = 5 \times 10^4$ and throughout the remaining test range of interest ($0.83 \leqslant l_P/\delta \leqslant 1.67$) without significantly extending into the free stream at high values of Re_D – when the boundary layer thickness reduces – thus mitigating detrimental effects on drag reduction. An optimum strategy for this sort of flow control device might be for the pin height to modulate with a change in boundary layer thickness, such that the pin protruded from the cylinder surface no

further than the limit of the boundary layer, where $u_\delta = 0.99U_\infty$, in the sub-critical Re_D range and became flush with the surface during the natural critical regime of a plain cylinder.

Figure 9.1 shows the cylinder test model converted from passive jets to pin protrusions. The stagnation point holes (used for the passive jets) are sealed over with sticky tape.

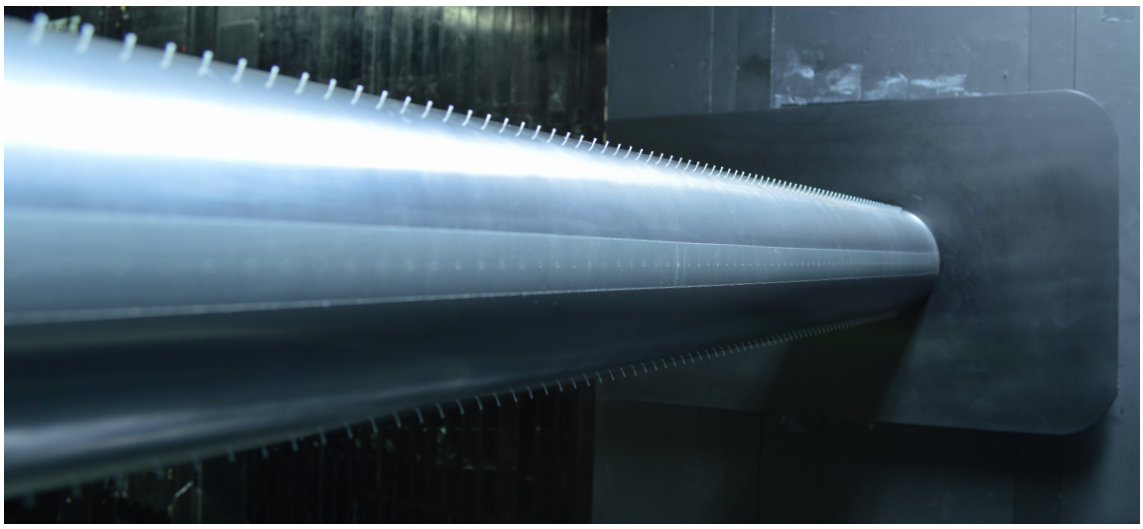

Figure 9.1 – Photograph of cylinder with "pin" protrusions test model mounted in the working section of the wind tunnel.

Similar methods have been employed to reduce bluff body drag by using tabs, (e.g. Choi, 2007; Choi et al., 2008; Park et al., 2006), and much research has been conducted on discrete and array positioning of vortex generators (e.g. Heine et al., 2010; Igarashi, 1985; Johnson and Joubert, 1969; Joubert and Hoffman, 1962), but to date the author is unaware of any literature charting attempts to use cylindrical protrusions in this way to reduce drag.

Schewe (1986) used a single, moveable 'pin' in a similar location on one side of a circular cylinder in order to trigger transition. Here, Schewe showed that once

transition was triggered locally by the pin, the critical regime could be induced on that side of the cylinder. The pin could then be retracted and the newly induced flow state would remain stable. Rather than using the pin as a method of drag reduction *per se*, the purpose of this experiment was for Schewe to provide an analogy for the flow state discovered by Bearman (1969) where a single bubble flow regime would exist and remain stable, presumed to be a result of a very small asymmetric perturbation, until an increase in Re_D would trigger transition on both sides of the cylinder.

Fric (1990) provides a detailed discussion on the differences between the formation of vorticity and wake development by a round transverse jet compared with a circular cylinder in cross-flow, and points out that one of the most fundamental differences is that with a jet in cross-flow there is an exchange of momentum between the jet and cross-flow (Coelho and Hunt, 1989), unlike the bluff protrusion of a cylinder which presents a momentum deficit to the cross-flow. Comparing the flow topology and wake interaction between jets and cylinders in cross-flow, the cross-flow is not only deflected by the jet, but it also interacts with the deflected flow and entrains fluid from it (Andreopoulos and Rodi, 1984), as opposed to the rigid, impermeable obstacle provided by the cylinder. This translates to significant differences in the formation of vorticity in the wake and hence transition and mixing within the cross-flow boundary layer.

The following sections of the thesis provide further evidence of some of the differences and, in this application, also some of the similarities between these two methods of passive flow control.

9.1 C_D v. Re_D characteristics

To begin with, the relationship between the drag coefficient and Reynolds number of the cylinder with pins is analysed with reference to the passive jets. Figure 9.2 plots the drag profiles for both pins and passive jets and it is immediately clear that the pins generate drag reducing mechanisms in their interaction with the cross-flow from a much lower Re_D. Due to the increased physical obstruction and hence momentum deficit presented by solid pins (Fric and Roshko, 1994) – as compared to fluid jets – the disturbance introduced into the cross-flow boundary layer is greater, particularly at low speeds, and critical C_D is achieved at a lower Re_D for the equivalent diameter and spacing of passive jets.

As is common with most fixed geometrical boundary layer protrusions, the effec-

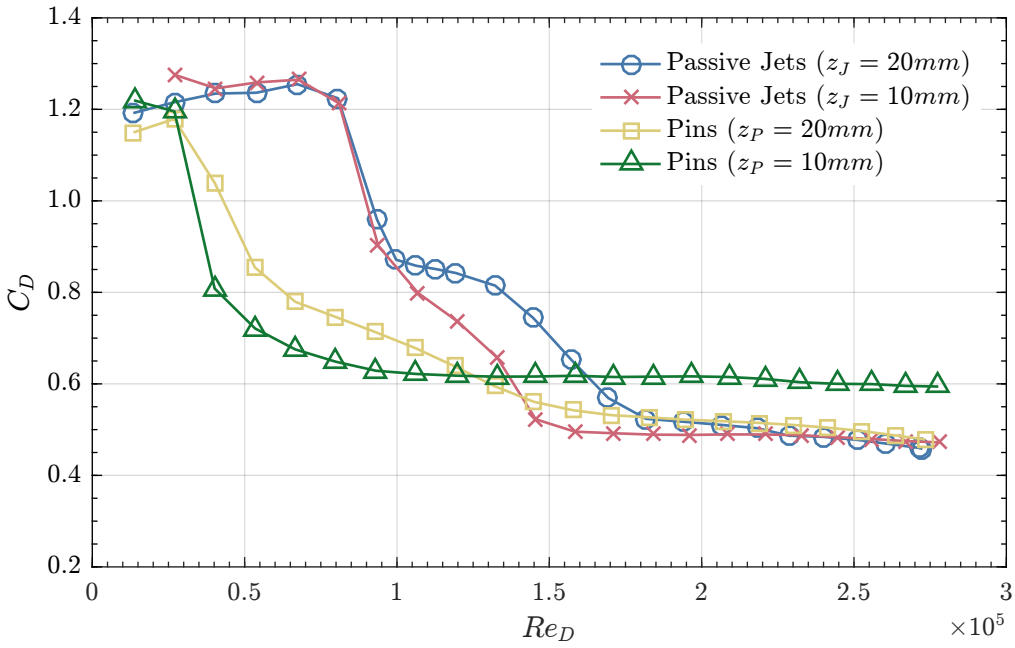

Figure 9.2 – Variation of C_D with Re_D for cylinder with "pins", $10mm \leqslant z_P \leqslant 20mm$, alongside passive jets, $10mm \leqslant z_J \leqslant 20mm$, for comparison.

tiveness of the more narrowly spaced pins ($z_P = 10mm$) in reducing drag coefficient gradually diminishes with increasing Re_D. After a very rapid drop to $C_D \approx 0.6$, there is very little improvement in drag coefficient from $Re > 9 \times 10^4$ for the $z_P = 10mm$ cylinder. For $Re_D > 1.25 \times 10^5$ the $z_P = 20mm$ cylinder overtakes the narrower spacing with a continual drop in C_D which eventually joins on to the steadily dropping curve of the $z_J = 20mm$ passive jets almost to the end of the Re_D range of testing. There is a slight improvement with the $z_J = 20mm$ jets at the highest Reynolds numbers, but the difference is not significant.

It is interesting to note the difference between the performance of each flow control method with respect to the spacing at mid to high Reynolds numbers – where the $z_P = 20mm$ cylinder does not lose too much to the equivalently spaced passive jets, the $z_P = 10mm$ pins cylinder has a significantly poorer drag profile than the $z_J = 10mm$ jets cylinder for $Re_D > 1.4 \times 10^5$. Both the narrower spaced cylinder setups do appear to continue to drop in C_D very gradually with increasing Re_D, which may indicate an advantage of discretely placed flow perturbations on the cylinder surface as opposed to homogeneous surface coverings which eventually tend to raise C_D with Re_D some time after reaching the minimum drag coefficient, $C_{D_{min}}$.

Passive jets appear to be more effective for C_D reduction than pins at high Reynolds numbers, though in the Re_D testing range here, the $z_P = 20mm$ pin cylinder provides overall the best performance. Regardless of the passive flow control method, however, the rate of C_D reduction slows dramatically when approaching $C_D = 0.5$.

9.1.1 Variation of pin spacing

A brief parametric study was made for pin spacing on the cylinder to identify its relationship with C_D reduction. The study was conducted simply by varying the pin spacing on the cylinder with $10mm$ hole spacing, such that no attempt was made to block or smooth over the holes left empty for pin spacing $z_P \geqslant 20mm$. Again, the holes at the cylinder stagnation point were sealed over to prevent the activation of any transverse jets. To validate the performance of the $z_P \geqslant 20mm$ setup on the $z_J = 10mm$ cylinder, the $z_J = 20mm$ cylinder was also tested in the $z_P = 20mm$ arrangement to test whether the exposed holes between pins exert a significant influence on C_D and it was found that the two arrangements follow nearly identical drag curves.

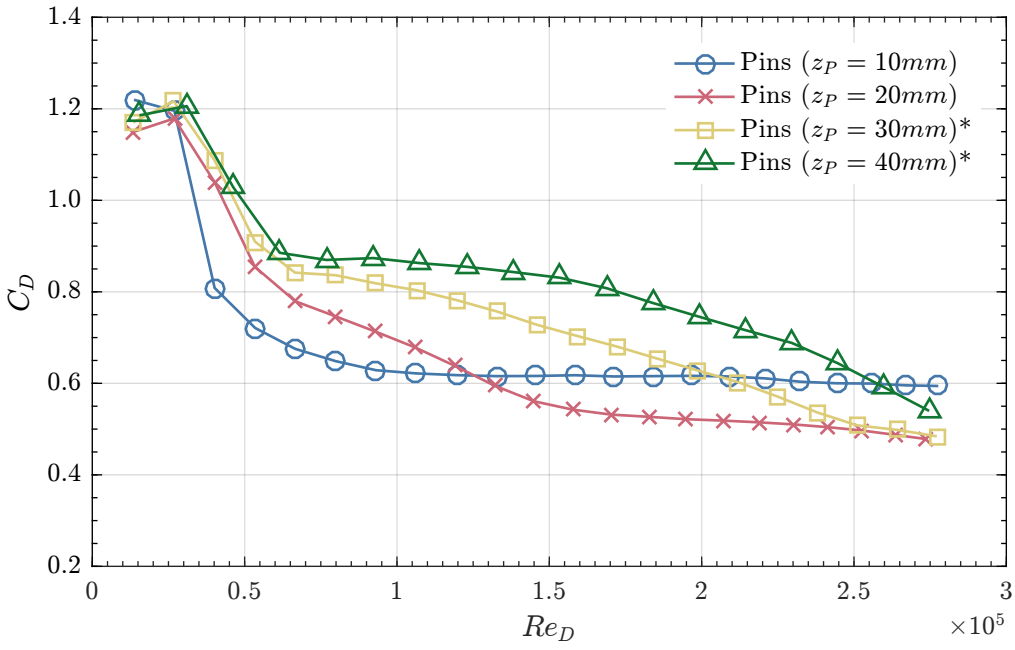

Figure 9.3 – Variation of C_D with Re_D for cylinder with "pins", $10mm \leqslant z_P \leqslant 40mm$. *Tests conducted on $z_J = 10mm$ cylinder where alternate pin placing left uncovered holes between pins.

Figure 9.3 shows there is a clear relationship between pin spacing and drag coefficient which is similar, in some ways, to surface roughness; the narrower the pin spacing, the lower the Re_D for which the critical C_D occurs, but the higher the critical minimum C_D which is eventually achieved. The effect of pins to reduce the critical Reynolds number, $Re_{D,crit}$, differs from surface roughness since with increasing Re_D beyond $Re_{D,crit}$, the cylinder drag coefficient does not increase but remains constant or even continues to drop gradually, as clearly shown with the plot of $z_P = 20mm$ cylinder.

It cannot be clearly defined with the limited Re_D range of test data available, but there appears to be a limitation to $C_{D_{min}}$ achievable via these methods; the plots of $z_P = 20mm$ and $z_P = 30mm$ pin spacing seem to asymptote to a common shallow gradient at high Reynolds numbers ($Re_D \geqslant 2.5 \times 10^5$), but it is difficult to confirm conclusively without testing at a higher Re_D than was limited by the experimental setup.

It is interesting, however, that the initial drop in C_D – for both pins and jets, respectively – seems to occur at a very similar Re_D regardless of the pin (or jet) spacing, indicating that there is a particular Re_D for which the flow control method becomes 'active' in terms of imparting drag reducing mechanisms to the boundary layer. In the case of the pins, from the calculated boundary layer height throughout the Re_D test range, it can be estimated that the critical regime is induced when $l_P/\delta > 0.83$. Thus, the optimum pin height is expected to be found in the range $0.83 < l_P/\delta \leqslant 1$.

For wider spaced pins ($30mm \leqslant z_P \leqslant 40mm$), another intriguing feature is that – after the C_D plateau following the initial steep drop to $C_D = 0.9$ at $Re_D = 6 \times 10^4$ – the rate of C_D reduction increases with Re_D. However, at $Re_D = 2.5 \times 10^5$, this

rate slows for the $z_P = 30mm$ cylinder as it converges with the C_D v. Re_D profile of the $z_P = 20mm$ cylinder, indicating again that there appears to be a common limiting factor to the minimum level of C_D achievable, for a given Re_D, by this flow control method.

9.2 Skin friction line patterns and flow topology

Doligalski et al. (1994) provide a succinct account of the horseshoe vortex generation from the interaction of cross-flow with a bluff wall protrusion (namely a cylinder, as shown in Figure 9.4, where 'necklace' is a synonym of the more commonly termed 'horseshoe' vortex). Doligalski et al. point out that as a boundary layer encounters a surface mounted (solid) protrusion, a complex, three-dimensional flow develops in

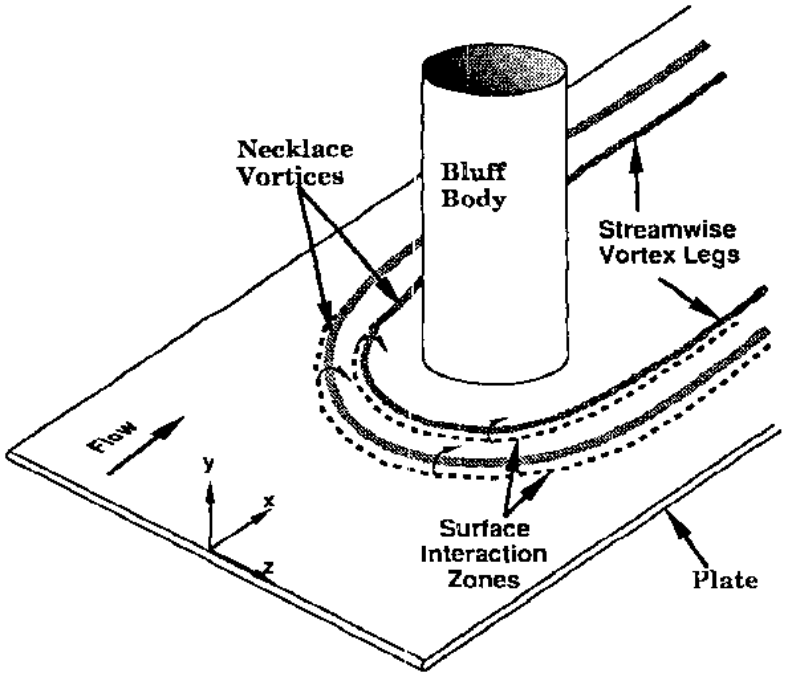

Figure 9.4 – Schematic of hairpin vortex formation around cylindrical protrusion, from Doligalski et al. (1994).

the local region of the obstruction. Immediately upstream of the protrusion, the cross-flow encounters an adverse stream-wise pressure gradient which, in tandem with the pressure gradients developed by the curvature of the surrounding cross-flow as it passes over the protrusion, produces a concentrated region of boundary layer vorticity (Doligalski et al., 1994). This, in turn leads to the development of a system of discrete vortices, which tend to wrap around the protrusion in the form of a horseshoe vortex, with the 'legs' of the horseshoe stretching downstream along the bounding wall as a pair of counter-rotating stream-wise vortices.

The photograph of the flow visualisation by Henri Werlè of Onera (Reynolds number unknown) in Figure 9.5 (a), as presented by Delery (2011), clearly shows the complex three-dimensional topology generated by the obstruction to the cross-flow presented by the surface mounted cylinder, with the turbulent wake region formed immediately downstream, in addition to the development of the horseshoe vortex. Critical point theory was applied by Delery (2001) in three dimensions to interpret this flow topology, and his schematic is presented in Figure 9.5 (b). That the surface mounted cylinder has a free end adds another level of complexity to the subsequent flow topology and this is highlighted by the additional pair of counter-rotating vortices, as drawn by Delery, formed from the roll-up of the separating shear layers and forced to fold over by the cross-flow over the top, free end, to again stretch downstream as a pair of counter-rotating vortices. The schematic presents an ideal, symmetric, time-mean arrangement which is useful for interpreting the flow mechanisms, however the vortex system of the wake vortices in particular is likely to be highly unsteady, hence the graphic difference between the more stable horseshoe and turbulent wake flow of Figure 9.5 (a).

Comparing the differences between the way cylindrical protrusions and trans-

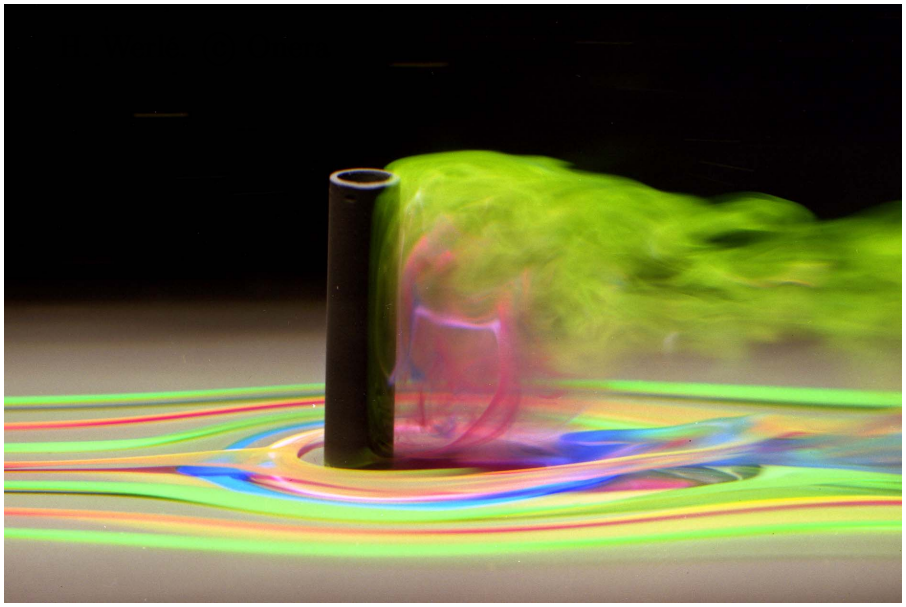

(a)

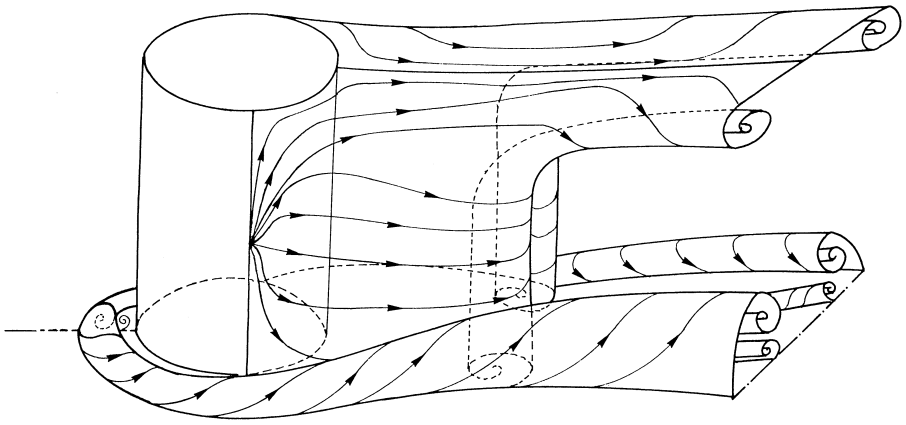

(b)

Figure 9.5 – Flow around a surface mounted cylindrical protrusion, where: (a) photograph of flow visualisation by Henri Werlé, © Onera, from Delery (2011); and, (b) three-dimensional topology schematic, from Delery (2001).

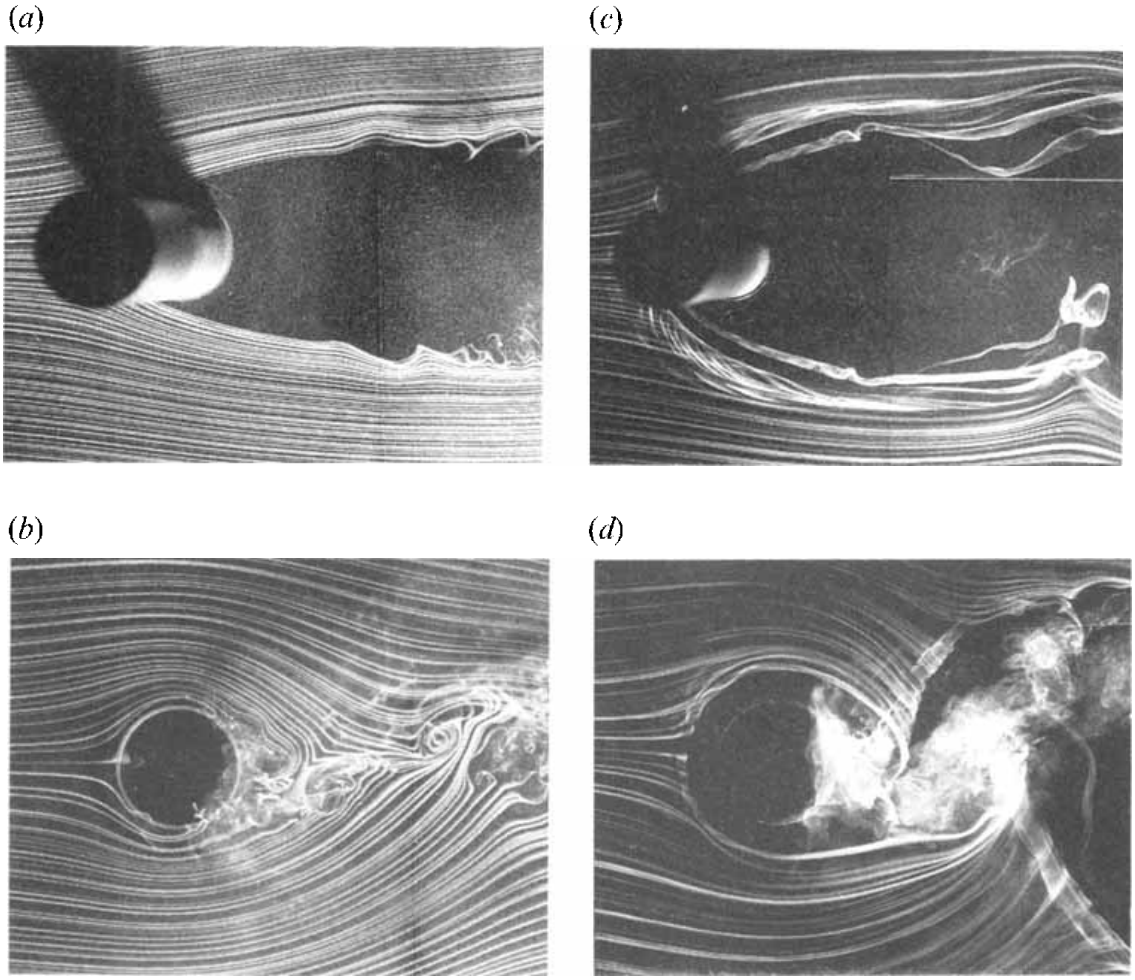

Figure 9.6 – Near wall flow, just above the boundary layer, for: (a) a cylindrical protrusion; and (b) a transverse jet. Cross-flow boundary layer flow for: (c) cylinder protrusion; and, (d) a transverse jet. Crossflow Reynolds number, $Re_{cf} = 3,800$. Jet to cross-flow ratio of (b) and (d) was $R = 4$. From Fric and Roshko (1994).

verse jets affect the flow when placed in a boundary layer, Fric and Roshko (1994) demonstrate in Figure 9.6 – for a jet to cross-flow velocity ratio $R = 4$ – that a primary distinction to be observed, from streaklines bordering the cross-flow boundary layer, is that the near wake region of the cylinder protrusion is open, and bounded by the separating streaklines, while for the jets this region is closed. This indicates that there is a significantly reduced momentum deficit produced by the transverse

jet as compared with the cylinder protrusion, but the increased perturbation to the flow by the cylinder increases the level of vorticity introduced to the boundary layer and hence will trigger transition of the cross-flow at lower Re_D.

9.2.1 Comparison of $z_P = 10mm$ & $z_P = 20mm$

Surface oil flow visualisation experiments were carried out to identify the effects on flow topology of the pins and how this compared to the transverse jets. The photographs in Figure 9.7 compare the time-mean skin friction patterns left by the tracer particles of the oil solution for the $z_P = 10mm$ and $z_P = 20mm$ pin configurations.

Traces of the horseshoe vortex system are immediately evident from Figure 9.7(a) of the $z_P = 10mm$ cylinder, which shows gradually diverging stream-wise trails of the counter-rotating vortex 'legs' emanating from each pin. These traces are also found for $z_P = 20mm$ setup and can be seen with close inspection of Figure 9.7(b). It appears at first glance that the skin friction line pattern of the $z_P = 20mm$ cylinder shares a lot of similarities with that of the $z_J = 20mm$ passive jets setup (section 7.2.1), however, the $z_P = 10mm$ cylinder appears to differ quite significantly from the skin friction line patterns observed in the passive jets studies. The first thing to notice is that the usually well-defined primary CRVP has all but disappeared, and secondly there is what appears to be an almost continuous, wavy separation line across the span – some way downstream of the initial laminar separation point. Where the primary CRVP is usually expected to form, small lines of separation can still be observed in small upside-down 'U' – shapes in downstream regions between the pins. The trails of the horseshoe vortices appear to terminate at the visible 'humps' or crests of the wavy separation line, and the troughs of

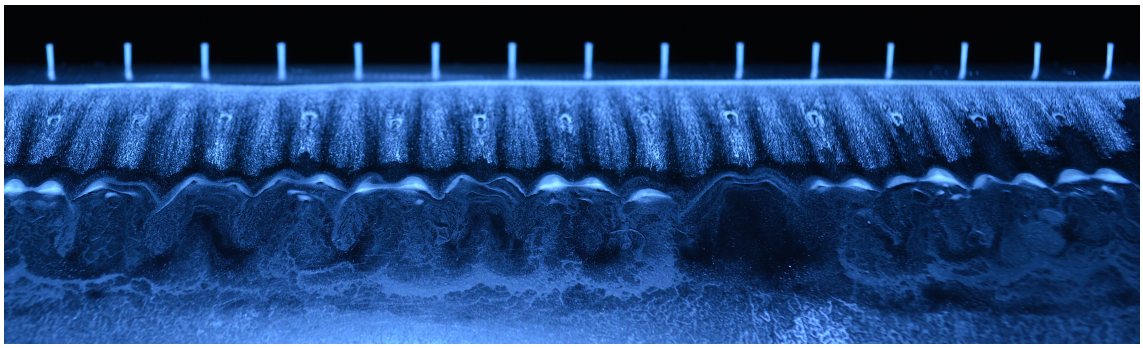

(a)

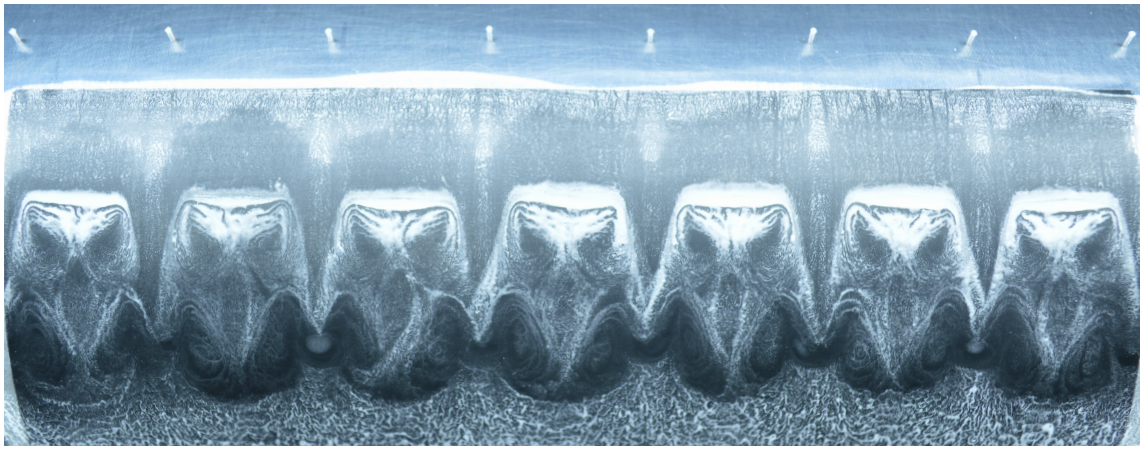

(b)

Figure 9.7 – Photograph of SOFV tests on cylinder with pins at $Re_D = 2.7 \times 10^5$, for: (a) $z_P = 10mm$; and, (b) $z_P = 20mm$. Free-stream direction is approximately: (a) out of the page; and, (b) top to bottom of the figure.

the same line appear downstream of the regions either side of each horseshoe leg. That there is a clear point of separation downstream of the initial, laminar 'U' – shape separation lines indicates that a reattachment of the flow still occurs. There is a distinct lack of clarity with regards to the possibility of a secondary CRVP structure forming downstream of the delayed separation line, however traces of fluid drawn from the base region are observed. Close inspection of this region reveals that the pattern is analogous to that formed by the $z_J = 10mm$ passive jets at $Re_D = 2.7 \times 10^5$ (see Figure 9.11) – where the coalescence of tracer particles in the

SOFV mixture gradually build a continuous barrier to the oncoming flow. Similarly, the pin-energised flow streams do persistently pass beyond this point to form weakly a secondary CRVP downstream of that first delayed separation line. In light of this, it is interesting to note that the level of C_D for the $z_P = 10mm$ pins is considerably higher than $z_P = 20mm$ and both passive jet arrangements, which all have similar C_D at the SOFV test Reynolds number of $Re_D = 2.7 \times 10^5$. The distinctive feature which differs between the $z_P = 10mm$ skin friction pattern and those of the other pin and passive jet setups is that of the separation bubble and the subsequent distance downstream that the reattached flow continues to before finally separating. For the $z_P = 10mm$ cylinder, this point is marked around $\phi_s = 102°$, whereas for the $z_P = 20mm$ setup it was $\phi_s = 110.5°$, and the passive jet arrangements had equivalent values of $\phi_s = 113.5°$ and $\phi_s = 119°$ for $z_J = 10mm$ and $z_J = 20mm$, respectively. The weakly forming CRVP of the $z_P = 10mm$ setup may also negatively affect its drag reducing properties by forming and shedding lower levels of stream-wise vorticity.

This contrasts with the $z_P = 20mm$ cylinder, where the most distinctive feature remains the initial laminar separation line enclosing a dominant, primary CRVP – leading to a substantial level of flow reattachment – and which still forms a clear and distinctive secondary CRVP. The impression given by the SOFV results of the $z_P = 20mm$ cylinder – in contrast that of the skin friction patterns generated by the $z_P = 10mm$ pins – is that there is significant shedding of stream-wise vortices into the separating shear layer and, therefore, the wake.

9.2.2 Schematic interpretation of skin friction patterns

A schematic of the surface skin-friction pattern of the three-dimensional topology interpreted by Delery for a surface mounted cylindrical protrusion (the three-dimensional representation of Figure 9.5 (b) is consistent with this arrangement of critical points) is shown in Figure 9.8 and reveals a somewhat familiar arrangement of saddle points, foci and node of attachment immediately downstream of the cylinder (schematics of owl type 2 separation bubbles can also be found in Figure 7.5 and Figure 7.6). The saddle point, labelled S_1, and subsequent attachment node, labelled N_1, upstream of the cylinder mark the bounds of the horseshoe vortex which

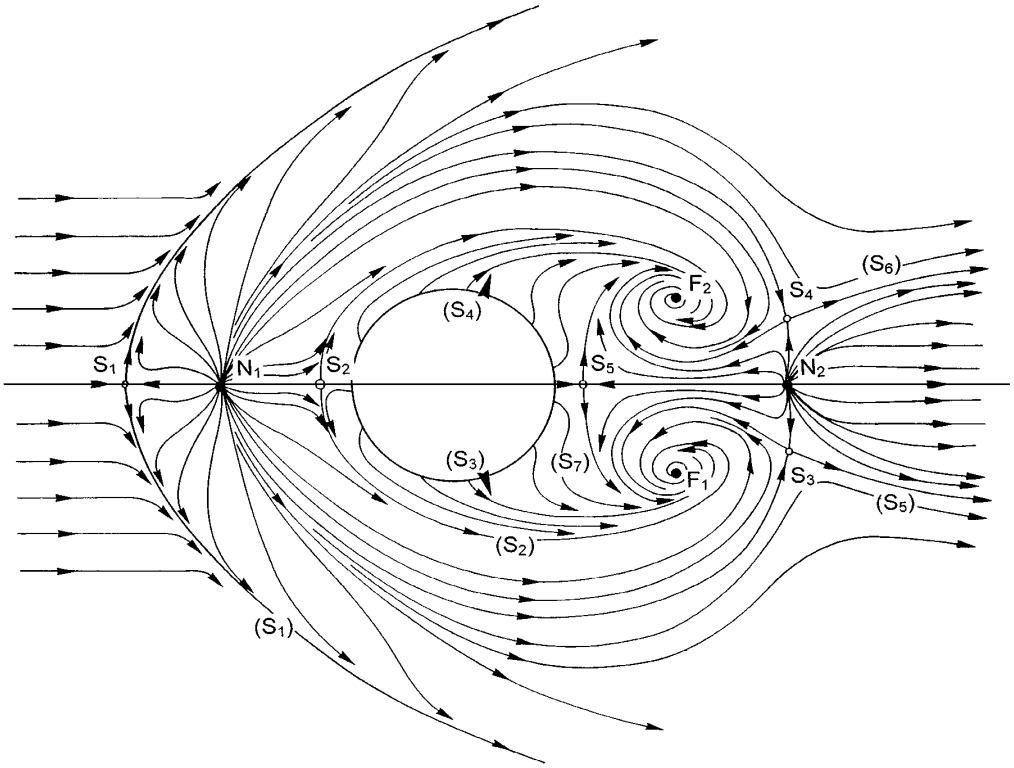

Figure 9.8 – Topology of the surface skin friction line pattern of the flow around a surface mounted cylindrical protrusion, from Delery (2001). Free-stream direction is left to right.

forms (above the surface) between them and wraps around the base of the protruding cylinder. The counter rotating vortex pair of foci F_1 and F_2 are the wake vortices of the cylinder protrusion which fold over with the cross-flow to be swept downstream, entraining and mixing with fluid from the wake before bursting to turbulence. The resulting, simplified flow topology close to the cross-flow wall is therefore two discrete, counter rotating, stream-wise vortices (the legs of the horseshoe vortex) which persist downstream and bound a turbulent channel of flow between them.

To further understanding of the flow mechanisms and aid comparisons of the flow topology, schematic interpretations of the SOFV patterns were produced for both $z_P = 10mm$ and $z_P = 20mm$ pin spacing arrangements, and are shown in Figure 9.9 and Figure 9.12, respectively.

For the $z_P = 10mm$ cylinder (Figure 9.9), as alluded to in the previous section, in place of the primary CRVP found in all other configurations tested there now appears to form a so-called 'U – shaped' separation bubble, enclosed by the separatrix of the S_1 saddle point. The oncoming flow separates and forms a span-wise vortex which curves round – much like a horseshoe vortex – with a small middle portion rolling over and reattaching at node N_1 and the resulting reattachment line curving round with the vortex. An oblique, three-dimensional topology schematic of a U – shaped separation bubble by Perry and Chong (1986) is shown in Figure 9.10. This topology is consistent with the observation of reattached flow and subsequent delayed separation downstream of the initial laminar separation.

In order to highlight the time-mean alignment of the legs of the horseshoe vortices emanating from the pins, angled lines – assumed to originate from an upstream attachment node – have been drawn from a location downstream of each pin. For simplicity – due to the complex nature of the assumed flow in the immediate vicinity

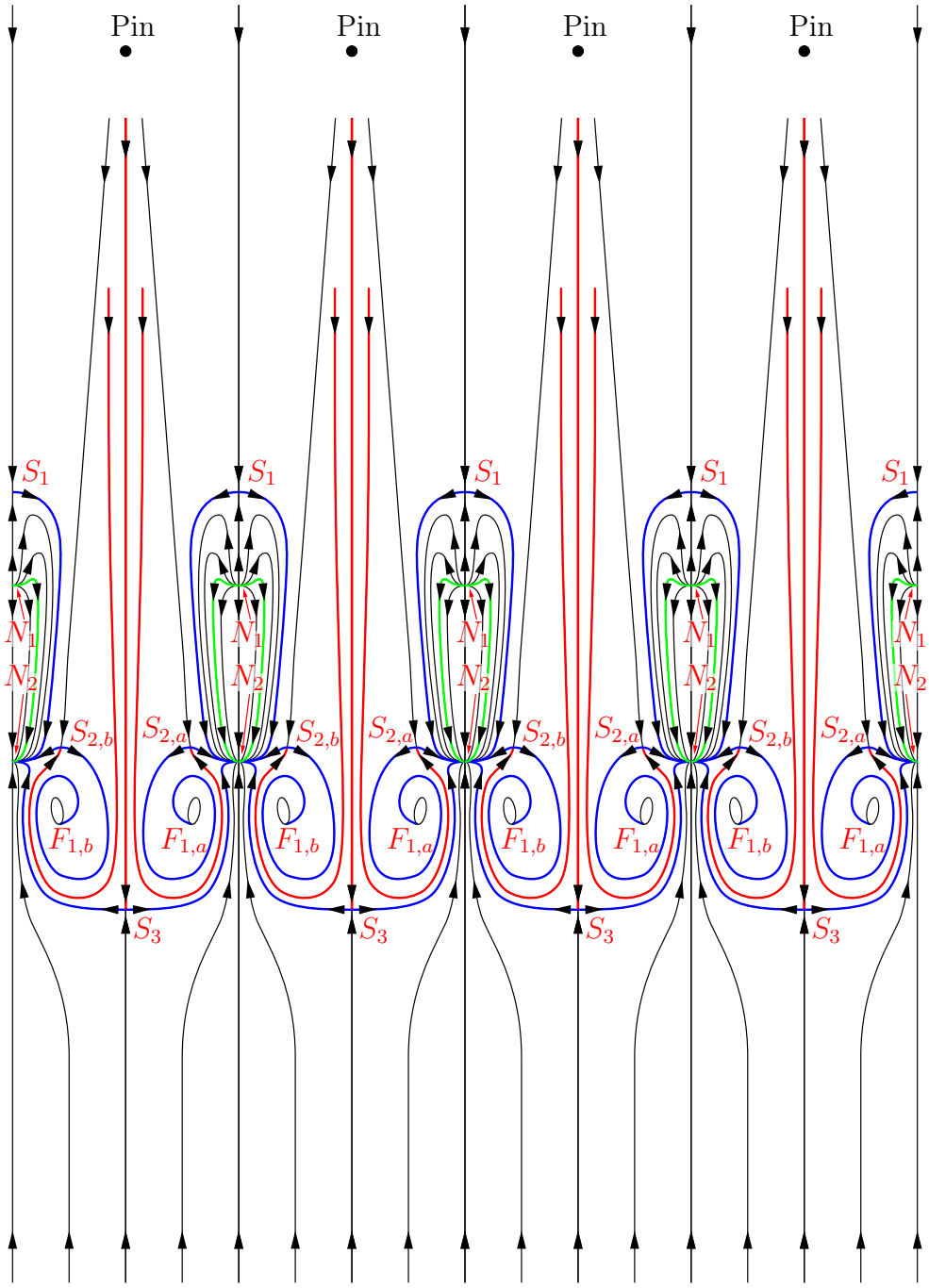

Figure 9.9 – Skin friction line schematic, $z_P = 10mm$, $Re = 2.7{\times}10^5$. Red lines represent skin friction lines from turbulent boundary layer flow, blue lines are saddle point separatrices (separation lines) and attachment node tangent lines (attachment lines) are shown in green. Text (black) and critical point (red) labels have the following meanings: Pin, location of pin; S, saddle point; N, node; F, focus.

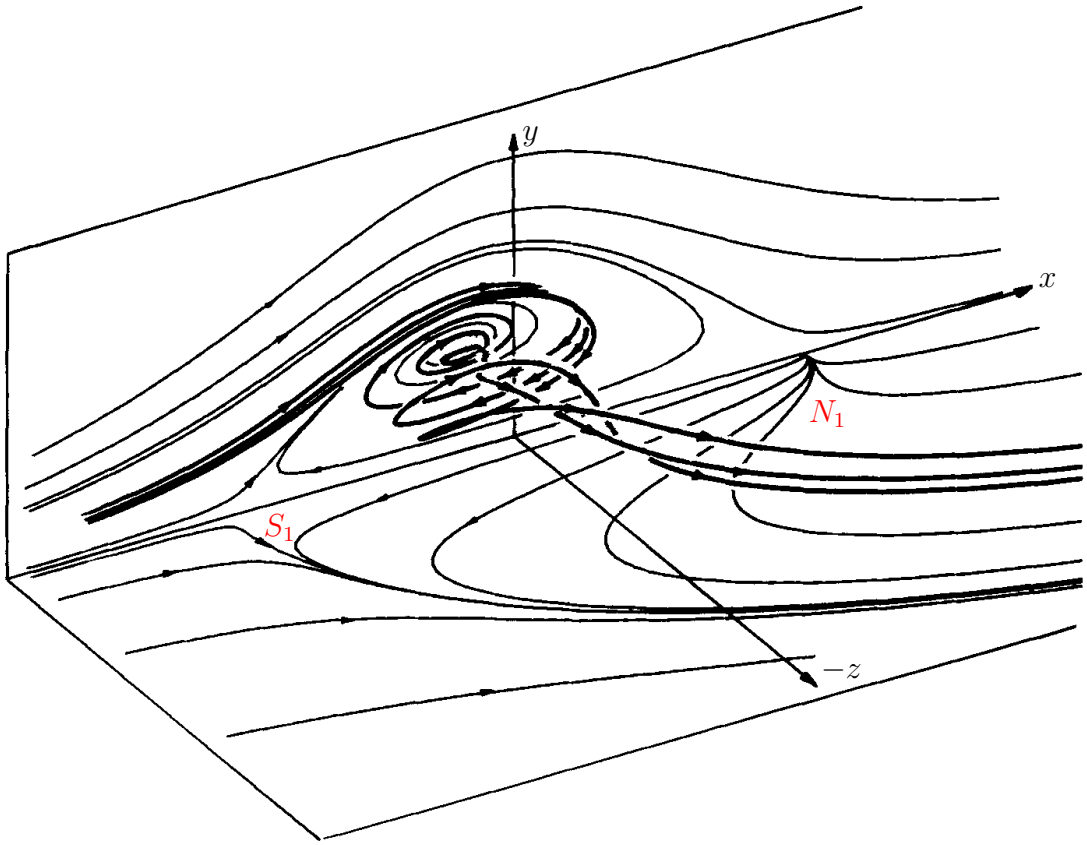

Figure 9.10 – Skin friction line schematic with oblique view of flow topology above the surface of a U-shaped separation bubble, from Perry and Chong (1986). Critical point labels, S_1 and N_1, are consistent with Figure 9.9.

of the pins – skin friction lines in this region have been omitted. As the horseshoe vortices travel downstream, they interact with those of the U – shaped separation bubble, which forms a vortex with legs of opposite sign of rotation to the adjacent horseshoe legs. Thus, pairs of counter-rotating stream-wise vortices separate along the lines of the separatrices of the S_2 saddle points and N_2 separation nodes across the cylinder span.

Within the diverging channel left by the skin friction lines associated with the horseshoe vortices, three red lines represent the pin-energised (and assumed turbulent) flow stream. This stream passes far beyond both the initial, laminar separation

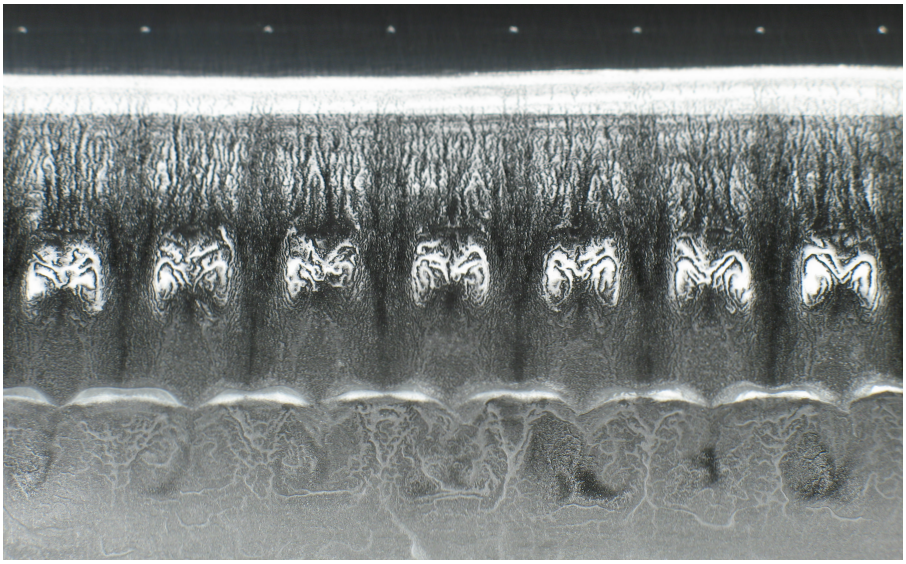

(a)

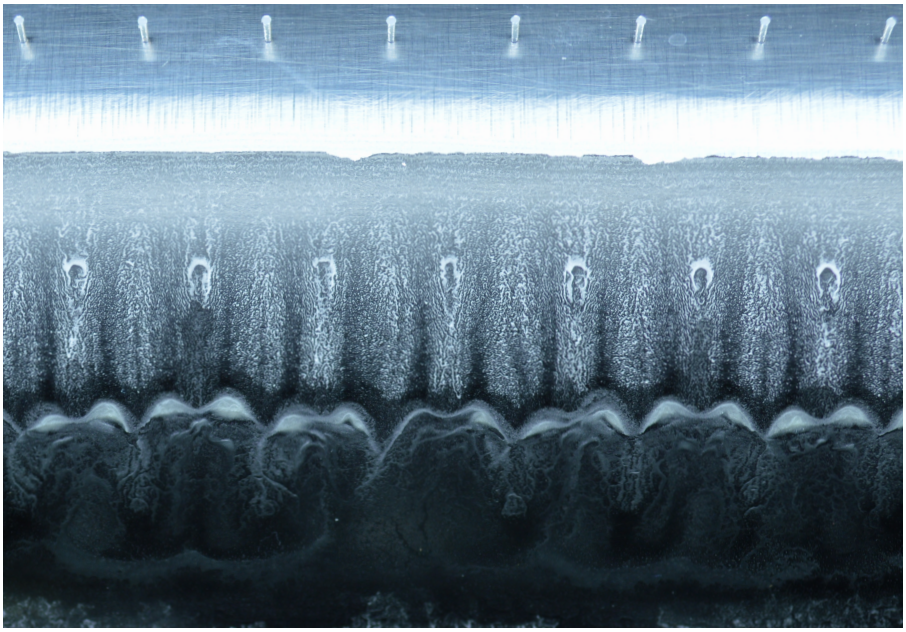

(b)

Figure 9.11 – Photographic comparison of surface oil flow visualisation test results, showing the time averaged skin friction line patterns for: (a) $z_P = 10mm$ pins; and, (b) $z_J = 10mm$ passive jets. $Re = 2.7{\times}10^5$, free-stream flow direction is approximately top to bottom.

line of S_1 and the subsequent delayed separation observed along the $S_{2,a}$ – N_2 – $S_{2,b}$ arrays to separate either via the separatrix which emanates from the S_2 saddle points which wraps up into the CRVP of $F_{1,a}$ and $F_{1,b}$, is itself swept into the CRVP, or along the separatrix of the S_3 saddle points – the furthest downstream point of separation. It is interesting to note here that compared to the secondary CRVP of the other configurations, the (only) CRVP formed downstream in the $z_P = 10mm$ skin friction pattern has shifted by half a phase – such that the pin-energised flow provides the supply of fluid to the foci of $F_{1,a}$ and $F_{1,b}$, rather than the reattached flow stream (see also the relative alignment of SOFV features presented in the comparison with $z_J = 10mm$ in Figure 9.11). This therefore suggests that this CRVP is more closely analogous to the primary CRVP with the sign of rotation and supply stream equivalent to all other configurations (including passive jets).

In the case of the $z_P = 20mm$ pin arrangement (Figure 9.12), the flow topology appears to be very similar to that of the $z_J = 20mm$ passive jets (Figure 7.5). They both clearly identify two sets of CRVP, where the primary CRVP are segregated by the energised streams of the jets or pins, and both generate a reattachment of the flow downstream of the initial laminar separation line – more clearly identifiable from photographs of the pins setup (Figure 9.13). While both 20mm spaced flow control methods share all of these features, they also have some noticeable differences. Perhaps the most obvious one is that the pin-energised stream produces a more vigorous channel of perturbed flow which ploughs a wider furrow through the initial laminar separation line before separating comparatively further downstream. This results in a narrower primary CRVP – and consequently region of separation bubble reattachment – as well as wedging apart of the upstream half of the secondary CRVP. Both of these features lead to the impression that the separation line formed

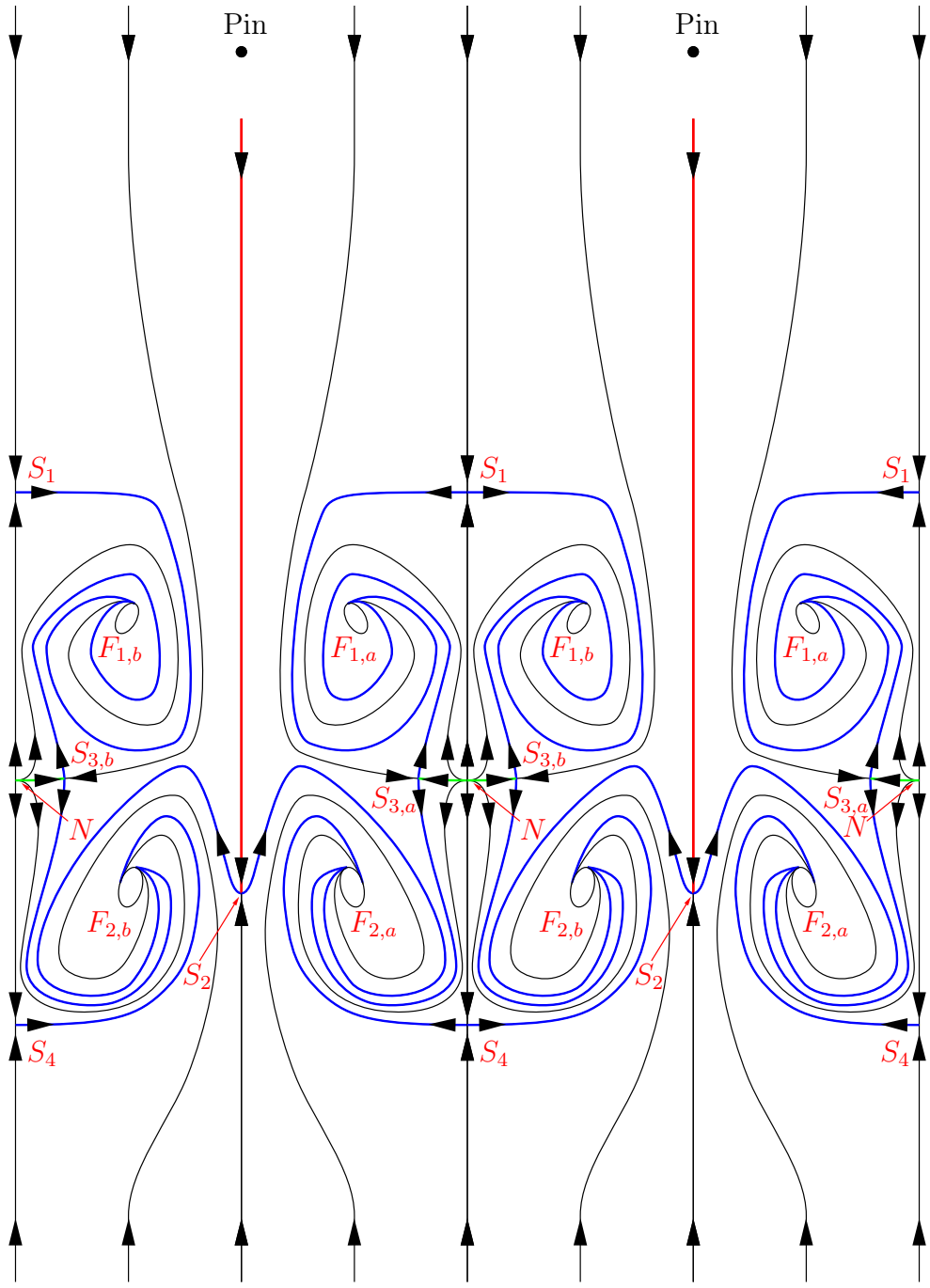

Figure 9.12 – Skin friction line schematic, $z_P = 20mm$, $Re = 2.7{\times}10^5$. Red lines represent skin friction lines from turbulent boundary layer flow, blue lines are saddle point separatrices (separation lines) and attachment node tangent lines (attachment lines) are shown in green. Text (black) and critical point (red) labels have the following meanings: Pin, location of pin; S, saddle point; N, node; F, focus.

from the separatrix of saddle point S_1 continues unbroken downstream to the saddle point S_2 in the wedge between the foci of the secondary CRVP. Here, again, there is evidence to suggest that this is an anomaly of the SOFV results, where the unstable positions of both primary and secondary CRVP lead to a smudging of the SOFV oil mixture which – with sufficient deposit and accumulation of tracer particles – can end up either altering the flow separation point or giving the impression of a continuous line of separation when the position of two lines of separation fluctuate and regularly overlap a position previously occupied by the other. The skin friction line pattern of Figure 9.12 shows a break in the separation lines formed by the separatrices of S_1 and S_2, where fluid drawn between the two adjacent vortices into the foci of either F_1 and F_2, or separating along the separatrix of S_3. As it turns out, the layout of the skin friction pattern for $z_P = 20mm$ pins is indeed simply a modified arrangement of the $z_J = 20mm$ passive jets, schematic (b) (see Figure 7.5) but with some subtle and important differences which are not immediately obvious without analysing additional data which is covered in the following sections. That said, the drag coefficient of both $z_P = 20mm$ and $z_J = 20mm$ cylinders is very similar at $Re_D = 2.7 \times 10^5$, suggesting that the increased delay in flow separation of the pin-energised stream is offset by the reduction in the size of flow reattachment region due to the narrower primary CRVP.

It is clear, not least from the work of Doligalski et al. (1994) and Fric and Roshko (1994), that the flow mechanisms induced by transversely placing round jets or round protrusions into wall-bounded cross-flow differ substantially. That difference, however, becomes more significant when the comparison is between low R jets and solid protrusions. This is because, as discussed in chapter 6, the mechanism of vorticity generation for low R jets is so different even to high R jets – which at the very least

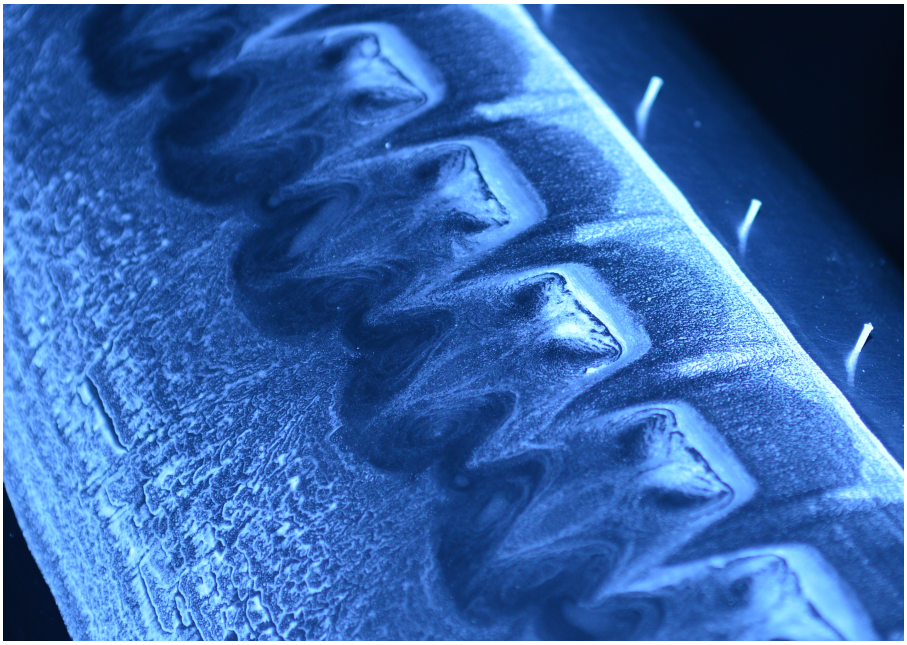

(a)

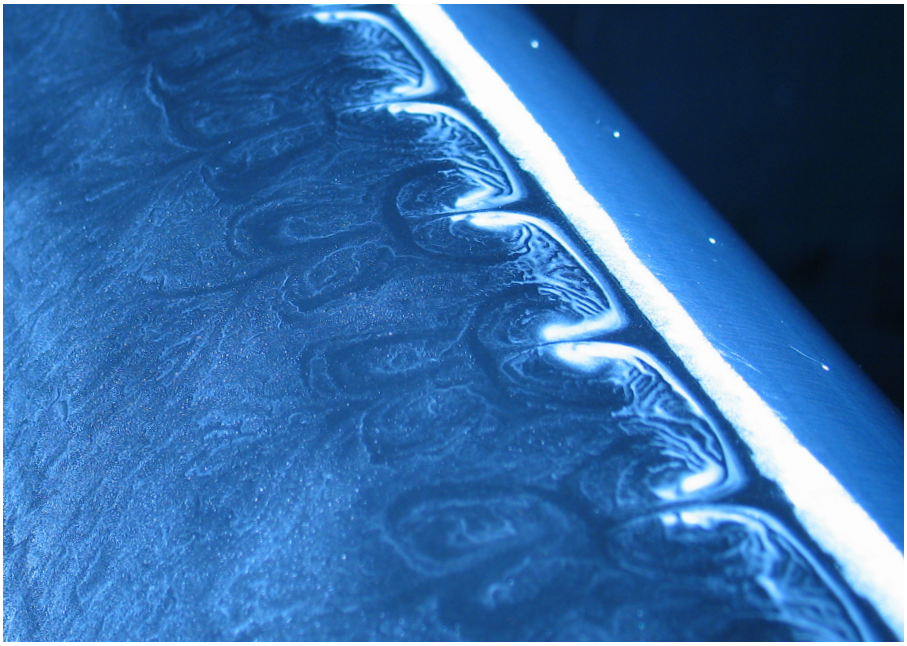

(b)

Figure 9.13 – Photographic comparison of SOFV test results, showing the time-averaged skin friction line patterns for: (a) $z_P = 20mm$ pins; and, (b) $z_J = 20mm$ passive jets. $Re = 2.7{\times}10^5$, free-stream flow direction is approximately right to left.

share the formation of horseshoe vortices with bluff wall protrusions. This is borne out in the way that the pin-energised flow imparts a significantly more pronounced disturbance to the cross-flow, in both stream-wise and span-wise directions, leading to an increased delay in flow separation in these span-wise locations than the passive jets. The down-side, however, is that the increased width of perturbed flow stream emanating from the pins leads to a restriction in the level of flow reattachment from the induced separation bubble by squeezing the span-wise space that it can occupy. In the case of the $z_P = 10mm$ cylinder, the separation bubble is significantly diminished and almost completely obliterated by the encroaching legs of the horseshoe vortex emanating from the upstream pin.

9.3 Shear layer development & wake dynamics

9.3.1 Comparison with passive jets at high Reynolds numbers

As was the case for the cylinder with $z_J = 20mm$ passive jets (section 8.3), stereoscopic PIV was utilised to analyse the separated shear layer and near wake structure in the (y, z) plane, immediately downstream of the cylinder with $z_P = 20mm$ discrete pin protrusions.

Figure 9.14 provides a comparison of the time-mean vorticity, Ω, and stream-wise component of velocity, u_x/U_∞, of the pins and passive jets flow control concepts at $Re_D = 2.54 \times 10^5$ to highlight the differences in shear layer and wake formation despite the similar C_D values (section 9.1) and surface skin friction line patterns (section 9.2.2) at this Reynolds number.

The immediately striking difference between the plots of near-wake vorticity, for

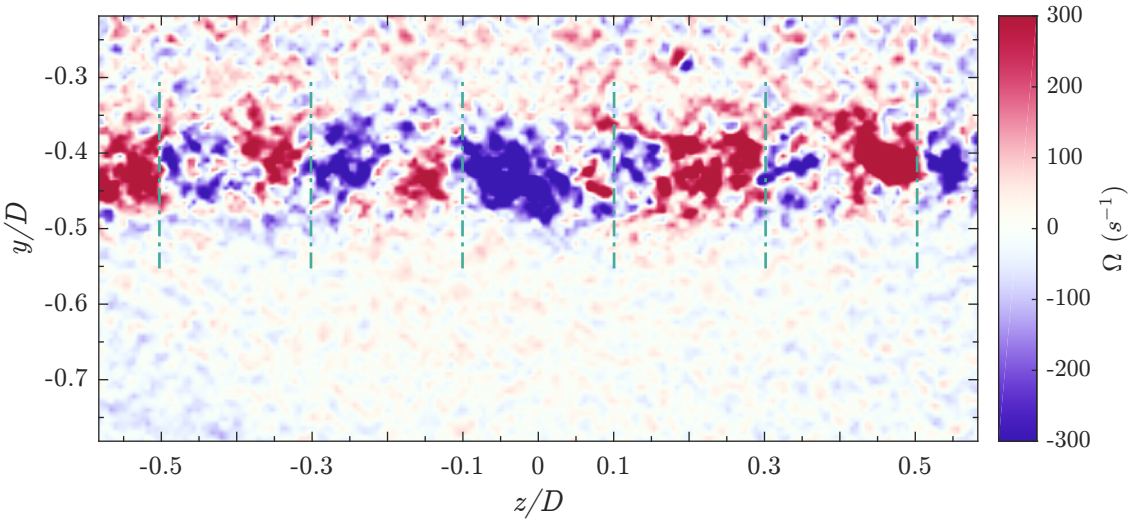

(a)

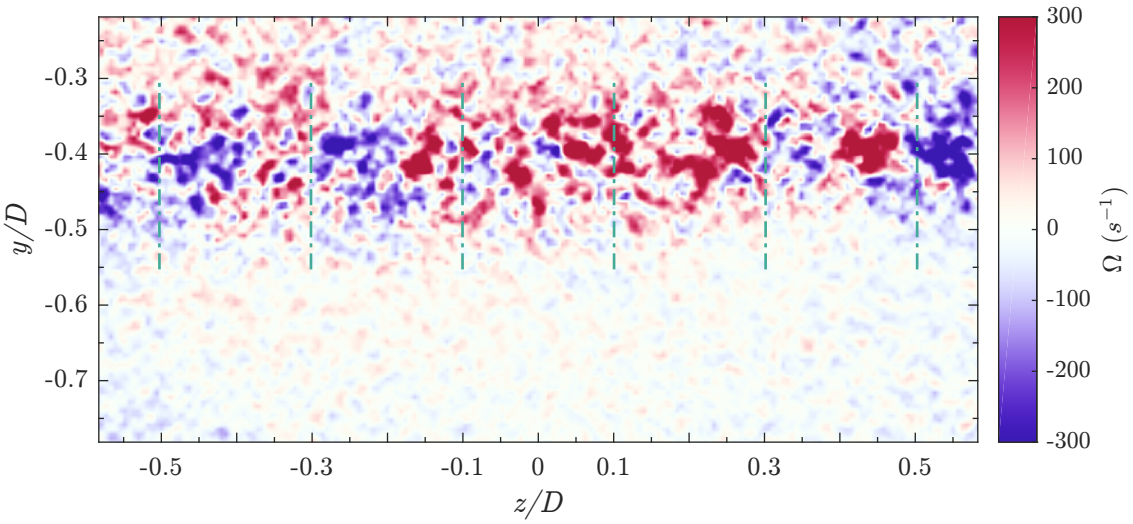

(b)

Figure 9.14 – (a) Ω, cylinder with $z_P = 20mm$ pins; and, (b) Ω, cylinder with $z_J = 20mm$ passive jets. Figure continues on following page – full caption follows final plot.

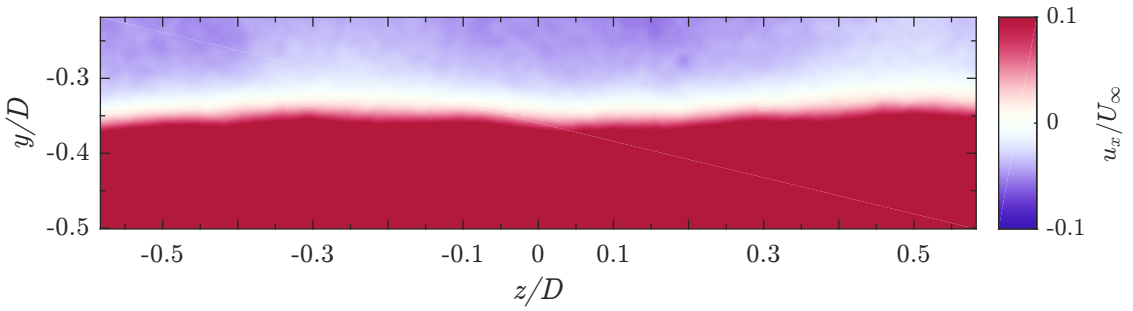

(c)

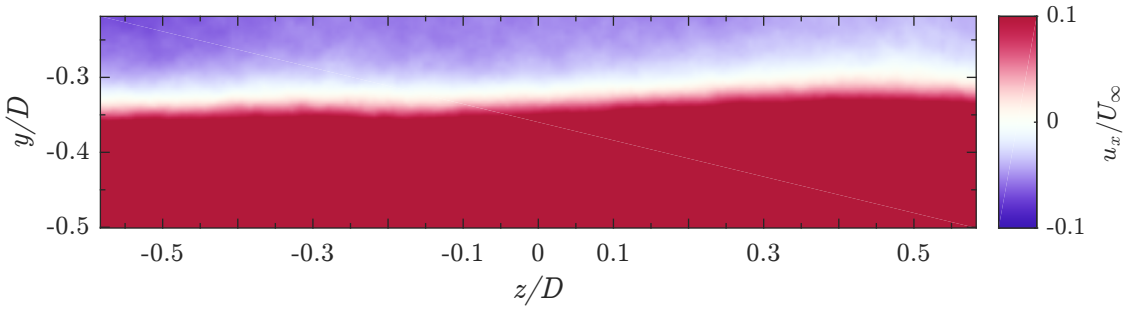

(d)

Figure 9.14 – See preceding page for figures (a) & (b). Comparisons of time-mean vorticity, Ω, and stream-wise velocity component, u_x/U_∞, in (y, z) plane of the near-wake of a cylinder with either pins or passive jets flow control, where: (a) Ω, cylinder with $z_P = 20mm$ pins, $D/U_\infty = 2.57\times10^{-3}$; (b) Ω, cylinder with $z_J = 20mm$ passive jets, $D/U_\infty = 2.57 \times 10^{-3}$.; (c) u_x/U_∞, cylinder with $z_P = 20mm$ pins; and, (d) u_x/U_∞, cylinder with $z_J = 20mm$ passive jets. $Re_D = 2.5 \times 10^5$ (uncorrected for blockage). In (a) & (b) dotted lines indicate span-wise locations of pins and holes, respectively.

the pins (Figure 9.14(a)) and passive jets (Figure 9.14(b)), is that: where there is an approximate correlation of the vorticity structure with passive jet spacing, there is a clear and distinct correlation with pin spacing. With the increased orderliness of the time-mean vorticity structure in the shear layer also comes a more compact band of vorticity across the span, indicating that there is less vertical motion (flapping) of the shear layer compared to the passive jets.

The plots of u_x/U_∞ (Figure 9.14(c), Figure 9.14(d)) reveal that while there is

increased vorticity in the shear layer with the application of pins, the mean wake width of the cylinder with passive jets is narrower. This finding seems to correlate with the relatively increased delay in flow separation of the reattached flow for the passive jets, which perhaps is balanced out (in terms of drag reduction) by an increase in base pressure generated by the increased stream-wise vorticity in the shear layer of the cylinder with pins. As with the shear layer shapes observed from the cylinder with passive jets at $Re_D = 1.02 \times 10^5$ and $Re_D = 1.53 \times 10^5$ (see section 8.6), there appears to be a time-mean waviness to the shear layer which correlates with the vorticity and, as a result, the pin spacing.

9.3.2 Correlation of skin friction line patterns with near-wake structure

In light of the distinct correlation of pin spacing with the stream-wise vorticity found in the shear layer of the near wake, a composite figure of the skin friction line pattern – observed through SOFV tests – and near wake vorticity in the (y, z) plane for the $z_P = 20mm$ cylinder was produced (Figure 9.15).

As with the similar plot produced for the $z_J = 20mm$ passive jets (Figure 8.7), the foci of the CRVP observed at the cylinder surface have been coloured in coordination with the vorticity colourbar (red – positive (anti-clockwise) vorticity, blue – negative (clockwise) vorticity). It is plainly clear from this figure that the rotation of the primary CRVP matches that of the time-mean vorticity structure observed in the near-wake shear layer at the same span-wise location. This conclusion was also drawn from Figure 8.7 for the passive jets, however the correlation for the pins is significantly more persuasive. A possible reason for the increased levels of vorticity

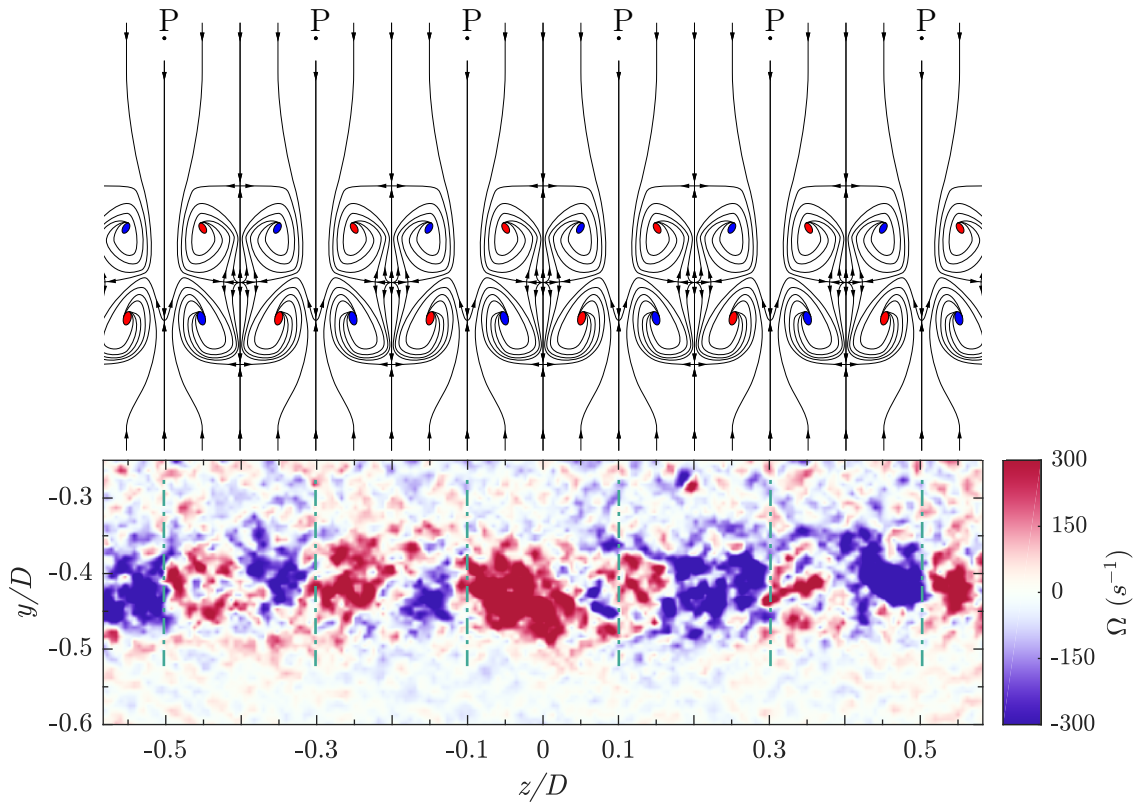

Figure 9.15 – Composite graphic of time-mean skin friction line pattern and near-wake vorticity for the 'pins' flow control method, $z_P = 20mm$. Pin locations are labelled 'P' and downstream wake positions in-line with pins are marked by green dashed lines. The foci of the CRVQ are coloured according to the vorticity colourbar scale, where positive vorticity – corresponding to anticlockwise rotation – is coloured red, negative is blue. $D/U_\infty = 2.57 \times 10^{-3}$.

matching the rotation of the CRVP in the case of the pins is that the sign of rotation of the 'legs' of the horseshoe vortices – which are generated at the junction of the wall mounted pins – matches that of the adjacent foci of the CRVP as it passes downstream. This being the case, these co-rotating vortices may merge and effectively strengthen the tornado-like vortices which are thought to shed from the cylinder surface.

9.3.3 Comparisons of near-wake characteristics of pins and passive jets in the low – mid Re_D range

PIV measurements were taken in the (y, z) plane throughout the same Re_D testing range as for the study on the cylinder with passive jets (see section 8.5) in order to chart the differences in wake appearance with the corresponding value of C_D, and for comparison with the equivalent data acquired for the cylinder with $z_J = 20mm$ passive jets. Figure 9.16 plots the C_D v. Re_D curve of the $z_P = 20mm$ cylinder overlaid with the acquisition Re_D for the SPIV experiments.

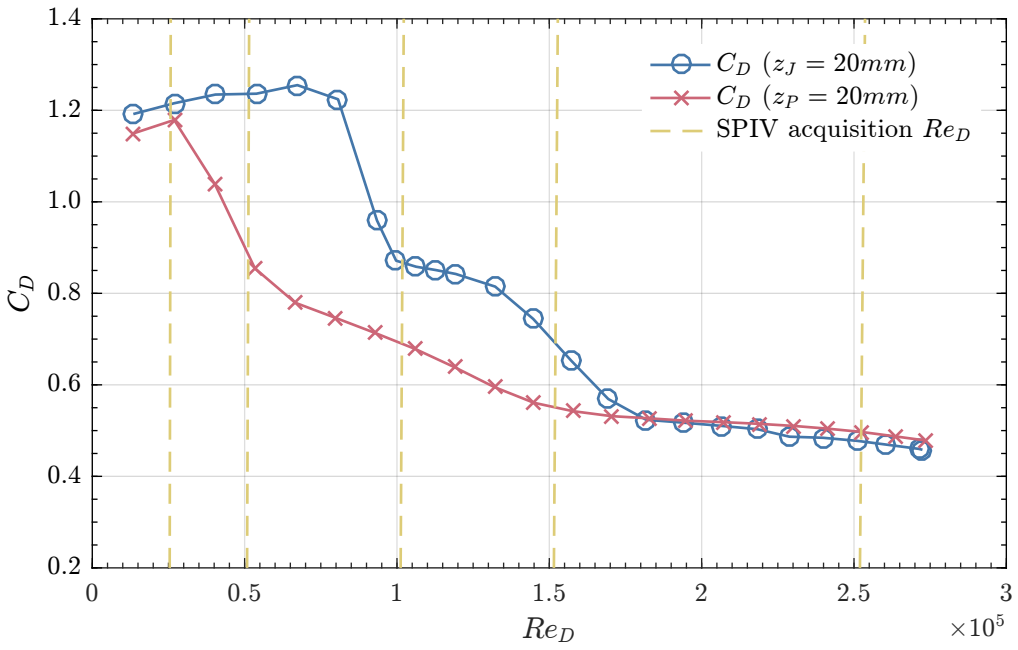

Figure 9.16 – C_D profile for $z_P = 20mm$ pins and $z_J = 20mm$ jets overlaid with vertical dashed lines to indicate the acquisition Re_D for the PIV measurements in the (y, z) plane.

Figure 9.17 presents a comparison of time-mean vorticity, Ω, observed in the shear layer and near wake, between the cylinder with $z_J = 20mm$ pins and $z_J = 20mm$ passive jets, as it develops through the Re_D testing range. An equivalent set

of plots of u_x/U_∞ – comparing pins with passive jets – can be found in Appendix G.3 for reference with this section.

As one would assume, there is no significant difference between the plots of vorticity for both $z_J = 20mm$ and $z_J = 20mm$ at $Re_D = 2.6 \times 10^4$ where both of these cylinder arrangements lie within the pre-critical regime.

Increasing the Reynolds number to $Re_D = 5.2 \times 10^4$ and one would expect there should be an observable difference in the wake structures, since the cylinder with $z_J = 20mm$ passive jets still resides within the pre-critical regime but the cylinder with pins has already exceeded the critical Reynolds number and C_D has begun to quickly drop. The plot of near-wake vorticity for the cylinder with pins, in Figure 9.17(c), does indeed provide a marked difference with Figure 9.17(d) which presents the equivalent result for the passive jets setup. The wake vorticity for the pins setup has become more concentrated in a span-wise band – roughly in the range $-0.6 \leqslant y/D \leqslant -0.45$ – as compared to the continuation of the largely homogeneous spread of vorticity in the wake of the cylinder with passive jets. This indicates that the pins have begun to stabilise the flapping of the shear layer, likely by the disruption of von Kármán vortex shedding.

For $Re_D = 1.02 \times 10^5$, where a large-scale, time-mean vorticity structure forms in the wake of the cylinder with passive jets as C_D begins to drop. The equivalent plot for the $z_P = 20mm$ arrangement appears to show a concentration of a similar band of vorticity seen at $Re_D = 5.2 \times 10^4$, but with the shear layer moving closer to the cylinder centreline, indicating an increased delay in flow separation with the resulting narrowing of the wake and reduction in C_D. The cylinder with pins has a reduced drag coefficient by comparison with the passive jets at this Re_D and this can be predicted by the larger spread of wake vorticity which again indicates a more

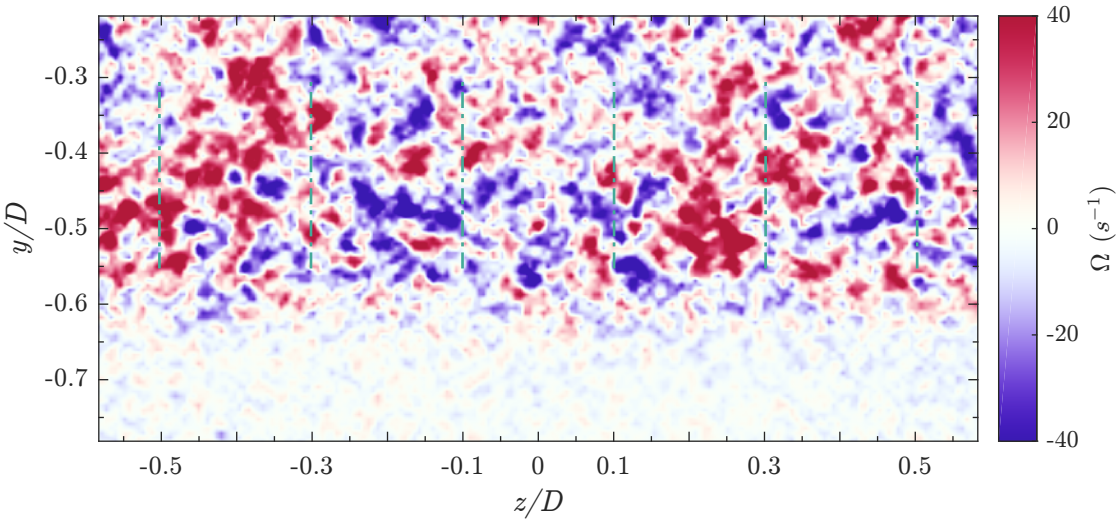

(a)

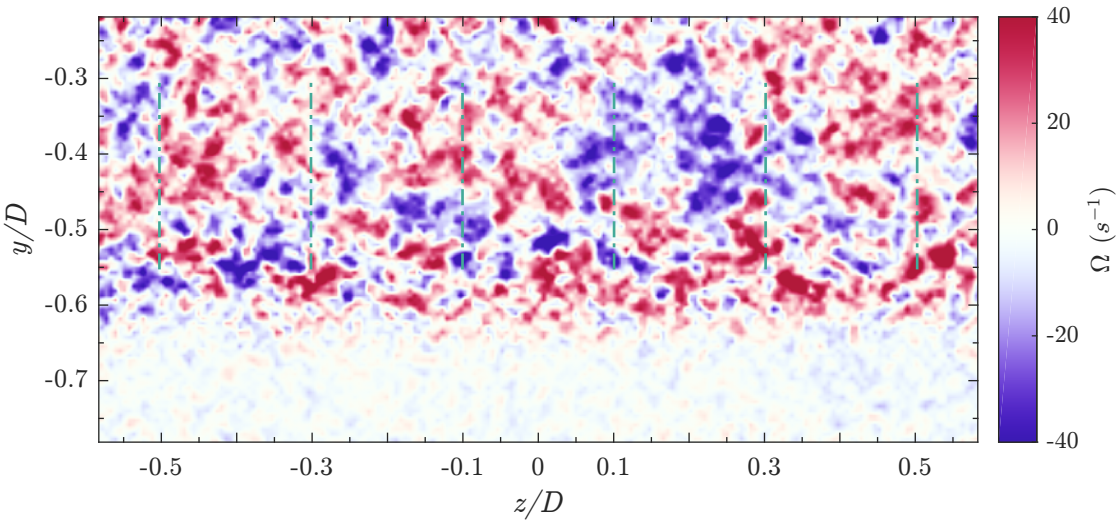

(b)

Figure 9.17 – Time-mean vorticity, Ω, in the near-wake at $Re_D = 2.6 \times 10^4$, for: (a) $z_P = 20mm$ pins; and, (b) $z_J = 20mm$ passive jets. Figure continues on following pages – full caption follows final plot.

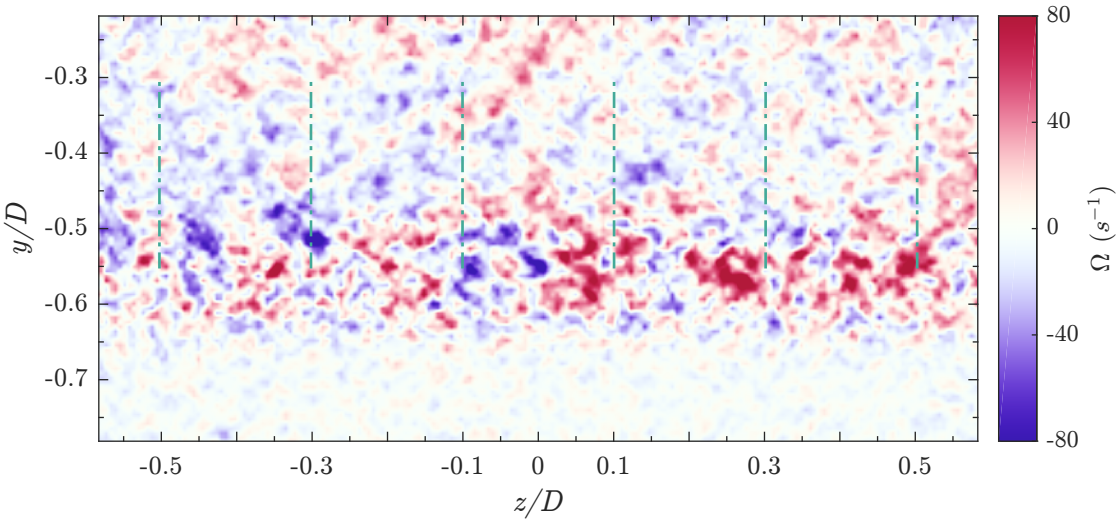

(c)

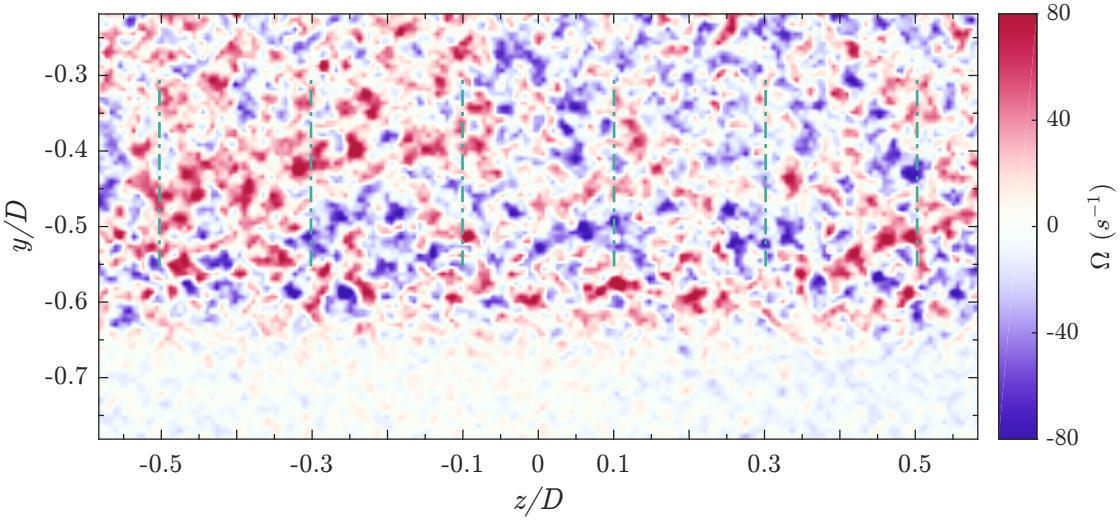

(d)

Figure 9.17 – Time-mean vorticity, Ω, in the near-wake at $Re_D = 5.2 \times 10^4$, for: (c) $z_P = 20mm$ pins; and, (d) $z_J = 20mm$ passive jets. Figure continues on following pages – full caption follows final plot.

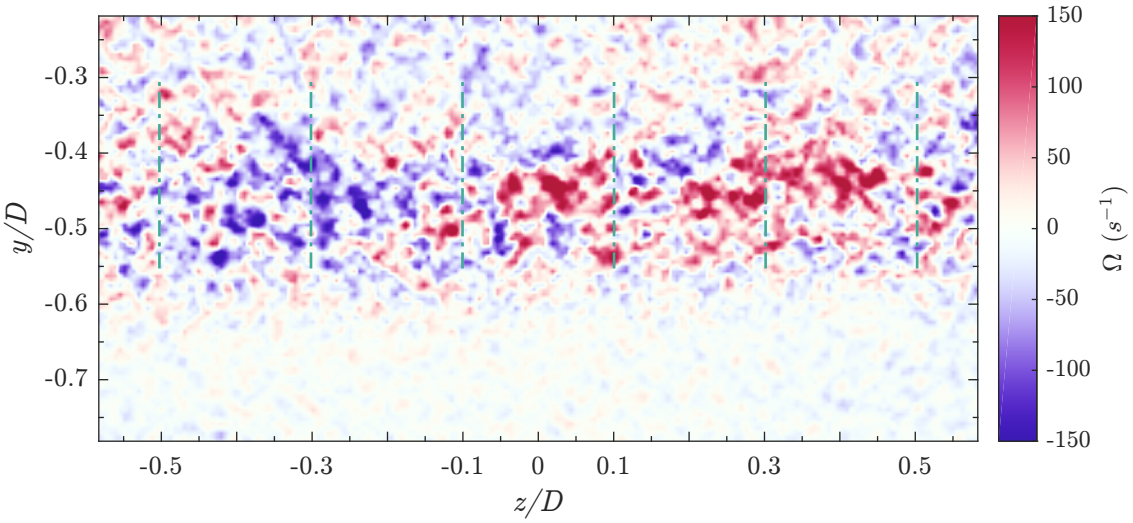

(e)

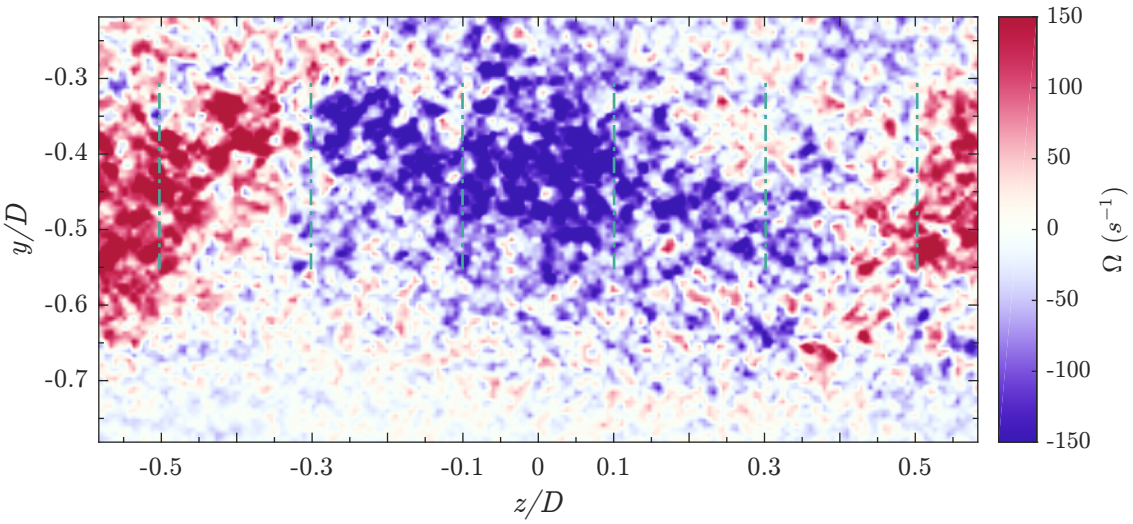

(f)

Figure 9.17 – Time-mean vorticity, Ω, in the near-wake at $Re_D = 1.02 \times 10^5$, for: (e) $z_P = 20mm$ pins; and, (f) $z_J = 20mm$ passive jets. Figure continues on following pages – full caption follows final plot.

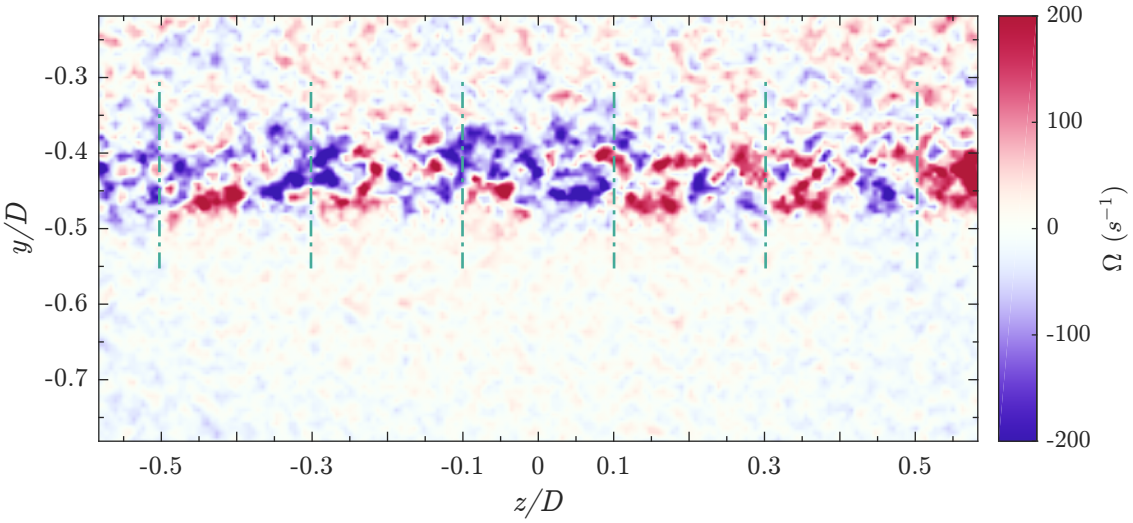

(g)

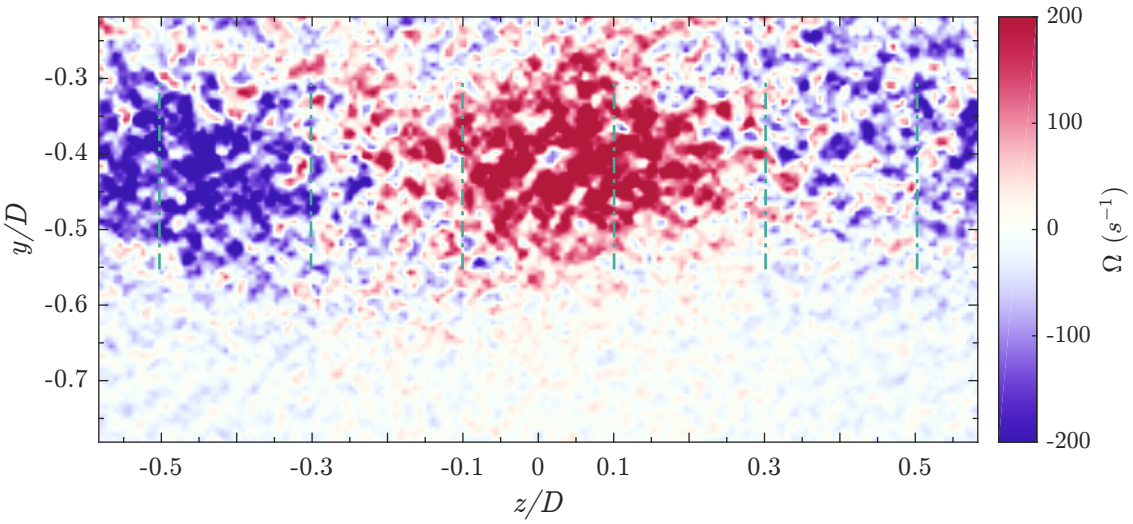

(h)

Figure 9.17 – Time-mean vorticity, Ω, in the near-wake at $Re_D = 1.53 \times 10^5$, for: (g) $z_P = 20mm$ pins; and, (h) $z_J = 20mm$ passive jets. Figure continues on following pages – full caption follows final plot.

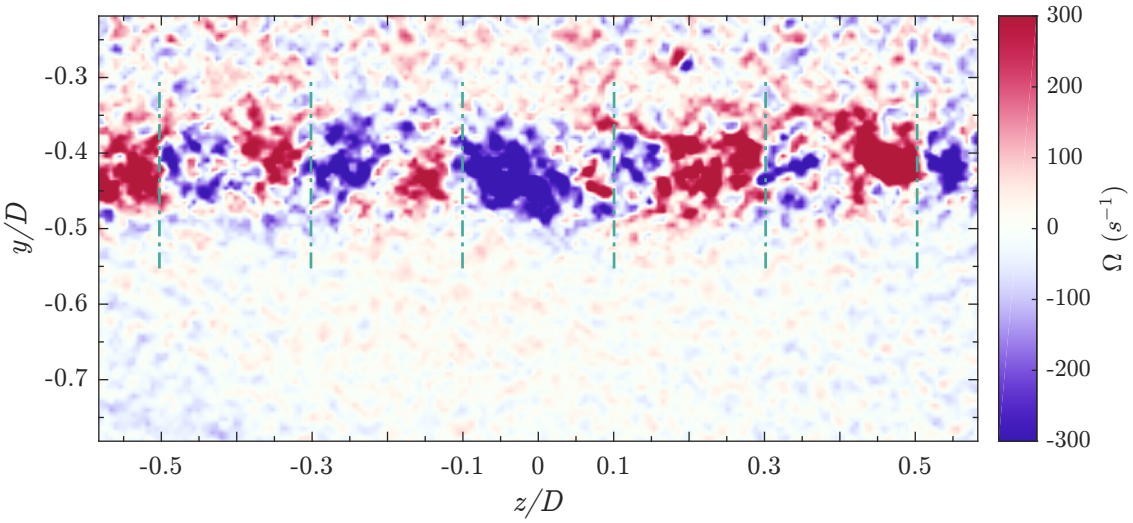

(i)

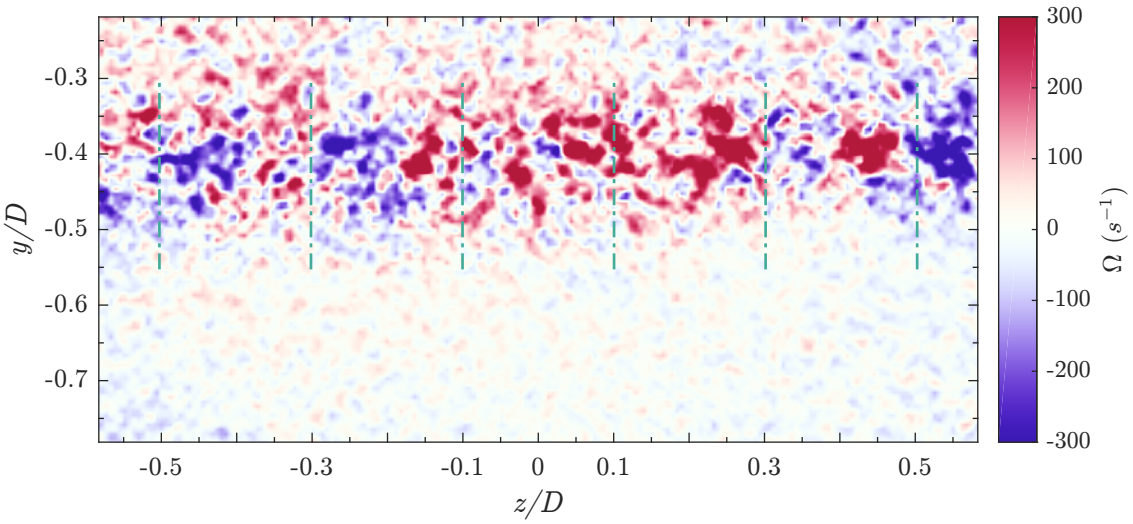

(j)

Figure 9.17 – Time-mean vorticity, Ω, in the near-wake at $Re_D = 2.54 \times 10^5$, for: (g) $z_P = 20mm$ pins; and, (j) $z_J = 20mm$ passive jets. Full caption on following page.

Figure 9.17 – See preceding pages for figures (a) – (j). Comparisons of separated shear layer from a cylinder with either pins or passive jets flow control at various Re_D. Plots of time-mean vorticity, Ω, in the (y, z) plane of the near wake of a cylinder, where: (a) $z_P = 20mm$ pins, $Re_D = 2.6 \times 10^4$, $D/U_\infty = 25.9 \times 10^{-3}$; (b) $z_J = 20mm$ passive jets, $Re_D = 2.6 \times 10^4$, $D/U_\infty = 25.9 \times 10^{-3}$; (c) $z_P = 20mm$ pins, $Re_D = 5.2 \times 10^4$, $D/U_\infty = 12.9 \times 10^{-3}$; (d) $z_J = 20mm$ passive jets, $Re_D = 5.2 \times 10^4$, $D/U_\infty = 12.9 \times 10^{-3}$; (e) $z_P = 20mm$ pins, $Re_D = 1.02 \times 10^5$, $D/U_\infty = 6.45 \times 10^{-3}$; (f) $z_J = 20mm$ passive jets, $Re_D = 1.02 \times 10^5$, $D/U_\infty = 6.46 \times 10^{-3}$; (g) $z_P = 20mm$ pins, $Re_D = 1.53 \times 10^5$, $D/U_\infty = 4.39 \times 10^{-3}$; (h) $z_J = 20mm$ passive jets, $Re_D = 1.53 \times 10^5$, $D/U_\infty = 4.30 \times 10^{-3}$; (i) $z_P = 20mm$ pins, $Re_D = 2.54 \times 10^5$, $D/U_\infty = 2.57 \times 10^{-3}$; and, (j) $z_J = 20mm$ passive jets, $Re_D = 2.54 \times 10^5$, $D/U_\infty = 2.57 \times 10^{-3}$.

substantial vertical oscillation of the free shear layers.

Increasing Reynolds number further still to $Re_D = 1.53 \times 10^5$ produces distinct time-mean structure in the near wake of both flow control concepts. For the cylinder with pins, there is now a very thin band of concentrated vorticity stretching in a straight line across the span, with the vertical location again shifting towards the cylinder centreline. The distinct correlation with pin spacing – and indeed the sign of rotation of the primary CRVP – is observed for the first time. The cylinder with jets continues to produce larger scale time-mean patches of vorticity covering a band of increased height across the span and this is again reflected in an increased value of C_D compared to that of the pins arrangement.

At the maximum tested Reynolds number, $Re_D = 1.53 \times 10^5$, the cylinder with passive jets finally begins to resemble the pattern of vorticity found in the wake of the cylinder with pins, as it forms a narrower, more concentrated band of vorticity across the span and accordingly the value of C_D drops below that of the cylinder with pins for the first time at equivalent Re_D. By contrast, the time-mean vorticity structure of the cylinder with pins has begun to diffuse somewhat as the time-mean

print of vorticity now covers a larger vertical distance, though the mean wake width has reduced slightly from $Re_D = 1.53 \times 10^5$, bringing with it a reduction in C_D by comparison.

Chapter 10

Summary of conclusions

While many conclusions arising from this research have been presented in the main body of results and discussion, there are some points which are useful to summarise here to provide a concise narrative of the work carried out.

10.1 General approach to passive drag reduction of bluff-bodies

- As first discussed in the chapter 2, in terms of maximising the delay of flow separation, an optimal approach might be to follow the process of the naturally occurring laminar separation bubble – generated in the critical regime of a circular cylinder – from which the minimum C_D is (passively) achieved. That is, to allow the laminar boundary layer to travel as far downstream as it can resist an adverse pressure gradient, induce transition of the shear layer as soon as it separates – such that the turbulent shear layer reattaches to the cylinder surface – and allow the newly energised boundary layer to proceed without

any additional hindrance before a final turbulent separation occurs some way downstream.

- The review experiments of some passive flow control methods in chapter 4 show that $C_{D(min)}$ can be maintained (throughout the sub-critical Re_D range of a plain cylinder) for unidirectional flow applications by eliminating boundary layer perturbations downstream of the initial trip.

10.2 Transverse jets: Primary investigations

- In the Re_D range tested, both $z_J = 10mm$ and $z_J = 20mm$ passive jet arrangements produce similar values of $C_{D(min)}$, however there is a substantial improvement in C_D reduction from the $z_J = 10mm$ cylinder in the mid-Re_D range ($1.1{\times}10^5 \leqslant Re_D \leqslant 1.7{\times}10^5$). At high Re_D ($1.8{\times}10^5 \leqslant Re_D \leqslant 2.8{\times}10^5$), the drag coefficient of the $z_J = 20mm$ cylinder appears to gradually, but continually, drop with increasing Re_D whereas the $z_J = 10mm$ setup has appeared to plateau. Higher Re_D testing is required (e.g. $2.8{\times}10^5 \leqslant Re_D \leqslant 5.0{\times}10^5$) to resolve post-critical regime behaviour for these particular passive flow control arrangements.

- Upon the inducement of the critical regime with passive jets by this particular cylinder design, there appears to be a bifurcation whereby the initiation of drag reduction occurs more favourably on one side of the cylinder than the other – and this can be altered with very small changes in the orientation of the cylinder to the free-stream. This is due to the use of a common plenum chamber (i.e. the cylinder volume) to supply both rows of jet holes. An improved design would provide independent supply channels to each row of jet

holes to prevent time-mean asymmetries in the cylinder pressure distribution (and hence lift force). It may also lead to a smoothing of the C_D v. Re_D curve throughout the test speed range.

- From the analysis of the passive jets feasibility results (section 5.3.1), there appears to be a considerable range of jet velocities (beyond a critical minimum) for which a particular jet spacing will generate the same C_D v. Re_D curve. This could provide flexibility in the design and application of this type of flow control, but also indicates a limitation to the C_D reduction achievable by positioning transverse jets in this way.

- Though optimised for a unidirectional flow application, the model with passive transverse jets offset by $\Delta\phi = \pm 10^{\circ}$ provided only a small decline in C_D reduction performance throughout the Re_D testing range and delivered the same value of C_D as the optimally aligned case for $Re_D \geqslant 2.0 \times 10^5$.

- For the $z_J = 20mm$ passive jets cylinder, an absence of von Kármán vortex shedding (KVS) was found for $Re_D > 6.6 \times 10^4$ which coincides with the initiation of the critical regime by this flow control setup; once the jet flow rate into the boundary layer is sufficient to destabilise straight-line separation from the cylinder surface, the resulting breakdown of KVS into the wake serves to immediately increase the base pressure and reduce C_D.

10.3 Transverse jets: Flow mechanisms

- The cylinders with passive jets developed for this research had a jet to cross-flow velocity ratio in the range $0.07 \leqslant R \leqslant 0.41$. Analysis of the data, in tandem with a study of the literature, points to the conclusion that the jet – cross-flow interaction leads to the formation of hairpin vortices on the leeward shear layer of the jet to produce a periodic instability whereby these hairpin vortices are shed at high-frequency into the cross-flow boundary layer. It is thought that as these hairpin vortices are swept downstream they breakdown to initiate transition of, and hence energise, the boundary layer.

- Hairpin vortex shedding was detected from $Re_D \geqslant 1.03 \times 10^5$, which coincides with a continual drop in C_D, however a detection of the instability was not found at $Re_D = 0.90 \times 10^5$ at which point C_D had already begun to drop. This is thought to be due to less persistent hairpin vortex shedding below a critical value of R.

- The Strouhal number of the hairpin vortex shedding forms a linear relationship with the cross-flow Reynolds number, Re_{cf}, and correlates well with data from the literature.

- Due to the low values of R generated by the specific designs of the passive jet arrangements tested, it is expected – from a review of similar studies – that the jet emission remains within the cross-flow boundary layer. This feature is thought to be of benefit to the entrainment of higher momentum flow towards the wall in addition to maintaining the energising action within the boundary layer rather than the outer-flow where its effect would be diminished. Publi-

cations investigating the effectiveness of transverse jets in turbine blade film cooling applications typically find that optimum boundary layer mixing characteristics occur with low values of jet to cross flow ratio ($R \leqslant 0.5$) – see discussion in section 6.4; emission from high R transverse jets tends to produce trajectories which pass through the boundary layer to promote mixing in the free stream – potentially limiting its influence on the boundary layer flow.

10.4 Transverse jets: Flow topology

- Schematics developed from the interpretation of skin friction patterns created during SOFV tests – conducted on the surface of the cylinder with $z_J = 20mm$ passive jets – reveal a repeating array of 'owl type 2' separation bubbles across the span, comprised of a distinctive (primary) CRVP wrapped in a laminar separation line with a nodal point of attachment following immediately downstream. The reattached flow subsequently separates significantly further downstream than the initial laminar separation line between a secondary CRVP – which forms immediately downstream of the primary pair and draw fluid from the base region. These laminar separation bubbles form as a result of the channels of jet energised boundary layer flow which pass through the line of initial laminar separation (which typically forms at this point on a plain cylinder at equivalent Re_D).

- Topologically coherent solutions to the critical points found at the cylinder surface presume that the two sets of CRVP shed tornado-like vortices through the separating shear layer into the wake – a feature which is corroborated through time-mean patterns of counter-rotating vorticity in the near-wake.

- Observations made of videos of SOFV tests for the passive jets tests illuminate the unsteady nature of the topological structure; as discussed in section 7.2.2, the skin-friction streakline pattern appears to alternate between arrangement (a) (Figure 7.4) and arrangement (b) (Figure 7.5). For simplicity, skin-friction line schematics were drawn to be symmetric, however, in reality the flow topology never reaches a perfectly stable arrangement and thus many asymmetric variations exist – due, at least in part, to the intrinsically three-dimensional nature of high Re_D cylinder flow (see discussion in section 8.5).

- As a result of the variation in the circumferential angle of separation points across the cylinder span, a 'wavy' final separation line forms – a feature which is well-know to prevent von Kármán vortex shedding and hence increase the cylinder base pressure.

- Reducing the spacing of the passive jets along the cylinder span affects the flow topology structure in the separation region; the jet energised channel of flow has an increased delay in separation but, by imposing a reduction in the size of the separation bubble which can form, there is a reduction in the separation delay of the reattached flow.

- The laminar separation bubbles (where a reattachment of the flow downstream of the initial laminar separation is observed) are only found at high Re_D, and indeed appear when the drag coefficient is approaching $C_{D(min)}$. For the $z_J = 10mm$ cylinder, laminar separation bubbles are detected at $Re_D = 1.70 \times 10^5$ – when C_D has already begun to plateau with increasing Re_D – but not at $Re_D = 1.38 \times 10^5$ while C_D continues to drop steeply with Re_D. There is no accompanying increase in R between $1.38 \times 10^5 \leqslant Re_D \leqslant 1.70 \times 10^5$, and hence

the formation of the separation bubble is due to an increase in the instability of the cross-flow through an increase in Re_D.

10.5 Transverse jets: Shear layer and wake dynamics

- The time-mean length of the recirculation zone is shown to increase with the application of passive jets compared to a plain cylinder, with span-wise variations in the time-mean length for passive jets according to jet spacing; the length of the recirculation zone is increased at span-wise locations between jet holes compared to locations in-line with jet holes.

- At high Re_D ($Re_D = 2.54 \times 10^5$), the time-mean vorticity structure found in the (y, z) plane of the near wake correlates with the span-wise position and sign of rotation of the primary CRVP found to form as part of the 'owl type 2' separation bubble on the cylinder surface. It is therefore concluded that tornado-like vortices are shed into the wake through the separating shear layer from the CRVP observed at the cylinder surface.

- At mid range Re_D ($1.02 \times 10^5 \leqslant Re_D \leqslant 1.53 \times 10^5$), larger-scale clumping of counter-rotating vorticity is found in the near wake, producing a time-mean wavy shear layer with a wavelength, λ, apparently uncorrelated with jet spacing approximately in the range ($1.2D \leqslant \lambda \leqslant 1.4D$). This appears to be related to an excitation of the three-dimensional 'mode B' instability, which naturally occurs for a plain circular cylinder.

10.6 Discrete boundary layer protrusions – "Pins"

- In comparison with passive jets, discrete cylindrical protrusions of the same diameter, arranged in the same way and extending a mean distance of $y_P = 2.5mm$ from the cylinder surface, promote the critical regime to lower Re_D. In the case of the $z_P = 20mm$ pin arrangement, $C_{D(min)}$ is only slightly inferior to the equivalently spaced passive jet setup. However, the value of $C_{D(min)}$ reached by the narrower $z_P = 10mm$ pin arrangement is relatively high compared to the all other novel configurations tested.

- The drag curves of cylinders with pin spacing of $z_P \geqslant 20mm$ appear to converge upon a common line with increasing Re_D, indicating a limiting factor in the $C_{D(min)}$ achievable by this flow control method.

- The pins produce a significantly greater momentum deficit to the cross-flow compared with the passive jets in addition to a greater level of vorticity generation – produced by the interaction of the cross-flow with a solid obstruction – with a horseshoe vortex forming at the upstream base of each pin. The 'legs' of the horseshoe vortices wrap around the pin and sweep downstream as a pair of diverging counter rotating vortices along the cylinder surface – the traces of which can clearly be identified from SOFV tests.

- The effect of the diverging horseshoe vortex legs is to widen the channel of energised flow swept downstream, with the consequence that for the narrower spaced ($z_P = 10mm$) pin arrangement, the space afforded to the formation of separation bubbles is almost eliminated. As a result, the reattached flow is greatly weakened – relative to the wider spaced setups – and this is reflected

in the high value of $C_{D(min)}$ achieved.

- In comparison with the $z_J = 20mm$ passive jets, the cylinder with the $z_P = 20mm$ pins produces a much clearer and distinctive time-mean counter-rotating vorticity structure in the near-wake which correlates both with pin spacing and the sign of rotation of the primary CRVP.

- For the passive jets, exchange of fluid between adjacent, primary CRVP foci appears to be a regular, repeating process – perhaps as a result of an inherently unstable flow topology caused by (with reference to Figure 7.4 and 7.5) the close proximity of the F_1 foci separated by the jet energised streams, and S_2 saddle points. The topological structure elucidated from photos of SOFV tests for both $z_P = 10mm$ and $z_P = 20mm$ pin arrangements, however, suggests that this behaviour is not possible. The increased perturbation – and hence energising action – of the flow stream by the pins leads to (with reference to Figure 9.12) the separatrices of the S_1 saddle points being prevented from winding up into the foci of adjacent cells; the increased resistance to separation of the pin-energised boundary layer flow generates an insurmountable barrier to fluid exchange between adjacent primary CRVP cells. This imposition of a more 'rigid' or stable topological structure is perhaps another reason that for the $z_P = 20mm$ pins arrangement there is greater prominence in location, strength and stability of the vorticity found in the near-wake compared to $z_J = 20mm$ passive jets; there is less variability in the strength and distribution of counter-rotating vortices across the cylinder span – brought about by the regular exchange of fluid between adjacent primary CRVP.

- Another reason that there was increased vorticity and structural correlation

with control element spacing in the near-wake of the $z_P = 20mm$ pins arrangement, compared to the $z_J = 20mm$ passive jets arrangement, could be as a result of the 'constructive' merging of the horseshoe vortices – generated by each pin protrusion – with the adjacent tornado-like vortices of the primary CRVP. The sign of rotation would be the same for each horseshoe 'leg' as for the adjacent focus of primary CRVP that it runs alongside; assuming they leave the cylinder surface close to one-another (and have core sizes beyond a critical fraction of the distance between them) they will be inclined to coalesce (see, for example, Leweke et al., 2016) – thus leading to increased vorticity of equal sign to the primary CRVP in the near-wake. This contrasts with the passive jets arrangement in that the 'legs' of the hairpin vortices (generated by the jet-cross-flow interaction) shed into the boundary layer have a sign of rotation counter to that of the primary CRVP. There is no evidence to suggest that these hairpin vortices maintain a coherent structure like that of the horseshoe vortices of the pins and, as discussed in section 7.2.2, it is thought that the hairpin vortices breakdown to initiate transition of the boundary layer prior to line of initial laminar separation (and subsequent formation of the primary CRVP) which occurs some $40d_J$ downstream of the jet holes.

- Throughout the Re_D testing range, the pin flow control method more strictly imposes vorticity distribution in the near wake and in doing so appears to reduce the vertical movement (flapping) of the shear layer compared to the passive jets. This results in improved C_D reduction for all but high Re_D ($Re_D \geqslant 1.7 \times 10^5$).

10.7 Final comments

- This body of research focused on two methods of passive drag reduction – passive jets and discrete cylindrical protrusions ('pins'). It was found that placing discrete (i.e. leaving space between a span-wise array of) surface perturbations allows for the inducement of certain types of laminar separation bubbles (the laminarly separated shear layer of which – if not continuously – regularly reattaches after transitioning before leading to a final turbulent separation) to form at Reynolds numbers significantly lower than that of the critical regime of a plain cylinder.

- If a tightly packed array of flow modifiers, or continuous span-wise disturbance is used to energise the boundary layer, laminar separation bubbles will at least be inhibited – and likely prevented – from forming. Reducing the spacing of the perturbations reduces the space available for separation bubbles to form and the smaller separation bubbles found here resulted in weaker streams of flow reattachment.

- The array of discrete boundary layer perturbations (jets and pins) splits the previously continuous laminar boundary layer (as anticipated on a plain cylinder) into a discontinuous span-wise array of laminar boundary layer sections, fenced-off by induced turbulent boundary layer wedges (of varying character and influence, depending on the type of perturbation). Between the discrete perturbations, the uninhibited laminar boundary layer sections continue downstream with much the same characteristics of a plain cylinder at equivalent Re_D, narrowing slightly with the gradual expansion of the bordering energised

flow streams.

- Because of the increased momentum and therefore enhanced resistance to separation in an adverse pressure gradient, the turbulent, energised streams remain attached and continue downstream beyond the point where the laminar sections separate – at much the same circumferential position, ϕ_s, as a plain cylinder at equivalent Re_D. From here it is thought that at the first point of laminar separation the energised streams continue to diffuse their momentum to the adjacent boundary layer flow before wrapping around the laminar sections into the low pressure region formed immediately downstream of the laminar separation line, thus forming the primary CRVP.

- The SOFV tests – first discussed in chapter 7 – confirm a nodal point of reattachment downstream of the central areas of the laminar separation lines and primary CRVP. Though not explicitly confirmed, it can be assumed that the reattachment is turbulent; the final separation occurs significantly downstream from the initial laminar separation so it is assumed that only an energised turbulent boundary layer would be able to persist so far downstream in an adverse gradient. It is therefore further assumed that the initially laminar separated shear layer undergoes transition induced by the disturbance created either by the adjacent energised flow streams or, by relation, the induced CRVP.

Chapter 11

Suggestions for further work

- This research was based on relatively high-Reynolds number, fluctuating, and three-dimensional flow dynamics. Unfortunately it was not possible to analyse anything other than the time-mean features from the PIV datasets acquired. Instantaneous PIV data shows clearly that the wake dynamics are highly unstable, fluctuating in all three dimensions continuously and erratically for all Reynolds numbers tested. Observing videos of the SOFV tests, it is evident that the laminar separation line is not stable at a fixed angle, ϕ_s, but it does not oscillate in a regular periodic motion either. To the naked eye, both the movement of the foci of the primary CRVP and the laminar separation line appear to be fairly arbitrary – without observable periodicity – around their respective time-mean positions. The weaker, secondary CRVP appear to be more stable, but the reduced fluid flow in these regions reduces the resolution of movements observable with the SOFV method. Time-resolved PIV may allow the very complicated wake dynamics to be clarified. This would provide the basis for modal analysis of the wake dynamics by, for example, proper orthog-

onal decomposition (POD), or dynamic mode decomposition (DMD) which would allow the wake modes to be characterised and hence provide some developments in understanding and predicting control strategies for these types of flows.

- Additionally, it is clear that two-dimensional analyses – even where all three components are resolved – provide a limited presentation of a flow-field which contains many strongly three-dimensional dynamics. For flows of the type studied for this research, an enhanced analysis and understanding would be gained from data acquired simultaneously in two planes or preferably in a volume. A 3D, or tomographic investigation of the flow field would provide a valuable means of future investigation on this topic.

- Higher Reynolds number testing (e.g. $2.8\times10^5 \leqslant Re_D \leqslant 5.0\times10^5$) would allow a better understanding of how the drag curves of the flow control concepts studied here might alter as they go beyond the critical regime. In the case of surface roughness, dimples and tripping wires, the drag coefficient tends to rise again in the post-critical regime. A system of discrete perturbations may develop different behaviour given their sparse application and span-wise variation.

- There are some gaps in the experimental data for this body of research, the acquisition of which would help clarify some assumptions made in the analyses. For example, direct acquisition of the cross-flow velocity in the region of the passive jet and measurement of the boundary layer thickness, by using a traversed boundary layer hot-wire probe.

- Additional development of the passive jets concept could be made by experi-

menting with the angle or shape of jet hole as it emits into the boundary layer. A redesign of the existing model might partition the passive supply to each row of jet holes – top and bottom – to prevent pressure feedback influencing the flow from one row of holes on the other.

- A development of the 'pins' concept might be to experiment with the materials and structural dynamics of the pins themselves; an optimal, passive, solution may involve pins or 'spines' which protrude normal to the cylinder wall at low speeds but which flatten gradually to the cylinder surface with increasing flow speed. This type of arrangement would have the advantage of providing a decreasing perturbation to the flow with increasing Reynolds number, which is desirable for C_D reduction in the sub-critical Re_D range; tuning this type of behaviour by manipulation of material response to a cross-flow could provide excellent passive drag reduction throughout the desired Re_D operating range.

- Finally, a CFD analysis may help to improve understanding of the complex fluid dynamics of this research and in particular the development of the interaction between the jet and cross-flow as it sweeps downstream to generate the complex three-dimensional separation and wake region. Indeed, some initial work was made on a CFD analysis for this research, however the complexity of the problem proved too great for the time available – thank you to J-E W Lombard of Imperial College London for the enthusiastic and illuminating conversations, in addition to the work, to this end. The resolution of the boundary layers of both the high Reynolds number cylinder cross-flow and the considerably lower Reynolds number jet 'pipe' flow make this a particularly difficult CFD challenge and really constitutes an entire project in itself.

References

Acarlar, M. S. and Smith, C. R. (1987*a*), 'A study of hairpin vortices in a laminar boundary layer. Part 1. Hairpin vortices generated by a hemisphere protuberance', *Journal of Fluid Mechanics* **175**, 1–41. [Cited on page 166.]

Acarlar, M. S. and Smith, C. R. (1987*b*), 'A study of hairpin vortices in a laminar boundary layer. Part 2. Hairpin vortices generated by fluid injection', *Journal of Fluid Mechanics* **175**, 43–83. [Cited on pages 166, 188, and 190.]

Achenbach, E. (1968), 'Distribution of local pressure and skin friction around a circular cylinder in cross-flow up to $Re = 5{\times}10^6$', *Journal of Fluid Mechanics* **34**(4), 625–639. [Cited on pages 19, 45, 47, 49, 52, 120, 153, 174, and 240.]

Achenbach, E. (1971), 'Influence of surface roughness on the cross-flow around a circular cylinder', *Journal of Fluid Mechanics* **46**(part 2), 321–335. [Cited on pages 19, 20, 42, 43, 56, 59, 60, 63, 64, 75, 77, and 153.]

Achenbach, E. (1972), 'Experiments on the flow past spheres at very high Reynolds numbers', *Journal of Fluid Mechanics* **54**(03), 565–575. [Cited on page 86.]

Achenbach, E. (1974*a*), 'The effects of surface roughness and tunnel blockage on the

flow past spheres', *Journal of Fluid Mechanics* **65**(Part 1), 113–125. [Cited on pages 81 and 86.]

Achenbach, E. (1974*b*), 'Vortex shedding from spheres', *Journal of Fluid Mechanics* **62**(02), 209–221. [Cited on page 166.]

Achenbach, E. (1977), 'The effect of surface roughness on the heat transfer from a circular cylinder to the cross flow of air', *International Journal of Heat and Mass Transfer* **20**(4), 359–369. [Cited on page 63.]

Ackeret, J. (1936), 'Der Winddruck auf Schornsteine mit Kreisquerschnitt [Wind load on chimneys of circular section]', *Schweizerische Bauzeitung* **108**(3), 25–26. [Cited on page 63.]

Allen, H. J. and Vincenti, W. G. (1944), Wall Interference in a two-dimensional-flow wind tunnel, with consideration of the effect of compressibility, Technical Report 782, NACA. [Cited on pages 91, 394, 395, and 397.]

Amaury Sport Organisation (2015), 'Le Tour de France 2015 Overall individual time classification', `http://www.letour.com/le-tour/2015/us/classifications.html`. Date accessed: 22/05/2016. [Cited on page 38.]

Amitay, M., Honohan, A., Trautman, M. and Glezer, A. (1997), Modification of the aerodynamic characteristics of bluff bodies using fluidic actuators, *in* '28th AIAA Fluid Dynamics Conference', number AIAA 97-2004, AIAA, Snowmass, Colorado. [Cited on page 120.]

Andreopoulos, J. and Rodi, W. (1984), 'Experimental investigation of jets in a crossflow', *Journal of Fluid Mechanics* **138**, 93–127. [Cited on pages 147, 192, and 272.]

Bearman, P. W. (1967), 'The effect of base bleed on the flow behind a two-dimensional model with a blunt trailing edge', *Aeronautical Quarterly* **18**(3), 207–224. [Cited on page 123.]

Bearman, P. W. (1968), The flow around a circular cylinder in the critical Reynolds number regime, NPL Aero Report 1257, National Physical Laboratory, Aerodynamics Division. [Cited on page 394.]

Bearman, P. W. (1969), 'On vortex shedding from a circular cylinder in the critical Reynolds number regime', *Journal of Fluid Mechanics* **37**(3), 577–585. [Cited on pages 19, 47, 48, 144, 272, and 364.]

Bearman, P. W. and Harvey, J. K. (1976), 'Golf Ball Aerodynamics', *Aeronautical Quarterly* **27**(May), 112–122. [Cited on pages 21, 80, 81, 84, 85, and 86.]

Bearman, P. W. and Harvey, J. K. (1993), 'Control of circular cylinder flow by the use of dimples', *AIAA Journal* **31**(10), 1753–1756. [Cited on pages 20, 21, 53, 81, 82, 83, 84, 110, 111, 115, and 117.]

Bearman, P. W., Harvey, J. K. and Gardner, C. M. (1976), Preliminary Calibration of the 4.5' x 4.0' (1.37m x 1.21m) Low Speed Wind Tunnel, Technical report, Department of Aeronautics, Imperial College of Science and Technology, London SW7 2BY. [Cited on page 89.]

Beck, S. and Collins, R. (2008), 'Moody Diagram', https://upload.wikimedia.org/wikipedia/commons/8/80/Moody_diagram.jpg. The Engineering ToolBox, Date accessed: 23/05/2012. [Cited on pages 26 and 346.]

Benade, A. H. (1959), 'On woodwind instrument bores', *The Journal of the Acoustical Society of America* **31**(2), 137–146. [Cited on page 177.]

Benade, A. H. (1960), 'On the mathematical theory of woodwind finger holes', *The Journal of the Acoustical Society of America* **32**(12), 1591–1608. [Cited on page 177.]

Bergeles, G., Gosman, A. D. and Launder, B. E. (1976), 'The Prediction of Three-Dimensional Discrete-Hole Cooling Processes - Part 1: Laminar Flow', *Journal of Heat Transfer* **98**(3), 379–386. [Cited on page 162.]

Buresti, G. (1981), 'The effect of surface roughness on the flow regime around circular cylinders', *Journal of Wind Engineering and Industrial Aerodynamics* **8**, 105–114. [Cited on pages 20, 56, 57, 58, and 59.]

Cambonie, T., Gautier, N. and Aider, J. L. (2013), 'Experimental study of counter-rotating vortex pair trajectories induced by a round jet in cross-flow at low velocity ratios', *Experiments in Fluids* **54**(1475), 1–13. [Cited on pages 22, 160, 161, 166, 169, and 173.]

Camussi, R., Guj, G. and Stella, A. (2002), 'Experimental study of a jet in a crossflow at very low Reynolds number', *Journal of Fluid Mechanics* **454**, 113–144. [Cited on page 147.]

Cantwell, B. J. (1976), A flying hot wire study of the turbulent near wake of a circular cylinder at a Reynolds number of 140,000, PhD thesis, California Institute of Technology. [Cited on page 152.]

Cantwell, B. J. and Coles, D. (1983), 'An experimental study of entrainment and transport in the turbulent near wake of a circular cylinder', *Journal of Fluid Mechanics* **136**, 321–374. [Cited on pages 152 and 245.]

Cengel, Y. A. and Turner, R. H. (2001), *Fundamentals of Thermal-fluid Sciences*, 1st, inter edn, McGraw-Hill. [Cited on pages 347 and 354.]

Choi, H. (2007), Control of Flow Over a Bluff Body, *in* 'TSFP', pp. 3–10. [Cited on page 271.]

Choi, H., Jeon, W.-P. and Kim, J. (2008), 'Control of Flow Over a Bluff Body', *Annual Review of Fluid Mechanics* **40**(1), 113–139. [Cited on page 271.]

Choi, J., Jeon, W.-P. and Choi, H. (2006), 'Mechanism of drag reduction by dimples on a sphere', *Physics of Fluids* **18**(4), 41702. [Cited on pages 83 and 86.]

Chomaz, J.-M. (2005), 'Global Instabilities in Spatially Developing Flows: Non-Normality and Nonlinearity', *Annual Review of Fluid Mechanics* **37**(1), 357–392. [Cited on page 168.]

Coelho, S. L. V. and Hunt, J. C. R. (1989), 'The dynamics of the near field of strong jets in crossflows', *Journal of Fluid Mechanics* **200**, 95–120. [Cited on page 272.]

Coles, D., Cantwell, B. and Wadcock, A. J. (1978), The Flying Hot Wire and Related Instrumentation, Technical Report NASA Contractor Report 3066, California Institue of Technology. [Cited on page 245.]

Cortelezzi, L. and Karagozian, A. R. (2001), 'On the formation of the counter-rotating vortex pair in transverse jets', *Journal of Fluid Mechanics* **446**, 347–373. [Cited on page 147.]

Crook, A. and Wood, N. J. (2001), Measurements and Visualisations of Synthetic Jets, *in* '39th Aerospace Sciences Meeting and Exhibit', number AIAA 2001-0145, AIAA, Reno, Nevada. [Cited on page 120.]

Dallmann, U. (1983), Topological structures of three-dimensional vortex flow sepa-

ration, *in* 'AIAA 16th Fluid and Plasma Dynamics Conference', number AIAA-83-1735, AIAA. [Cited on pages 207 and 208.]

Davitian, J., Getsinger, D., Hendrickson, C. and Karagozian, A. R. (2010), 'Transition to global instability in transverse-jet shear layers', *Journal of Fluid Mechanics* **661**, 294–315. [Cited on page 162.]

de B. Alves, L. S., Kelly, R. E. and Karagozian, A. R. (2008), 'Transverse-jet shear-layer instabilities. Part 2. Linear analysis for large jet-to-crossflow velocity ratio', *Journal of Fluid Mechanics* **602**, 383–401. [Cited on page 163.]

Defraeye, T., Blocken, B., Koninckx, E., Hespel, P., Verboven, P., Nicolai, B. and Carmeliet, J. (2014), 'Cyclist drag in team pursuit: Influence of cyclist sequence, stature, and arm spacing', *Journal of Biomechanical Engineering* **136**, 1–9. [Cited on page 37.]

Delery, J. M. (2001), 'Robert Legendre and Henri Werlé: Toward the elucidation of three-dimensional separation', *Annual Review of Fluid Mechanics* **33**, 129–154. [Cited on pages 25, 194, 196, 278, 279, and 284.]

Delery, J. M. (2011), Separation in three-dimensional flow: critical points, separation lines and vortices, *in* 'ONERA Information Resources', ONERA. [Cited on pages 25, 193, 278, and 279.]

Doligalski, T. L., Smith, C. R. and Walker, J. D. A. (1994), 'Vortex Interactions with Walls', *Annual Review of Fluid Mechanics* **26**, 573–616. [Cited on pages 25, 277, 278, and 291.]

Drazin, P. G. and Reid, W. H. (2004), *Hydrodynamic Stability*, second edn, Cambridge University Press. [Cited on page 174.]

Dwyer, H. A. and McCroskey, W. J. (1973), 'Oscillating flow over a cylinder at large Reynolds number', *Journal of Fluid Mechanics* **61**(4), 753–767. [Cited on page 238.]

Engineeringtoolbox.com (2012), 'Roughness & Surface Coefficients of Ventilation Ducts', http://www.engineeringtoolbox.com/surface-roughness-ventilation-ducts-d_209.html. The Engineering ToolBox, Date accessed: 23/05/2012. [Cited on page 345.]

Fage, A. (1929), 'The air-flow around a circular cylinder in the region where the boundary layer separates from the surface', *The London, Edinburgh, and Dublin Philosophical Magazine and Journal of Science* **7**(42), 253–273. [Cited on pages 87, 153, and 240.]

Fage, A. and Warsap, J. H. (1930), The effects of turbulence and surface roughness on the drag of a circular cylinder, Technical Report Ae 429, Aeronautical Research Committee, London. [Cited on pages 19, 20, 53, 55, 56, 57, 61, 63, 64, 66, 67, 77, 110, 112, and 153.]

Fairlie, B. D. (1980), Flow separation on bodies of revolution at incidence, *in* 'Proceedings of the 7th Australasian Hydraulics and Fluid Mechanics Conference', Brisbane, pp. 338–341. [Cited on pages 26, 208, 209, and 373.]

Farell, C. and Arroyave, J. (1990), 'On uniform flow around rough circular cylinders at critical Reynolds numbers', *Journal of Wind Engineering and Industrial Aerodynamics* **36**, 621–631. [Cited on page 63.]

Farell, C. and Fedeniuk, S. K. (1988), 'Effect of end plates on the flow around rough cylinders', *Journal of Wind Engineering and Industrial Aerodynamics* **28**(1), 219–230. [Cited on page 63.]

Fargie, D. and Martin, B. W. (1971), 'Developing laminar flow in a pipe of circular cross-section', *Proceedings of the Royal Society of London. Series A, Mathematical and Physical Sciences* **321**, 461–476. [Cited on page 159.]

Fearn, R. and Weston, R. P. (1974), 'Vorticity Associated with a Jet in a Cross Flow', *AIAA Journal* **12**(12), 1666–1671. [Cited on page 147.]

Foss, J. F. (1980), Interaction region phenomena for the jet in a cross-flow problem, Technical report, Sonderforschungsbereich 80: Ausbreitungs- und Transportvorgange in Stromungen, Universitat Karlsruhe, Karlsruhe. [Cited on pages 24, 147, 150, 162, 170, 226, 227, and 228.]

Fric, T. F. (1990), Structure in the Near Field of the Tranverse Jet, PhD thesis, California Institure of Technology. [Cited on page 272.]

Fric, T. F. and Roshko, A. (1994), 'Vortical structure in the wake of a transverse jet', *Journal of Fluid Mechanics* **279**, 1–47. [Cited on pages 25, 147, 149, 150, 164, 165, 174, 273, 280, and 291.]

Fujita, H., Takahama, H. and Kawai, T. (1985), 'Effects of Tripping Wires on Heat Transfer from a Circular Cylinder in Cross Flow : 1st Report, The Pressure Distribution around the Cylinder and the Drag Coefficient', *Bulletin of the JSME - Japan Society of Mechanical Engineers* **28**(235), 80–87. [Cited on pages 67 and 87.]

Gad-el Hak, M. (2000), *Flow Control: Passive, active, and reactive flow management*, Cambridge University Press. [Cited on page 39.]

Glezer, A. and Amitay, M. (2002), 'Synthetic jets', *Annual Review of Fluid Mechanics* **34**, 503–529. [Cited on page 120.]

Gopalan, S., Abraham, B. M. and Katz, J. (2004), 'The structure of a jet in cross flow at low velocity ratios', *Physics of Fluids* **16**(6), 2067–2087. [Cited on pages 147 and 167.]

Güven, O., Farell, C. and Patel, V. C. (1980), 'Surface-roughness effects on the mean flow past circular cylinders', *Journal of Fluid Mechanics* **98**(04), 673–701. [Cited on page 77.]

Harris, D. M. and Williamson, C. H. K. (2012), 'Instability of secondary vortices generated by a vortex pair in ground effect', *Journal of Fluid Mechanics* **700**(April), 148–186. [Cited on page 207.]

Heine, B., Schwermer, T. and Raffel, M. (2010), The effect of vortex generators on the flow around a circular cyliner, *in* '15th International Symposium on Applications of Laser Techniques to Fluid Mechanics', Lisbon. [Cited on pages 87 and 271.]

Higuchi, H., Kim, H. J. and Farell, C. (1989), 'On flow separation and reattachment around a circular cylinder at critical Reynolds numbers', *Journal of Fluid Mechanics* **200**, 149–171. [Cited on page 152.]

Humphreys, J. S. (1960), 'On a circular cylinder in a steady wind at transition Reynolds numbers', *Journal of Fluid Mechanics* **9**(04), 603–612. [Cited on page 229.]

Hunt, J. C. R., Abell, C. J., Peterka, J. A. and Woo, H. (1978), 'Kinematical studies of the flows around free or surface-mounted obstacles; applying topology to flow visualization', *Journal of Fluid Mechanics* **86**(1), 179–200. [Cited on page 194.]

Igarashi, T. (1985), 'Effect of vortex generators on the flow around a circular clinder normal to an airstream', *Bulletin of JSME* **28**(236), 274–282. [Cited on page 271.]

Igarashi, T. (1986), 'Effect of Tripping Wires on the Flow around a Circular Cylinder Normal to an Airstream', *Bulletin of the Jsme-Japan Society of Mechanical Engineers* **29**(255), 2917–2924. [Cited on pages 20, 68, 69, 70, and 87.]

Ilak, M., Schlatter, P., Bagheri, S. and Henningson, D. S. (2012), 'Bifurcation and stability analysis of a jet in cross-flow: onset of global instability at a low velocity ratio', *Journal of Fluid Mechanics* **696**, 94–121. [Cited on pages 22, 149, 163, 164, 165, 166, 167, 168, 169, 186, 187, 188, 189, and 228.]

James, D. F. and Truong, Q. S. (1972), 'Wind load on cylinder with spanwise protrusion', *Journal of the Engineering Mechanics Division* **98**(6), 1573–1589. [Cited on pages 67 and 110.]

James, W. D., Paris, S. W. and Malcolm, G. N. (1980), 'A study of viscous cross-flow effects on circular cylinders at high Reynolds numbers', *AIAA Journal* **18**(9), 1066–1072. [Cited on pages 152, 184, and 185.]

Johnson, T. R. and Joubert, P. N. (1969), 'The influence of vortex generators on the drag and heat transfer from a circular cylinder normal to an airstream', *Journal of heat transfer* **91**, 91–99. [Cited on pages 20, 72, 73, 74, 75, and 271.]

Joubert, P. N. and Hoffman, E. R. (1962), 'Drag of a circular cylinder with vortex generators', *Journal of the Royal Aeronautical Society* **66**, 456–457. [Cited on pages 72 and 271.]

JSME (1988), *Visualized flow; compiled by the Japan Society of Mechanical Engineers, ed. by Nakayama, Y., Woods, W. A., Clark, D.G.*, English edn, Pergamon Press. [Cited on page 193.]

Kelso, R. M., Lim, T. T. and Perry, A. E. (1996), 'An experimental study of round jets in cross-flow', *Journal of Fluid Mechanics* **306**, 111–144. [Cited on pages 22, 163, 164, and 165.]

Kelso, R. M. and Smits, A. J. (1995), 'Horseshoe vortex systems resulting from the interaction between a laminar boundary layer and a transverse jet', *Physics of Fluids* **7**(1), 153–158. [Cited on pages 148 and 149.]

Kimura, T. and Tsutahara, M. (1991), 'Fluid dynamic effects of grooves on circular cylinder surface', *AIAA Journal* **29**(12), 2062–2068. [Cited on pages 20, 78, 79, 80, and 82.]

Ko, N. W. M., Leung, Y. C. and Chen, J. J. J. (1987), 'Flow past V-groove circular cylinders', *AIAA Journal* **25**(6), 806–811. [Cited on pages 20, 75, 76, and 77.]

Legendre, R. (1956), 'Séparation de l'écoulement laminaire tridimensionnel', *La Recherche Aéronautique* **54**, 3–8. [Cited on page 194.]

Leschziner, M. A. and Lardeau, S. (2011), 'Simulation of slot and round synthetic jets in the context of boundary-layer separation control', *Philosophical Transactions of the Royal Society A: Mathematical, Physical and Engineering Sciences* **369**, 1495–1512. [Cited on page 120.]

Leung, Y. C. and Ko, N. W. M. (1991), 'Near wall characteristics of flow over grooved circular cylinder', *Experiments in Fluids* **10**(6), 322–332. [Cited on pages 75 and 76.]

Leung, Y. C., Ko, N. W. M. and Tang, K. M. (1992), 'Flow past circular cylinder with different surface configurations', *Journal of fluids engineering* **114**, 170–177. [Cited on page 78.]

Leweke, T., Le Dizès, S. and Williamson, C. H. K. (2016), 'Dynamics and Instabilities of Vortex Pairs', *Annual Review of Fluid Mechanics* **48**(1), 507–541. [Cited on pages 206, 207, and 316.]

Lighthill, M. J. (1963), Boundary Layer Theory, *in* L. Rosenhead, ed., 'Laminar Boundary Layers', Oxford University Press, chapter II, pp. 46–113. [Cited on pages 194 and 196.]

Lim, T. T., Kelso, R. M. and Perry, A. E. (1992), A study of a round jet in cross-flow at different velocity ratios, *in* '11th Australasian Fluid Mechanics Conference', Hobart, pp. 1089–1092. [Cited on pages 164, 165, and 186.]

Lock, C. N. H. (1925), 'CXVII. On the system of vortices generated by a circular cylinder in steady motion through a fluid', *Philosophical Magazine Series 6* **50**(299), 1083–1089. [Cited on page 114.]

Mahesh, K. (2013), 'The Interaction of Jets with Crossflow', *Annual Review of Fluid Mechanics* **45**(1), 379–407. [Cited on pages 148, 160, 164, and 165.]

Massey, B. S. (2012), *Mechanics of fluids*, 9th edn, Spon Press. [Cited on pages 344 and 353.]

Maxworthy, T. (1969), 'Experiments on the Flow Around a Sphere at High Reynolds Numbers', *Journal of Applied Mechanics* **36**(3), 598–607. [Cited on page 86.]

McMahon, H. M., Hester, D. D. and Palfery, J. G. (1971), 'Vortex shedding from a turbulent jet in a cross-wind', *Journal of Fluid Mechanics* **48**(01), 73–84. [Cited on pages 148, 150, and 170.]

Megerian, S., Davitian, J., de B. Alves, L. S. and Karagozian, A. R. (2007), 'Transverse-jet shear-layer instabilities. Part 1. Experimental studies', *Journal of Fluid Mechanics* **593**, 93–129. [Cited on pages 22, 163, 169, 170, 171, 175, 186, and 188.]

Mizuno, S. (1970), 'Effects of three-dimensional roughness elements on the flow around a circular cylinder', *J. Sci. Hiroshima Univ., Ser. A-II* **34**(3), 215–258. [Cited on pages 23, 87, 214, 215, and 216.]

Moody, L. F. (1944), 'Friction factors for pipe flow', *Transactions of the ASME* **66**(8), 671–684. [Cited on page 345.]

Moussa, Z. M., Trischka, J. W. and Eskinazi, S. (1977), 'The near field in the mixing of a round jet with a cross-stream', *Journal of Fluid Mechanics* **80**(1), 49–80. [Cited on pages 150 and 174.]

Muppidi, S. and Mahesh, K. (2005), 'Study of trajectories of jets in crossflow using direct numerical simulations', *Journal of Fluid Mechanics* **530**, 81–100. [Cited on pages 169 and 173.]

Naumann, A. and Quadflieg, H. (1968), Aerodynamic aspects of wind effects on cylindrical buildings, *in* 'Symposium on Wind Effects on Buildings and Structures', Royal Aeronautical Society, Loughborough University of Technology. [Cited on page 142.]

New, T. H., Lim, T. T. and Luo, S. C. (2006), 'Effects of jet velocity profiles on a round jet in cross-flow', *Experiments in Fluids* **40**, 859–875. [Cited on page 173.]

Niemann, H.-J. and Holscher, N. (1990), 'A review of recent experiments on the flow past circular cylinders', *Journal of Wind Engineering and Industrial Aerodynamics* **33**(1-2), 197–209. [Cited on pages 20, 64, and 65.]

Nikuradse, J. (1933), 'Laws of flow in rough pipes [English translation of Stromungsgesetze in rauhen Rohren]', *VDI-Forschungsheft 361. Beilage zu "Forschung auf dem Gebiete des Ingenieurwesens" [Translation from NACA Technical Memorandum 1292]* **4**(B). [Cited on page 63.]

Norberg, C. (2003), 'Fluctuating lift on a circular cylinder: review and new measurements', *Journal of Fluids and Structures* **17**(1), 57–96. [Cited on page 184.]

Oswatitsch, K. (1958), Die Ablösungsbedingung von Grenzschichten, *in* H. Görtler, ed., 'Grenzschichtforschung', Springer Berlin Heidelberg, chapter VIII, pp. 257–367. [Cited on page 194.]

Oxlade, A. R. (2013), High-frequency Pulsed Jet Forcing of an Axisymmetric Bluff Body Wake, PhD thesis, Imperial College London. [Cited on page 104.]

Park, H., Lee, D., Jeon, W.-P., Hahn, S., Kim, J., Kim, J., Choi, J. and Choi, H. (2006), 'Drag reduction in flow over a two-dimensional bluff body with a blunt trailing edge using a new passive device', *Journal of Fluid Mechanics* **563**, 389–414. [Cited on page 271.]

Perry, A. E. and Chong, M. S. (1982), 'On the mechanism of wall turbulence', *Journal of Fluid Mechanics* **119**, 173–217. [Cited on page 196.]

Perry, A. E. and Chong, M. S. (1986), 'A series-expansion study of the Navier-Stokes equations with applications to three-dimensional separation patterns', *Journal of Fluid Mechanics* **173**, 207–223. [Cited on pages 23, 25, 194, 206, 208, 209, 210, 285, and 287.]

Perry, A. E. and Chong, M. S. (1987), 'A description of eddying motions and

flow patterns using critical-point concepts', *Annual Review of Fluid Mechanics* **19**(1), 125–155. [Cited on page 194.]

Perry, A. E. and Lim, T. T. (1978), 'Coherent structures in coflowing jets and wakes', *Journal of Fluid Mechanics* **88**(3), 451–463. [Cited on pages 166 and 169.]

Peterson, S. D. and Plesniak, M. W. (2004), 'Evolution of jets emanating from short holes into crossflow', *Journal of Fluid Mechanics* **503**, 57–91. [Cited on pages 22, 170, 171, and 172.]

Potter, M. C. and Wiggert, D. C. (2002), *Mechanics of Fluids*, 3rd edn, Brooks/Cole. [Cited on pages 344 and 353.]

Prandtl, L. (1961), *Gesammelte Abhandlungen zur angewandten Mechanik, Hydro- und Aerodynamik (Collected Works), ed. Tollmien, W., Schlichting, H., Gortler, H., Riegels, F. W.*, Vol. 1-3, Springer-Verlag, Berlin. [Cited on page 54.]

Ramsey, J. W. and Goldstein, R. J. (1971), 'Interaction of a Heated Jet With a Deflecting Stream', *Journal of Heat Transfer* **93**, 365–372. [Cited on page 162.]

Rivero, A., Ferré, J. A. and Giralt, F. (2001), 'Organized motions in a jet in crossflow', *Journal of Fluid Mechanics* **444**, 117–149. [Cited on page 164.]

Roshko, A. (1961), 'Experiments on the flow past a circular cylinder at very high Reynolds number', *Journal of Fluid Mechanics* **10**(03), 345–356. [Cited on pages 37, 51, and 153.]

Salewski, M., Stankovic, D. and Fuchs, L. (2008), 'Mixing in circular and non-circular jets in crossflow', *Flow, Turbulence and Combustion* **80**, 255–283. [Cited on page 150.]

Sau, R. and Mahesh, K. (2008), 'Dynamics and mixing of vortex rings in crossflow', *Journal of Fluid Mechanics* **604**, 389–409. [Cited on pages 22, 163, 164, 165, 166, 167, 168, 183, 190, and 228.]

Scarano, F. and Poelma, C. (2009), 'Three-dimensional vorticity patterns of cylinder wakes', *Experiments in Fluids* **47**(1), 69–83. [Cited on page 260.]

Schewe, G. (1986), 'Sensitivity of transition phenomena to small perturbations in flow round a circular cylinder', *Journal of Fluid Mechanics* **172**, 33–46. [Cited on pages 271 and 272.]

Schiller, L. and Linke, W. (1933), 'Druck-und Reibungswiderstand des zylinders bei Reyonldsschen zahlen 5,000 bis 40,000 (Pressure and frictional resistance of a cylinder at Reynolds numbers 5,000 to 40,000)', *Zeitschrift für Flugtechnik und Motorluftschiffahrt* **24**(7). [Cited on pages 246 and 247.]

Schlatter, P., Bagheri, S. and Henningson, D. S. (2011), 'Self-sustained global oscillations in a jet in crossflow', *Theoretical and Computational Fluid Dynamics* **25**(1-4), 129–146. [Cited on pages 148, 165, and 168.]

Schlichting, H. (1936), 'Experimentelle untersuchungen zum rauhigkeitsproblem', *Ingenieur - Archiv* **7**(1), 1–34. [Cited on page 63.]

Schlichting, H. (1964), *Grenzschicht-Theorie [Boundary-layer theory]*, Vol. 5, Springer, Berlin; London. [Cited on page 63.]

Son, K., Choi, J., Jeon, W.-P. and Choi, H. (2011), 'Mechanism of drag reduction by a surface trip wire on a sphere', *Journal of Fluid Mechanics* **672**, 411–427. [Cited on pages 20, 21, 68, 69, 71, and 86.]

Stansby, P. K. (1974), 'The effects of end plates on the base pressure coefficient of a circular cylinder', *Aeronautical Journal* **78**(757), 36–37. [Cited on page 91.]

Stuart, J. T. (1963), Hydrodynamic stability, *in* L. Rosenhead, ed., 'Laminar Boundary Layers', Oxford University Press, chapter IX, pp. 492–579. [Cited on page 174.]

Szechenyi, E. (1975), 'Supercritical Reynolds number simulation for two-dimensional flow over circular cylinders', *Journal of Fluid Mechanics* **70**(3), 529–542. [Cited on page 64.]

Tanner, M. (1972), 'A method for reducing the base drag of wings with blunt trailing edge', *The Aeronautical Quarterly* **23**, 15–23. [Cited on page 142.]

Tanner, M. (1975), 'Reduction of base drag', *Progress in Aerospace Sciences* **16**(4), 369–384. [Cited on page 123.]

Tobak, M. and Peake, D. J. (1982), 'Topology of three-dimensional separated flows', *Annual Review of Fluid Mechanics* **14**, 61–85. [Cited on pages 194 and 196.]

Tol, P. (2012), Colour Schemes, SRON Technical Note (SRON/EPS/TN/09-002) 2.2, Netherlands Institute for Space Research. https://personal.sron.nl/~pault/, Date accessed: 21/11/2016. [Cited on page 9.]

Tombazis, N. and Bearman, P. W. (1997), 'A study of three-dimensional aspects of vortex shedding from a bluff body with a mild geometric disturbance', *Journal of Fluid Mechanics* **330**, 85–112. [Cited on page 246.]

Walters, D. K. and Leylek, J. H. (1997), A detailed analysis of film-cooling physics. Part 1: Streamwise injection with cylindrical holes, *in* 'ASME 1997 International

Gas Turbine and Aeroengine Congress and Exhibition', ASME, Orlando, Florida. [Cited on pages 171 and 172.]

Welch, P. D. (1967), 'The Use of Fast Fourier Transform for the Estimation of Power Spectra: A Method Based on Time Averaging Over Short, Modified Periodograms', *IEEE Transactions on Audio and Electroacoustics* **15**(2), 70–73. [Cited on pages 142, 177, and 179.]

White, F. M. (2011), *Fluid Mechanics*, seventh edn, McGraw-Hill. [Cited on page 152.]

Wieselsberger, C. (1914), 'Der Luftwiderstand von Kugeln', *Zeitschrift für Flugtechnik und Motorluftschiffahrt* **5**, 140–145. [Cited on page 86.]

Wieselsberger, C. (1921), 'New data on the laws of fluid resistance [An english translation of Neuere Feststellungen über die Gesetze des Flüssigkeits-und Luftwiderstandes]', *Physikalische Zeitschrift* **22**, 321–328. [Cited on pages 42 and 43.]

Williamson, C. H. K. (1996*a*), 'Three-dimensional wake transition', *Journal of Fluid Mechanics* **328**, 345–407. [Cited on page 257.]

Williamson, C. H. K. (1996*b*), 'Vortex dynamics in the cylinder wake', *Annual Review of Fluid Mechanics* **28**, 477–539. [Cited on pages 257 and 260.]

Wolfe, J. and Smith, J. (2003), 'Cutoff frequencies and cross fingerings in baroque, classical, and modern flutes', *The Journal of the Acoustical Society of America* **114**(4), 2263–2272. [Cited on page 177.]

Wood, C. J. (1964), 'The effect of base bleed on a periodic wake', *Journal of the Royal Aeronautical Society* **68**(July), 477–482. [Cited on page 123.]

Zdravkovich, M. M. (1990), 'Conceptual overview of laminar and turbulent flows past smooth and rough circular cylinders', *Journal of Wind Engineering and Industrial Aerodynamics* **33**, 53–62. [Cited on pages 19 and 51.]

Zdravkovich, M. M. (1997), *Flow around circular cylinders : A comprehensive guide through flow phenomena, experiments, applications, mathematical models, and computer simulations. Vol. 1: Fundamentals*, Oxford Science Publications. [Cited on pages 43, 44, 45, 53, 152, 161, and 270.]

Zdravkovich, M. M. (2003), *Flow around circular cylinders : A comprehensive guide through flow phenomena, experiments, applications, mathematical models, and computer simulations. Vol. 2: Applications*, Oxford Science Publications. [Cited on pages 54, 58, 63, 64, 71, 73, 75, 78, 81, and 153.]

Zdravkovich, M. M., Ashcroft, M. W., Chisholm, S. J. and Hicks, N. (1996), Effect of cyclist's posture and vicinity of another cyclist on aerodynamic drag, *in* S. Haake, ed., 'The Engineering of Sport', Balkema, Rotterdam, pp. 21–28. [Cited on pages 37 and 38.]

Appendix A

Feasibility study: Calculations for passive jet flow

A.1 Method: Part 1

The following provides a calculation methodology for estimating the flow rate of air tapped from the stagnation point of a circular cylinder to a lower pressure region on the cylinder surface.

The Darcy formula (see Potter and Wiggert, 2002, pp. 306, and Massey, 2012, pp. 248), or commonly termed Darcy-Weisbach equation, for fully developed flow through straight pipes:

$$h_f = \frac{\Delta p^*}{\rho g} = \frac{fl}{d}\frac{\bar{u}^2}{2g} \tag{A.1}$$

Re-arranging for piezometric pressure difference gives:

$$\Delta p^* = \frac{1}{2}\rho\left(\frac{fl}{d}\right)\bar{u}^2 \tag{A.2}$$

Cylinder pressure coefficient, C_p:

$$C_p = \frac{(p - p_\infty)}{\frac{1}{2}\rho {U_\infty}^2} \tag{A.3}$$

The difference between the pressure coefficient at the stagnation point, C_{p_0}, and any other point on the surface of the cylinder, C_{p_ϕ}, (where $\phi = 0°$ is the angular position of the stagnation point) is thus:

$$C_{p_0} - C_{p_\phi} = \Delta C_p = \left(\frac{(p - p_\infty)}{\frac{1}{2}\rho {U_\infty}^2}\right)_0 - \left(\frac{(p - p_\infty)}{\frac{1}{2}\rho {U_\infty}^2}\right)_\phi \tag{A.4}$$

$$\therefore \Delta C_p = \frac{(p_0 - p_\phi)}{\frac{1}{2}\rho {U_\infty}^2} \tag{A.5}$$

Rearranging Equation A.5 in terms of pressure difference:

$$p_0 - p_\phi = \Delta p^* = \frac{1}{2}\rho \Delta C_p {U_\infty}^2 = \frac{1}{2}\rho \left(\frac{fl}{d}\right) \bar{u}^2 \tag{A.6}$$

With reference to Figure 5.2, let the parameters and variables associated with the 'pipe' at the stagnation point ($\phi = 0°$) be subscripted '1' and those associated with a 'pipe' at $\phi = 65°$ be subscripted '2'. Accounting for the two pipe losses in the passive jet system, comprising one straight entry pipe at $\phi_1 = 0°$ and one straight exit pipe at $\phi_2 = 65°$ (since the pressure loss through each of the two exit pipes at $\phi = \pm 65°$ is assumed to be equal), and by setting the piezometric pressure drop through the pipes equal to the static pressure difference between the stagnation point ($\phi = 0°$) and $\phi = \pm 65°$, the application of Darcy's formula becomes Equation A.7.

$$\Delta p^* = \frac{1}{2}\rho \Delta C_p {U_\infty}^2 = \frac{1}{2}\rho \left(\frac{f_1 l_1}{d_1}\right) \bar{u}_1^2 + \frac{1}{2}\rho \left(\frac{f_2 l_2}{d_2}\right) \bar{u}_2^2 \tag{A.7}$$

The surface roughness height, k, of machined aluminium surfaces is in the range $0.001mm \leqslant k \leqslant 0.002mm$ (Engineeringtoolbox.com, 2012). The friction factor, f, can thus be extracted from a Moody chart (Moody, 1944 – see Figure A.1) given the relative roughness, k/d, and Reynolds number, Re, of the flow through the pipe.

$$f = \frac{64}{Re_{pipe}} \tag{A.8}$$

From initial estimates of the average flow velocity through the jet entry and exit pipes (using the above equation with a combination of known and estimated values), the pipe-flow Reynolds number, Re_{pipe}, falls within the laminar range ($Re_{pipe} < 2,000$) throughout the test range of cylinder Reynolds number, Re_D, for this research. As such, the friction factor can be assumed to follow the linear relation for

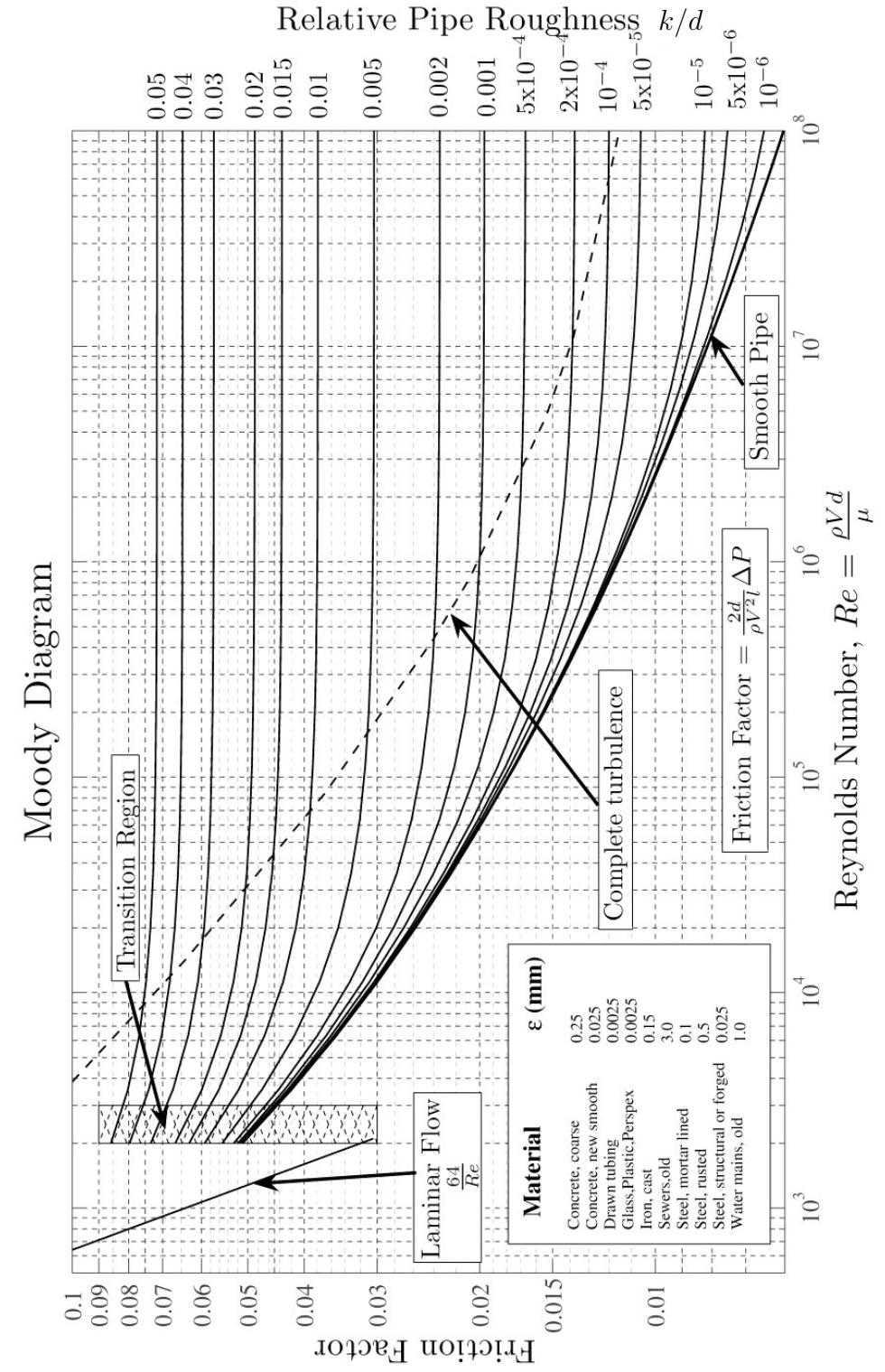

Figure A.1 – Moody chart, by Beck and Collins (2008)

fully developed, laminar flow through a pipe (Equation A.8).

A.1.1 Pipe-flow ancillary losses

Depending on the arrangement for channelling the flow from entry to jet exit, there may be losses associated with:

- Pipe bends/junctions (adverse pressure gradients generate losses from 'secondary flow' and possibility of separated flow);
- Pipe entry (sudden contraction);
- Pipe exit (sudden expansion).

A.1.1.1 Bends and junctions

The head loss, h_l, associated with ancillaries such as bends and junctions can be presented as shown in Equation A.9.

$$h_l = k\left(\frac{\bar{u}^2}{2g}\right) \tag{A.9}$$

The value of k varies with a number of factors, including: total angle of bend, i.e. angular change in flow direction; radius of bend; pipe size; pipe section i.e. square or circular; roughness of bend walls (friction factor, f); connection losses i.e. flanged, threaded or seamless bend; use of turning vanes. For example, a 90° elbow bend without turning vanes and a bend radius to pipe diameter ratio, $\frac{r}{d} < 0.6$, has a loss coefficient generally quoted around $k = 1.1$, whereas a flanged, 90° 'smooth' bend ($\frac{r}{d} > 2$) the value drops considerably to $k = 0.3$ (Cengel and Turner, 2001).

A.1.1.2 Entry and exit losses

The entry and exit losses of the 'pipes' used in this experiment are associated with significantly larger volumes than the pipe, and these losses can be quantified with a 'k'-factor as with bends and other fittings.

Entry loss (where $A_\infty >> A_{pipe}$):

$$h_l = \frac{1}{2}\left(\frac{\bar{u}^2}{2g}\right) \tag{A.10}$$

$\implies k = 0.5$

Exit loss (where $A_{pipe} << A_\infty$):

$$h_l = \left(\frac{\bar{u}^2}{2g}\right) \tag{A.11}$$

$\implies k = 1$

With this simplification, the loss coefficient values, k, of all ancillaries can be summed to a total value, k_t and incorporated into the Darcy-Weisbach equation in the manner outlined by Equation A.12 and Equation A.13.

$$h_l = \frac{\Delta p^*}{\rho g} = k_1\frac{\bar{u}^2}{2g} + k_2\frac{\bar{u}^2}{2g} + \cdots + k_n\frac{\bar{u}^2}{2g} \tag{A.12}$$

$$k_t = \sum_n^1 k_n \tag{A.13}$$

With reference to Figure 5.2, the pressure losses within the system of passive jets was assumed to be a summation of the friction losses within the entry and exit 'pipes' plus the entry and exit losses associated with each. The losses associated with the flow through the cylinder plenum volume are assumed to be negligible.

Thus, the total ancillary loss coefficient for each pipe is $k_t = 1.5$.

A.2 Method: Part 2

Returning to the modified Darcy-Weisbach equation (Equation A.6) for fully developed flow in straight pipes, the entry and exit losses are incorporated to form Equation A.14.

$$\frac{1}{2}\rho\Delta C_p {U_\infty}^2 = \frac{1}{2}\rho\left(\frac{f_1 l_1}{d_1}\right)\bar{u}_1^2 + \frac{1}{2}\rho\left(\frac{f_2 l_2}{d_2}\right)\bar{u}_2^2 + \frac{1}{2}\rho\left(k_{t1}\right)\bar{u}_1^2 + \frac{1}{2}\rho\left(k_{t2}\right)\bar{u}_2^2 \tag{A.14}$$

For the passive jet arrangement of the present research, Equation A.14 is simplified with the following parameter relations:

$$k_{t1} = k_{t2} = k_t \tag{A.15}$$

$$l_1 = l_2 = l_J \tag{A.16}$$

$$d_1 = 2d_2 \tag{A.17}$$

$$\therefore A_1 = \frac{1}{4}A_2 \tag{A.18}$$

But since there are double the number of exit to entry holes, i.e. $n_{exit} = \frac{1}{2}n_{entry}$:

$$\implies \bar{u}_1 = \frac{1}{2}\bar{u}_2 = \frac{1}{2}\bar{V}_J \tag{A.19}$$

... where V_J is the mean jet velocity.

$$\therefore Re_1 = \frac{1}{2} Re_2 \tag{A.20}$$

... where:

$$Re_2 = \frac{\bar{u}_2 d_2}{\nu} \tag{A.21}$$

$$\implies f_1 = \frac{64}{\frac{1}{2} Re_2} = \frac{128}{Re_2} \tag{A.22}$$

By substituting Equation A.15 – Equation A.22 into Equation A.14 and simplifying, one arrives at Equation A.23 which shows that – for this model – the pressure loss to friction through the jet exit pipe is four times greater than that through the entry pipe:

$$\Delta C_p {U_\infty}^2 = 16\nu \frac{l_J}{{d_2}^2} \bar{V}_J + 64\nu \frac{l_J}{{d_2}^2} \bar{V}_J + \frac{5}{4} k_t \bar{V}_J^2 \tag{A.23}$$

Simplifying and rearranging in terms of mean jet velocity, $\bar{V}_J$:

$$\bar{V}_J^2 + \bar{V}_J \left(\frac{64\nu l_J}{{d_2}^2 k_t} \right) - \frac{4}{5} \frac{\Delta C_p {U_\infty}^2}{k_t} = 0 \tag{A.24}$$

The mean jet velocity, $\bar{V}_J$, is now solved as a quadratic equation:

$$\bar{V}_J = \frac{1}{2} \left(-\frac{64\nu l_J}{{d_2}^2 k_t} \pm \sqrt{\frac{64\nu l_J}{{d_2}^2 k_t} + \frac{16}{5} \frac{\Delta C_p {U_\infty}^2}{k_t}} \right) \tag{A.25}$$

Because the first set of terms is negative there is always one positive and one negative root of the polynomial (Equation A.25); the realistic solution is always the

positive root and hence the equation for finding the average pipe-flow velocity can be written in the following format (Equation A.26), with only one possible solution:

$$\bar{V}_J = \frac{1}{2}\left(-\frac{64\nu l_J}{{d_2}^2 k_t} + \sqrt{\frac{64\nu l_J}{{d_2}^2 k_t} + \frac{16}{5}\frac{\Delta C_p {U_\infty}^2}{k_t}}\right) \tag{A.26}$$

A.3 Example calculation: jet velocity prediction

The mean jet velocity, $\bar{V}_J$, and hence flow rate through the cylinder, Q_t, is estimated for the following parameter values for the model setup detailed in Figure 5.6:

$d_J = 0.5\ mm$

$D = 0.1\ m$

$Re_D = 1 \times 10^5$

$\phi = 65°$

$\nu = 1.568 \times 10^{-5}\ m^2/s$

$k_t = 1.5$

$n_J = 116$

Approximate C_{p_ϕ} from Figure 2.2 at $\phi = 65°$ is $C_p \approx -1.7$, therefore:

$$\Delta C_p = 2.7 \tag{A.27}$$

Calculate free-stream velocity from cylinder Reynolds number:

$$U_\infty = Re_D \frac{\nu}{D} = 15.7\ m/s \tag{A.28}$$

Assuming laminar flow through the pipe, the velocity is calculated using Equation A.26:

$$\bar{V}_J = \frac{1}{2}\left(-\frac{64\nu l_J}{{d_2}^2 k_t} + \sqrt{\frac{64\nu l_J}{{d_2}^2 k_t} + \frac{16}{5}\frac{\Delta C_p {U_\infty}^2}{k_t}}\right) \tag{A.29}$$

Plug numbers into equation and solve:

$$\bar{V}_J = 8.7\ m/s \tag{A.30}$$

Check pipe Reynolds number corresponds with laminar flow:

$$Re_J = \frac{\bar{V}_J d_J}{\nu} \approx 280 \tag{A.31}$$

Since $Re_J < 2,000$, laminar flow through the pipe can be assumed* (see Appendix A.5). The mean volume flow rate through the pipe (i.e. the jet flow rate), Q_J, is therefore:

$$Q_J = A\bar{V}_J = \frac{\pi d^2}{4} \times 8.7 = 1.7\ ml/s \tag{A.32}$$

Hence, the total mean volume flow rate through the cylinder, Q_t, can be found by multiplying this value by the total number of jet exit holes, n_J, which, for the case of the $z_J = 20mm$ cylinder, is $n_J = 116$:

$$Q_t = Q_J \times n_J = 11.9\ l/min \tag{A.33}$$

A.4 Laminar flow velocity profile

From Potter and Wiggert (2002) and Massey (2012):

For laminar, fully developed pipe-flow (Poiseuille flow), the velocity at any point is given by:

$$V = -\frac{1}{4\mu}\left(\frac{dp}{dx}\right)\left(r^2 - {r_i}^2\right) \tag{A.34}$$

Where r is the radius of the pipe, and r_i is the radial position between the centreline and wall of the pipe, such that $0 \leqslant r_i \leqslant r$.

The maximum velocity occurs at the centreline of the pipe, where $r_i = 0$:

$$V_{max} = -\frac{dp}{dx}\left(\frac{r^2}{4\mu}\right) \tag{A.35}$$

Integrating for the volume flow rate over the cross-section of the pipe:

$$Q = -\frac{dp}{dx}\left(\frac{\pi r^4}{8\mu}\right) \tag{A.36}$$

...and dividing by the pipe cross-sectional area to get the mean velocity:

$$\overline{V} = -\frac{dp}{dx}\left(\frac{r^2}{8\mu}\right) \tag{A.37}$$

Comparing Equation A.35 and Equation A.37 we see that the mean velocity is exactly half the maximum:

$$\overline{V} = \frac{1}{2}V_{max} \tag{A.38}$$

A.5 Note on the calculation methodology

The methodology outlined does not account for the fact that the flow in the 'pipes' for this experiment rarely transfer fully developed flow. The calculation for the entry length (length of pipe required to produce fully-developed flow) of a laminar pipe, from Cengel and Turner (2001):

$$L_h \approx 0.06Re \cdot d \tag{A.39}$$

Applying this to the actual jet flow rates acquired, the flow does not become fully developed over the length of the jet exit 'pipe' beyond $Re_D \approx 1.2 \times 10^5$, with only half of the length becoming fully developed below $Re_D \approx 8 \times 10^4$. Because the diameter of an air supply hole at the stagnation point is twice that of a jet exit hole (hence the area is four times that of a jet exit hole) but there are double the number of jets than there are supply holes, the Reynolds number for a supply pipe is half that of a jet exit pipe. Thus, from Equation A.39, the entry length for the supply holes is equal to that of the jet exit holes.

As such, from the acquired measurements of jet flow rates (section 6.3), flow does not fully develop over the stroke length of both the supply and jet exit pipes above $Re_D \approx 1.35 \times 10^5$, and beyond $Re_D \approx 8 \times 10^4$ the flow does not become fully developed over half the stroke length of both the supply and jet exit pipes. This means that the average friction factor in the 'pipes' will be higher than the constant evaluated from the linear relationship for laminar, fully developed flow (Equation A.8) used in the calculation method; the friction factor is highest at the pipe inlet where the thickness of the boundary layer is zero and decreases gradually

as the boundary layer thickens and fully developed flow is established, whereas for fully developed flow the friction factor can be assumed to be constant. The pressure drop is therefore highest at the entry regions to pipes and where the flow is not fully developed – this can add significantly to the average friction factor over the length of short pipes and should be considered in applications of this type. It is clear, from a comparison of jet flow rates calculated using Equation A.26 and the measured values detailed in section 6.3 for the $z_J = 20mm$ cylinder, that the mathematical model developed for the prediction of jet flow rates closely matches the measured data at low to mid-range values of Re_D, but that for $Re_D \geqslant 1.2 \times 10^5$ it increasingly overestimates the jet velocity, perhaps as a result of failing to take account of the increased entry lengths, L_h, of the supply and jet exit pipes (and hence increased friction losses) as Reynolds number increases.

Appendix B

Feasibility study: Supplementary test results

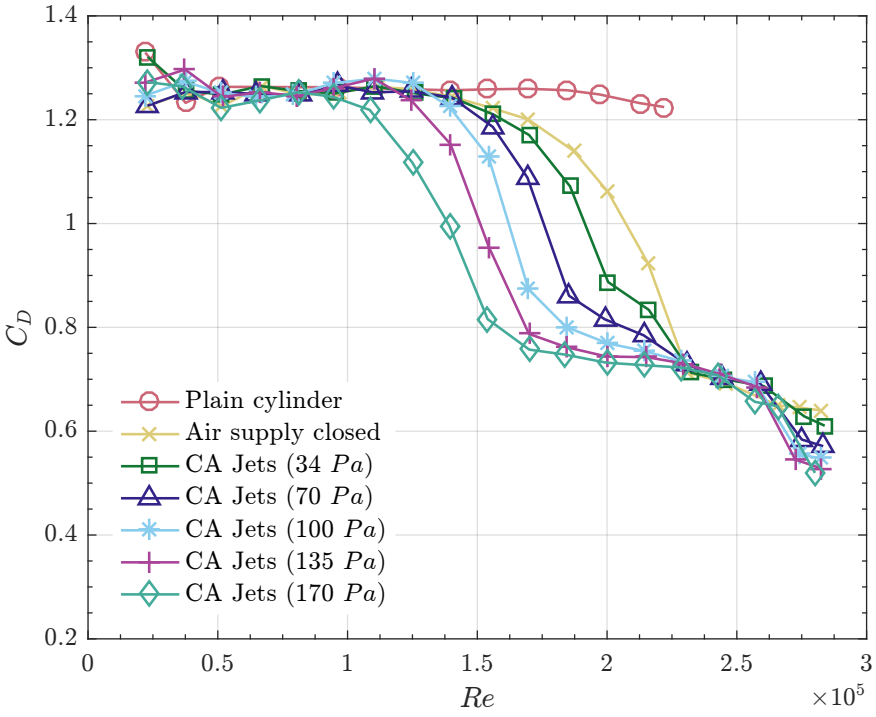
1.4
1.2
1
0.8
0.6
0.4
0.2
C_D
0
0.5
1
1.5
2
2.5
3
Re
$\times 10^5$
Plain cylinder
Air supply closed
CA Jets (34 Pa)
CA Jets (70 Pa)
CA Jets (100 Pa)
CA Jets (135 Pa)
CA Jets (170 Pa)

(a)

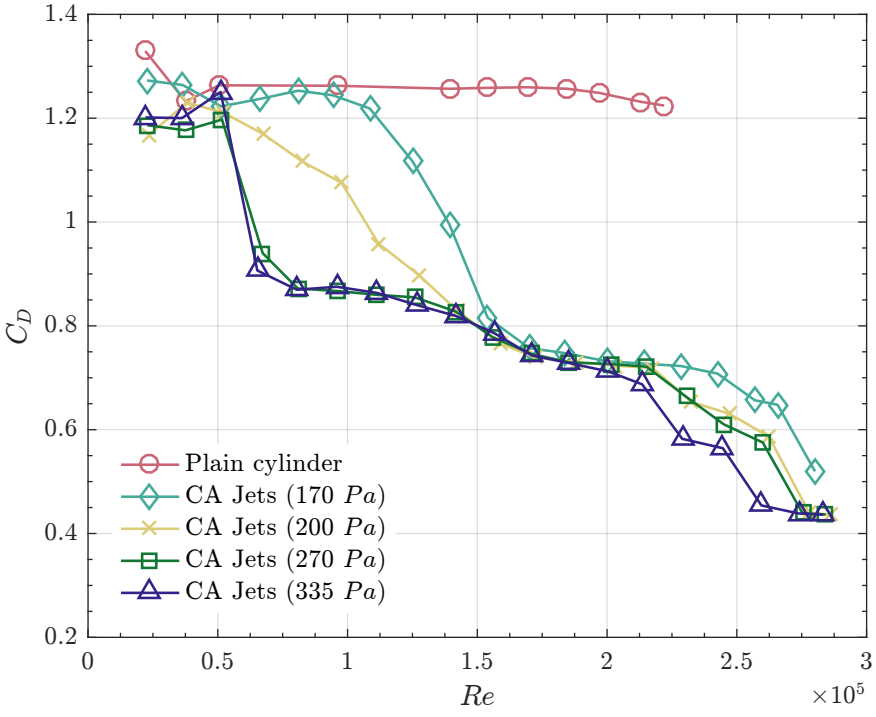
1.4
1.2
1
0.8
0.6
0.4
0.2
C_D
0
0.5
1
1.5
2
2.5
3
Re
$\times 10^5$
Plain cylinder
CA Jets (170 Pa)
CA Jets (200 Pa)
CA Jets (270 Pa)
CA Jets (335 Pa)

(b)

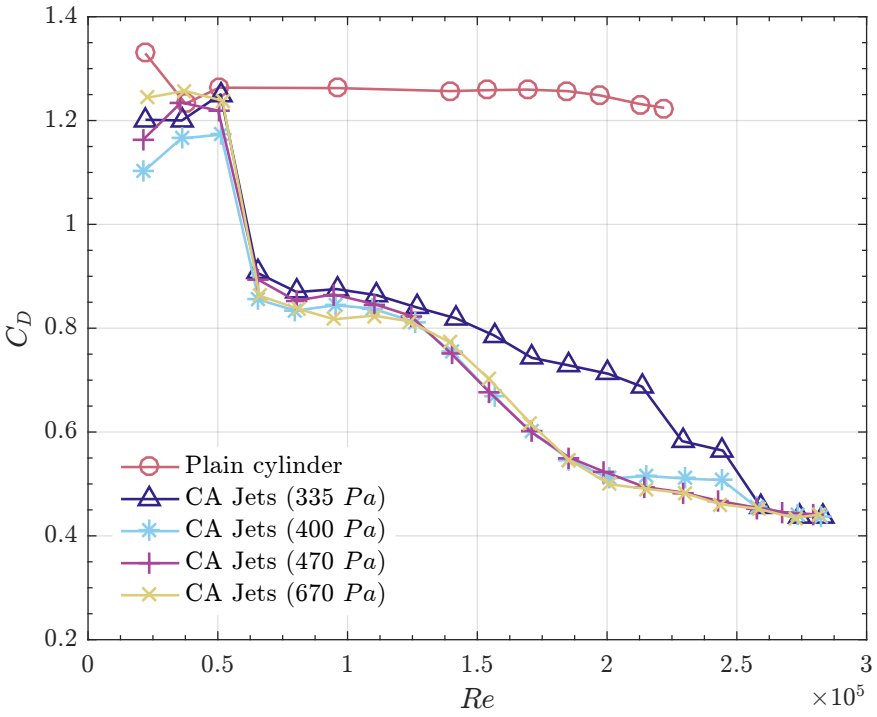

(c)

Figure B.1 – C_D v. Re curves for various levels of added cylinder pressure, conducted as part of a feasibility study for passive jets, with reference to a plain cylinder. See the preceding page for figures (a) and (b). A compressed air (CA) supply was used to maintain a fixed amount of additional pressure, p_{add}, to the internal cylinder volume (noted in brackets) over the following ranges: (a) $0 \leqslant p_{add} \leqslant 170\ Pa$; (b) $170 \leqslant p_{add} \leqslant 335\ Pa$; and, (c) $335 \leqslant p_{add} \leqslant 670\ Pa$.

Based on the pipe-flow calculations (see preceding sections in appendix Appendix A) and pressure measurements of the feasibility study (Figure B.1), a table of values for C_D v. Re was produced and is plotted in Figure B.2 on 360 along with the actual results from the passive jets cylinder arrangement (see section 5.3).

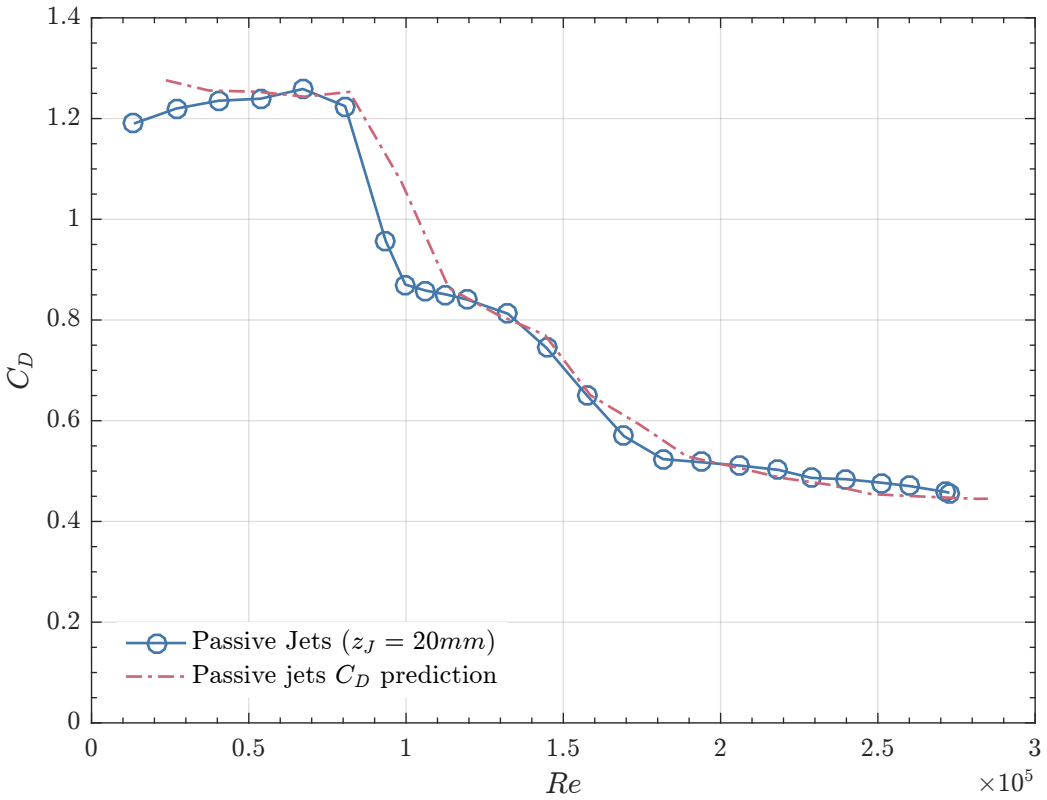

Figure B.2 – C_D v. Re results for 20mm spaced passive jets overlaid with the prediction made from the feasibility study.

Appendix C

Mass flux coefficient, C_J, of passive jets system

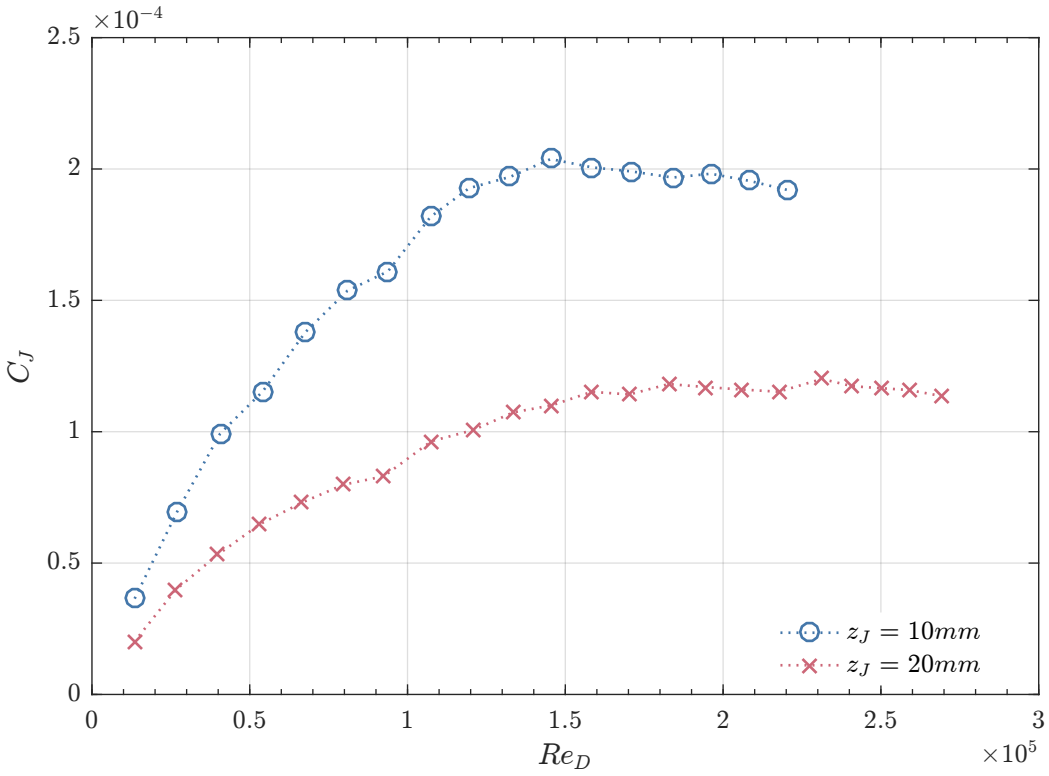

Figure C.1 – Variation of mass flux coefficient, C_J, with cylinder Reynolds number, Re_D for two passive jet arrangements . The cylinder with $z_J = 10mm$ spacing had a total of 230 passive jets along the span (two rows of 115 jets, positioned $\phi_J = \pm 65°$), whereas the $z_J = 20mm$ spacing setup had 116 passive jets (two rows of 58 jets, positioned $\phi_J = \pm 65°$). See Equation 5.1 for details of mass flux coefficient calculation.

Appendix D

von Kármán vortex shedding: Supplementary periodogram covering full Re_D test range

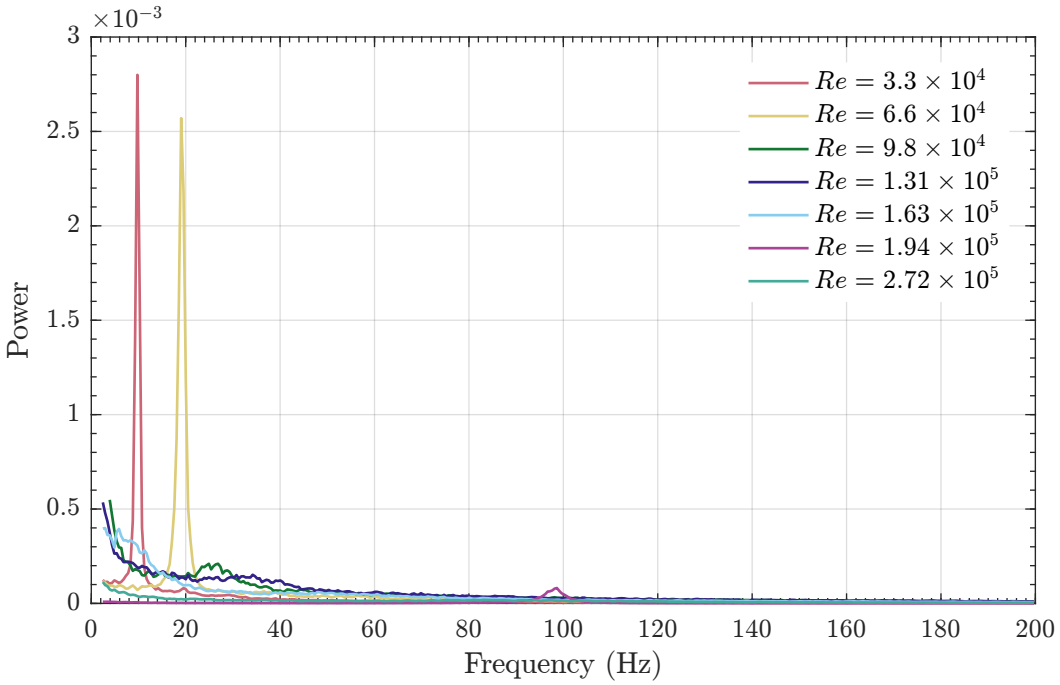

Figure D.1 – Plot of power spectral density (PSD) of cylinder wake with passive jets showing an absence of any signal peak to indicate von Kármán vortex shedding above $Re = 6.6 \times 10^4$. There is a weak 'hump' peaking at $98.6Hz$, which only appears in the PSD for $Re = 1.94 \times 10^5$, equating to $St = 0.33$; a Strouhal number of this value could exist around the critical regime – see for example Bearman (1969) – however it is difficult to explain how a regular shedding could appear suddenly for this Re and not be found at surrounding Re. As such, it is thought that this could be a natural frequency of the hot wire probe holder which may have been excited at this particular flow speed.

Appendix E

Jet instability: Supplementary periodograms

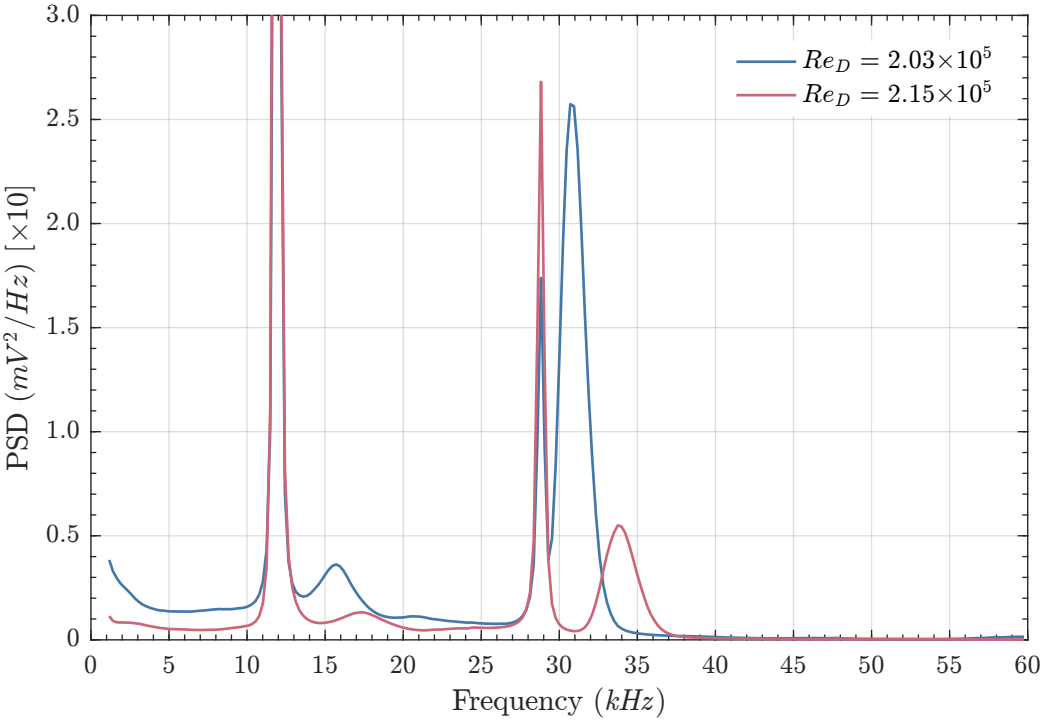

Figure E.1 – Periodogram of hot-wire signal acquired in immediate vicinity of jet exit hole, indicating the frequency of the jet instability in the range $2.03 \times 10^5 \leqslant Re \leqslant 2.15 \times 10^5$. As Re_D increases, the standing waves increase in prominence on the PSD as the ability to pick up a strong signal from the jet instability diminishes; the reduction in thickness of the boundary layer (within which the jet emission was largely contained) and increased dynamic pressure on the hot-wire probe made it very difficult to position the hot-wire within the detection region of the jet instability at high Re. Here, standing waves of $12kHz$ and $29kHz$ overshadow the jet shear layer instabilities found at $30.7kHz$ and $33.8kHz$ for $Re_D = 2.03\times10^5$ and $Re_D = 2.15\times10^5$ respectively.

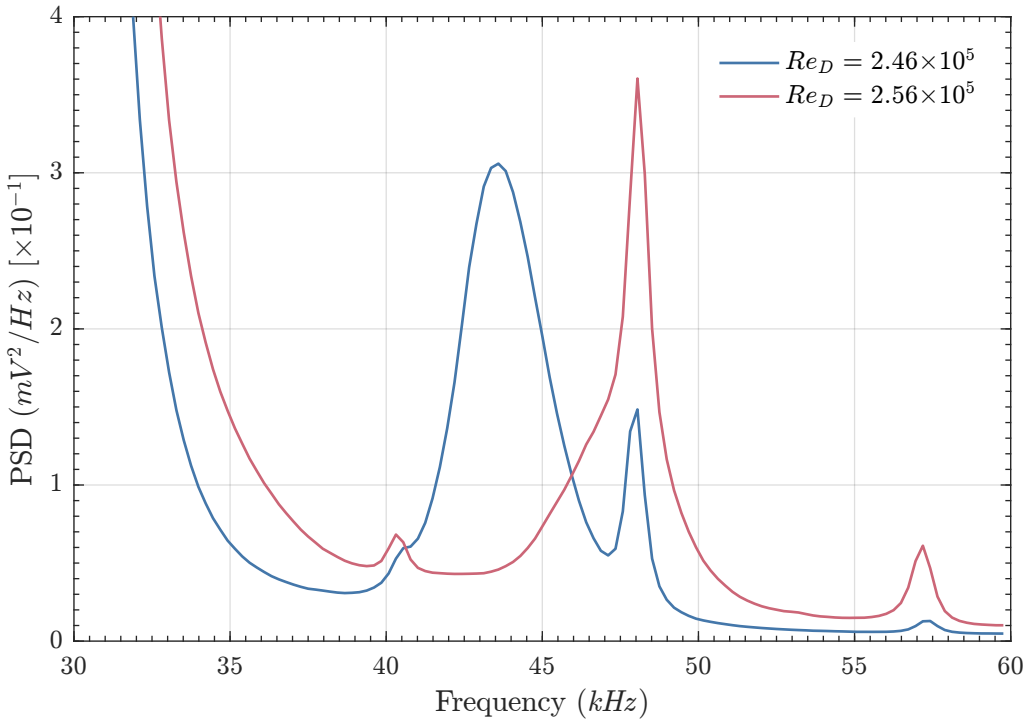

Figure E.2 – Periodogram of hot-wire signal acquired in immediate vicinity of jet exit hole, indicating the frequency of the jet shear layer instability in the range $2.46 \times 10^5 \leqslant Re_D \leqslant 2.56 \times 10^5$. Detection of the instability is weak but still identifiable in the PSD trace by its characteristically smooth, broadband peak of frequencies and correlation with the trend found at lower Re_D. Here, the signal of the instability at $Re_D = 2.56 \times 10^5$ has been subsumed by a sharp peak indicating a standing wave at approximately $48kHz$, but can still be made out by the shallower gradients of the trunk of this peak in the region $(44 \leqslant f(kHz) \leqslant 47$ and $49 \leqslant f(kHz) \leqslant 51)$ with the peak of the jet instability estimated to occur around $47.5kHz$.

Appendix F

Flow topology: Supplementary results & graphics

F.1 Variation in skin friction line patterns with Re_D, $z_J = 10mm$ passive jets

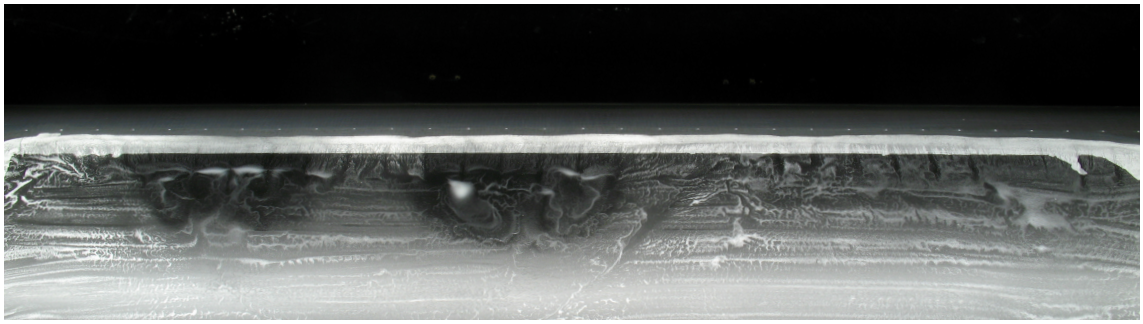

(a)



(b)

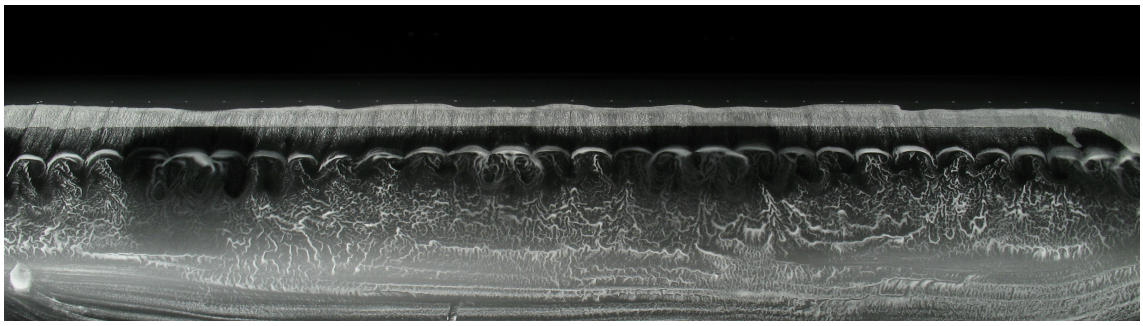

(c)

Figure F.1 – Figure continues with full caption on following page.

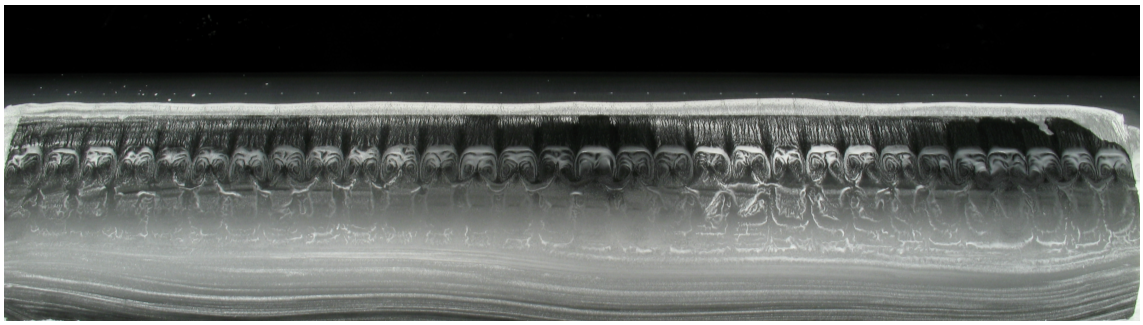

(d)

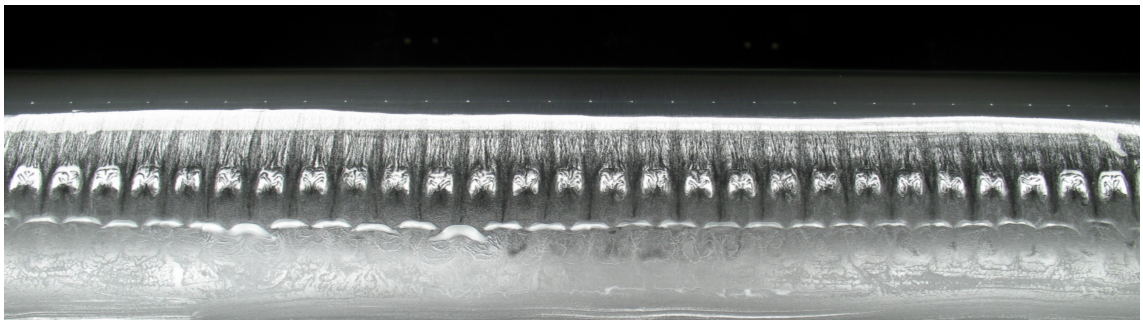

(e)

Figure F.1 – See preceding page for figures (a) – (c). Photographic comparison of surface oil flow visualisations (SOFV) on cylinder with passive jets, spaced at $z_J = 10mm$ intervals, throughout the Re_D testing range: (a) $Re_D = 0.94 \times 10^5$; (b) $Re_D = 1.13 \times 10^5$; (c) $Re_D = 1.38 \times 10^5$; (d) $Re_D = 1.70 \times 10^5$; and, (e) $Re_D = 2.74 \times 10^5$

F.2 Proof of attachment node, $z_J = 20mm$

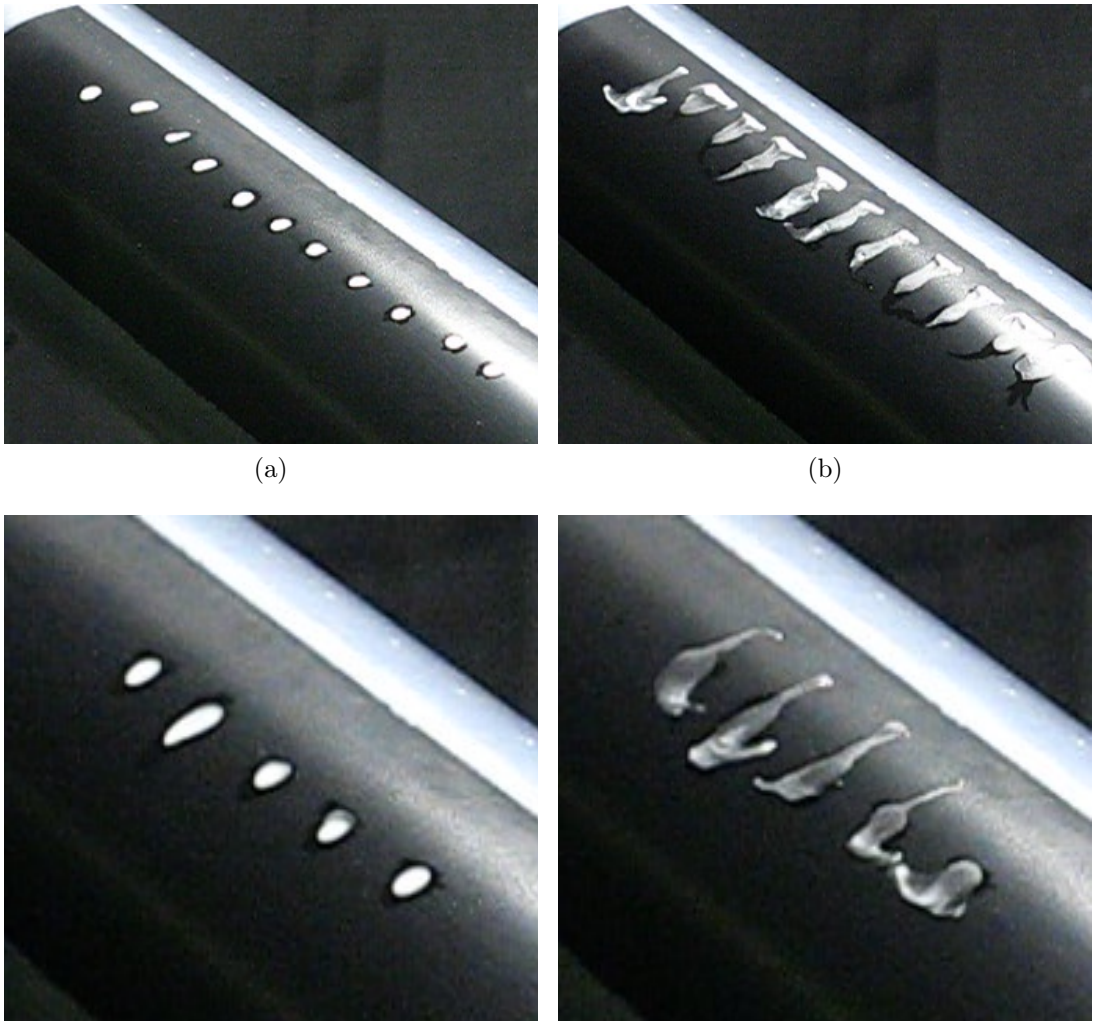

(a) (b)

(c) (d)

Figure F.2 – Experimental proof of (re)attachment node: SOFV tests were conducted by placing droplets of oil mixture in the predicted area of nodal attachment before bringing the wind tunnel quickly up to speed and observing the behaviour of the droplets. Images taken before and after two of these tests are shown here, showing that the droplets spread both upstream and downstream in a manner characteristic of fluid in the vicinity of an attachment node: (a) Test 1: Before; (b) Test 1: After; (c) Test 2: Before; (d) Test 2: After.

F.3 Alternative flow topology, owl type-2 skin friction pattern

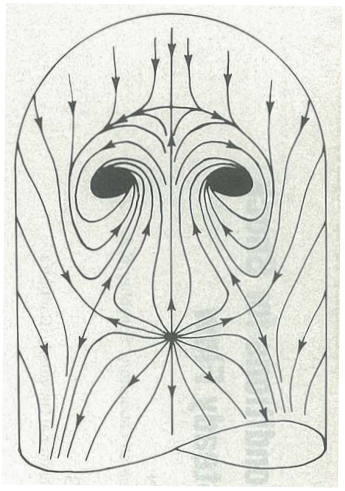

(a)

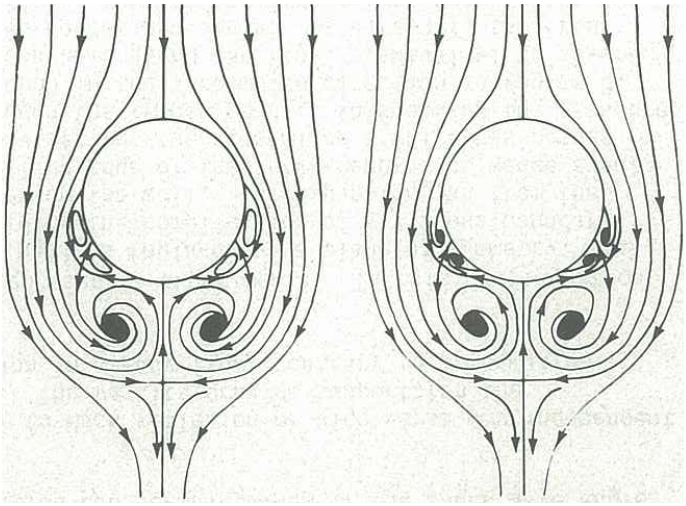

(b)

Figure F.3 – Skin friction lines and topology schematics of an 'owl type-2' separation bubble occurring on the leeward side of an inclined cylinder with hemispherical cap – from Fairlie (1980), where: (a) is an interpretation of skin friction lines and; (b) are two apparent solutions to the flow topology above the surface, in cross-sectional view.

Appendix G

Shear layer development & wake dynamics: Supplementary results

G.1 (x, y) plane

G.1.1 Cross-flow velocity, u/U_∞

Figure G.1 – (Plots on following page) PIV scalar plots in the (x, y) plane of non-dimensional local cross-flow velocity, u/U_∞, in the vicinity of $\phi = 65°$ from the stagnation point (marked by the black segment of the green cylinder outline). The free stream Reynolds number was $Re_{D,\infty} = 1.5 \times 10^5$. Data was acquired at two different span-wise locations: (a) in-line with a jet exit hole (the black marker represents the position and approximate size of the hole); and, (b) between two jet exit holes (the black marker is only a reference point for $\phi = 65°$). These plots clearly illustrate the difference in stream-wise flow velocity at different span-wise locations for the cylinder with passive jets; the velocity of the flow is significantly increased at the span-wise locations in-line with the jet exit holes, leading to a delayed separation point in comparison to the span-wise locations between the jets.

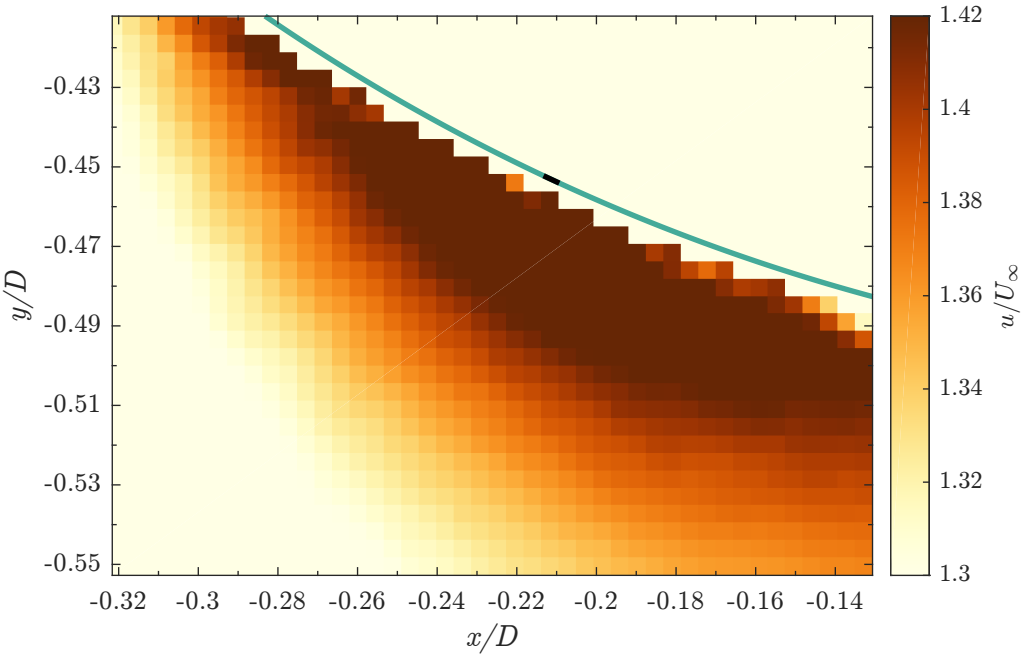

(a)

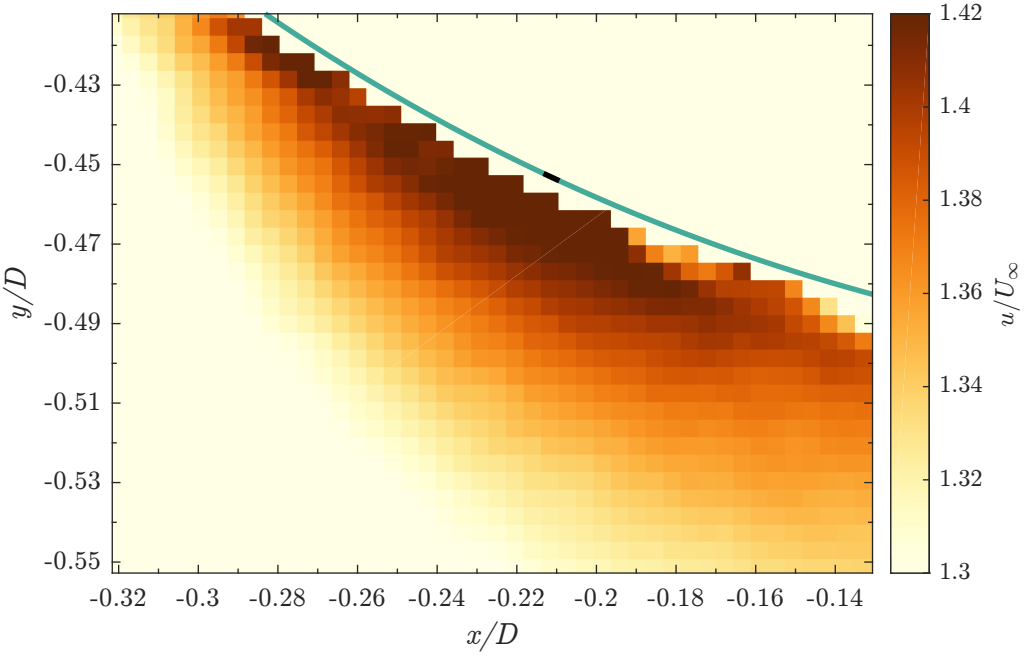

(b)

Figure G.1 – Caption on preceding page

G.1.2 Plots of u_x/U_∞ with full velocity scale

The following plots are scaled to give the full velocity range ($\bar{u}_x/U_\infty$) of the data acquired. Plots within the body of the thesis have foreshortened scales in order to accentuate particular features of the flow. Full scale plots are shown here for completeness.

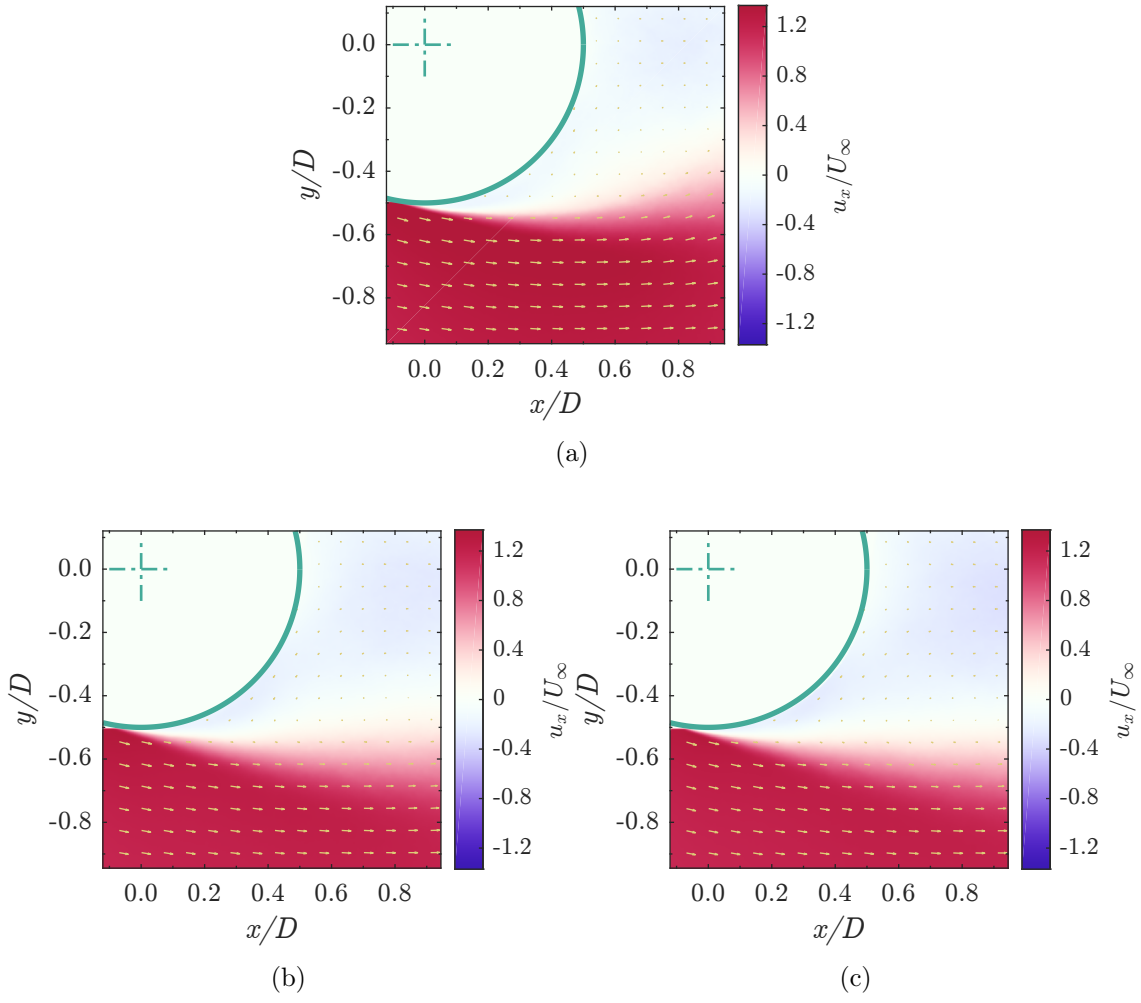

Figure G.2 – Mean u_x/U_∞ at full velocity scale for: (a) Plain cylinder; (b) Cylinder with passive jets, at span-wise position in line with jet exit hole; and, (c) Cylinder with passive jets, at span-wise position between two jet exit holes

The following plots in Figure G.3 are the stitched shear layer and wake formation region at full (non-dimensionalised) velocity scale, showing full diffusion of shear layer to free-stream at $Re = 1.5 \times 10^5$. See section 8.2 for more details on these plots. The colourbar here has been set to the common scale of ± the maximum local velocity of all sets shown (non-dimensionalised by free-stream velocity – uncorrected for blockage, u_x/U_∞), rather than the maximum velocity measured in each figure so that a direct comparison can be made of each setup. Note, however, that each test was conducted in dynamically similar conditions (i.e. Re_D was maintained at the same level for each experiment).

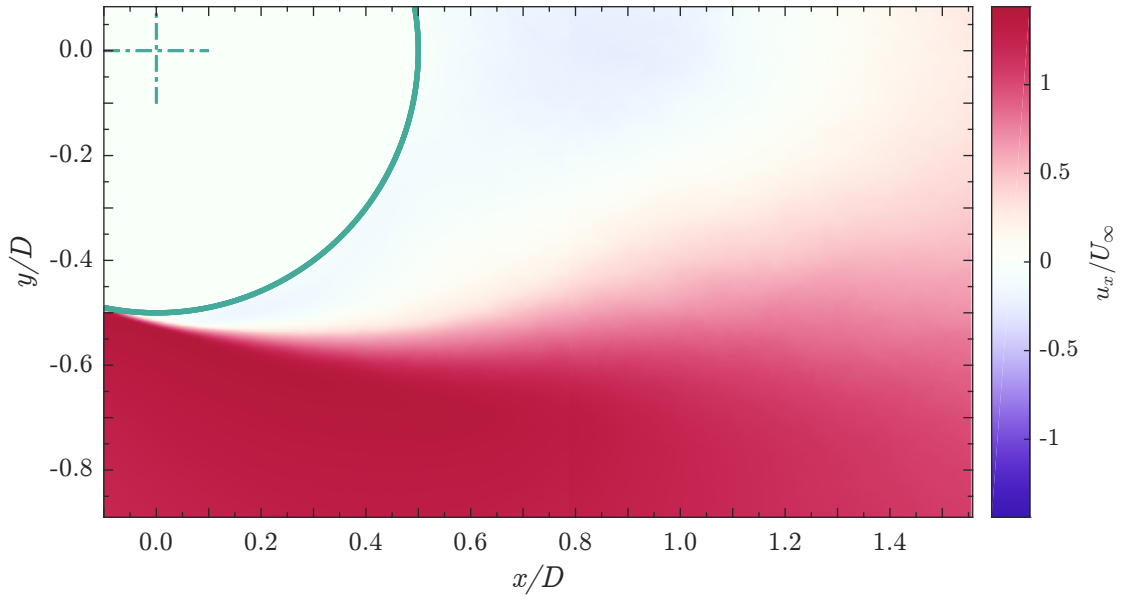

(a)

Figure G.3 – Figure continues with full caption on following page

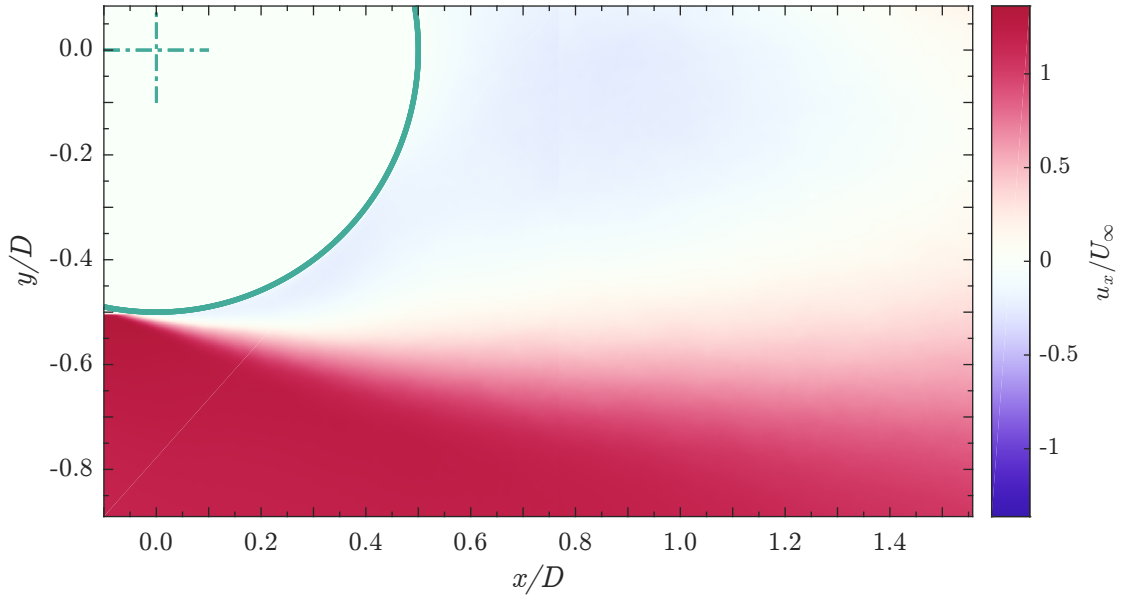

(b)

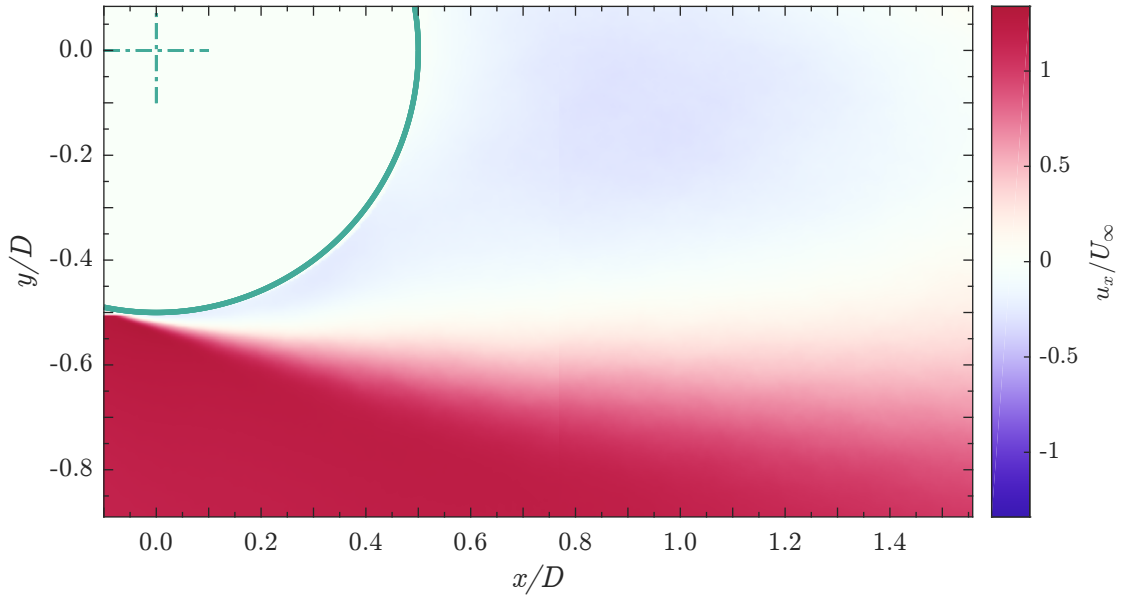

(c)

Figure G.3 – See preceding page for figure (a). Full velocity scale ($\bar{u}_x/U_\infty$) plots showing mean shear layer position, wake formation and diffusion at $Re = 1.5 \times 10^5$, for: (a) Plain cylinder; (b) Cylinder with passive jets, at span-wise position in line with jet exit hole; and, (c) Cylinder with passive jets, at span-wise position in between two jet exit holes

G.2 (y, z) plane

G.2.1 Plain cylinder reference data: Vorticity, Ω

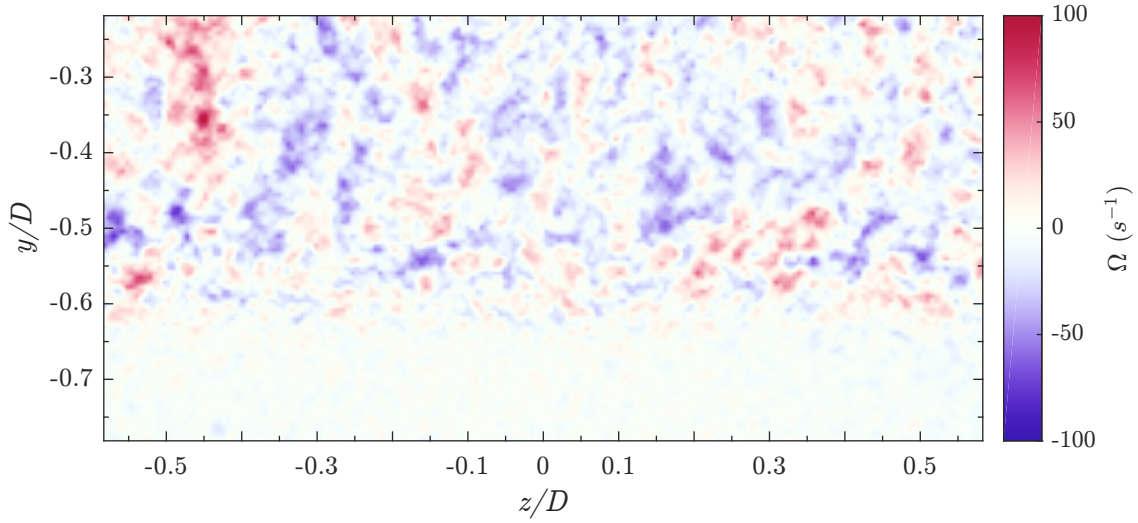

(a)

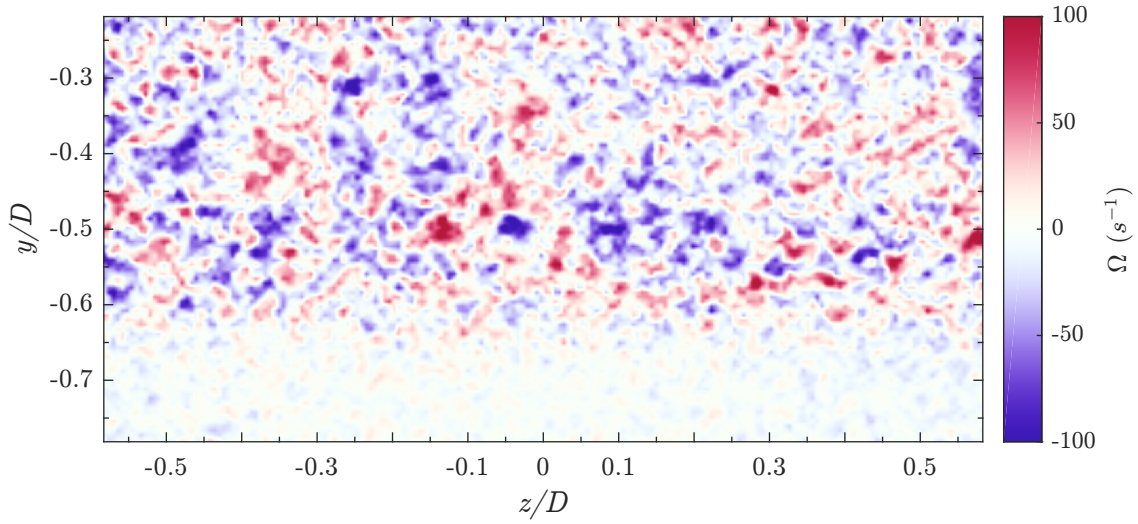

(b)

Figure G.4 – Near-wake vorticity in (y, z) plane, of a plain cylinder at: (a) $Re_D = 2.6 \times 10^4$; and, (b) $Re_D = 5.2 \times 10^4$. Figure continues on following pages – full caption follows final plot.

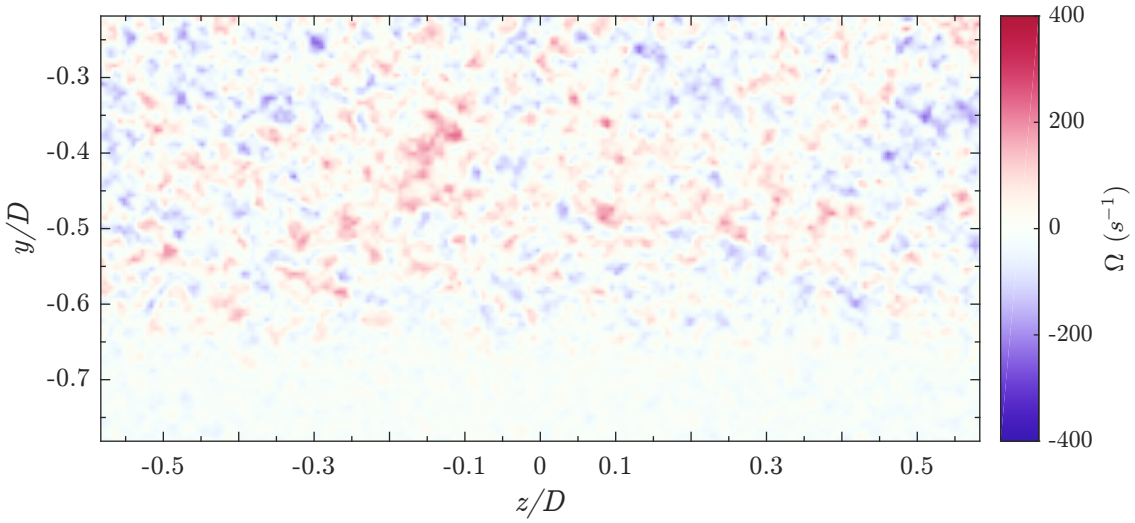

(c)

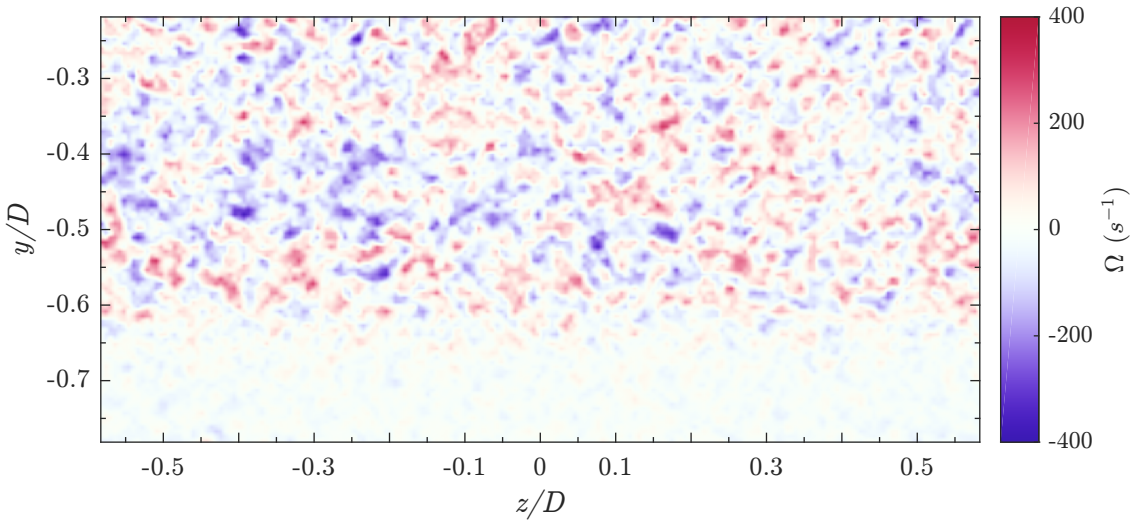

(d)

Figure G.4 – Near-wake vorticity in (y, z) plane, of a plain cylinder at: (c) $Re_D = 1.02 \times 10^5$; and, (d) $Re_D = 1.53 \times 10^5$. Figure continues with full caption on following page.

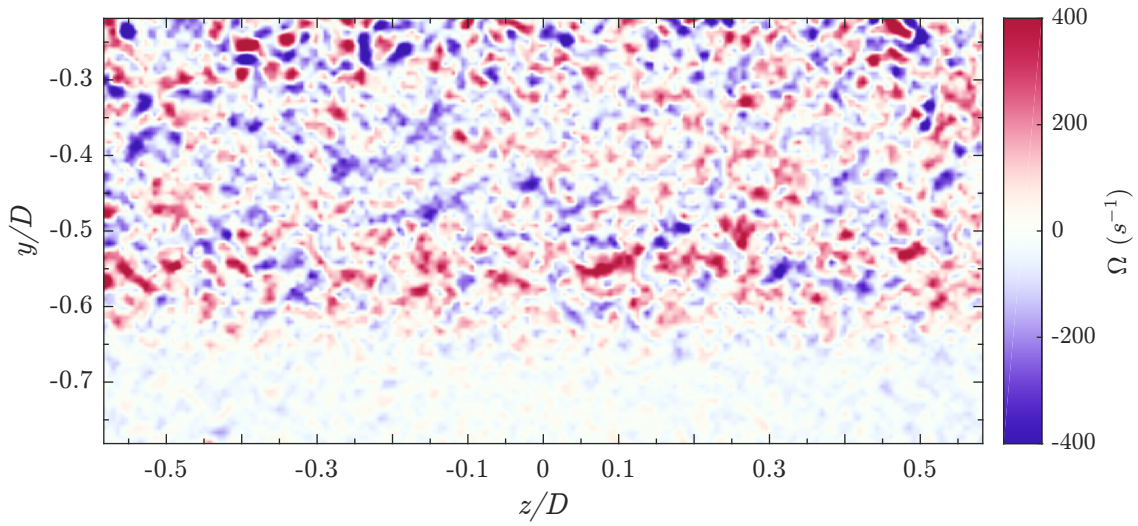

(e)

Figure G.4 – See preceding pages for figures (a) – (d). Time-mean vorticity, Ω, in the (y, z) plane of the near wake for a plain cylinder, at: (a) $Re_D = 2.6 \times 10^4$, $D/U_\infty = 25.6{\times}10^{-3}$; (b) $Re_D = 5.2{\times}10^4$, $D/U_\infty = 12.8{\times}10^{-3}$; (c) $Re_D = 1.02{\times}10^5$, $D/U_\infty = 6.40 \times 10^{-3}$; (d) $Re_D = 1.53 \times 10^5$, $D/U_\infty = 4.24 \times 10^{-3}$; and, (e) $Re_D = 2.54 \times 10^5$ (all uncorrected for blockage), $D/U_\infty = 2.54 \times 10^{-3}$.

G.2.2 Plain cylinder reference data: Free-stream velocity component, u_x/U_∞

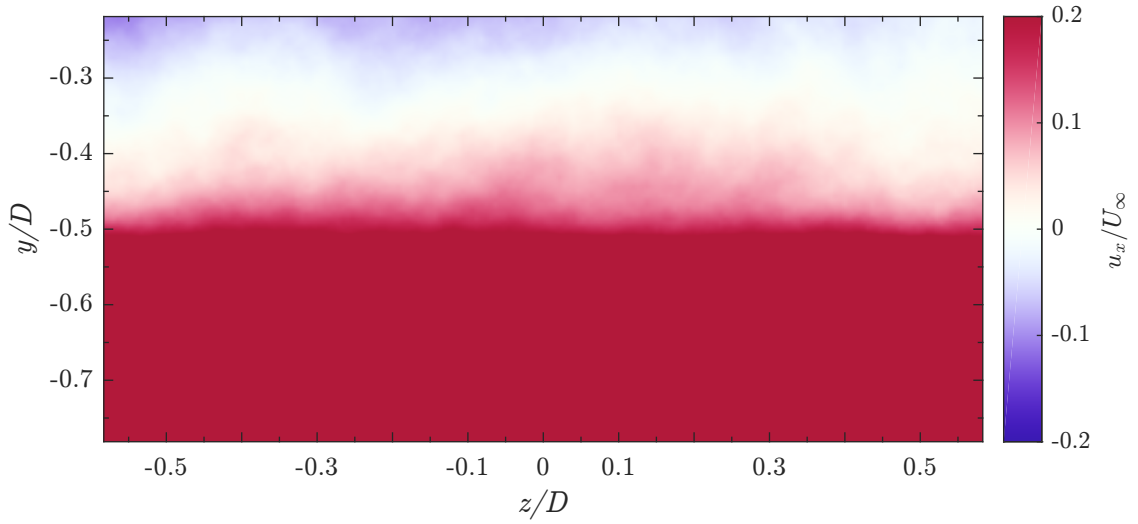

(a)

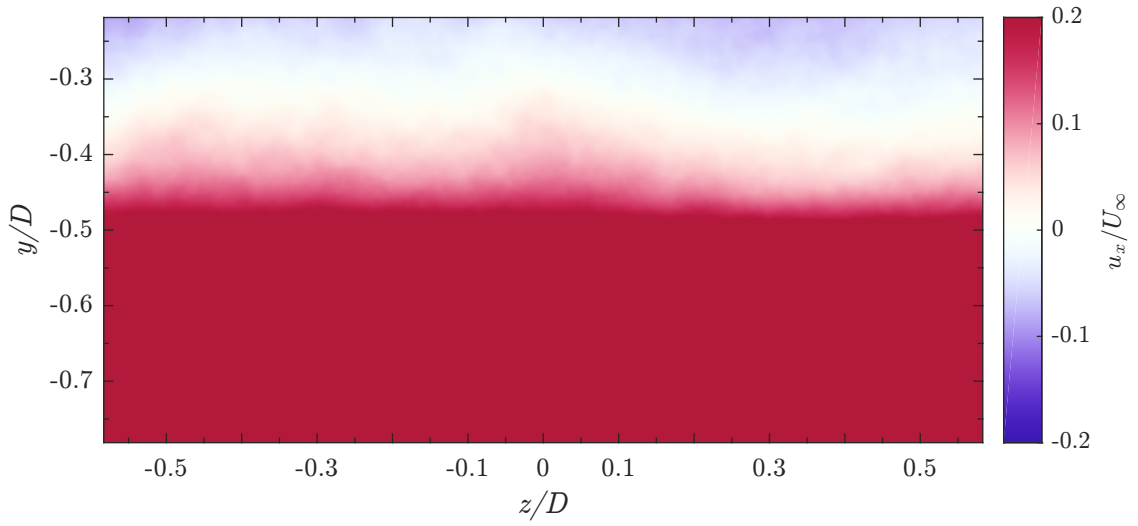

(b)

Figure G.5 – Mean u_x/U_∞ plotted in (y, z) plane of the near wake of a plain cylinder at: (a) $Re_D = 2.5 \times 10^4$; and, (b) $Re_D = 5.0 \times 10^4$. Figure continues on following pages – full caption follows final plot.

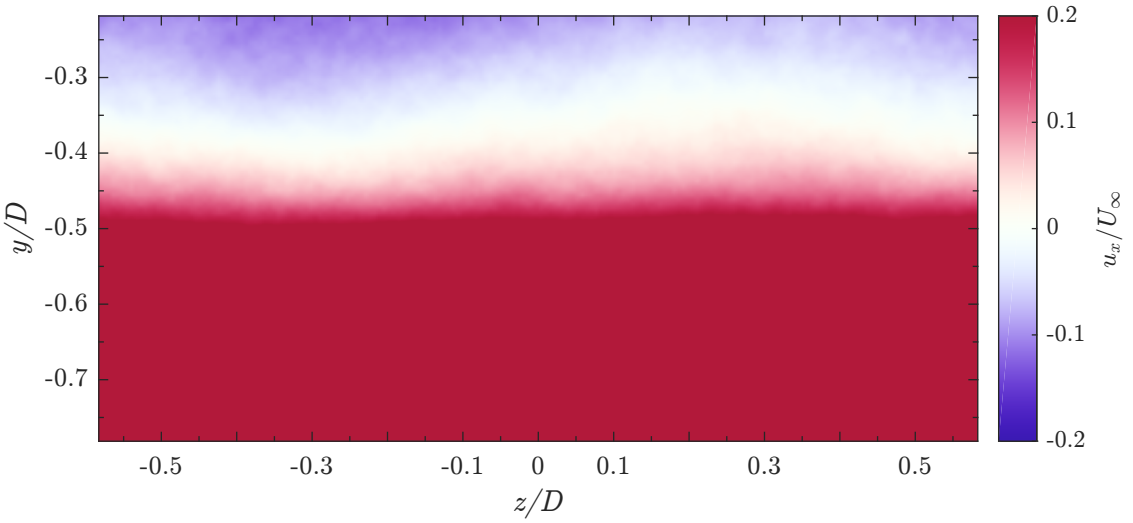

(c)

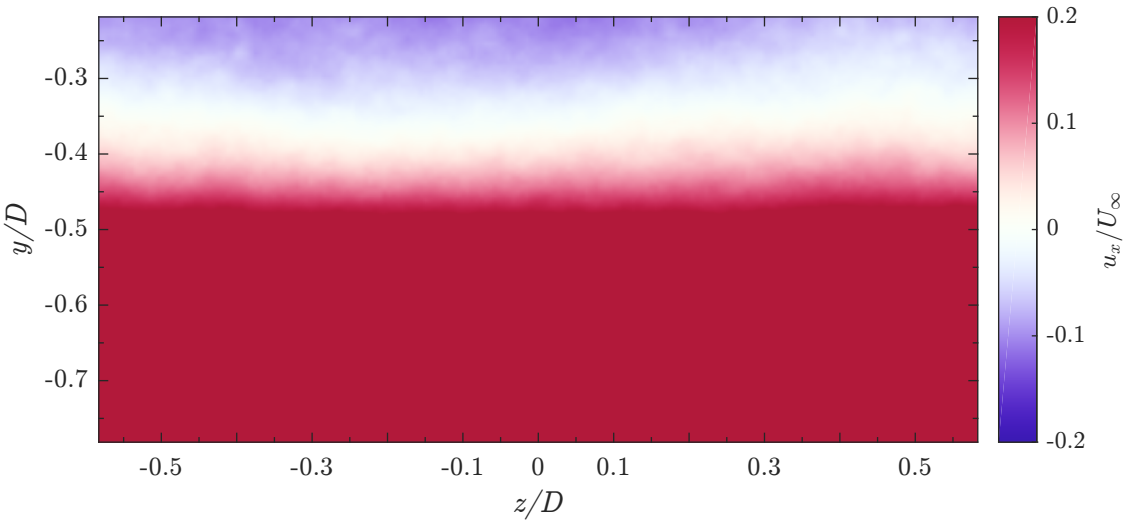

(d)

Figure G.5 – Mean u_x/U_∞ plotted in (y, z) plane of the near wake of a plain cylinder at: (c) $Re_D = 1.0 \times 10^5$; and, (d) $Re_D = 1.5 \times 10^5$. Figure continues with full caption on following page.

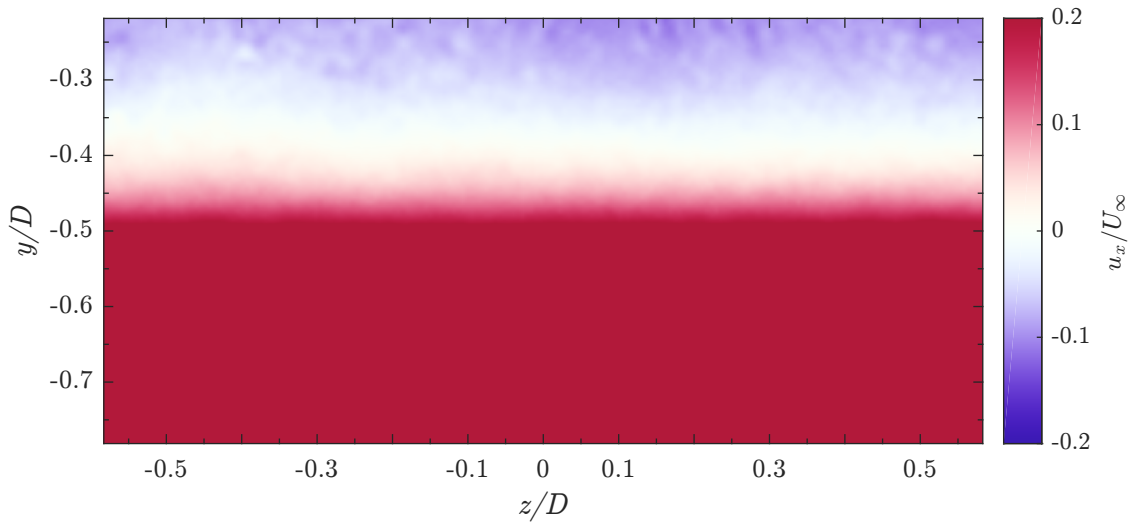

(e)

Figure G.5 – See preceding pages for figures (a) – (d). Plots of time-mean velocity in the free-stream direction (out of the page), u_x/U_∞, as viewed in the (y, z) plane of the near wake for a plain cylinder, at: (a) $Re_D = 2.5 \times 10^4$; (b) $Re_D = 5.0 \times 10^4$; (c) $Re_D = 1.0 \times 10^5$; (d) $Re_D = 1.5 \times 10^5$; and, (e) $Re_D = 2.5 \times 10^5$ (all uncorrected for blockage)

G.3 Near-wake u_x/U_∞ in (y, z) plane for cylinder with $z_P = 20mm$ pins

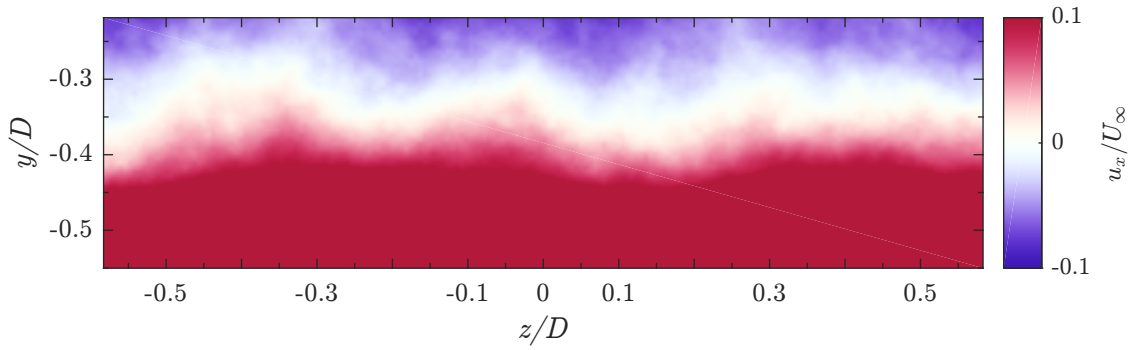

(a)

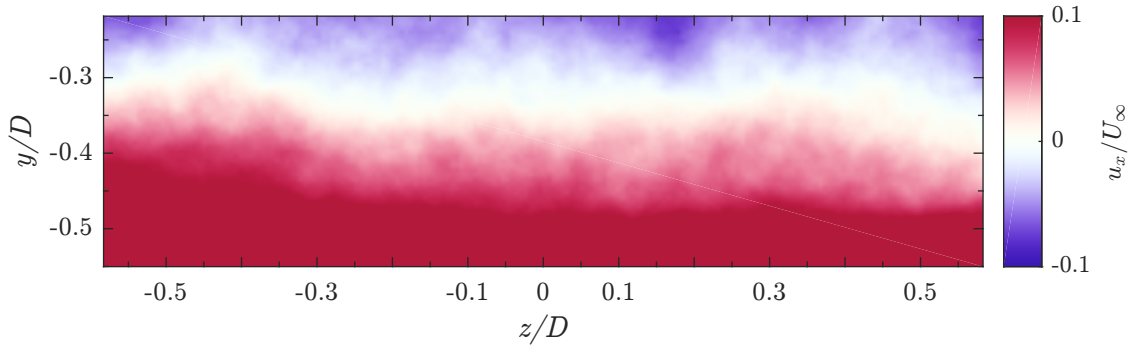

(b)

Figure G.6 – Mean u_x/U_∞ in (y, z) plane of the near wake of cylinder at $Re_D = 2.6 \times 10^4$, for: (a) $z_P = 20mm$ pins; and, (b) $z_J = 20mm$ passive jets. Figure continues on following pages – full caption follows final plot.

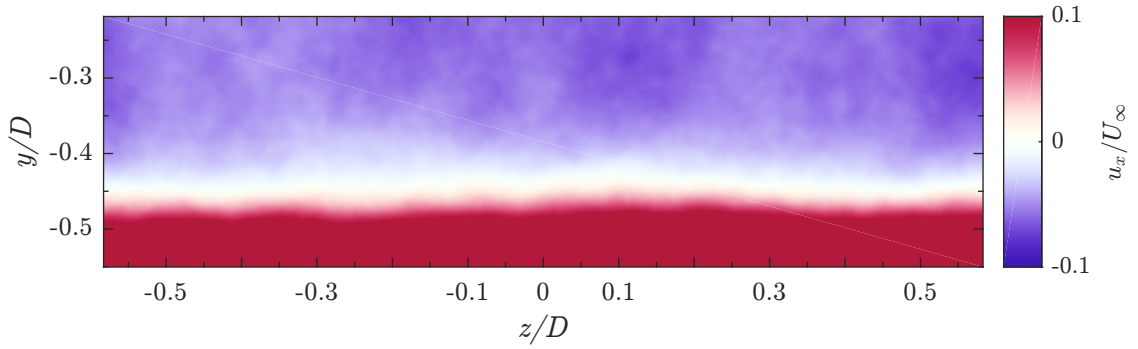

(c)

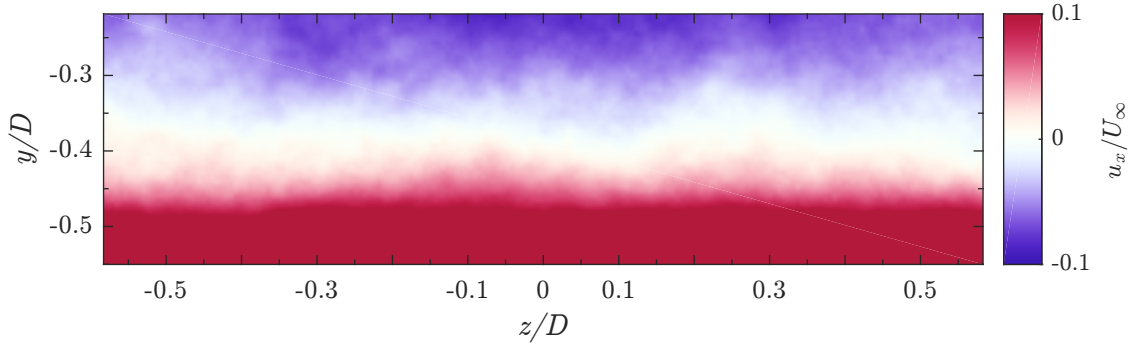

(d)

Figure G.6 – Mean u_x/U_∞ in (y, z) plane of the near wake of cylinder at $Re_D = 5.2 \times 10^4$, for: (c) $z_P = 20mm$ pins; and, (d) $z_J = 20mm$ passive jets. Figure continues on following pages – full caption follows final plot.

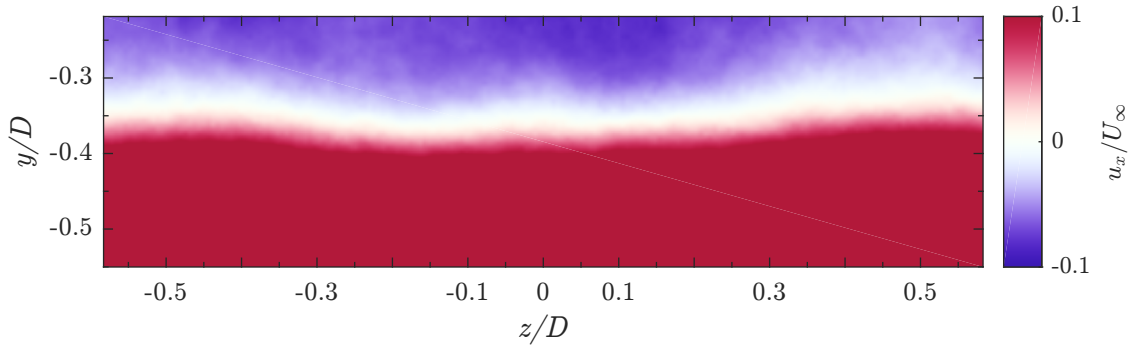

(e)

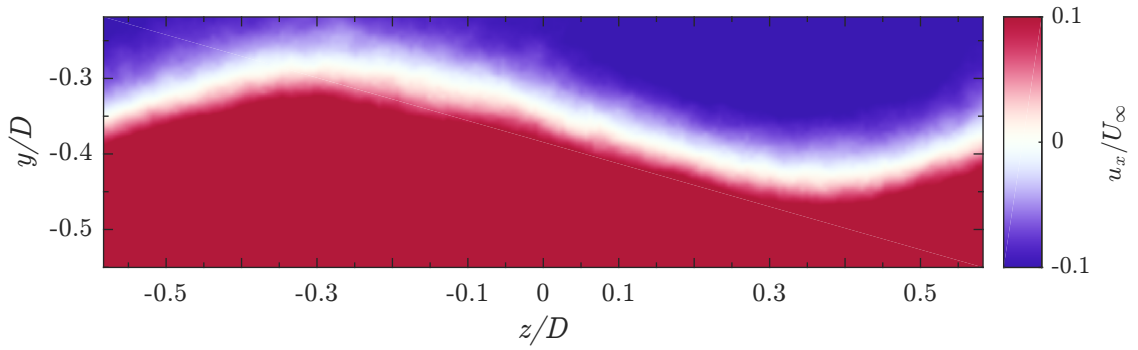

(f)

Figure G.6 – Mean u_x/U_∞ in (y, z) plane of the near wake of cylinder at $Re_D = 1.02 \times 10^5$, for: (e) $z_P = 20mm$ pins; and, (f) $z_J = 20mm$ passive jets. Figure continues on following pages – full caption follows final plot.

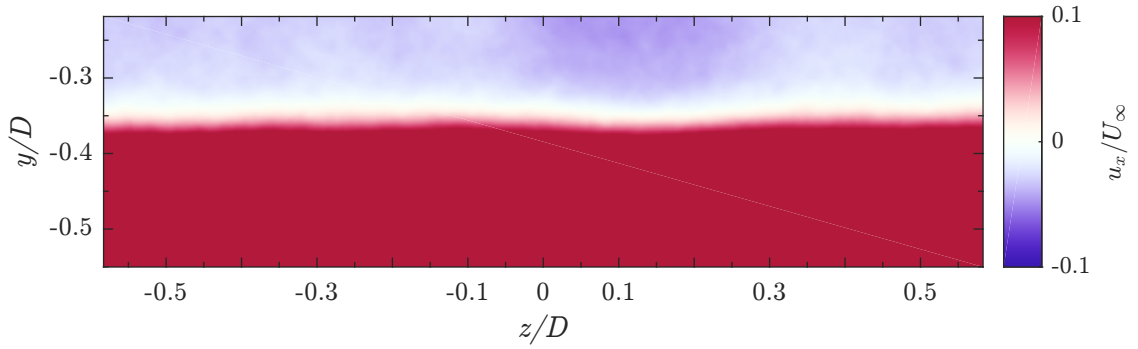

(g)

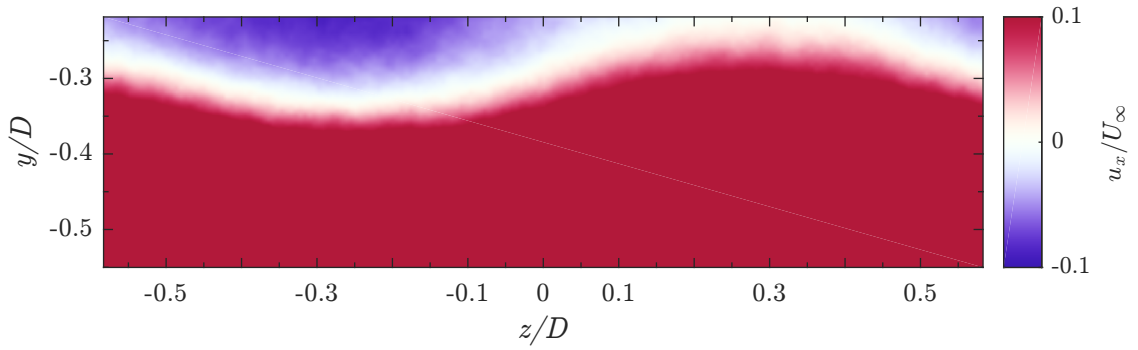

(h)

Figure G.6 – Mean u_x/U_∞ in (y, z) plane of the near wake of cylinder at $Re_D = 1.53 \times 10^5$, for: (g) $z_P = 20mm$ pins; and, (h) $z_J = 20mm$ passive jets. Figure continues on following pages – full caption follows final plot.

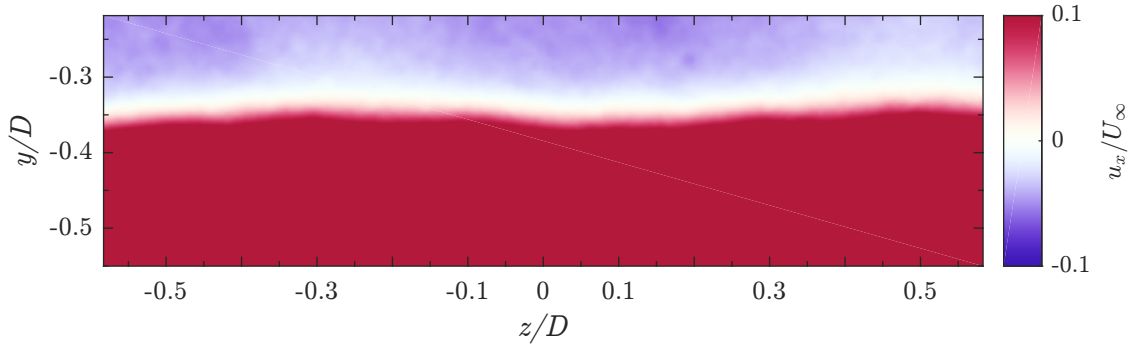

(i)

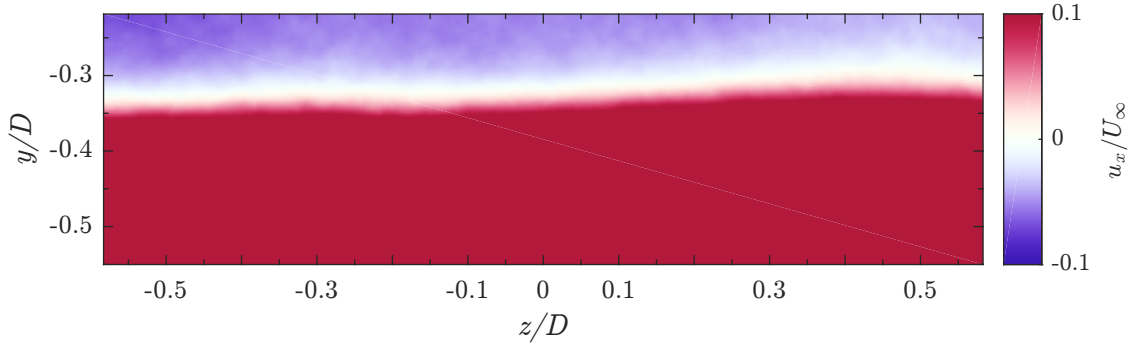

(j)

Figure G.6 – See preceding pages for figures (a) – (h). Comparisons of separated shear layer from a cylinder with either pins or passive jets flow control at various Re_D. Plots of time-mean velocity in the free-stream direction (out of the page), u_x/U_∞, as viewed in the (y, z) plane of the near wake of a cylinder, with: (a) $z_P = 20mm$ pins, $Re_D = 2.6 \times 10^4$; (b) $z_J = 20mm$ passive jets, $Re_D = 2.6 \times 10^4$; (c) $z_P = 20mm$ pins, $Re_D = 5.2 \times 10^4$; (d) $z_J = 20mm$ passive jets, $Re_D = 5.2 \times 10^4$; (e) $z_P = 20mm$ pins, $Re_D = 1.02 \times 10^5$; (f) $z_J = 20mm$ passive jets, $Re_D = 1.02 \times 10^5$; (g) $z_P = 20mm$ pins, $Re_D = 1.53 \times 10^5$; (h) $z_J = 20mm$ passive jets, $Re_D = 1.53 \times 10^5$; (i) $z_P = 20mm$ pins, $Re_D = 2.54 \times 10^5$; and, (j) $z_J = 20mm$ passive jets, $Re_D = 2.54 \times 10^5$.

Appendix H

Wind tunnel blockage corrections

Wind tunnel correction methods vary throughout the literature since no one-size-fits-all data revision exists which can appropriately account for the impact on all measured quantities – for the multitude of flow characteristics effected by all shapes of bluff and streamlined models – by all wind tunnels. In many cases the application of a particular 'correction' method is more a practical rule of thumb adjustment and it is doubtful whether any method can be said to be truly accurate outside of specific test cases. It is important to clearly state, therefore, the method of corrections made to the measured data – in the first instance to understand the method used, and in the second to provide readers a means of extracting the measured data from the presented results in order to re-apply different or additional forms of correction not used here.

Following the rationale of Bearman (1968) by considering the complete testing range of Reynolds number and values of C_D obtained in these experiments, it seemed reasonable to apply the method of Allen and Vincenti (1944) in the majority of cases, and as a practical measure it was used for all testing arrangements. Accordingly, the equations used to correct the measured values of U_∞, C_D, C_L and C_p are outlined. For incompressible flow, corrections to Reynolds number, Re, scale accordingly with the corrected value for velocity, U:

$$\frac{Re}{Re_m} = \frac{U}{U_m} \tag{H.1}$$

... where U_m and Re_m are the measured values of velocity and Reynolds number, respectively.

H.1 Free stream velocity , U_∞

The corrected free stream velocity, U_∞, is given by:

$$U_\infty = U_{\infty,m}\left\{1 + \frac{1}{\left(1 - {M_m}^2\right)^{3/2}}\Lambda\sigma + \frac{1 + 0.4{M_m}^2}{1 - {M_m}^2}\tau C_{D,m}\right\} \tag{H.2}$$

... where $C_{D,m}$ is the measured value of drag coefficient. The dimensionless body-shape factor, Λ, is taken from Table I of Allen and Vincenti (1944); for a cylindrical body with an (x, y)-plane aspect ratio of 1.0, $\Lambda = 4.0$.

The two blockage coefficients, σ and τ, are given by:

$$\sigma = \frac{\pi^2}{48}B^2 \tag{H.3}$$

$$\tau = \frac{1}{4}B \tag{H.4}$$

... where, given the cylinder model and 'dummy' ends extend the full width of the tunnel, the blockage ratio, B, is defined here as:

$$B = \left(\frac{D}{H}\right) \tag{H.5}$$

... where D is the cylinder diameter and H is the height of the wind tunnel working section. Inputting the above expressions into Equation H.2 and noting that, for incompressible flow, the measured Mach number, $M_m \to 0$, the free steam velocity correction becomes:

$$U_\infty = U_{\infty,m}\left\{1 + \frac{\pi^2 B^2}{12} + \frac{B}{4}C_{D,m}\right\} \tag{H.6}$$

H.2 Drag coefficient, C_D

The corrected drag coefficient, C_D, is given by:

$$C_D = C_{D,m}\left\{1 - \frac{3 - 0.6{M_m}^2}{\left(1 - {M_m}^2\right)^{3/2}}\Lambda\sigma - \frac{\left(2 - {M_m}^2\right)\left(1 + 0.4{M_m}^2\right)}{1 - {M_m}^2}\tau C_{D,m}\right\} \tag{H.7}$$

...where $C_{D,m}$, M_m, Λ, σ and τ are as defined in Appendix H.1 for the free stream velocity correction. Similarly, assuming incompressible flow, $M_m \to 0$, and simplifying, the corrected drag coefficient, C_D, becomes:

$$C_D = C_{D,m}\left\{1 - \frac{\pi^2 B^2}{4} - \frac{B}{2}C_{D,m}\right\} \tag{H.8}$$

H.3 Lift coefficient , C_L

The corrected lift coefficient, C_L, is given by:

$$C_L = C_{L,m}\left\{1 - \frac{\sigma}{1 - {M_m}^2} - \frac{2 - {M_m}^2}{\left(1 - {M_m}^2\right)^{3/2}}\Lambda\sigma - \frac{\left(2 - {M_m}^2\right)\left(1 + 0.4{M_m}^2\right)}{1 - {M_m}^2}\tau C_{D,m}\right\} \tag{H.9}$$

...where $C_{L,m}$ is the measured value of lift coefficient. Following the procedure as before for velocity (Appendix H.1) and drag coefficient (Appendix H.2), the corrected lift coefficient, C_L, becomes:

$$C_L = C_{L,m}\left\{1 - \frac{3\pi^2 B^2}{16} - \frac{B}{2}C_{D,m}\right\} \tag{H.10}$$

H.4 Pressure coefficient, C_p

The corrected pressure coefficient, C_p, is given by:

$$C_p = 1 - \left(\frac{U_m}{U}\right)^2 (1 - C_{p,m}) \tag{H.11}$$

... where $C_{p,m}$ and U_m are the measured values of pressure coefficient and velocity, respectively. The following explicitly outlines the derivation of Equation H.11 from Allen and Vincenti (1944):

For the correction of wind tunnel pressure coefficient measurements, Allen and Vincenti use the following relation:

$$S_p = S_{p,m}\left(\frac{q_m}{q}\right) \tag{H.12}$$

... where q is the dynamic pressure, and S is the pressure coefficient based on the total pressure, p_0:

$$S = \frac{p_0 - p}{q} \tag{H.13}$$

This is related to the static pressure coefficient, C_p by:

$$S = (1 + \eta) - C_p \tag{H.14}$$

... where η is a compressibility factor. For incompressible flow, $\eta \to 0$, hence for these experiments:

$$S = (1 - C_p) \tag{H.15}$$

By combining Equation H.15 with Equation H.12:

$$(1 - C_p) = (1 - C_{p,m}) \left(\frac{q_m}{q} \right) \tag{H.16}$$

Thus, for an isodensity, incompressible flow, the dynamic pressure ratio simplifies to a squared velocity ratio and the corrected pressure coefficient, C_p, is therefore reduced to Equation H.11.